Deliverable 4.5: Technical report describing numerical method improvement and their transferability in numerical tools as well as benchmarks realization.

Work Package Development/improvement of numerical methods & tools for modelling coupled processes (DONUT)

The project leading to this application has received funding from the European Union's Horizon 2020 research and innovation programme under grant agreement No 847593.

Document information

Project Acronym	**EURAD**
Project Title	**European Joint Programme on Radioactive Waste Management**
Project Type	**European Joint Programme (EJP)**
EC grant agreement No.	**847593**
Project starting / end date	**1st June 2019 – 30 May 2024**
Work Package No.	**4**
Work Package Title	**D**evelopment and Improvement **O**f **NU**merical methods and **T**ools for modelling coupled processes
Work Package Acronym	**DONUT**
Deliverable No.	**4.5**
Deliverable Title	**Technical report describing numerical method improvement and their transferability in numerical tools as well as benchmarks realization**
Lead Beneficiary	**Andra**
Contractual Delivery Date	**M52**
Actual Delivery Date	**M60**
Type	**Report**
Dissemination level	**PU**
Authors	**Clement Cancès (INRIA) and Francis Claret (BRGM) compiled a multi authors contribution. For each contribution compiled in this document an author list is associated**

To be cited as:

Cancès, C. Claret, F. (2024): Technical report describing numerical method improvement and their transferability in numerical tools as well as benchmarks realization. Final version as of 16.05.2024 of deliverable D4.5 of the HORIZON 2020 project EURAD. EC Grant agreement no: 847593.

Disclaimer

Acknowledgement

This document is a deliverable of the European Joint Programme on Radioactive Waste Management (EURAD). EURAD has received funding from the European Union's Horizon 2020 research and innovation programme under grant agreement No 847593.

Status of deliverable		
	By	Date
Delivered (Lead Beneficiary)	Andra	16.05.2024
Verified (WP Leader)	F. Claret	10.05.2024
Reviewed (Reviewers)	Several experts from Andra	22.04.2024
Approved (PMO)	B. Grambow	14.05.2024
Submitted to EC	Andra (Coordinator)	17.05.2024

Executive Summary

Task 2 on Numerical methods for high performance computing of coupled processes of the DONUT work-package aimed at the development of numerical models for the simulation of several highly complex physical phenomena that play a key role in the context of subsurface geological storage. A well identified challenge is to understand the migration of gas, especially of H2, in a complex porous medium that has been impacted by the digging process. Here a link was done during the project with the WP GAS. H2 production is linked to iron corrosion, and one contribution is about the modelling of iron corrosion at the level of the thin magnetite layer covering the iron canisters where radioactive wastes are stored, bearing in mind the second principle of thermodynamics.

Then several contributions are about the simulation of complex flows in natural or engineered porous media in order. The goal is to assess the impact of various factors on the possibly multiphase and multi-component flows occurring around subsurface repositories. Challenges could be of modelling nature, as one aims at finely understanding the behaviour of (hypo-)plastic and low permeability deformable porous media, as it is the case for instance of the bentonite. The robust and accurate capture of severe capillary effects at material discontinuities for multiphase porous media flows was also the purpose of a research project presented hereafter, as well as the coupling of free flows in the gallery and porous media flows in the surrounding porous matrix. The simulation (and the coupling) of chemical, mechanical and thermal phenomena with the flow requires the development of efficient softwares, that can either be developed from scratch by contributors to this task (as for ORCHESTRA), or be larger codes on which contributors of this task do rely (DUMUX, PHREEQC, Flow123d,…).

Although one contribution presented below is of pure numerical nature analysis -- it is devoted to the certification thanks to a posteriori error estimator of the numerical approximation of contact problems in mechanics --, several contributions are focusing on adapted numerical strategies that are suitable to handle the multiphysics models required in the context of deep geological storage. The trade-off between computational efficiency and accuracy is central in a contribution where splitting strategies are investigated for highly coupled reactive porous media flows. The acceleration of reactive transport simulation thanks to the use of surrogate models for chemistry also shows to be a promising track towards a digital twin of the subsurface repositories..

The different contribution are organized by chapter as followed :

Thermodynamically consistent modelling of the corrosion of iron in the context of deep subsurface nuclear waste repositories

[1]Cancès, C., [1]Chainais-Hillairet, C., [1]Merlet, B., [2]Raimondi, F. and [3]Venel, J.

[1]Univ. Lille, CNRS, Inria, UMR 8524 - Laboratoire Paul Painlevé, F-59000 Lille, France

[2]Department of Mathematics, Università di Salerno, 84084, Fisciano, SA, Italy

[3]Univ. Polytechnique Hauts-de-France, CERAMATHS, FR CNRS 2037, F-59313 Valenciennes, France

The project leading to this application has received funding from the European Union's Horizon 2020 research and innovation programme under grant agreement No 847593.

Abstract

Corrosion occurring in subsurface nuclear waste repositories yields the production of dihydrogen (H_2), the possible accumulation of which being a major security concern. The development of accurate and theoretically assessed mathematical and numerical models is therefore a priority to quantify the *in situ* production of H_2 along large time scales. Despite important efforts of the mathematical community during the last 15 years, there is so far no satisfactory mathematical framework for the so-called Diffusion Poisson Coupled Model (DPCM) proposed by Bataillon and collaborators (Bataillon et al., 2012, 2010). This model describes the evolution of the oxide layer covering the metal by taking into account the oxidation of the metal, the transfer within the oxide layer of the charge carriers driven by some self-consistent electric potential, and the dissolution of the oxide at the interface with some aqueous solution.

The main reason for the aforementioned gap in the theory is that no thermodynamic potential, serving as a Lyapunov functional, has been shown to be dissipated along time, in accordance to the second principle of thermodynamics. Assuming temperature to be constant, Helmoltz free energy is indeed expected to decay, up to some exchange with the surrounding metal and solution. We propose an update of the DPCM model which fulfils some variant of Onsager's reciprocal relation, ensuring therefore the compatibility of the model with the second principle of thermodynamics.

The main differences with the original DPCM model are the following: (i) the transport of ferric cations and oxygen vacancies in the oxide are driven by a vacancy diffusion process with a nonlinear mobility including a saturation effect; (ii) the motion of the interfaces is driven by the difference of grand potential (or Landau free energy) density rather than by a difference of chemical potential as in the original DPCM; (iii) a correction in the charge carrier fluxes is incorporated to take the volume expansion stemming from the iron oxidation into account; (iv) an update of the boundary condition for the electrons between the oxide and the metal.

Significance Statement

Corrosion occurring in subsurface nuclear waste repositories yields the production of dihydrogen (H_2), the possible accumulation of which being a major security concern. The development of accurate and theoretically assessed mathematical and numerical models is therefore a priority to quantify the *in situ* production of H_2 along large time scales. Despite important efforts of the mathematical community during the last 15 years, there is so far no satisfactory mathematical framework for the so-called Diffusion Poisson Coupled Model (DPCM) proposed by Bataillon and collaborators (Bataillon et al., 2012, 2010). This model describes the evolution of the oxide layer covering the metal by taking into account the oxidation of the metal, the transfer within the oxide layer of the charge carriers driven by some self-consistent electric potential, and the dissolution of the oxide at the interface with some aqueous solution.

The main reason for the aforementioned gap in the theory is that no thermodynamic potential, serving as a Lyapunov functional, has been shown to be dissipated along time, in accordance to the second principle of thermodynamics. Assuming temperature to be constant, Helmoltz free energy is indeed expected to decay, up to some exchange with the surrounding metal and solution. We propose an update of the DPCM model which fulfils some variant of Onsager's reciprocal relation, ensuring therefore the compatibility of the model with the second principle of thermodynamics.

The advantage of having some stability encoded by the second principle of thermodynamics is manyfold. First, this stability property is essential to establish the well-posedness of the system of partial differential equations (PDEs) derived along the modelling process for arbitrary large time. It also paves the way to the design of stable numerical methods that remain accurate even for large time horizons.

Table of content

List of figures

1. Modelling corrosion for nuclear waste repository safety

1.1 General context and motivation

The strategy of the French agency for radioactive waste management (Andra) for the long term storage of long life and high activity nuclear wastes relies on the subsurface storage in deep geological layers. Galleries dug in a clay geological layer should host iron canisters containing vitrified wastes. Assessing the security of the whole system on large time periods – up to millennials – is a challenge involving a large scientific community gathering researchers and engineers.

In such a scenario, the corrosion of the iron canisters will lead to the generation of dihydrogen (H_2), the accumulation of which being a source of explosion risk. The precise quantification of the H_2 source over long time period is therefore a scientific priority. It is the motivation to the work reported here, that was carried out in the framework of our research project supported by the EURAD program.

1.2 State of the art and scientific positioning

There has been an important effort by Andra to develop a model and a numerical tool to simulate in an accurate way the evolution of the magnetite layer protecting the iron canister to be stored in geological repositories. The code CALIPSO, the main developer of which being Christian Bataillon, is currently the reference code for the simulation of the complex model – referred to in the literature as DPCM for diffusion coupled Poisson model – described in (Bataillon et al., 2012, 2010).

The continuous model addressed here consists in one-dimensional convection diffusion equations for the charge carriers coupled with a self-consistent electric potential governed by a Poisson equation. Non-trivial boundary conditions across the interfaces strengthen the coupling. Moreover, the geometry of the oxide layer evolves along time due to the oxidation of the model and to the dissolution of the oxide (see section 2.1 for a similar construction).

From a numerical point of view, the method (Bataillon et al., 2012) implemented in CALIPSO relies on finite volumes for the space discretization, and on a fully coupled backward Euler scheme for the time discretization. A similar strategy is adopted in our work.

Even though CALIPSO gives good results and looks to be stable, only very few elements of mathematical analysis have been provided so far. Let us mention for instance (Chainais-Hillairet and Lacroix-Violet, 2014, 2012) where solutions to a reduced model with fixed interface are studied in the steady and transient case respectively. In the case of a mobile domain, the existence of pseudo-stationary (or travelling-wave) solution has been studied in (Chainais-Hillairet and Gallouët, 2016) under an electric neutrality assumption for the oxide layer, and in (Breden et al., 2021) thanks to a computer assisted proof, but for a single set of parameters. The lack in mathematical foundations for the CALIPSO code stems from the lack of theoretically proven stability for the DPCM model.

Whereas the stability of scalar partial differential equations can take many forms, it becomes much more complex when it comes to highly coupled systems. In such a case where elementary calculations can no longer be carried out, it is now well understood since a few decades that the stability should come from the second principle of thermodynamics. Indeed, thermodynamical potentials like the (Helmoltz) free energy provide natural candidates as Lyapunov functionals. However, proving such a decay requires a very specific structure for the model, which is in general not fulfilled by models built by the apposition of physical laws to model distinct phenomena. A global approach to capture off-diagonal effects is needed. Furthermore, the boundary conditions and the bulk equations should be set accordingly. The DPCM model was not derived in this spirit. Our goal in this project was to update it so that it becomes compatible with thermodynamics, in the sense that the free energy decays along time.

2. A thermodynamically consistent DPCM model

2.1 Model description

In the same spirit as (Bataillon et al., 2012, 2010), we are interested in a one-dimensional model, the space variable x being the dimensionless rescaled[1] width of the oxide layer made of magnetite (Fe_3O_4) protecting the metal. In our setting, magnetite is thought of as a one-dimensional lattice made of one fixed ferric cation located on a tetrahedral site surrounded by 4 oxygen anions which are allowed to jump from one octahedral site to a neighbouring one. Two additional mobile ferric cations Fe^{3+} occupying octahedral sites may jump to available neighbouring sites following a vacancy diffusion process too. We also consider the displacement of electrons e^- in the conduction band. Rather than the number of oxygen anions O^{2-} per elementary oxide pattern, we keep track of the concentration of oxygen vacancies V^{2+}, the number of which per elementary pattern being equal to 4 minus the number of oxygen anions. We denote by u_1, u_2 and u_3 the concentration of ferric cations, electrons and oxygen vacancies respectively, while $z_1 = +3, z_2 = -1$ and $z_3 = +2$ denote their respective (rescaled) charge. We also denote by $\overline{u}_1 = 2$ and $\overline{u}_3 = 4$ the maximal number of mobile ferric cations and oxygen vacancies per elementary magnetite pattern.

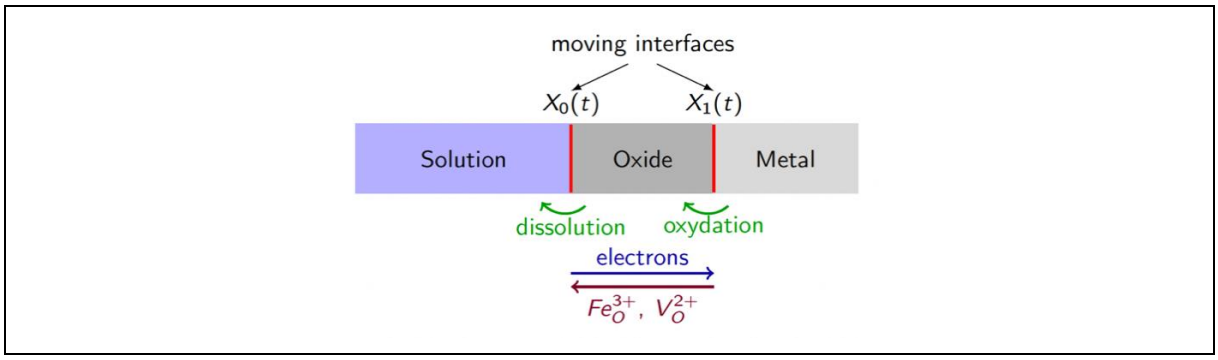

Figure 1 – Schematic representation of the oxide layer

The position of the interface between the oxide and the solution (resp. the metal) is denoted by X_0 (resp. X_1) and is assumed to evolve along time. Therefore, X_0 and X_1 are unknowns of our problem, as well as the self-consistent electrostatic potential Ψ which is deduced from the charge carrier concentrations thanks to a Poisson equation (Bataillon et al., 2010).

More precisely, we set

$$-\lambda^2 \, \partial_{xx}\Psi = \rho_{hl} + \sum_{i=1}^{3} z_i u_i \quad \text{in } (X^0, X^1) \tag{1}$$

where $\rho_{hl} = -5$ stands for the charge of the host lattice made of one iron atom at the tetrahedral site together with 4 oxygens at octahedral sites. The rescaled Debye length is denoted by λ. The above Poisson equation is complemented with Robin boundary conditions modelling the interfaces as capacitors. More precisely, we set

$$-\gamma^0 \, \partial_x \Psi\big(t, X^0(t)\big) + \Psi\big(t, X^0(t)\big) - \Delta\Psi^0_{pzc} = 0 \tag{2}$$

and

$$\gamma^1 \, \partial_x \Psi\big(t, X^1(t)\big) + \Psi\big(t, X^1(t)\big) - V + \Delta\Psi^1_{pzc} = 0. \tag{3}$$

[1] The nondimensionalization of the system is not discussed in this contribution. We refer to (Breden et al., 2021) for details on that purpose.

In the above formula, γ^0 and γ^1 are positive parameters involving the capacity of the interfaces and the rescaled Debye length, whereas V is the electric potential in the metal (the reference potential in the solution is set to 0), and $\Delta\Psi^0_{\mathrm{pzc}}$ (resp. $\Delta\Psi^1_{\mathrm{pzc}}$) is the voltage drop due to the charge accumulation in the Helmoltz layer at the solution/oxide (resp. oxide/metal) interface, see *Figure 2*. In what follows, we make use of the shorten notation Ψ^0 and Ψ^1 for $\Psi\big(t, X^0(t)\big)$ and $\Psi\big(t, X^1(t)\big)$ respectively.

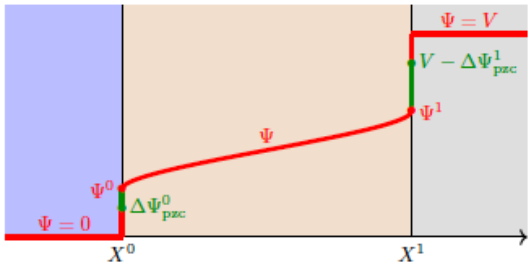

Figure 2 – Schematic representation of the self-consistent electric potential in the oxide

The equations governing the evolution of the electric potential are fully similar to what was proposed in (Bataillon et al., 2012, 2010). This is also the case of the equations governing the flux of cations and oxygen vacancies across the interfaces, which are prescribed by Butler-Volmer laws. More precisely, at the solution/oxide interface, we set

$$\mathrm{F}_{\mathrm{i}}^0 = -\mathrm{k}_{\mathrm{i}}^0 \mathrm{u}_{\mathrm{i}}^0 \mathrm{e}^{\mathrm{z}_{\mathrm{i}}\beta_{\mathrm{i}}^0 \Psi^0} \mathrm{m}_{\mathrm{i}}^0 + (\overline{\mathrm{u}}_{\mathrm{i}} - \mathrm{u}_{\mathrm{i}}^0)\mathrm{e}^{-\mathrm{z}_{\mathrm{i}}\alpha_{\mathrm{i}}^0 \Psi^0}, \quad \mathrm{i} = 1 \text{ and } \mathrm{i} = 3, \tag{4}$$

with k_i^0 and m_i^0 being positive parameters, and α_i^0 and β_i^0 being nonnegative parameters summing to 1. Similarly, for the flux of iron atoms through the interface X^1, we have

$$\mathrm{F}_1^1 = \mathrm{m}_1^1 \mathrm{u}_1^1 \mathrm{e}^{\mathrm{z}_1 \beta_1^1 (\Psi^1 - \mathrm{V})} \mathrm{k}_1^1 - (\overline{\mathrm{u}}_1 - \mathrm{u}_1^1)\mathrm{e}^{-\mathrm{z}_1 \alpha_1^1 (\Psi^1 - \mathrm{V})}. \tag{5}$$

There is no flux of oxygen atoms through the oxide/metal interface. Translating this fact in terms of flux of oxygen vacancies yields the following formula linking the vacancy flux with the interface motion:

$$\mathrm{F}_3^1 = -\overline{u}_3 \dot{X}^1. \tag{6}$$

Denoting by $a_2^{\mathrm{p}}(t) = a_2\left(u_2\big(t, X^{\mathrm{p}}(t)\big)\right)$ the activity of the electrons at the interface X^{p}, $p \in \{0,1\}$, then the electronic exchange with the metal writes

$$F_2^1 = m_2^1 \, a_2^1 \, e^{z_2 \beta_2^1 (\Psi^1 - V)} - k_2^1 \, a_2^{\mathrm{met}} e^{-z_2 \alpha_2^1 (\Psi^1 - V)}, \tag{7}$$

with $\mathrm{a}_2^{\mathrm{met}}$ standing for the activity of the electrons in the metal. The aforementioned expression slightly differs from the one proposed in (Bataillon et al., 2010), which however suggests to set the parameters $\beta_2^1 = 0$ and $\alpha_2^1 = 1$.

Still in (Bataillon et al., 2010), it is suggested that the flux of electrons between the aqueous domain and the oxide has two origins. The ferrous release (FR), which accounts for the reduction of ferric into ferrous cations in the solution, is described by the Butler-Volmer type relation

$$F_2^{0,\mathrm{FR}} = m_2^{0,\mathrm{FR}} e^{-z_2 \alpha_2^{0,\mathrm{FR}} \Psi^0} - k_2^{0,\mathrm{FR}} a_2^0 \, e^{z_2 \beta_2^{0,\mathrm{FR}} \Psi^0}, \tag{8}$$

for positive $m_2^{0,\mathrm{FR}}$ and $k_2^{0,\mathrm{FR}}$ respectively depending on the activity of the ferrous and ferric cations in the solution. Besides, proton reduction (PR) also induces a flux of electrons governed by

$$F_2^{0,\mathrm{PR}} = m_2^{0,\mathrm{PR}} e^{-z_2 \alpha_2^{0,\mathrm{PR}} \Psi^0} - k_2^{0,\mathrm{PR}} a_2^0 \, e^{z_2 \beta_2^{0,\mathrm{PR}} \Psi^0}, \tag{9}$$

with $m_2^{0,\mathrm{PR}}$ and $k_2^{0,\mathrm{PR}}$ respectively depending on the activity of dissolved H_2 in the solution and on the pH. The electron flux across X^0 is then given by

$$F_2^0 = F_2^{0,\mathrm{FR}} + F_2^{0,\mathrm{PR}}. \tag{10}$$

Denote by R_{PB} the Pilling-Bedworth ratio, i.e. the ratio between one elementary cell of oxide over the volume occupied by the required number of iron atoms to form such a pattern (3 for the magnetite). In our case, this ratio is close to 2 for the magnetite and in particular greater than 1, meaning that the oxide has a smaller concentration of iron atoms than the metal. The inertial frame of the oxide then moves with velocity

$$v_{\mathrm{ox}} = (1 - R_{\mathrm{PB}})\dot{X}^1. \tag{11}$$

The conservation of the species $\mathrm{i} \in \{1,2,3\}$ then writes

$$\partial_t u_i + \partial_x J_i = 0, \tag{12}$$

where J_i denotes the flux of species i in the inertial frame of reference. Owing to (11), it relates to the flux G_i in the inertial frame of the oxide through formula

$$J_i = G_i + u_i v_{\mathrm{ox}}. \tag{13}$$

The ferric cations and oxygen vacancies bulk fluxes G_i, $\mathrm{i} \in \{1,3\}$, have nonlinear convection and linear diffusion

$$G_i = -d_i(\partial_x u_i + \eta_i(u_i) z_i \, \partial_x \Psi), \qquad \eta_i(u_i) = \frac{u_i(\overline{u}_i - u_i)}{\overline{u}_i}, \quad i \in \{1,3\}, \tag{14}$$

where $d_i > 0$ stands for the diffusion coefficient of the species i. Define by

$$\mu_{\mathrm{i}} = \mu_{\mathrm{i}}^* + \log \frac{\mathrm{u_i}}{\overline{\mathrm{u}}_{\mathrm{i}} - \mathrm{u_i}}, \qquad \mathrm{i} = 1 \text{ and } \mathrm{i} = 3, \tag{15}$$

the chemical potentials of the ferric cations and of the oxygen vacancies – the reference chemical potential μ_i^* depends on the temperature and on the pressure only, which are assumed to be given constants throughout this report –, and by

$$\xi_i = \mu_i + z_i \Psi \tag{16}$$

their electrochemical potential. Then the ferric cation and oxygen vacancy fluxes $\mathrm{G_i}$ rewrite

$$G_i = -d_i \eta_i(u_i) \, \partial_x \xi_i, \qquad i \in \{1,3\}. \tag{17}$$

The nonlinear convection in (14) is characteristic of a vacancy diffusion process. In contrast, there is no limit on the number of electrons in the band conduction provided enough energy is afforded. Denote by $a_2 = e^{\mu_2 - \mu_2^*}$ the activity of the electrons, which is supposed to depend on u_2 only but neither on u_1 nor u_3, then the flux of electrons in the frame of the oxide is given by

$$G_2 = -d_2(\partial_x a_2 + z_2 a_2 \, \partial_x \Psi) = -d_2 a_2 \, \partial_x \xi_2. \tag{18}$$

As pointed out in (Bataillon et al., 2012), the boundary fluxes F_i^p relate to the bulk fluxes thanks to the relation

$$F_i^p = J_i^p - u_i^p \dot{X}^p, \qquad i \in \{1,2,3\}, \; p \in \{0,1\}. \tag{19}$$

In the case of interest where a Boltzmann statistics is used for the electrons, i.e. $\mu_2 = \log(u_2)$, then one recovers the same linear drift-diffusion flux (18) as in (Bataillon et al., 2010) up to the term corresponding to the change of inertial frame in (13). This is not the case for the ferric cations and the oxygen vacancies as, additionally to the correction corresponding to the change of frame, convection in our model is nonlinear (14), in opposition to the linear convection postulated in (Bataillon et al., 2012, 2010). These corrections to the reference model (Bataillon et al., 2012) of the state of the art already yield important differences that are highlighted in (Cancès et al., 2023a) when the evolution of the oxygen vacancies – and thus the motion of the interfaces – is neglected.

We introduced a more conceptual difference to handle the evolution of the geometry of the oxide layer and the motion of the interfaces X^0, X^1. While the displacement of the interfaces was implicitly driven by

the difference of some electrochemical potential in (Bataillon et al., 2010), this is no longer the case in our model. For thermodynamic reasons that will be made explicit in the next section, we postulate that the displacement of the interface is driven by the jump in the density of the grand potential (or Landau free energy), or equivalently up to a change of sign, to what we refer to as the electrochemical pressure. Denote by $A_i(u_i)$ the chemical contribution to the free energy of species i, so that $\mathrm{d}A_i = \mu_i \mathrm{d}u_i$, then the electrochemical pressure is defined by

$$\Pi = \sum_{i=1}^{3} u_i \mu_i - A_i(u_i) - \rho_{\mathrm{hl}} \Psi - \frac{\lambda^2}{2} |\partial_x \Psi|^2, \tag{20}$$

then one readily checks that $\partial_x \Pi = \sum_{i=1}^{3} u_i \, \partial_x \xi_i$. In particular, Π depends on all the species and not only on the oxygen vacancies density, in opposition to the original model (Bataillon et al., 2010). In our model, we suppose that

$$\dot{X^1} = \kappa^1 Z^1 \big(\Pi(X^1) - \overline{u}_3 \big(\mu_3(X^1) + z_3 \Psi(X^1)\big) - \Pi^{\mathrm{met}}\big), \tag{21}$$

$$\dot{X^0} = v_{\mathrm{d}}^0 + (1 - R_{\mathrm{PB}}) \dot{X^1}. \tag{22}$$

The dissolution velocity of the oxide v_{d}^0 is assumed to have the form

$$v_{\mathrm{d}}^0 = -\kappa^0 Z^0 \big(\Pi(X^0) - \Pi^{\mathrm{sol}}\big). \tag{23}$$

In the above expressions, κ^1 and κ^0 are nonnegative functions of the densities and the electrical potential at the interfaces, while Z^0 and Z^1 are nondecreasing functions of the jump of electrochemical pressure at the interfaces satisfying $Z^0(0) = Z^1(0) = 0$. The parameters Π^{sol} and Π^{met} stand for the (electrochemical) pressures in the solution and in the metal respectively and are assumed to be given.

The fact that the displacement of the interfaces is driven by the grand potential seems to be new in the context of corrosion modeling. However, such a fact was suggested in the seminal book (Pimpinelli and Villain, 1999), and used in relatively close contexts by (Cermelli and Jabbour, 2005; Li et al., 2009), but in the absence of electrical effects.

2.2 Onsager's reciprocal relation and free energy dissipation

The model we propose has been designed in order to ensure the decay along time of some thermodynamical potential, namely the Helmoltz free energy of the full system made of the solution, the oxide and the metal.

Define $\mathcal{G}_{\mathrm{ox}}(t)$ the free energy of the oxide at time t as the sum of a chemical contribution $\mathcal{A}_{\mathrm{ox}}(t)$ and an electrical contribution $\mathcal{E}_{\mathrm{ox}}(t)$ respectively defined by

$$\mathcal{A}_{\mathrm{ox}} = \int_{X^0}^{X^1} \left(A_{\mathrm{hl}} + \sum_{i=1}^{3} A_i(u_i) \right) \mathrm{d}x \tag{24}$$

and

$$\mathcal{E}_{\mathrm{ox}} = \frac{\lambda^2}{2} \left(\int_{\mathrm{X}^0}^{\mathrm{X}^1} |\partial_{\mathrm{x}} \Psi|^2 \, \mathrm{dx} + \frac{1}{\gamma^0} \left(|\Psi^0|^2 - \left|\Delta\Psi_{\mathrm{pzc}}^0\right|^2 \right) + \frac{1}{\gamma^1} \left(|\Psi^1|^2 - \left|\mathrm{V} - \Delta\Psi_{\mathrm{pzc}}^1\right|^2 \right) \right) \tag{25}$$

with Ψ deduced from the u_i thanks to the Poisson equation (1)–(3) detailed previously. Then one shows that $\frac{\delta \mathcal{A}_{\mathrm{ox}}}{\delta u_i} = \mu_i$ and $\frac{\delta \mathcal{E}_{\mathrm{ox}}}{\delta u_i} = z_i \Psi$, so that $\frac{\delta \mathcal{G}_{\mathrm{ox}}}{\delta u_i} = \xi_i$ owing to (16). Here $\frac{\delta \mathcal{G}_{\mathrm{ox}}}{\delta u_i}$ stands for the first variation of $\mathcal{G}_{\mathrm{ox}}$ with respect to u_i. Therefore, the time evolution of the free energy writes

$$\frac{\mathrm{d}}{\mathrm{d}t} \mathcal{G}_{\mathrm{ox}} = \sum_{i=1}^{3} \int_{X^0}^{X^1} \xi_i \, \partial_t u_i \mathrm{d}x \, . \tag{26}$$

After a few calculations to be detailed in a forthcoming article building on the model equations described in the previous section, one gets that

$$\frac{\mathrm{d}}{\mathrm{d}t}\mathcal{G}_{\mathrm{ox}} = \int_{X^0}^{X^1} \sum_{i=1}^{3} G_i\, \partial_x \xi_i \,\mathrm{d}x - \sum_{i=1}^{3} (F_i^1 \xi_i^1 - F_i^0 \xi_i^0) - R_{\mathrm{PB}} \dot{X}^1 \pi^1 + \pi^0 v_{\mathrm{d}}^0. \tag{27}$$

Each contribution in the integral of the right-hand side is nonnegative because of (17) and (18). The other terms correspond to exchange terms with the solution and with the metal. Their sign is not clear, motivating the introduction of an augmented free energy accounting for the solution and the metal. We set

$$\mathcal{G}_{\mathrm{tot}}(t) = \mathcal{G}_{\mathrm{ox}}(t) + \int_0^t \sum_{i=1}^{3} [F_i^1(\tau)\xi_i^{\mathrm{met}} - F_i^0(\tau)\xi_i^{\mathrm{sol}}]\mathrm{d}\tau + (X^1(t) - X^1(0))[R_{\mathrm{PB}}\Pi^{\mathrm{met}} + (1 - R_{\mathrm{PB}})\pi^{\mathrm{sol}}] - (X^0(t) - X^0(0))\Pi^{\mathrm{sol}}.$$

Then it follows from the calculations detailed above that

$$\frac{\mathrm{d}}{\mathrm{d}t}\mathcal{G}_{\mathrm{tot}} = \int_{X^0}^{X^1} \sum_{i=1}^{3} G_i \partial_x \xi_i \mathrm{d}x + \sum_{p\in\{0,1\}} \sum_{i\in\{1,3\}} F_i^p \Delta\xi_i^p + F_2^1 \Delta\xi_2^1 + F_2^{0,\mathrm{PR}} \Delta\xi_2^{0,\mathrm{PR}} + F_2^{0,\mathrm{FR}} \Delta\xi_2^{0,\mathrm{FR}} + R_{\mathrm{PB}} \dot{X}^1 \Delta\Pi^1 + v_{\mathrm{d}}^0 \Delta\Pi^0.$$

In the above right-hand side, for $i = 1$ and $i = 3$, we have set $\Delta\xi_i^0 = \xi_i(X^0) - \xi_i^{\mathrm{sol}}$ with $\xi_i^{\mathrm{sol}} = \log\left(\frac{m_i^0}{k_i^0}\right)$ being the electrochemical potential of species $i = 1$ and $i = 3$ in the solution. Similarly, for $i \in \{1,2,3\}$, we have set $\Delta\xi_i^1 = \xi_i^{\mathrm{met}} - \xi_i(X^1)$, with $\xi_i^{\mathrm{met}} = \log\left(\frac{k_i^1}{m_i^1}\right) + z_i V$. For the fluxes of electrons across the solution/oxide interface, we have to introduce two electrochemical potentials $\xi_2^{0,\mathrm{PR}}$ and $\xi_2^{0,\mathrm{FR}}$, but the reasoning is similar. Then as highlighted for instance in (Cancès et al., 2023a), the structure of the Butler-Volmer laws (4)-(5) and (7)-(10) is such that all the contributions corresponding to fluxes across the interfaces in the above right-hand side are nonnegative.

To establish the decay of the augmented free energy along time, it only remains to check that the two last terms related to the motion of the interfaces yield nonnegative contributions. This stems from the fact that the functions Z^p are equal to 0 at 0 and increasing.

To conclude this section, let us remark that the decay of the free energy for our model is a consequence of the particular mathematical structure of our model. Indeed, our model has been derived as the generalized gradient flow of the augmented free energy (Mielke, 2011; Peletier, 2014; Peletier et al., 2022).

3. A reduced model with fixed interfaces

3.1 Model simplification

In the spirit of previous contributions of the literature – see for instance (Chainais-Hillairet and Lacroix-Violet, 2014, 2012) – we have focused on the simplified model where oxygen vacancies are neglected. Thanks to this simplifications, interfaces can be assumed to be fixed, and after rescaling the width of the oxide layer can be assumed to be constant along time and equal to 1. This simplification may sound strong, but the reduced model allows to give good insights for the production rate of dihydrogen H_2. Moreover, it can be used for the calibration of the full model and its numerous parameters.

3.2 Mathematical analysis

In the reduced model we proposed in (Cancès et al., 2023a), the unknowns are u_1 and u_2, as well as the self-consistent electrostatic potential Ψ solving the Poisson equation. There is no further need of the

oxygen vacancy density u_3, neither on the grand potential Π, but the other ingredients remain the same: Butler-Volmer law for the fluxes across the interface, nonlinear convection-diffusion equation for the ferric cations and linear convection-diffusion equation for the electrons. Furthermore, the system can still be interpreted as the generalized gradient flow of some augmented free energy. This ensures in particular some stability for the model on which we build to establish the global in time existence of a solution to the system in (Cancès et al., 2023a).

It is worth noticing that we do not impose restrictions on the parameters, in opposition to what was necessary in the previous work (Chainais-Hillairet and Lacroix-Violet, 2014). Moreover, we also establish the physically relevant bounds $0 < u_1 < \overline{u}_1$, $0 < u_2$ and $0 < u_3 < \overline{u}_3$ among other technical estimates we do not detail here, cf. (Cancès et al., 2023a) for interested readers. These bounds are all consequences of the control of the free energy and of its dissipation rate, following the methodology of (Gajewski and Gröger, 1989; Jüngel, 2015).

3.3 Numerical approximation

As a step towards the development of a finite volume scheme for the full model, we addressed the reduced model. The preservation of the consistency of our model with the second principle of thermodynamics at the discrete level has been a priority when designing the numerical method. This led us to consider two-point flux approximation (TPFA) finite volumes in space and a backward in time Euler time discretization. For the fluxes in the drift-diffusion equations for the conservation of the charge carriers, we either use so-called Scharfetter-Gummel (SG) fluxes for the linear equation corresponding to electrons, or a new extension of the squareroot approximation (SQRA) fluxes to the case of nonlinear mobilities for ferric cations (Cancès and Venel, 2023). We also developed and analysed mathematically in (Cancès et al., 2023b) a new variant of the SG scheme which shares the main features with the new SQRA scheme, that are the preservation of the physical bounds and the decay of some discrete free energy functional.

Even though this would not lead to particular problem, we did not prove rigorously so far the convergence of our scheme towards the global in time solution to the reduced model exhibited in (Cancès et al., 2023a). We rather focused on the simulation of the reduced model thanks to a prototype code developed in Python, and to its comparison with the model obtained from the original DPCM (Bataillon et al., 2010) after similar simplifications consisting in neglecting the oxygen vacancies. We refer to (Cancès et al., 2023a) for the values assigned to the parameters in our tests.

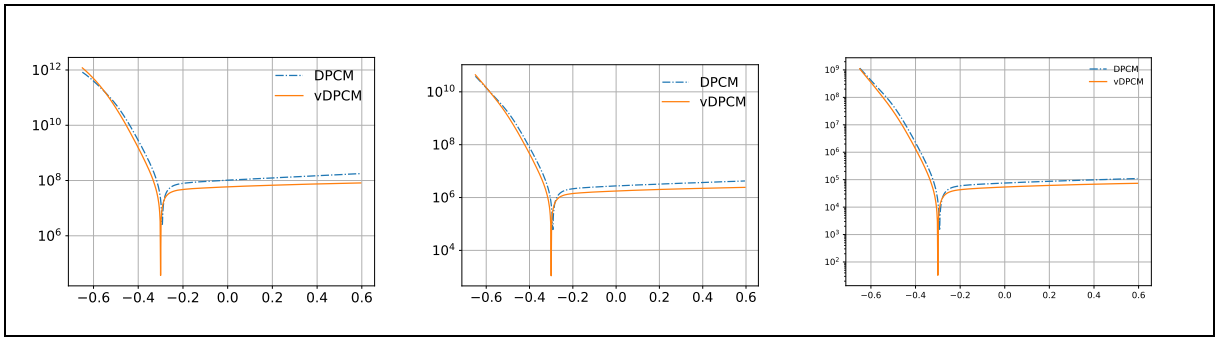

Figure 3 – Comparison of the current-voltage characteristics corresponding to the new thermodynamically consistent reduced model (vDPCM, orange solide line) and to the original reduced model (DPCM, dashed blue line) for pH = 7 (left), pH = 8,5 (center) and pH = 10 (right).

It appears that from a macroscopic point of view, our new reduced model (referred to as vDPCM in what follows) gives similar results as the reduced model building on the original model (still referred to as DPCM in the figures below). This can for instance be observed on the i-v curves depicted on *Figure 3*.

However, it clearly appears on *Figure 4* that the original model does not preserve the physical bound $u_i < \overline{u}_i$ on the density of ferric cations (for which $\overline{u}_1 = 2.005$), in opposition to our new model.

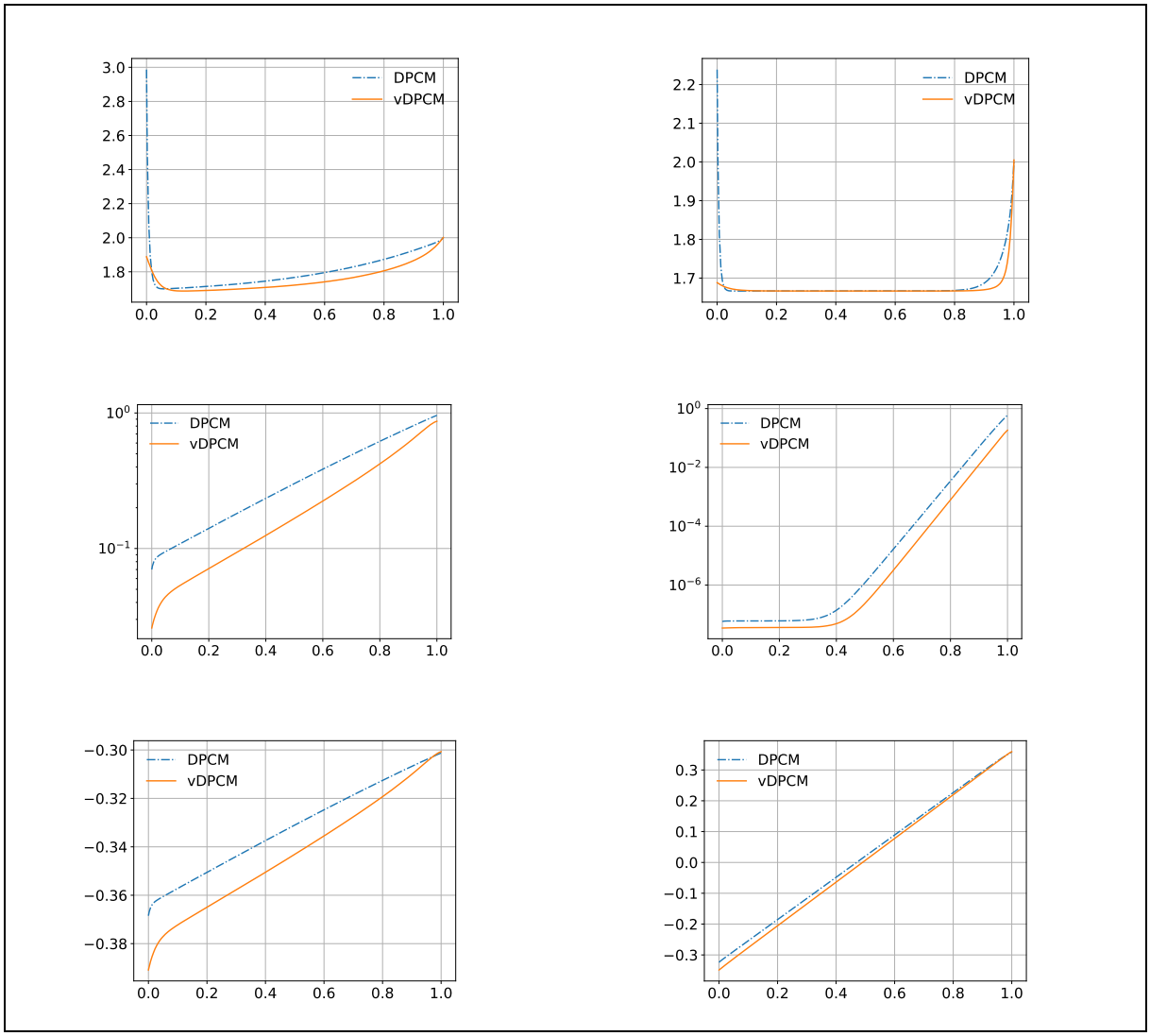

Figure 4 – Profiles of the scaled densities of cations (top), electrons (middle) and the electrostatic potential (bottom, in Volts, the physical unit) at the steady state for two values of the applied potential V, that are -0.4 Volts (left) and 0.3 Volts (right).

4. Conclusion and prospects

4.1 Conclusion

We proposed a new model which can be seen as an update of the model proposed in (Bataillon et al., 2012, 2010) to accurately represent the magnetite layer protecting the iron canister to be stored in geological repositories. Our new model is designed to be compatible with the second principle of thermodynamics. More precisely, we built the model as a generalized gradient flow so that Onsager reciprocal relation is automatically satisfied.

We performed in (Cancès et al., 2023a) the mathematical and numerical analysis of a simplified model where oxygen vacancies have been neglected, so that the geometry of the domain does not evolve along time. The new model we propose provides close results from a macroscopic point of view on the few cases we assessed, but significant differences are observed in terms of the repartition of the charge carriers in the oxide layer. In particular, our model preserves the physical range for the ferric cation

occupation rate, in opposition to the simplified model (Chainais-Hillairet and Lacroix-Violet, 2014) built from the original model (Bataillon et al., 2010).

New contributions to the theory of finite volumes have been needed to properly handle the nonlinear mobilities in the convection-diffusion of cations. We proposed in (Cancès et al., 2023b; Cancès and Venel, 2023) some schemes that are free energy diminishing while keeping a small computational cost.

Let us finally mention the work (Merlet et al., 2022) where another simplification is addressed. A reduced model accounting only for oxygen vacancies (but with moving interfaces) is proposed and analysed thanks to tools from calculus of variations and Wasserstein gradient flow theory.

4.2 Prospects

We still have to develop an efficient numerical tool to simulate the full model sketched in section 2.1. On top of the non-trivial treatment of the time discretization, the discretization of the grand potential Π requires a particular attention. The highly coupled and nonlinear nature of the problem makes the effective resolution difficult as we enforce strong constraints on the computational cost and the robustness of the tool so that it can be coupled to THMC platforms without significantly increasing the computational time.

Among the other challenges we will have to face in the near future, the calibration of our model has to be done carefully. Indeed, the calibration procedure that was employed to fix the parameters in the original DPCM model cannot be used directly and must be adapted. In particular, the choice of the functions Z^0, Z^1 and κ^0, κ^1 governing the motion of the interfaces is left open so far. Advanced discussions with electrochemists and specialists of material science will be required here.

Once our Python prototype code will be finalized, then we plan to use it to train a surrogate model to get a fast solver to be used in the context of uncertainty quantification and sensibility analysis.

Code source

We make use of a private Python prototype code which is not mature enough to be published on public repositories. The code will be made available when finalized and calibrated.

References

Bataillon, C., Bouchon, F., Chainais-Hillairet, C., Desgranges, C., Hoarau, E., Martin, F., Perrin, S., Tupin, M., Talandier, J., 2010. Corrosion modelling of iron based alloy in nuclear waste repository. Electrochimica Acta 55, 4451–4467. https://doi.org/10.1016/j.electacta.2010.02.087

Bataillon, C., Bouchon, F., Chainais-Hillairet, C., Fuhrmann, J., Hoarau, E., Touzani, R., 2012. Numerical methods for the simulation of a corrosion model with moving oxide layer. Journal of Computational Physics 231, 6213–6231. https://doi.org/10.1016/j.jcp.2012.06.005

Breden, M., Chainais-Hillairet, C., Zurek, A., 2021. Existence of traveling wave solutions for the Diffusion Poisson Coupled Model: a computer-assisted proof. ESAIM: M2AN 55, 1669–1697. https://doi.org/10.1051/m2an/2021037

Cancès, C., Chainais-Hillairet, C., Merlet, B., Raimondi, F., Venel, J., 2023a. Mathematical analysis of a thermodynamically consistent reduced model for iron corrosion. Z. Angew. Math. Phys. 74, 96. https://doi.org/10.1007/s00033-023-01970-6

Cancès, C., Herda, M., Massimini, A., 2023b. Finite volumes for a generalized Poisson-Nernst-Planck system with cross-diffusion and size exclusion.

Cancès, C., Venel, J., 2023. On the square-root approximation finite volume scheme for nonlinear drift-diffusion equations. Comptes Rendus. Mathématique 361, 535–558. https://doi.org/10.5802/crmath.421

Cermelli, P., Jabbour, M., 2005. Multispecies epitaxial growth on vicinal surfaces with chemical reactions and diffusion. Proc. R. Soc. A. 461, 3483–3504. https://doi.org/10.1098/rspa.2005.1495

Chainais-Hillairet, C., Gallouët, T.O., 2016. Study of a pseudo-stationary state for a corrosion model: Existence and numerical approximation. Nonlinear Analysis: Real World Applications 31, 38–56. https://doi.org/10.1016/j.nonrwa.2016.01.010

Chainais-Hillairet, C., Lacroix-Violet, I., 2014. On the existence of solutions for a drift-diffusion system arising in corrosion modeling. DCDS-B 20, 77–92. https://doi.org/10.3934/dcdsb.2015.20.77

Chainais-Hillairet, C., Lacroix-Violet, I., 2012. The existence of solutions to a corrosion model. Applied Mathematics Letters 25, 1784–1789. https://doi.org/10.1016/j.aml.2012.02.012

Gajewski, H., Gröger, K., 1989. Semiconductor Equations for variable Mobilities Based on Boltzmann Statistics or Fermi-Dirac Statistics. Mathematische Nachrichten 140, 7–36. https://doi.org/10.1002/mana.19891400102

Jüngel, A., 2015. The boundedness-by-entropy method for cross-diffusion systems. Nonlinearity 28, 1963–2001. https://doi.org/10.1088/0951-7715/28/6/1963

Li, B., Lowengrub, J., Rätz, A., Voigt, A., 2009. Geometric evolution laws for thin crystalline films: modeling and numerics. Commun. Comput. Phys 6, 433–482.

Merlet, B., Venel, J., Zurek, A., 2022. Analysis of a one dimensional energy dissipating free boundary model with nonlinear boundary conditions. Existence of global weak solutions. HAL:03888607. https://hal.science/hal-03888607

Mielke, A., 2011. A gradient structure for reaction–diffusion systems and for energy-drift-diffusion systems. Nonlinearity 24, 1329–1346. https://doi.org/10.1088/0951-7715/24/4/016

Peletier, M.A., 2014. Variational Modelling: Energies, gradient flows, and large deviations. arXiv:1402.1990 [math-ph].

Peletier, M.A., Rossi, R., Savaré, G., Tse, O., 2022. Jump processes as generalized gradient flows. Calc. Var. 61, 33. https://doi.org/10.1007/s00526-021-02130-2

Pimpinelli, A., Villain, J., 1999. Physics of Crystal Growth, Physics of Crystal Growth.

Numerical simulation of coupled processes in porous media

[1]Ahusborde, E., [1]Amaziane, B., El Ossmani, M., Tabrizinejadas, S.

[1] Université de Pau et des Pays de l'Adour, E2S UPPA, CNRS, LMAP, Pau, France (CNRS-LMAP)

The project leading to this application has received funding from the European Union's Horizon 2020 research and innovation programme under grant agreement No 847593.

Abstract

This report summarizes the contribution of the CNRS-LMAP within the DONUT work package. We mainly focused on the development and the implementation of numerical methods for modelling coupled thermal-hydrological-mechanical-chemical (THMC) processes in porous media. Precisely, we have been involved in two activities.

The first activity concerns the development and implementation in the DuMu^X platform of a parallel finite volume method for the simulation of coupled thermal-hydrological-chemical (THC) processes in variably saturated, non-isothermal, porous media. We first developed a fully implicit finite volume method that has been validated by several test cases related to nuclear waste management, including a non-isothermal multiphase flow and reactive transport benchmark for radioactive waste disposal proposed in Task 5. Despite the capacity of DuMu^X in integrating the full complexity of THC coupled processes, its use is still relatively limited due to the constraints in integrating with realistic chemical descriptions of fluids and rocks. As a consequence, we also implemented a sequential coupling between DuMu^X and PHREEQC to benefit from the flexibility of this latter in defining and solving complex chemical system.

The second activity concerns the development and implementation in the DuMu^X platform of a finite volume method for the simulation of the coupling between geomechanics and multiphase multicomponent flow to study coupled hydrological-mechanical (HM) processes in porous media. Precisely, we coupled a cell-centered finite volume method for the discretization of the multiphase flow problem with a control volume finite element method (CVFEM) to discretize the geomechanical model. The coupling is done in a fully implicit manner. The methodology has been validated by several one-, two-, and three-dimensional consolidation problems: Terzaghi's problem, Mandel's problem and Cryer's problem.

Significance Statement

Performance and safety assessment of nuclear waste repository require robust and accurate numerical simulations. Indeed due to the timescales considered (hundreds of thousands or even millions of years), experiments become impossible and numerical simulation of highly coupled physical phenomena is pivotal. In this context, CNRS-LMAP focused on the development and implementation of numerical methods to solve Thermo-Hydro-Chemical (THC) and Hydro-Mechanical (HM) processes. Precisely, we developed and implemented in the free and open source platform DuMu^{x} fully implicit and sequential strategies using stated of the art methods to solve coupled processes. In the fully implicit method, all the physical processes are solved together leading to a hard numerical challenge such as a highly non-linear system, involving a very large and ill-conditioned linear systemto solve. In the sequential strategy, the Thermo-Hydro and Chemical processes are solved sequentially, using DuMu^{x} and PHREEQC respectively. This duality of fully implicit and sequential strategies in a unique free and open source platorm is very important since it allows for comparing both strategies in the same numerical environment, whereas these approaches are usually compared in different codes of computer facilities.

Tables of content

List of figures

Glossary

FV	Finite-Volume
HM	Hydro-Mechanical
PDE	Partial differential equation
SNIA	Sequential non iterative approach
THC	Thermo-Hydrological-Chemical
THMC	Thermo-Hydrological-Mechanical-Chemical

1. Introduction

The aim of our contribution was to develop efficient and robust parallel numerical methods for simulating coupled Thermal-Hydrological-Mechanical-Chemical (THMC) interactions.

More precisely, we contributed to the activities within Task 2 in the following two areas:

- Development and implementation of a parallel finite volume method for simulation of coupled thermal-hydrological-chemical (THC) processes in variably saturated, non-isothermal, porous media.

- Numerical modelling of the coupling between geomechanics and multiphase multicomponent flow to study hydrological-mechanical (HM) processes.

2. Numerical modelling of THC processes

2.1 Fully implicit approach

We developed a fully coupled fully implicit finite volume (FV) method for solving the nonlinear coupling induced in THC processes in porous media (Ahusborde et al., 2023). The problem is modelled by a highly nonlinear system of degenerate partial differential equations (PDEs governing a compositional two-phase flow model) coupled to ordinary and/or algebraic differential equations (modelling kinetic and equilibrium chemical reactions respectively). The spatial discretization uses a cell centred FV scheme. After discretizing in time with an implicit Euler scheme, the resulting systems of nonlinear algebraic equations are solved with Newton's method and the linear are solved efficiently and in parallel with an algebraic multigrid method. We have developed and implemented this scheme in a new module in the context of the parallel open-source platform DuMu^{X} (Koch et al., 2021). Parallelization was performed using the DUNE parallel library package (Bastian et al., 2021).

The effectiveness and efficiency of our strategy have been demonstrated by solving several 1D-2D and 3D examples from the literature. In this contribution, we consider a 3D problem modelling scenario of nuclear waste management (Nardi et al., 2014). In this example, the evolution of the buffer and backfill materials during long-term storage is assessed from a THC perspective. The considered problem involves heat generation in the canister, groundwater inflow through a fracture intersecting the deposition tunnel and the saturation of the initially unsaturated clay materials (buffer and backfill), solute transport, and geochemical reactions (see Figure 5 (Left) for the configuration). Figure 5 (Right) represents the temperature after 25 years of simulation as well as the water saturation at several times. After 25 years of simulation, the maximum temperature reaches 350K close to the canister due to heat generation. The system is progressively saturated by the surrounding groundwater entering the backfill through the intersection with the fracture plane. After 400 years, the backfill is totally saturated.

Some parallel computations up to 512 processors on a grid composed of 1548800 elements have been performed. Figure 6 represents the CPU times and the speed up for the first two iterations of the computations. It can be observed that as expected, the speed up moves away from the ideal behaviour as the number of processors increases. Precisely, a very good parallel efficiency (close to 1) is obtained up to 64 processors and then, the efficiency falls to 0.5. As a consequence, using 64 processors represents an optimal balance between calculation time and efficiency.

The fully implicit has also been used in the framework of a “Non-isothermal multiphase flow and reactive transport benchmark for radioactive waste disposal" proposed by ENRESA-UDC in Task 5 but these results are not discussed here.

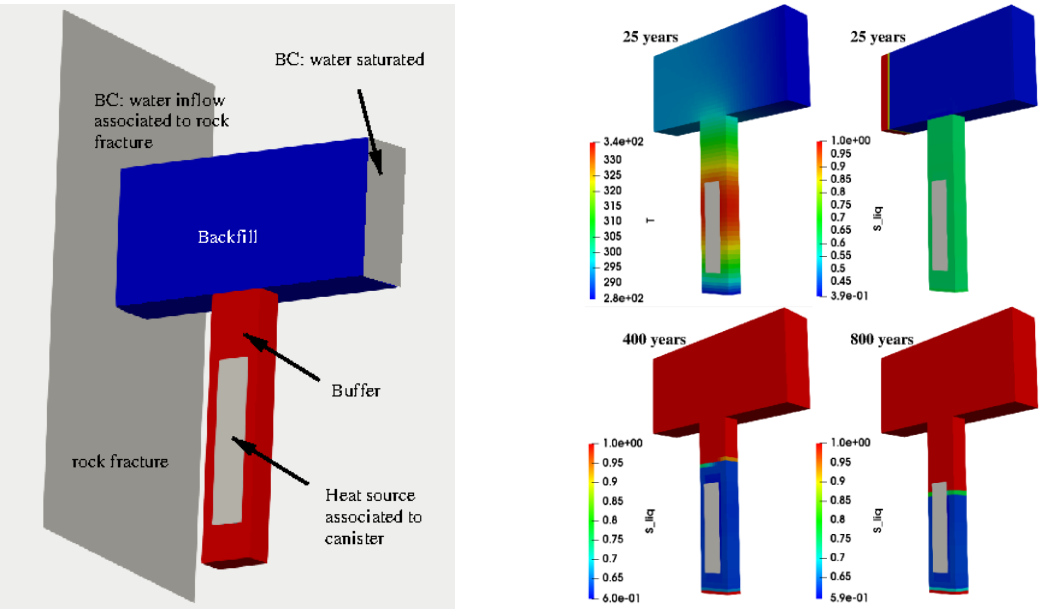

Figure 5: (left) Schematic representation of the conceptual model considered in the simulation. BC stands for boundary condition (adapted from Nardi et al., 2014). (right) Temperature in K at 25 years and evolution of the water saturation as a function of time.

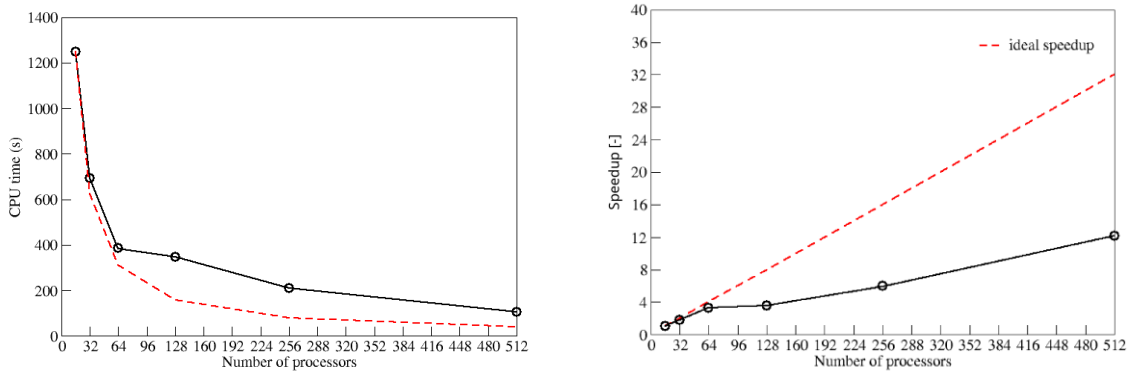

Figure 6: CPU time (left) and speed up (right) as a function of the number of processors. The dotted red lines represent the ideal behaviours.

2.2 Sequential coupling between DuMu^x and PHREEQC

Despite the capacity of DuMu^x in integrating the full complexity of THC coupled processes, its use is still relatively limited due to the constraints in integrating with realistic chemical descriptions of fluids and rocks. Therefore, we decided to decouple the flow and chemical sub-problems and solve the latter with a geochemical code for handling complex chemical systems. Among the variety of geochemical codes, the software package PHREEQC (Parkhurst and Appelo, 2013) a code for simulating aqueous speciation and reaction path, has gained popularity due to its convenience of defining and solving the desired geochemical system via basic scripts. Coupling DuMu^x with PHREEQC brings the convenience of efficient modelling of the multi-physical processes together with access to the rich chemical database of PHREEQC and flexibility in defining the chemical system.

The coupling between the flow part in DuMu^x and the chemical reaction part in PHREEQC has been done through a sequential non-iterative approach (SNIA) using PhreeqcRM (Parkhurst and Wissmeier, 2015). PhreeqcRM is called in each time step as the reaction engine for updating the values of element concentrations, which are given by DuMu^x after a transport step.

Firstly, we validated our approach considering a 1D single-phase reactive flow and a calcite dissolution benchmark, which is proposed in (Jara et al, 2017). Figure 7 compares the concentrations of mobile elements as well as minerals obtained with coupled DuMu^{X}-PHREEQC and the reference solution given by PHREEQC. Calcium and carbonate are initially at equilibrium in the solution. With the progressive introduction of magnesium, calcite starts to dissolve and dolomite precipitates. A very good accordance in the results is observed. The extension of this sequential coupling to deal with multiphase reactive flows is in progress.

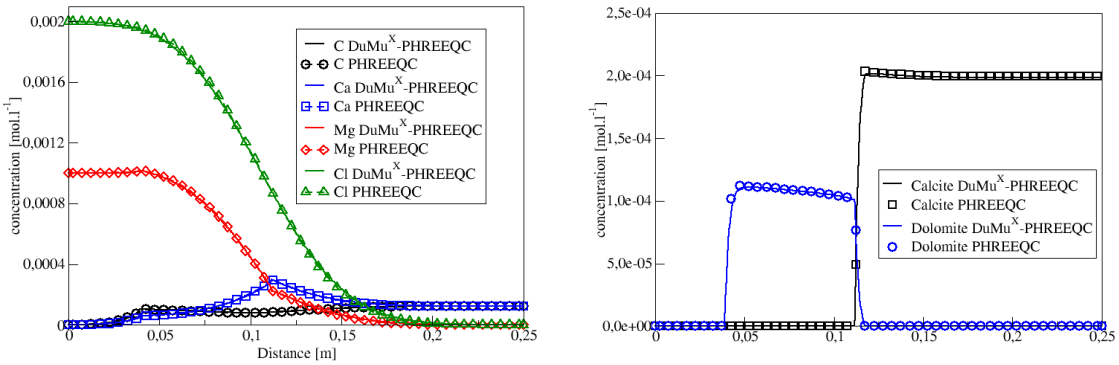

Figure 7*: Profile for total mobile concentration of elements (left) and concentrations of minerals (right) at t=10000s for the test case presented in (Jara et al, 2017).*

3. Numerical modelling of HM processes

We have also been interested in the numerical modelling of the coupling between geomechanics and multiphase multicomponent flow to study hydrological-mechanical (HM) processes. Precisely, we developed and implemented a fully implicit strategy where a cell-centred finite volume scheme is formulated for the flow part combined with a control volume finite element method (CVFEM) for the poromechanical part. The coupling between the two parts is performed through the effective pressure and the effective density, which influence the stress calculations. However, porosity and permeability variations as a function of mechanical displacements contribute to flow modifications. The implementation of the model was performed in DuMu^{X}.

In general, when soils are subjected to vertical loading, porosity decreases, resulting in less space available for pore water, which is forced to move to where pore space is available. This process is known as consolidation. In the literature there are generally three famous problems: Terzaghi's problem, Mandel's problem (Mandel, 1953) and Cryer's problem (Cryer, 1963). These three tests are designed to gradually increase in complexity and cover the typical range of consolidation problems. They also offer the advantage of the existence of analytical solutions, which are useful to produce accurate verification

and thus validate the model coupling. As a consequence we validated our numerical strategy for modelling HM processes on Mandel's and Cryer's problems.

3.1 Two-dimensional Mandel's consolidation problem

The well-known Mandel's problem was developed as a benchmark to test the validity of numerical codes for poroelasticity (Mandel, 1953).

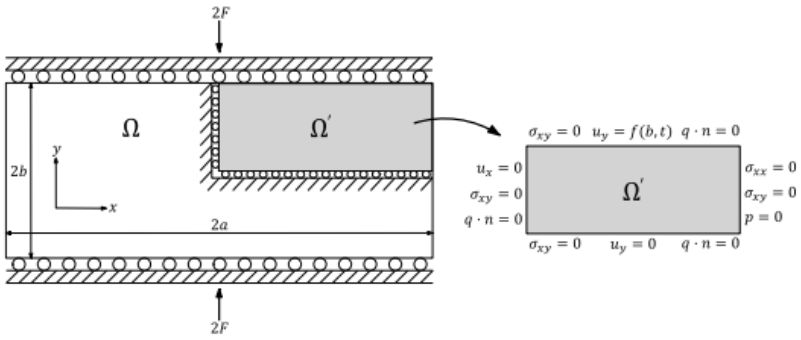

Figure 8Figure 8

Figure 8: Configuration of the 2D Mandel consolidation problem (taken from Keilegavlen et al, 2021).

This problem defines a two-dimensional rectangular sample of saturated poroelastic material loaded by a constant compressive force of intensity 2F applied on rigid impervious plates (see Figure 8).

The load is applied immediately after the initial time, as before. The sample is free to drain laterally and the lateral edges are stress-free. Due to the biaxial symmetry of the problem, the computational domain is restricted to the quarter of the original physical domain, as shown in the schematic of the configuration in Figure 8.

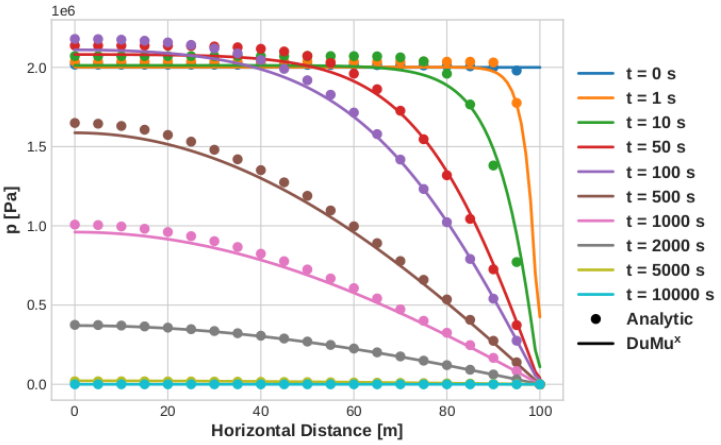

Figure 9: Evolution of the liquid pressure for the 2D consolidation as a function of time.

Figure 9 compares the analytical and numerical results for several times and clearly shows two different trends in the results. The first trend is represented by a pressure increase for short times and a maximum 10% rise is reached at about 100 s. This increase is mainly due to undrained conditions and is identified as the Mandel-Cryer effect (Mandel, 1953). This phenomenon demonstrates a non-monotonic pressure response under constant boundary conditions and highlights the coupling effects between fluid flow and geomechanics that cannot be captured by uncoupled models. Finally, after some time, the second trend appears as a gradual decrease in pressure until consolidation is achieved. The material is then

completely drained by the boundary condition. The results presented here are in agreement with the analytical values.

3.2 Three-dimensional Cryer's consolidation problem

The Three-dimensional Cryer's consolidation problem (Cryer, 1963) consists of a poroelastic, spherical, porous medium fully saturated by a fluid; hence a single-phase flow is considered.

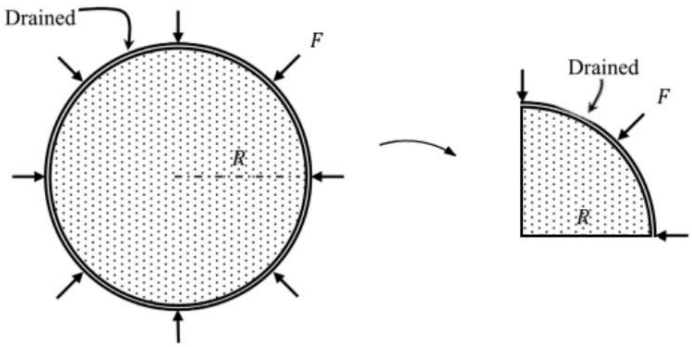

Figure 10

Figure 10: Configuration of Cryer's consolidation problem (Haagenson et al, 2019)

Figure 10 gives a schematic of the case configuration. The triaxial symmetry allows the domain study to be limited to one octant of a sphere. The curved surface is instantaneously loaded by a constant force and also defines a drained region through which the fluid can flow. However, the plane surfaces are fixed to prevent normal displacements. Initially, a zero pressure is considered throughout the domain as well as zero displacements. A constant compressive force F is applied at the initial time, generating a pressure increase due to mechanical coupling and causing drainage of the fluid through the spherical boundary.

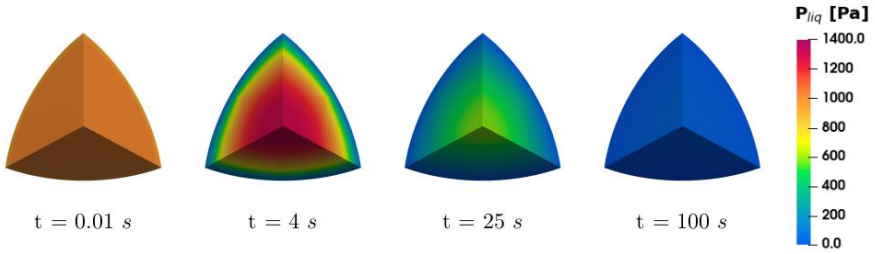

Figure 11: Evolution of the liquid pressure in the domain as a function of time.

At t=0.01s, a sudden rise in pressure is captured due to the application of compressive force to the outer surface, as can be seen in Figure 11. The increase corresponds exactly to the load value. At later stages, the Mandel-Cryer effect can also be seen. Indeed, the pressure rises above the value imposed by the compressive load in the central region of the sphere, where the maximum is reached at about 4 s. This non-monotonic increase in pressure is mainly due to a transfer of the load towards the centre of the sphere, which becomes effectively stiffer as a result of the consolidation process. Then, under the effect of the drainage boundary condition, the pressure gradually dissipates. Finally, the spherical domain returns to its initial pressure state when consolidation is complete.

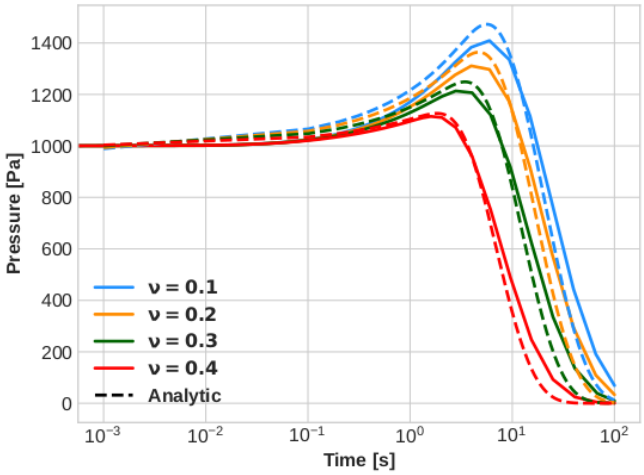

Figure 12

Figure 12: Comparison of the evolution of the pressure for different values of the Poisson coefficient as a function of time.

Figure 12 shows the time evolution of the pressure at the centre of the sphere for four values of the Poisson coefficient. The results are in good agreement with the analytical solutions shown by the dashed lines, but also with the literature, it is noticeable that the non-monotonic pressure rise, known as the Mandel-Cryer phenomenon, is affected by the value of Poisson's coefficient. For small values of Poisson's coefficient; the pressure rise appears to be more pronounced and to occur later than for larger values.

Consequently, the proposed mathematical model and numerical framework have been verified for their ability to capture the coupling effect induced by fluid flow and geomechanical interactions, using the well-known consolidation examples of a fluid-saturated poroelastic medium. This coupling effect is mainly related to the Mandel-Cryer phenomenon, which reflects a significant non-monotonic pressure increase that needs to be considered for flow problems in geological reservoirs.

4. Conclusions

Two implicit and sequential strategies have been considered for the numerical modeling of THC processes in porous media. Both strategies have their own set of advantages and disadvantages. Consequently, they each have their proponents and critics, making challenging a choice between one or the other. Both methods have been assessed for accuracy, specifically regarding mass conservation. While the implicit method maintains perfect mass conservation, the sequential approach may introduce errors such as mass conservation error due to splitting. In terms of performance, both approaches have been evaluated based on computational time and the sequential strategy is faster in most of the configurations because the numerical difficulites are reduced in comparison with the implicit method. The sequential method allows also the use of software specifically designed to solve complex chemical equilibrium, making the transition to complex and realistic configurations more flexible. Numerous cutting-edge projects are currently directed towards solving chemical equilibrium problems with the aid of artificial intelligence, significantly reducing the computational time of this step, which constitutes a bottleneck in the overall computational time of sequential couplings. Thus, depending on whether precision or computational time is prioritized, one may choose either the implicit or sequential method, respectively.

Regarding the numerical modeling oh HM processes in porous, a fully implicit strategy has been developed and verified for problems involving water-saturated poromechanics. The ongoing work involves validating this HM formulation for more complex scenarios, such as multiphase flows. Integrating temperature effects into this HM coupling framework poses a significant challenge. THM coupling processes consider non-isothermal multiphase flow alongside equations of state that depend on temperature variations. These temperature fluctuations impact stress calculations by modifying their constitutive relationship. Implementing a THM module within DuMuX could be achieved through either a fully implicit approach or a sequential method, utilizing external software like Code_Aster (https://code-aster.org) for the geomechanical aspect. Ultimately, the long-term objective is to encompass in DuMu^{X} the entire spectrum of THMC processes, where temperature variations, multiphase flow, geomechanics, and chemical interactions are interlinked.

5. Code source

https://dumux.org/ and https://git.iws.uni-stuttgart.de/dumux-repositories/dumux Homepage and source code of DuMu^{X}

https://www.usgs.gov/software/phreeqc-version-3 Homepage and source code of PHREEQC and PhreeqcRM

6. References

Ahusborde, E., et al, 2023. Numerical Simulation of a Thermal-Hydraulic-Chemical Multiphase Flow Model for CO_2 Sequestration in Saline Aquifers, Mathematical Geosciences, https://doi.org/10.1007/s11004-023-10093-72023.

Koch, T., et al., 2021. DuMu^x 3 – an open-source simulator for solving flow and transport problems in porous media with a focus on model coupling, Computers and Mathematics with Applications 81, 423–443.

Bastian, P., et al., 2021. The DUNE framework: Basic concepts and recent developments. Computers & Mathematics with Applications 81, 72–112.

Nardi, A., Idiart, A., Trinchero, P., de Vries, L.M., Molinero, J., 2014. Interface COMSOL-PHREEQC (iCP), an efficient numerical framework for the solution of coupled multiphysics and geochemistry, A reaction module for transport simulators based on the geochemical model PHREEQC. Computers & Geosciences 69, 10-21.

Parkhurst, D., Appelo, C.A.J., 2013. Description of input and examples for PHREEQC version 3-A computer program for speciation, batch-reaction, one-dimensional transport, and inverse geochemical calculations, U.S. Geological Survey Techniques and Methods.

Parkhurst, D., Wissmeier, L., 2015. PhreeqcRM: A reaction module for transport simulators based on the geochemical model PHREEQC. Advances in Water Resources 83, 176-189.

Jara, D., de Dreuzy, J.R., Cochepin, B., 2017. TReacLab: An object-oriented implementation of non-intrusive splitting methods to couple independent transport and geochemical software, Computers & Geosciences, 109, 281-294.

Mandel, J., 1953. Consolidation des sols (étude mathématique), Geotechnique, 3, 287-299.

Cryer, C.W., 1963. A comparison of the three-dimensional consolidation theories of Biot and Terzaghi, The Quarterly Journal of Mechanics and Applied Mathematics, 16, 401-412.

Keilegavlen, E. et al., 2021. Porepy: an open-source software for simulation of multiphysics processes in fractured porous media. Computational Geosciences, 25, 243-265.

Haagenson, R. et al., 2019. A generalized poroelastic model using FEniCS with insights into the Noordbergum effect. Computers & Geosciences, 135, 104399.

Computer implementation of Coupled Thermo-Hygro-Mechanical Models of Bentonite in Engineered Barrier of Nuclear Waste Repository

[1]Kruis, J., [1]Koudelka T., [1]Krejčí, T., [2]Mašín, D.

[1]Czech Technical University in Prague, Faculty of engineering, Department of Mechanics, Czech Republic

[2]Charles University, Faculty of Science, Czech Republic

The project leading to this application has received funding from the European Union's Horizon 2020 research and innovation programme under grant agreement No 847593.

Abstract

The computer implementation of thermo-hygro-mechanical model (THM model) of bentonite in engineered barrier of nuclear waste repository combines a hypoplastic mechanical model for expansive clays in the mechanical part with an extended micromechanical-based model for heat and moisture transfer in deforming medium in the transport part. The THM model was implemented in an in-house open-source FE code SIFEL [1] exploiting parallel computation in three stages.

In the first stage, a coupled heat and moisture transfer model was developed and implemented for deforming porous media. It is based on a micromechanical-based model presented by Lewis and Schrefler in [2]. Primarily, the model was developed for the one-phase (water) flow conditions and validated and tested on small-scale experiments at isothermal conditions. This model in connection with the principle of effective stresses was extended by an effect of volume changes on the global moisture accumulation function (suction curve) observed mainly in expansive soils, and coupled, in the mechanical part, with a hypoplastic model including a double-structure framework enhanced with thermo-hydraulic and thermo-mechanical couplings at micro-structural and macro-structural levels [3]. The hypoplastic formulation proved successful in model simulations with a reasonable match between predicted and experimental trends of saturation, volume change, and swelling pressure.

In the second stage, the THM model was developed and extended for the temperature conditions up to 150˚C. The mathematical model introduces the effect of water and moist air transport under elevated temperatures. Material parameters are assumed as non-linear and dependent on the state quantities, mainly on temperature and saturation degree. The THM model was completed in the staggered algorithm, and it was verified and validated against small-scale experiments heated to 150˚C. The main attention was paid to the effects of non-linear relations for the main parameters, e.g., intrinsic permeability, relative permeabilities of water and gas, and diffusivity, on the model response and its computational stability.

The fully coupled algorithm, where both transport and mechanical parts are running together and lead to fully coupled matrix form in the numerical solution, was developed in the last stage together with the parallel computing.

In addition to the finite element formulation development, the implementation of the THM constitutive model for the mechanical part has further been developed. Within the DONUT work package of EURAD, emphasis was put on the development of numerical aspects of the implementation to improve robustness and efficiency of the simulations.

Significance Statement

The bentonite backfill will be subjected to hydration from the surrounding rock, the nuclear waste's heating up, and various mechanical effects that interact in a complex coupled thermo-hygro-mechanical (THM) phenomena. It is necessary to understand the processes in the near mass and their time evolution to design a safe and reliable repository. Recent research proved the need to perform large-scale or medium-scale heating tests simulating repository conditions in underground laboratories. A lot of facilities are being used around the world. Several of them are built in the Czech Republic.

In-situ tests in underground laboratories are generally intensively instrumented. A large amount of data obtained are required to define the appropriate parameters of coupled THM numerical models. From the soil mechanics point of view, in-situ experiments provide the opportunity to examine the behaviour of swelling clays under controlled conditions and validate coupled THM formulations and associated computer codes.

Recent research in modelling the hydro-mechanical or thermo-hydro-mechanical behaviour of unsaturated soils shows the need to couple mechanical and hydraulic responses. The volumetric deformation of the soil skeleton influences the degree saturation and the value of suction, which affects the effective stress and mechanical properties. The finite element discretization of complex coupled thermo-hydro-mechanical problems transforms the system of partial differential equations into the system of the algebraic equations, which can be usually non-linear and non-symmetric. The mechanical problems are generally described by three unknown displacements. The temperature and partial pressures are assumed in the nodes in the heat and moisture transfer, leading to three unknowns of the system of non-linear partial differential equations. So, the general three-dimensional case is described by six unknowns in every node of the mesh. It implies that the requirements on computers are very high, and they increase rapidly with the increasing number of nodes in the mesh used. The number of nodes in the mesh is influenced by the size and complexity of the geometry as well as by the boundary conditions and used materials, which often require adopting fine mesh due to steep gradients of the unknown function. The advantages of parallel computing are effectively used for such problem.

In order to improve the model performance, the computation can be distributed across several computers or processor cores. In the in-house open-source FE code SIFEL, two approaches to parallel code execution were established:

- multi-thread approach (MPA) based on OpenMP interface

- domain decomposition method (DDM) approach based on the OpenMPI library

MPA was found to be helpful in the loop for assembling the stress resultant vector.

Both were tested on the problem of model parameter calibration based on laboratory permeameter test. The implemented strategies exhibited good scaling 8 (MPA) or 4 (DDM) processors. Increasing the number of processors over that limit does not improved computational times because of communication overhead (DDM) or atomic memory access (MPA).

Table of content

List of figures

List of Tables

1. Thermo-hygro-mechanical model

1.1 Model formulation

The presented THM is composed from two main parts – transport part which solves coupled heat and moisture transport in porous medium, and mechanical solves the mechanical response. The presented model developed for computer simulations of bentonite material behaviour combines a hypoplastic mechanical model for expansive clays in the mechanical part with an extended micromechanical-based model for heat and moisture transfer in the transport part.

1.1.1 Transport part

In the transport part, the coupled heat and moisture transfer in deforming porous media such as soils is described by a micromechanical-based model presented by Lewis and Schrefler in [2], which uses an averaging process assuming that dry air, vapor, and moist air occupy the same volume fraction in the volume together with the solid phase and the liquid water. Three primary unknowns are defined in the material point - pore water pressure, p_w, pore gas pressure, p_g, and temperature, T for the transport part. Generally, three unknown displacements u, v, w, are defined for the mechanical part. This model in connection with the principle of effective stresses is extended by an effect of volume changes on the global moisture accumulation function (suction curve) observed mainly in expansive soils.

1.1.2 Mechanical part

In the mechanical part, a hypoplastic model is used. It includes a double-structure framework enhanced with thermo-hydraulic and thermo-mechanical couplings at micro-structural and macro-structural levels [3]. The hypoplastic formulation proved successful in model simulations with a reasonable match between predicted and experimental trends of saturation, volume change, and swelling pressure. Further models are underway to offer better formulations of microstructural behaviours and improved computational efficiency. The model contains 22 parameters that have to be determined due to experiments. This model was implemented into the SIFEL open-source code, which was developed at the Department of Mechanics at the Faculty of Civile Engineering CTU in Prague [1]. The main capabilities of the model are:

- The dependence of swelling strain on applied stress at the same dry density and, dually, the dependence of swelling stress on dry density at the same stress level
- Irreversibility of strains in wetting/drying cycles
- Dependence of swelling pressure on dry density
- Stress path dependence from unsaturated to saturated state
- Account for double structure/porosity and temperature cycles on ORC or stress
- Water retention curve hysteresis and dependence on void ration

The explicit integration Runge-Kutta-Fehlberg (RKF) algorithm with sub stepping has been selected and implemented in SIFEL code to integrate hypoplastic model in a material point.

The finite element discretization of driving equations in transport and mechanical parts leads to a system of non-linear and non-symmetric system of ordinary differential equations. The time integration of this system of equations is based on the general trapezoidal rule. The solution can be found via a staggered algorithm, where both transport and mechanical parts running subsequently and only the important data are transferred between these parts. On the other hand, the derivation of driving equations in transport and mechanical parts can be proceed together and coupled into a fully coupled algorithm which seems to have a better convergence.

1.2 Model validation and verification

1.2.1 Isothermal small-scale experiments

The computer implementation of the hypoplastic model in connection with Lewis and Schrefler's approach was tested on several examples and benchmarks. Suitable benchmarks can be laboratory tests presented in [4] and [5]. These studies focus on the impact of using high hydraulic gradients on combined measurements of hydraulic conductivity and swelling pressure. The hydraulic conditions are supposed to be consistent with possible water pressures in a deep repository. Both parameters are determined in a full saturation state. Measuring these parameters in such a low-permeable bentonite material requires much time. Therefore, the high hydraulic gradients may accelerate the determination of these parameters. Experiments with the Czech bentonite 75 (B75) from Černý vrch deposit were selected for numerical simulations. The material was uniaxially compacted in the laboratory to reach the required dry density ρ_d = 1200 to 1750 kg/m^3 . The tested samples have a diameter of 30 mm, and a height of 20 mm. The initial values of hydraulic conductivity and swelling pressure were evaluated using a saturation pore water pressure p_w = 1 MPa corresponding to the gradient of grad p_w = 50 MPa/m (hydraulic gradient 5000) [4]. A unique device was used to measure the hydraulic conductivity and the swelling pressure (Figure 1). The setup of this device is described in detail in the reference [4].

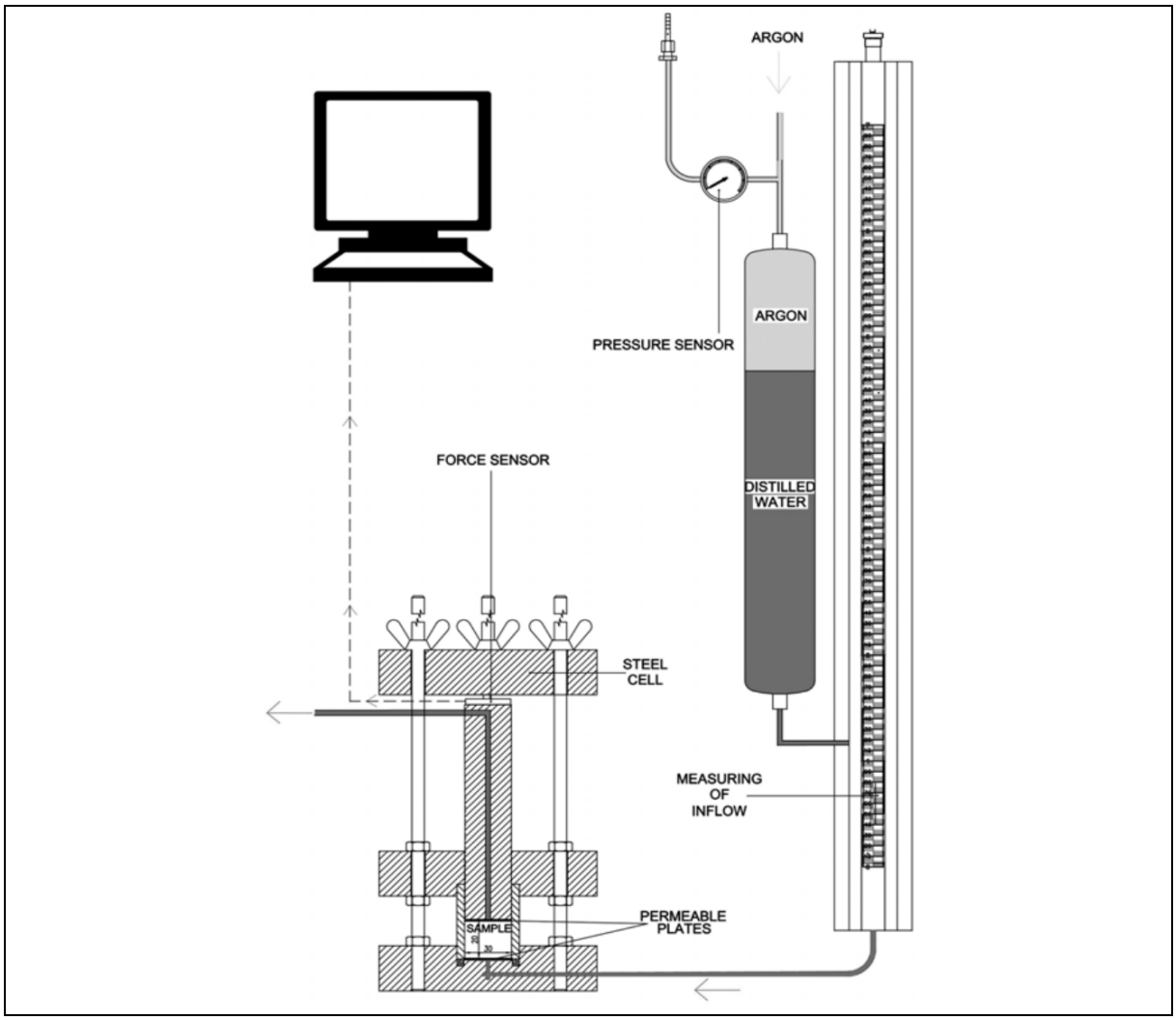

Figure 13 – Scheme of the measuring device [4]

The finite element mesh consists of 20 axisymmetric quadrilateral elements in the vertical direction. Linear approximation functions are used in the transport part and quadratic in the mechanical part. The watering process was modelled as a prescribed pore water pressure from the bottom with the values taken from the measurements. Two switching boundary conditions model the top permeable surface. For the first, the water flux is prescribed zero on the boundary until the water head reaches the closest material point, equal to zero water pressure. Then, the conditions are changed to the Dirichlet boundary condition with prescribed zero water pressure. This procedure is commonly used for free soil surface modelling. The initial pore water pressure p_{w0} = -100 MPa is set for all benchmarks. The soil parameters used in the simulations are used from the recent calibration for bentonite B75 [6]. The sample is fixed to avoid its swelling, and no friction between bentonite material and the steel structure of the testing device is neglected. Three tests with dry density ρ_d =1298 kg/m^3 , ρ_d = 1498 kg/m^3 , and ρ_d = 1743 kg/m^3 were used for verification and validation of coupling of mentioned material models in SIFEL computer code and setup of their parameters. A comparison of selected results for different configurations of dry density and hydraulic conductivity is presented. Figures 2 and 3 show the history of swelling stress for bentonite samples of dry densities ρ_d = 1498 kg/m^3 and ρ_d = 1743 kg/m^3 , respectively. From the considerable number of computations, the best results closed to the measurements are obtained by using of Bogacki-Shampine integration scheme [7] for the hypoplastic model in connection with the smoothed water retention curve [6] and for maximum time step t_{max} = 1000 s [8]. It must be mentioned that such numerical simulations are strongly non-linear, time step length-dependent, and time-consuming. Most of them took from 10 to 20 hours, despite the use of multithreading architecture via OpenMP system. Attained levels of swelling pressure at full saturation depend only on the setup of initial dry densities. This fact corresponds to the previous experiments and hypoplastic model calibration. The swelling stress for bentonite with ρ_d = 1498 kg/m^3 is about 3 MPa, and for ρ_d = 1743 kg/m^3 is 10.5 MPa, respectively. The initial swelling pressures growth is influenced by the sample saturation rate, related to intrinsic permeability (or hydraulic conductivity). The permeability was assumed constant for all benchmarks. For better compliance with the measurements in the initial phase, the application of a relationship dependent on saturation degree can be successfully used. The coincidence between simulations and measurements is validated as relatively good. The trends of watering with loading water pressure jumps are captured well. From the analysis of the results, it can be concluded that coupling the hypoplastic model in connection with Lewis and Schrefler's approach in a staggered scheme works well. However, the model response is primarily dependent on the hypoplastic model setup.

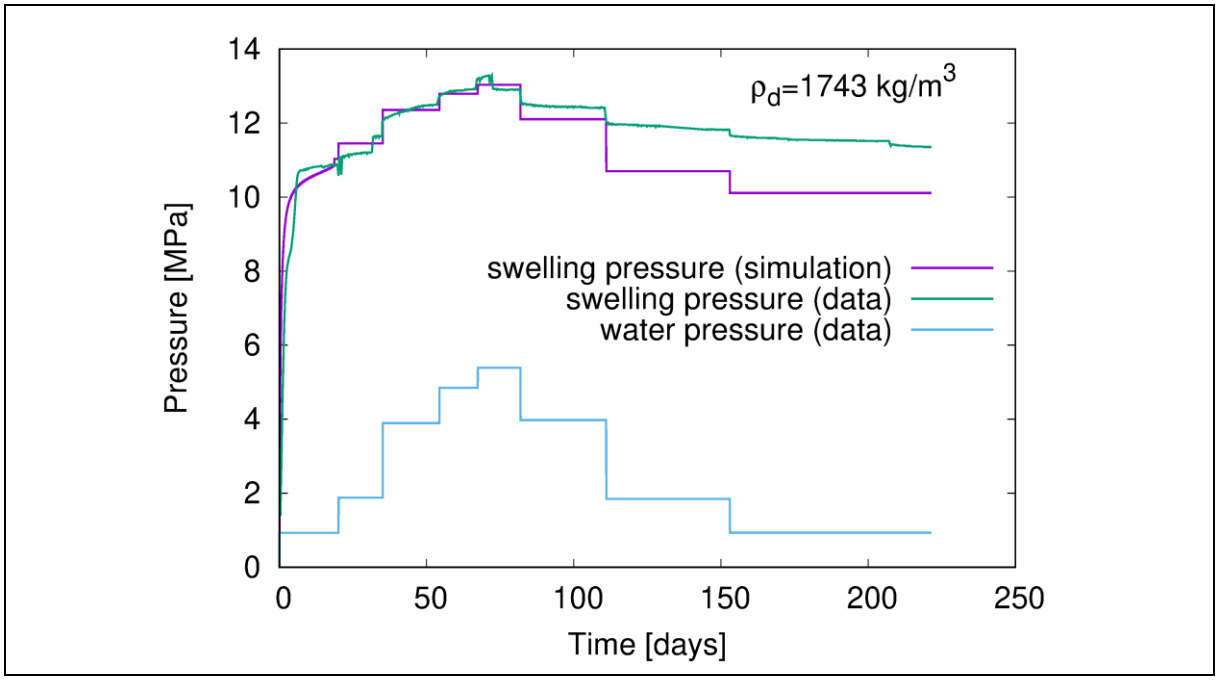

Figure 14 – History of water pressure and swelling pressure for bentonite B75 ρd = 1743 kg/m^3 [8]

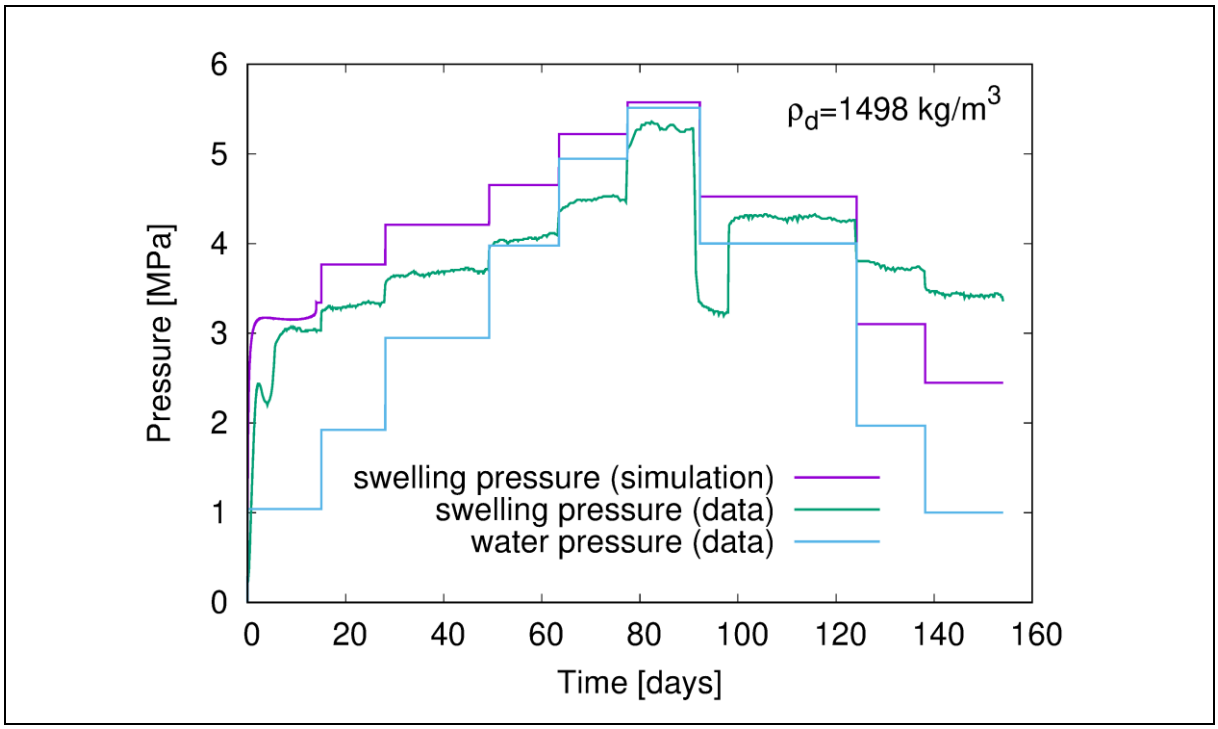

Figure 15 – History of water pressure and swelling pressure for bentonite B75 ρd = 1498 kg/m³ [8]

1.2.2 Small-scale experiments at high temperatures

The aim of the small-scale experiment (chamber of ø 30 cm, height 30 cm) was the investigating the influence of long-term thermal loading (dry and wet materials loaded at 150°C for 6, 12, and 24 months) on bentonite material. Attention was paid to analyses of water content and dry density changes and obtaining data for mathematical modelling - measuring the geotechnical parameters – hydraulic conductivity, swelling pressure, liquid limit, etc. The experiment was performed in the Josef Underground Research Facility (URF) laboratory of the Faculty of Civil Engineering Czech Technical University in Prague, Czech Republic [6]. Two runs of the experiment were performed. For the first, the BCV (bentonite from Černý Vrch repository) of the initial dry density 900 kg/m³ was used. The material was saturated with 6 bars of water pressure and heated up to 150˚C. Phases of watering and heating were performed simultaneously to avoid water boiling. In the second run, the experiment was heated up to 150˚C the first and then watered. For this setup, the water boiling is expected in the middle of the chamber. The BCV initial dry density was 1400 kg/m³. This second run simulates the conditions in the nuclear waste repository more precisely.

The presented numerical model simulates the experiment's first run with the simultaneous watering and heating phases. Unfortunately, the hypoplastic model could not be calibrated to the experimental dry density 900 kg/m³ - powder state. It is developed for compacted block bentonite with higher dry density. The dry density 1440 kg/m³, which is relevant for the repository, was used in the simulation. The water pressure boundary condition was idealized and simplified into the piecewise linear graph to ensure the stability of the computation.

From the analysis of the results, it can be concluded that the saturation process ends approximately after 274 days. The swelling pressure evolution corresponds to the prescribed water pressure (Figure 7). The value of 4 MPa corresponds to the zero water pressure (water contact), and the value of 10 MPa reaches the swelling pressure for the water pressure level of 8 MPa. A good coincidence is observed for the evolution of temperatures between computation and measurement.

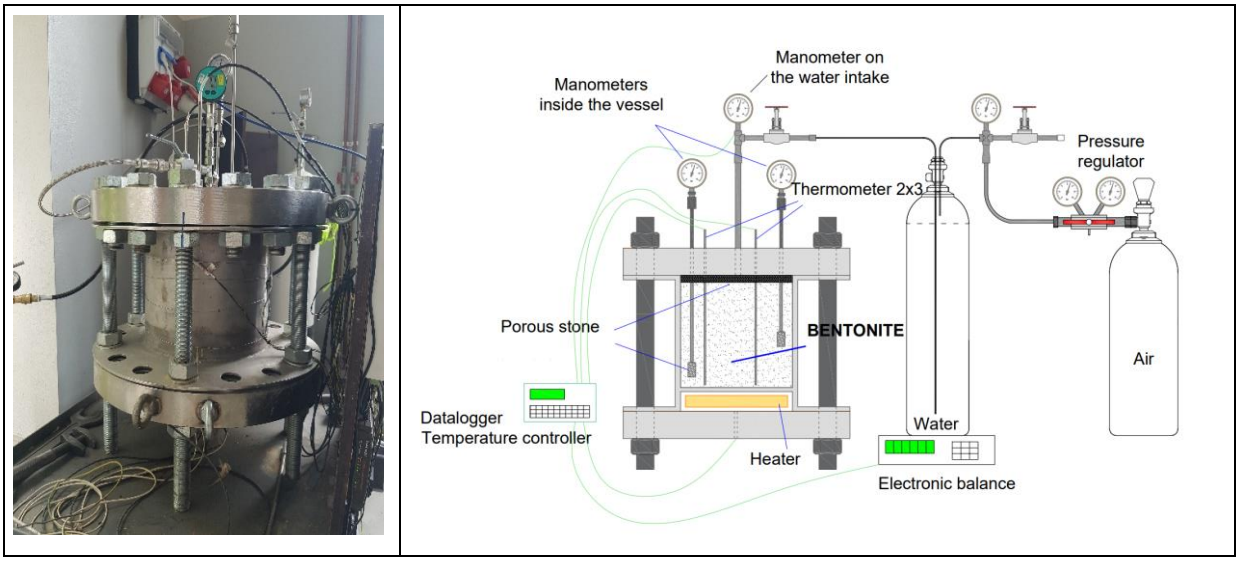

Figure 16 – Installation and the setup of the heated experiment

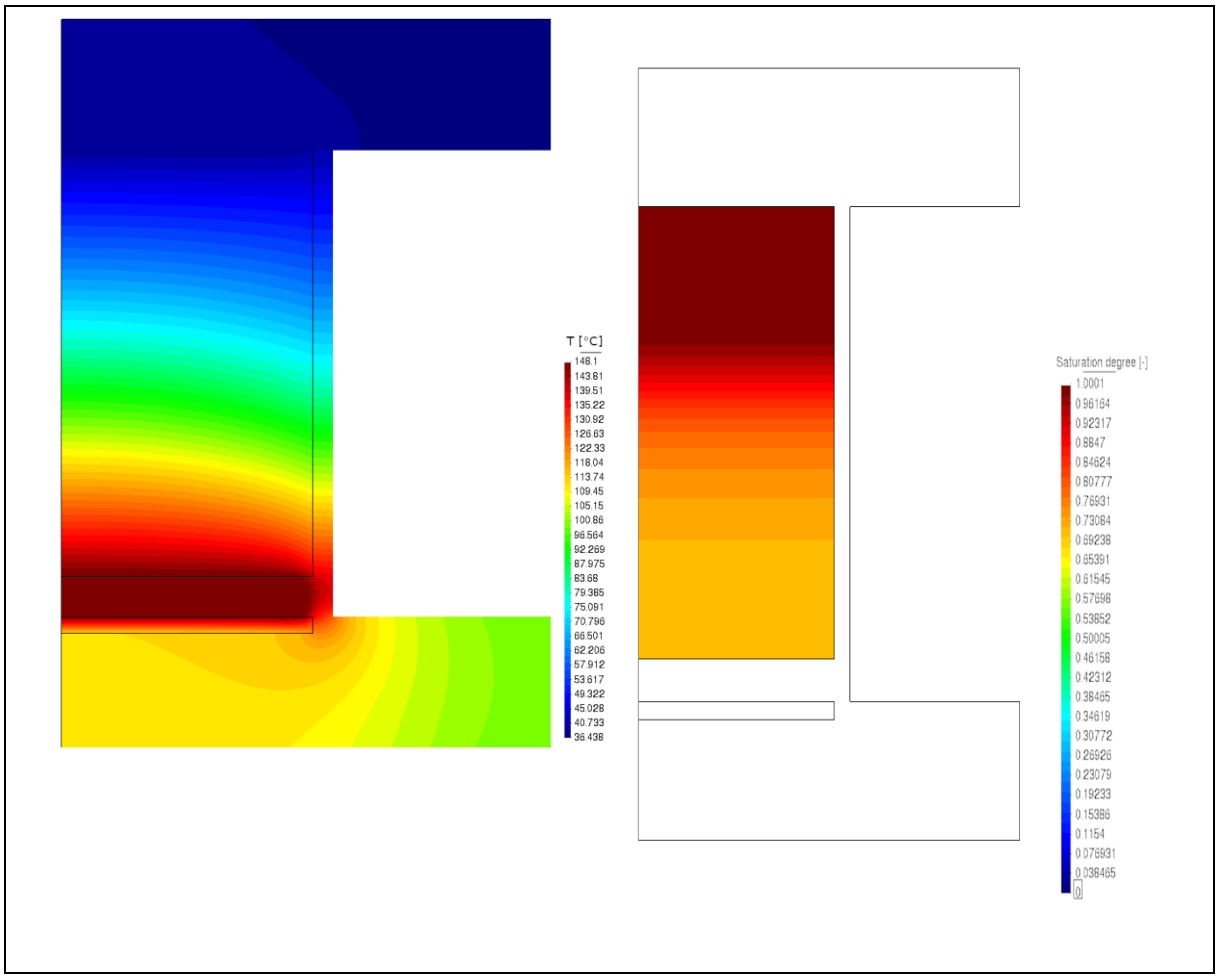

Figure 17 – Temperature profile after 30 days (left), FE mesh of the axisymmetric domain and the saturation degree profile after 30 days (right)

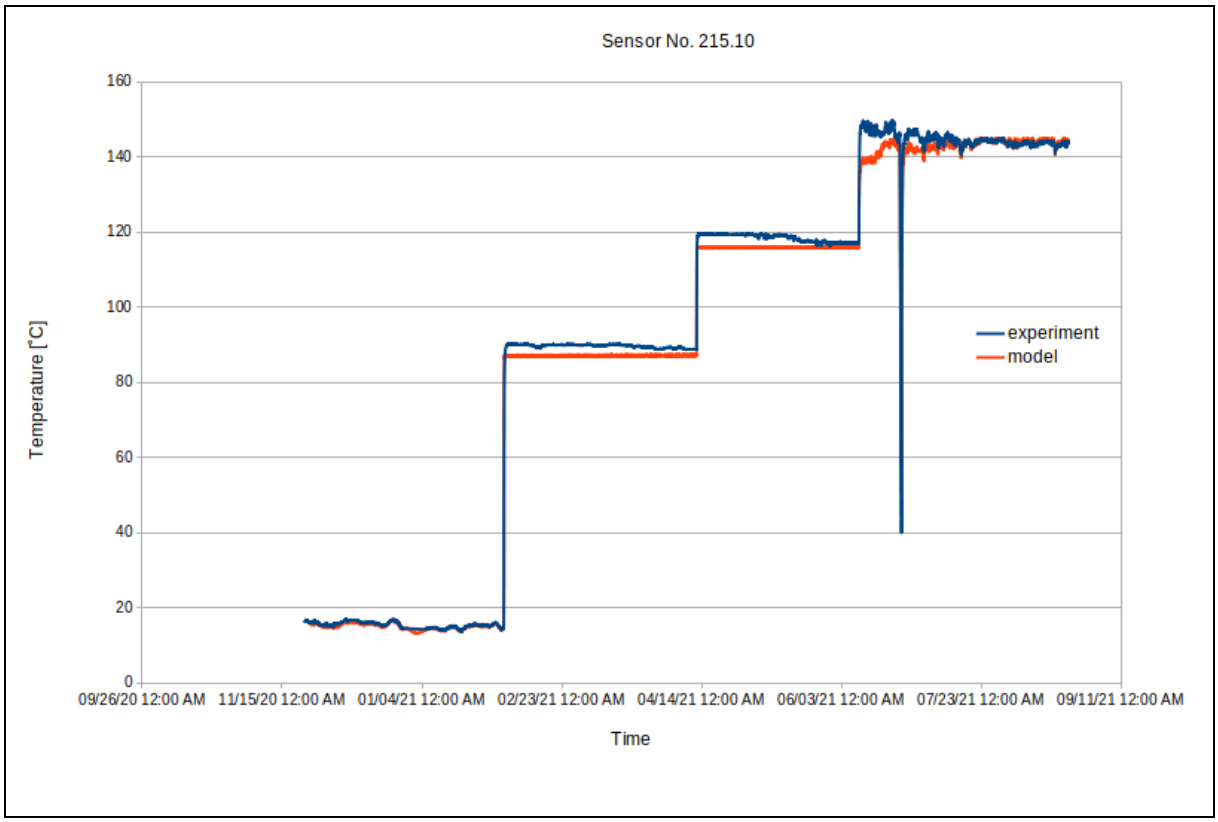

Figure 18 – Temperature history in a selected sensor No. 215.10

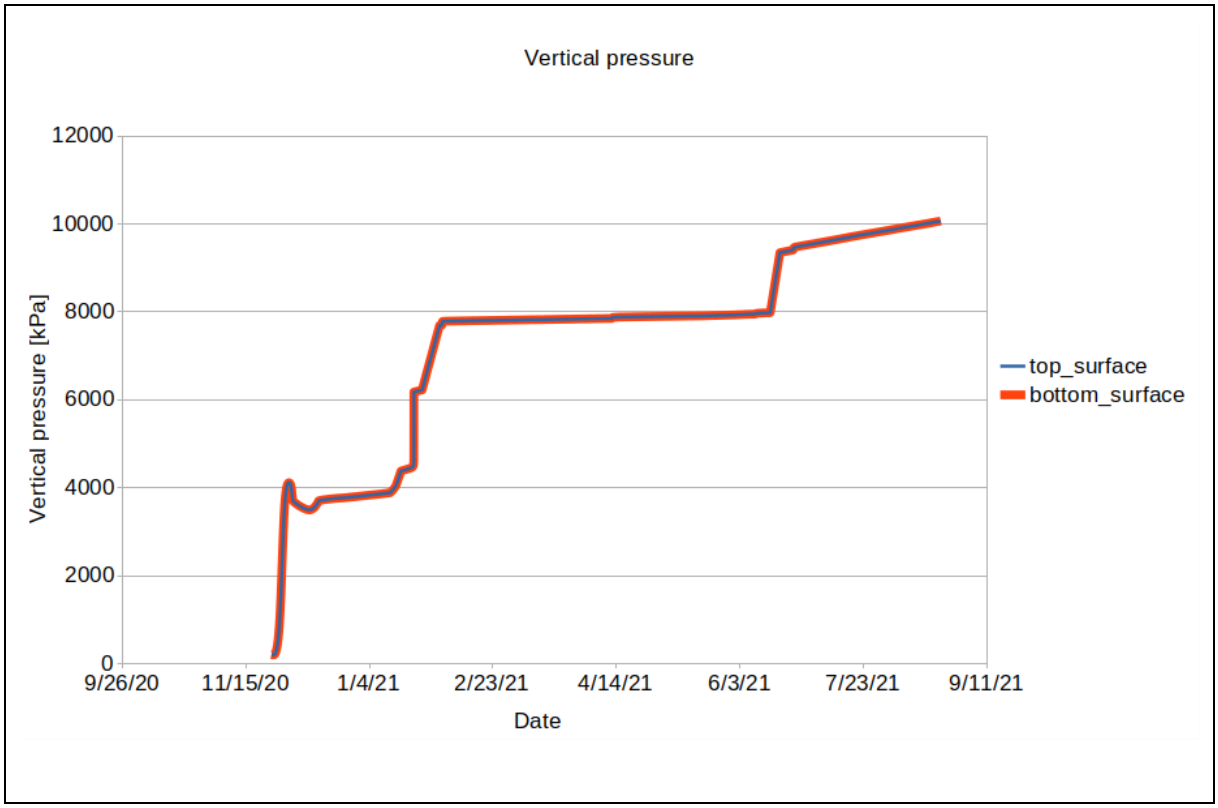

Figure 19 – Swelling pressure history

1.3 Multithread approach

This approach was motivated by a very complex and comprehensive bentonite model based on hypoplasticity which was proposed at Charles University in Prague. The model requires integration by explicit adaptive Runge-Kutta-Fehlberg method that often leads to short integration steps and many iterations and therefore evaluation of a stress state is very computationally demanding. In the case of SIFEL computer code, there is a loop for the evaluation of stress resultant vector on all elements, which was found worth for multithread approach. The multithread approach was tested on the permeameter test used for the model calibration. The following table summarizes elapsed times for single and multithread runs:

Number of threads	Total time in multithread procedure [s]	Total elapsed time [s]
1	31	33
2	16	18
4	8	10
8	5	8
16	6	9

Table 1 – Elapsed times for single and multithread approaches without element reordering

1.4 Domain decomposition approach

Domain decomposition approach is intended for large problems with shared as well as distributed memory. By default, scattering local vectors to the master processor and gathering results from global vectors is implemented in terms of degrees of freedom (DOF) defined at nodes. The problem arised when the norm of residual vector is scaled by the norm of attained load vector in the coupled problems where no mechanical load is being applied, e.g. swelling tests where the stress/load is generated by change of suction and, consequently, swelling strain/pressure evolution. If the tolerance threshold would be compared with the absolute value of residual norm then the convergence could not be attained for higher swelling pressure values. In these cases, it was necessary to implement scaling by the norm of reaction vectors at nodes, i.e. in the constrained DOFs not involved in the system matrix and vectors. Implemented domain decomposition method for staggered solution of coupled problems was tested on the same permeameter test as multithread approach but on different hardware.

Number of threads/processors	Total time in multithread procedure [s]	Total elapsed time multithread [s]	Total elapsed time of domain decomposition method [s]
1	86	92	--
2	42	48	44
4	22	26	23

Table 2 – Elapsed times for multithread and domain decomposition approaches

1.5 Conclusions

Conclusions made from numerical simulations provide valuable information not only for the setup of the numerical model but mainly for the production of the physical model, which brings several uncertainties. The numerical model using the hypoplastic model for expansive soils in connection with the micromechanical-based approach for hygro-thermal transport appears to be very promising in modelling interaction experiments and engineered barriers. The multi-thread approach accelerates assembling of matrices and vectors significantly because the hypoplastic model requires enormous number of arithmetic operations.Large problems can be solved with the help of domain decomposition methods, where each subdomain can use the multi-thread approach described above.

2. Constitutive hypoplastic model

Within DONUT work package, constitutive hypoplastic model was studied from the numerical implementation perspective and various aspects of the code have been improved to increase robustness and efficiency of the simulations. This is described in this chapter. For more details of the model formulation and previous studies, see [3,10,11].

2.1 Improvement of hypoplastic model formulation to predict oedometric swelling capacity

It has been pointed out at the stage of preparation of the project proposal that the THM hypoplastic model underpredicts oedometric swelling capacity if its swelling properties are calibrated using swelling pressure and isotropic swelling experimental results. It has been presumed this discrepancy is due to the missing microstructural strain anisotropy within the model formulation and planned that this anisotropy will be included in model formulation. Research within DONUT package has, however, identified that the main cause of the swelling capacity underprediction is not anisotropy of model formulation, but rather swelling limit defined by normal compression line combined with the particular effective stress formulation for macrostructure and highly anisotropic evolution of total stresses during oedometric swelling process. This finding has been used to improve model predictions during oedometric swelling, as demonstrated in the following.

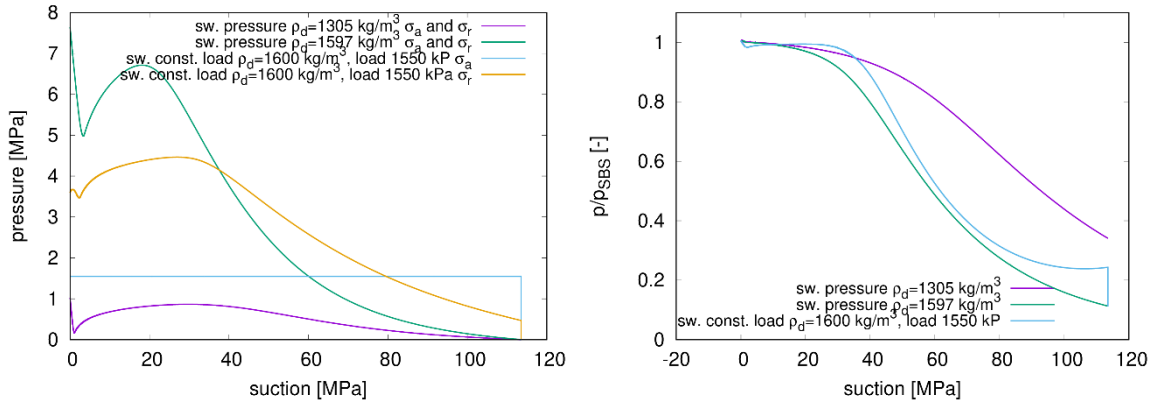

Figure 20 – Comparison of predictions of selected swelling pressure tests and oedometric swelling under constant load tests.

Figure 20 left shows evolution of radial and axial stresses in swelling pressure (constant volume) and swelling under constant load (oedometric conditions) tests. It is clear that the swelling under constant load experiment led to development of significant total stress anisotropy, i.e. radial stress having much larger value than the (constant) vertical stress. As a consequence of this stress anisotropy, soil state reaches state boundary surface (ratio of p vs. p_{SBS}) at much larger values of suction than during swelling pressure tests. As state boundary surface limits swelling potential, swelling potential in oedoemetric swelling is lower than swelling potential in isotropic swelling or swelling pressures developed in constant volume swelling.

To remedy this problem, macrostructural effective stress formulation is updated in such a way that mean effective stress is reduced during wetting process by increasing the value of macrostructural water retention curve slope λ_{p0}. As a consequence, soil state does not reach state boundary surface early during suction decrease, which, at the end, increases soil swelling potential. Reasonable predictions of the both swelling strains and swelling pressures are demonstrated in *Figure 21*.

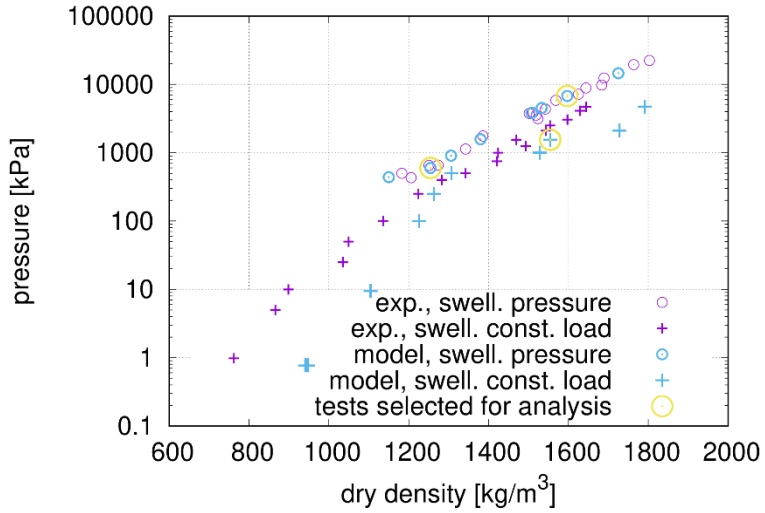

Figure 21: Pressure vs. dry density diagram for swelling pressure and swelling under constant load tests as predicted by hypoplastic model and as experimentally measured.

2.2 Improvement of microstructural iterations on the swelling/compression transition

One of the not so common features of hypoplastic model with double structure is its implicit formulation on the material point level. The reason for it is as follows. The general formulation, described in [3], reads

$$\dot{\boldsymbol{\sigma}}^M = f_s[\boldsymbol{\mathcal{L}}:(\dot{\boldsymbol{\epsilon}} - f_m\dot{\boldsymbol{\epsilon}}^m) + f_d\mathbf{N}\|\dot{\boldsymbol{\epsilon}} - f_m\dot{\boldsymbol{\epsilon}}^m\|] + f_u(\mathbf{H_s} + \mathbf{H_T}) \quad (1)$$

where $\dot{\boldsymbol{\sigma}}^M$ is the rate of macrostructural effective stress, $\dot{\boldsymbol{\epsilon}}$ is total strain rate and $\dot{\boldsymbol{\epsilon}}^m$ is microstructural strain rate. The microstructural strain rate depends on the total stress evolution, which thus appears not within the formulation of $\dot{\boldsymbol{\sigma}}^M$, as normal in mechanical constitutive models, but also on the right-hand side of hypoplastic equation. Eq. (1) further involves scalar variables f_s , f_u and f_m and tensorial variables $\boldsymbol{\mathcal{L}}$, $\mathbf{N}$, $\mathbf{H}_s$ and $\mathbf{H}_T$ whose meaning is explained in [3]. Because the microstructural strain rate appears within the Euclidian norm of a sum of two tensorial arguments, the equation cannot be explicitly solved for the rate of total stress based on the known rate of strain and the solution becomes implicit. As the aim is to find a microstructural strain rate, the implicit solution is denoted as microstructural iterations. The flowchart of the solution procedure has been defined in [3]:

$$
\begin{aligned}
&\mathrm{TOL} = \mathrm{round\_to\_digits}(\|\dot{\boldsymbol{\epsilon}}\|/1000);\\
&\text{if } (\mathrm{TOL} < 1.e-10) \text{ then } \mathrm{TOL} = 1.e-10;\\
&i = 1;\\
&\mathrm{tr}\dot{\boldsymbol{\epsilon}}_{\mathrm{iter}}^{m(i)} = 0;\\
&\mathrm{err}^{(i)} = 1;\\
&\text{calculate } \boldsymbol{\mathcal{L}},\ f_d,\ f_u;\\
&\textbf{While } \mathrm{err}^{(i)} > \mathrm{TOL} \textbf{ do};\\
&\quad \text{calculate } f_m^{(i)};\\
&\quad \text{calculate } \lambda_{\mathrm{act}}^{*(i)};\\
&\quad \text{calculate } \mathbf{N}^{(i)},\ \mathbf{H}_T^{(i)},\ \mathbf{H}_s^{(i)},\ f_s^{(i)};\\
&\quad \dot{\boldsymbol{\epsilon}}_{\mathrm{iter}}^{m(i)} = \tfrac{1}{3}\mathrm{tr}(\dot{\boldsymbol{\epsilon}}_{\mathrm{iter}}^{m(i)});\\
&\quad \dot{\boldsymbol{\epsilon}}^{M(i)} = \dot{\boldsymbol{\epsilon}} - f_m^{(i)}\dot{\boldsymbol{\epsilon}}_{\mathrm{iter}}^{m(i)};\\
&\quad \dot{e}^{M(i)} = (1+e^M)\mathrm{tr}[\dot{\boldsymbol{\epsilon}}^{M(i)} + (f_m^{(i)}-1)\dot{\boldsymbol{\epsilon}}_{\mathrm{iter}}^{m(i)}];\\
&\quad \overset{\circ\,\mathrm{net}(i)}{\boldsymbol{\sigma}} = f_s^{(i)}(\boldsymbol{\mathcal{L}}{:}\dot{\boldsymbol{\epsilon}}^{M(i)} + f_d\mathbf{N}^{(i)}\|\dot{\boldsymbol{\epsilon}}^{M(i)}\|) + f_u(\mathbf{H}_s^{(i)} + \mathbf{H}_T^{(i)}) +\\
&\qquad \mathbf{1}S_r^M\left[(1-\gamma r_\lambda)\dot{s} - \gamma s\frac{\dot{e}^{M(i)}}{e^M} + \frac{\gamma s b\dot{T}}{a+bT}\right];\\
&\quad \dot{p}^{m(i)} = \tfrac{1}{3}\mathrm{tr}\overset{\circ\,\mathrm{net}(i)}{\boldsymbol{\sigma}} - \dot{s};\\
&\quad \mathrm{tr}\dot{\boldsymbol{\epsilon}}^{m(i)} = f_{ul}\left(\alpha_s\dot{T} - \frac{\kappa_m}{p^m}\dot{p}^{m(i)}\right);\\
&\quad \mathrm{err}^{(i)} = |\mathrm{tr}\dot{\boldsymbol{\epsilon}}^{m(i)} - \mathrm{tr}\dot{\boldsymbol{\epsilon}}_{\mathrm{iter}}^{m(i)}|;\\
&\quad \mathrm{tr}\dot{\boldsymbol{\epsilon}}_{\mathrm{iter}}^{m(i+1)} = (\mathrm{tr}\dot{\boldsymbol{\epsilon}}^{m(i)} + 3\mathrm{tr}\dot{\boldsymbol{\epsilon}}_{\mathrm{iter}}^{m(i)})/4;\\
&\quad i = i+1;\\
&\textbf{end}
\end{aligned}
$$

Flowchart of the hypoplastic model implicit solution procedure (from [3], for definition of additional variables see [3]).

While using the model in general loading scenarios during finite element solution procedure, however, the following problem occasionally appears. The solution requires quantification of the double structure coupling factor f_m which depends on the sign of $\dot{p}^m$. In the cases where $\dot{p}^m$is close to zero, oscillation between the two values of $f_m$occurred as the sign of $\dot{p}^m$could be changing within the microstructural iterations loop.

Within DONUT, it was first necessary to identify this problem. Once the problem was understood, a remedy was introduced into the code, such that the sign of $\dot{p}^m$is approximated by the sign of $\dot{s}$ in the case if THM loading involving variable suction. As $\dot{s}$ is a prescribed variable (it is a factor withing the generalised strain rate), it is not prone to oscillation during iterations. At the same time, it was verified that the assumption does not have significant effect on solution results.

2.3 Improvement of the description of the stiffness matrix in the iterative solving process

A key component controlling convergence of the global finite element iteration is the Jacobian (stiffness matrix) generated at the integration point by the constitutive model. While some constitutive models in combination with certain time integration methods allow for explicit analytical derivation of the Jacobian, in many cases of advanced non-linear models an analytical derivation of the Jacobian is not feasible

and thus an approximation must be used. The approximation does not allow for quadratic convergence of the global iteration scheme, however, this only leads to more global iterations needed to minimise unbalanced forces. If the iteration process is robust, the increased number of global iterations is not problematic and, at most, leads to increased simulation times.

Within DONUT, several methods for definition of Jacobian matrix have been tested and their effect on simulation robustness and speed has been studied. The following cases were evaluated:

(a) Numerical calculation of consistent Jacobian by the generalised strain increment perturbation for all components of the generalised strain rate tensor.
(b) Numerical calculation of consistent Jacobian by the generalised strain increment perturbation for suction component of the generalised strain rate tensor, direct approximation using hypoplastic L tensor for mechanical components of the generalised strain rate tensor
(c) Hybrid scheme, in which (a) is adopted for the first predefined number of iterations, switched to (b) in the case of non-converging simulation.

While, in principle, case (a) should lead to more efficient simulations as quadratic convergence of the global Newton-Raphson scheme should be guaranteed, it was found that in some cases (in particular those involving disallowed states, see Sec. 2.4), severe divergence would occur. At the same time, for large strain increment with many sub-increments involved in model integration at the Gauss point level, numerical calculation of consistent Jacobian is very inefficient. As a consequence, it was found that most efficient and robust simulation is achieved through numerically cheap approximation of Jacobian matrix using hypoplastic L- tensor. This case (b), was still better than the hybrid scheme (c), where switch to (a) was activated after non-convergence of (b) was identified.

2.4 More efficient mathematical error control and disallowed state correction

Hypoplastic model is a complex non-linear model. Although its formulation based on asymptotic state concept should, in principle, guarantee, that the state remains within physical bounds, numerical errors can lead to states which are disallowed from the model perspective. Such states may lead to undefined mathematical operations errors and, obviously, divergence of simulation. As these problems are scarce and can occur at various places in the code, a complex error-management system had to be introduced into the model implementation. A special two-level algorithm was defined, in which the known potential problems are first checked and a correction is attempted using a new *correct_statev_values* function. Subsequently, the code is checked for math errors through check of the generic C++ *errno*[2] variable. If math error occurred and could not be remedied by *correct_statev_values* function, current step solution is rejected and a message is sent to the finite element code, which then attempts to overcome the problem by decreasing the global step size.

The above described two-level error control check is run many times during the simulation, actually, at each and every call of the constitutive model within the adaptive Runge-Kutta integration scheme.

The following problems are checked within *correct_statev_values* function:

(a) As soon as any normal components of the macrostructural effective stress tensor becomes tensile, that component of total stress tensor is corrected such that the effective stress calculation yields that stress tensor component equal to zero.
(b) Non-mechanical component of the Jacobian stiffness matrix dSr/ds is checked for remaining positive.

Subsequently, general math error algorithm which first checks that all components of generalised strain tensor, generalised strain increment tensor, generalised stress tensor and state variable vector are not equal to NAN. Finally, *errno* values are being monitored to identify errors which were not spotted using algorithm described above.

[2] The errno variable is an integer variable and set by system calls and library functions to indicate the source of an error

2.5 Correction of stress increment at states close to full saturation

Previous version hypoplastic model yielded the following transient response of stress evolution in benchmark experiments, in which bentonite is saturated from the as-compacted states under the globally constant volume conditions.

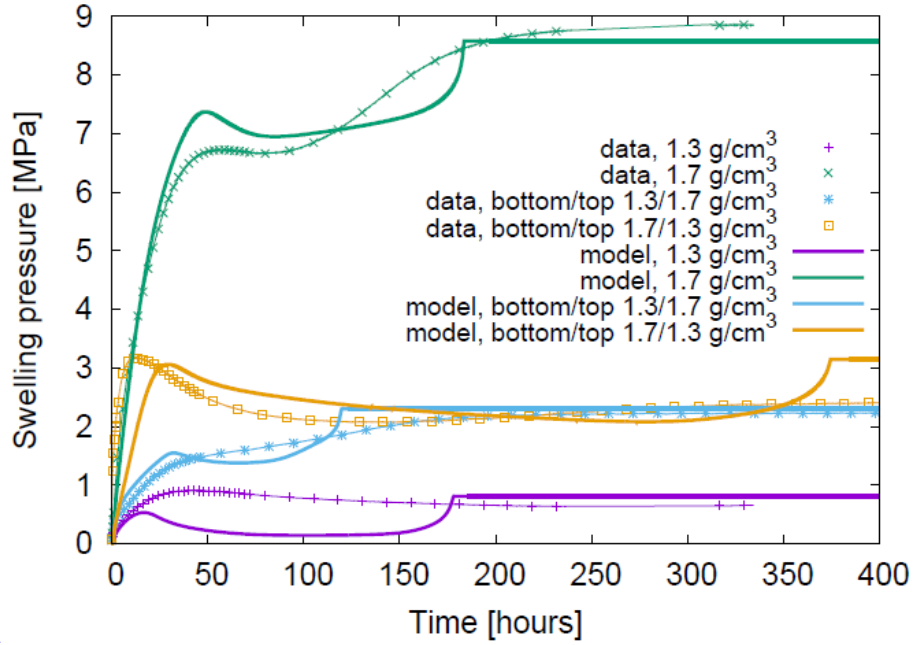

Figure 22: Swelling pressure evolution during saturation experiment performed using 2022 version of hypoplastic model from [10].

While the predictions are, in general, relatively accurate, a fast increase of swelling pressure followed by sharp switch to zero pressure increment can be observed at states close to full saturation. The reason for this behaviour has been identified in the adopted water retention curve, see Figure 23. Originally, it has been assumed that the problem was in bi-linear Brooks and Corey-type of WRC model, adopted originally in [3]. A smoothed version of WRC was thus developed and implemented in [10], leading the the WRC curves with smoothed saturation transition (see Figure 23, “model 22” curve). The smoothing of WRC improved numerical stability of finite element simulations close to full saturation, however, it still leads to a sharp king in swelling pressure temporal evolution of swelling pressure identified in Figure 22. This is because swelling pressure evolution is governed by the effective stress evolution with suction, where one-to-one relationship holds true when soil is fully saturated (as the Bishop chi-factor is equal to one). Thus, when suction is decreased from the initial value of, by example, 100 MPa, swelling pressure increases by 1 MPa (which can be of the order of 15% of the total swelling pressure for 1.7 g/cm^3 dry density specimen) during suction decrease from 1 MPa to 0 MPa (which is 1% of the total suction decrease in that specific test).

To remedy this problem, even more rounded shape of water retention curve must be adopted for wetting branch of WRC, as shown in Figure 23 (model 2023). This remedy is not only useful from the standpoint of numerical stability, but also better represents experimental data which do not show an abrupt change of water retention curve slope at a specific air-entry value of matric suction. This is accomplished by substantial decrease of S_{lim} parameter from [10], which originally was equal to 0.75 and newly equal to 0.2. Also, the parameter p_{wett} was decreased from 1.1 to the new value of 1.0. With the new formulation, full saturation is reached at much lower value of suctions (“model 23” in Figure 23), leading to the smooth shape of swelling pressure evolution curve.

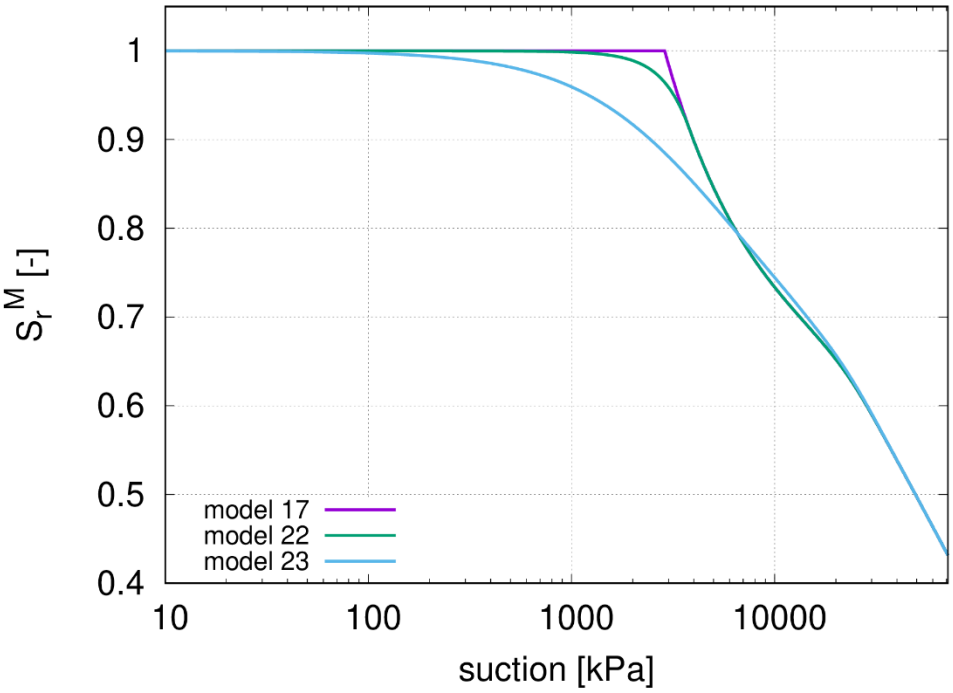

Figure 23: Water retention curves used in 2017, 2022 and 2023 versions of hypoplastic model

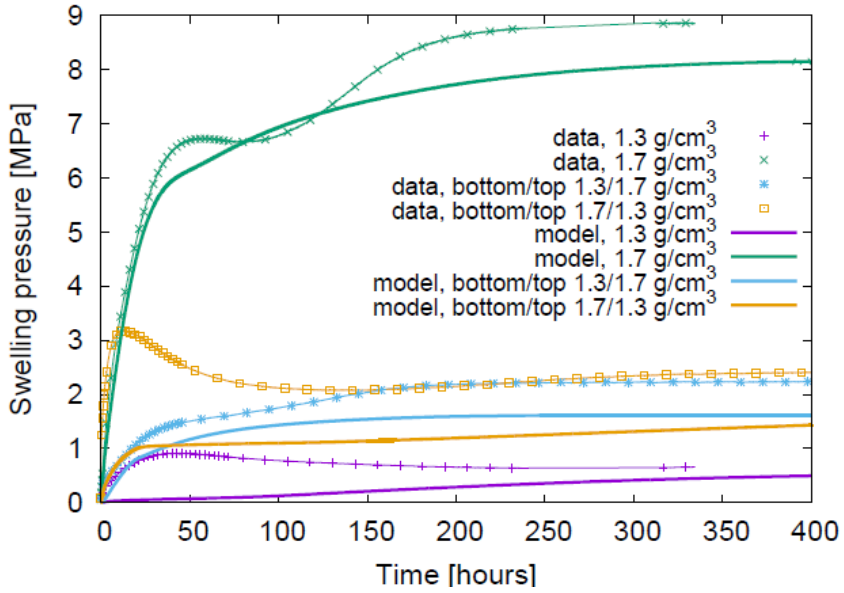

Figure 24: Swelling pressure temporal evolution calculated using the 2023 version of the hypoplastic model.

2.6 Controll of the temporal pressure decrease peak in saturation experiments

As shown, for example, in Figure 22, the model predicts a temporal peak in the swelling pressure evolution curves, occurring before full saturation takes place. While this peak is often also noticeable in experiments, previous version of hypoplastic model was not capable of controlling this peak, which often lead to its significant overestimation.

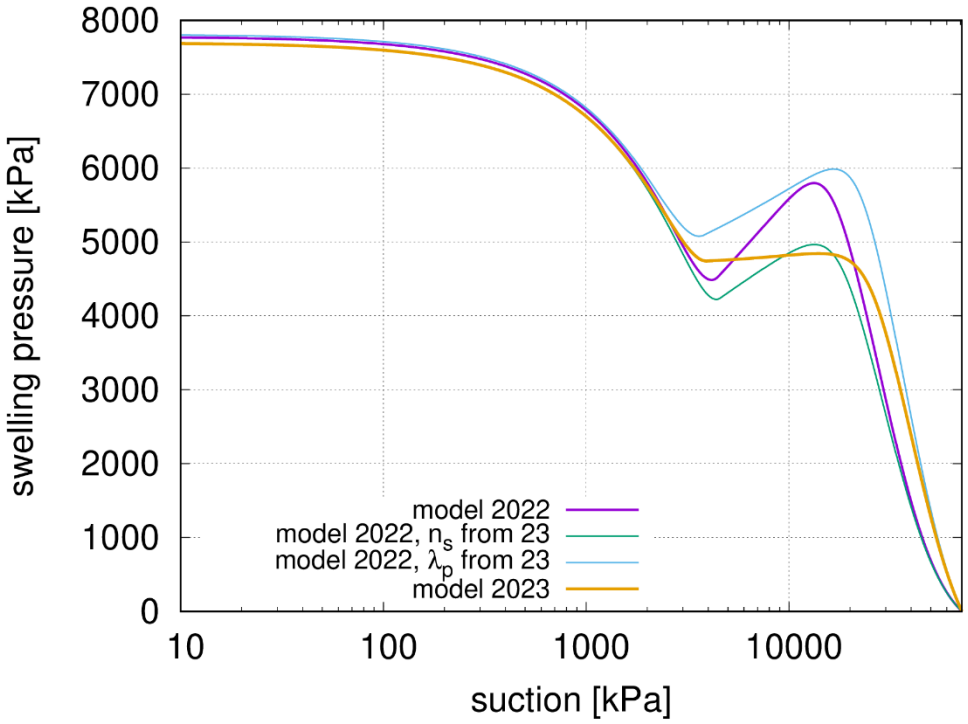

Figure 25: Evolution of swelling pressure during constant volume suction decrease at the element level.

A study was undertaken, investigating the effect of individual model components on this peak. It was found linked to a combination of the wetting-induced collapse controlled by parameter n_s, in combination with the slope of the effective stress parameter χ controlled by a parameter λ_p. Counter-intuitively, individual change of these parameters has only little effect on peak (see Figure 25), but it can be reduced dramatically when both parameters are changed simultaneously (see Figure 25). The user of the model has thus now a means to control the temporal pressure peak by varying both parameters λ_p and n_s. Simulations in Figure 24 have been obtained with parameter set reducing the peak, where the values of λ_p and n_s were changed from the original values of -0.005 and 0.7 to the new values of 0.0 and 1.0. These values were also adopted while generating results for Figure 25.

2.7 Conclusions

A number of numerical problems related to the formulation of THM hypoplastic double structure model has been targetted in the DONUT work package of EURAD project, The resulting model provides more accurate predictions of bentonite behaviour and also helps to make the finite element simulations more robust and efficient, enabling thus to reach the solution and reducing the needed CPU resources and CPU time.

Code source

https://mech.fsv.cvut.cz/~sifel/

References

[1] Kruis, J., Koudelka, T., and Krejčí, T. (2001–2023). SIFEL package. http://ksm.fsv.cvut.cz/~sifel/.

[2] Schrefler, B. A. and Lewis, R. W. (1998). The Finite Element Method in the Static and Dynamic Deformation and Consolidation of Porous Media. 2nd Edition. John Wiley & Sons.

[3] Mašín, D. (2017). Coupled thermohydromechanical double-structure model for expansive soils. Journal of Engineering Mechanics, 143(9).

[4] Hausmannová, L. and Vašíček, R. (2014). Measuring hydraulic conductivity and swelling pressure under high hydraulic gradients. Geological Society London Special Publications, 400.

[5] Hausmannová, L. (2017). The influence of water pressure on the hydraulic conductivity and swelling pressure of Czech bentonites. PhD thesis, Czech Technical University in Prague. In Czech.

[6] Sun, H., Scaringi, G., Mašín, D., and Najser, J. (2021). An experimental investigation on the swelling behavior of compacted b75 bentonite. Engineering Geology, page 106452.

[7] Koudelka, T., Krejčí, T., and Kruis, J. (2017). Coupled hydro-mechanical model for expansive clays. AIP Conference Proceedings, 1863(1):290008.

[8] Scaringi, G., Mašín, D., Najser, J., Sun, H., and Sun, Z. (2022). Thermo-hydro-mechanical hypoplastic modelling of bentonite buffers for nuclear waste disposal: model calibration and performance. In In preparation for Proceedings of the 20th International Conference on Soil Mechanics and Geotechnical Engineering, Sydney 2022.

[9] Josef Underground Research Facility (URF), https://ceg.fsv.cvut.cz.

[10] Svoboda, J., Mašín, D., Najser, J. Vašíček, R., Hanusová, I. and Hausmannová, L. (2022). BCV bentonite hydromechanical behaviour and modelling. Acta Geotechnica 18, 3193-3211.

[11] Mašín, D. (2013). Double structure hydromechanical coupling formalism and a model for unsaturated expansive clays. Engineering Geology 165, 73-88.

Hydro-mechanical models for fractured porous media and their parallel solution contribution

[1]Sysala, S., [1]Béreš, M., [1]Horák, D., [1]Kružík, J., [1]Ligurský, T., [1]Luber, T.

[2]Stebel, J., [2]Březina, J., [2]Exner, P.

[1]Institute of Geonics of the Czech Academy of Sciences, Czech Republic

[2]Technical University of Liberec, Czech Republic

The project leading to this application has received funding from the European Union's Horizon 2020 research and innovation programme under grant agreement No 847593.

Abstract

This report describes selected results achieved by teams from the Technical University of Liberec and Institute of Geonics of the Czech Academy of Sciences within Task 2 of WP 12 DONUT. We present mainly the results focused on modelling, numerical solution and implementation of coupled hydro-mechanical processes in fractured granite-type rocks related to deep geological repositories. In particular, the so-called discrete fracture-matrix approach is used and enriched by selected nonlinear effects on fractures. Within numerical solution of related problems, our results are based on stochastic generation of the fracture network, the mixed finite element method, domain decomposition techniques, splitting procedures and state-of-the-art iterative solvers for linear and nonlinear systems. Open-source in-house libraries are developed and combined to solve the problems. A benchmark in 3D including a borehole excavation in fractured rocks is suggested in accordance with in-situ experiments known from literature and used for illustration of the solution concept. Other achievements of the teams within Task 2 are briefly summarized.

Significance Statement

Many countries plan to construct deep geological repositories of spent nuclear fuels (DGR) in rock masses of granite types. Such rocks are naturally fractured due to their brittleness. The fracture network in rocks can create preferential paths for transport of radionuclides. The network can be influenced by the construction of DGR leading to the so-called excavation damage zones (EDZ). Later, thermal and chemical processes related to the spent nuclear fuels can also influence the network.

Modelling of coupled (at least hydro-mechanical) processes in granite rocks is important for description and understanding of observed or expected phenomena and for consequent numerical simulations. A particular interest is devoted to permeability changes in EDZ. Such models are complex and demanding, especially if the rock mass is interconnected with the fracture network and non-linear effects on fractures are considered.

Numerical solution of the proposed models is beyond the possibilities of current commercial codes and computers. Therefore, it is necessary to develop in-house libraries enabling to solve such problems on supercomputers. Open-source platforms are used to make our research more transparent.

Finally, it is important to validate the developed mathematical models and numerical simulations on in-situ and other experiments. To this end we have prepared tools supporting uncertainty treatment. They enable to generate the fracture network or fit parameters of the developed models on basis of expected experimental data. To the best of our knowledge there has not been performed any sufficiently complex in-situ experiment enabling the validation of our model. Therefore, our achievements could also motivate experimental researchers.

Table of content

List of figures

List of tables

Glossary

DFM - discrete fracture-matrix model

DFN - discrete fracture network

DGR - deep geological repositories

EDZ – excavation damage zones

FETI – finite element tearing and interconnect method

HM – hydro-mechanical

IGN – Institute of Geonics of the Czech Academy of Sciences

QP – quadratic programming

THM - thermo-hydro-mechanical

TUL – Technical University of Liberec

1. Introduction

This report describes selected results achieved by teams from the Technical University of Liberec (TUL) and Institute of Geonics of the Czech Academy of Sciences (IGN) within Task 2 of WP 12 DONUT. We present mainly the results focused on modelling and numerical simulations of coupled hydro-mechanical (HM) processes in fractured granite-type rocks related to deep geological repositories (DGR), see Sections 2–5. For more details, we refer to Stebel et al. (2024), Březina and Stebel (2024) and Blaheta et al. (2020).

In particular, in Section 2, we introduce the so-called discrete fracture-matrix (DFM) approach suggested for modelling of intact rock mass with discrete fracture network and enrich it by selected nonlinear effects on fractures. In Section 3, we present numerical solution of the DFM problem arising from the mixed finite element method, splitting procedures which separate coupled HM processes and state-of-the-art iterative solvers for linear and nonlinear systems. We also add details to our open-source in-house libraries used for the solution. In Section 4, we illustrate our solution concept on a 3D benchmark problem simulating a borehole excavation. The benchmark is inspired by real in-situ experiments known from literature. Concluding remarks to the main result (DFM modelling) can be found in Section 5.

Other valuable results of the teams achieved within the solution of Task 2 are briefly summarized in Section 6. They include: a) development of other iterative solvers convenient for coupled processes and related saddle-point problems; b) modelling of selected HM processes in bentonite barriers and soils.

2. DFM model for poroelasticity with non-linear effects

The DFM approach combines advantages of continuum-based and discrete fracture network (DFN) approaches. Fractures are modelled as lower-dimensional objects which interact with an intact (continuum-based) rock matrix where the equilibrium and mass balance equations are satisfied. On the other hand, it is necessary to neglect or smear small-size scaled fractures within the DFM approach, see Figure 26.

In the rest of this section, we briefly explain main ideas leading to the derivation of the DFM model. First, we arise from the continuum-based Biot model (see Section 2.1) including a weaker and more permeable material in zones representing the fractures. Then, a dimensional reduction is applied to the weaker zones, see Section 2.2. Finally, conditions on interfaces between the rock matrix denoted as Ω_m and the fracture network Ω_f have to be introduced to complete the model, see Section 2.3.

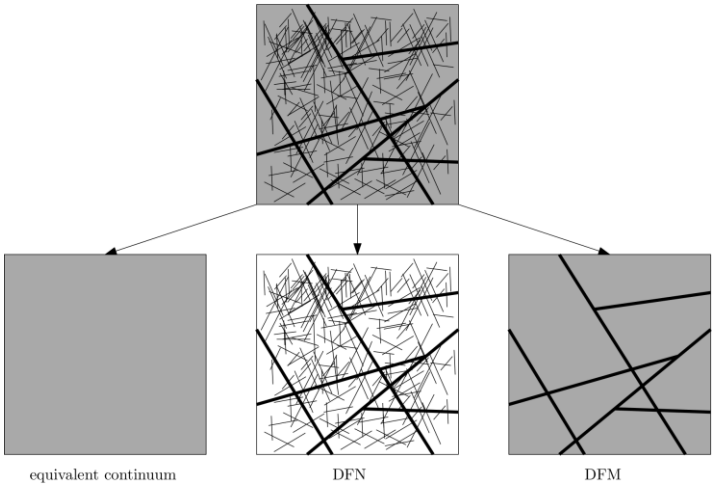

Figure 26 - Schematic comparison of the continuum-based, DFN and DFM approaches to modelling of fractured rocks.

The geometry of the DFM model for simplified 2D case is depicted in Figure 27. Each fracture is assumed to be a lower dimensional manifold with the orientation given by the normal vector $\boldsymbol{\nu} = \boldsymbol{\nu}^+ = -\boldsymbol{\nu}^-$ and with a cross-section parameter δ.

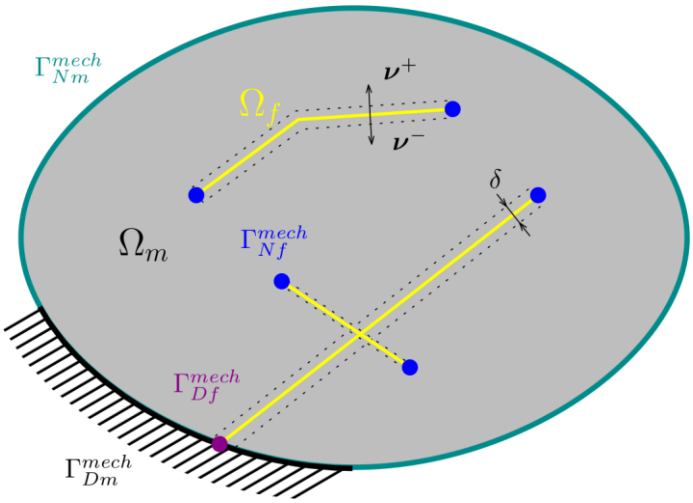

Figure 27 - The geometry of the discrete fracture-matrix model. We refer to Stebel et al. (2024) for more details to the used notation.

The DFM model of poroelasticity is described in terms of the pressure head p, the Darcy flow velocity $\boldsymbol{v}$, the displacement $\boldsymbol{u}$ and the effective stress $\boldsymbol{\sigma}$. Each of these unknown fields is split into two parts representing the rock matrix Ω_m and the fracture network Ω_f. Therefore, we shall write $p = (p_m, p_f)$, etc.

2.1 Biot's model for rock matrix

The mechanical behaviour of the rock matrix is based on the equilibrium equation

$$-\operatorname{div} \boldsymbol{\sigma}_m + \alpha_m \varrho g \nabla p_m = \boldsymbol{f}_m \text{ in } I \times \Omega_m, \tag{1}$$

where $\boldsymbol{\sigma}_m$ is the effective stress tensor, α_m is the Biot-Willis coefficient, ϱ is the density of the liquid, g is the gravitational acceleration, p_m is the pressure head, $\boldsymbol{f}_m$ is the load and $I = (0, T)$ is a time interval. The mass balance in the rock is given by the equation

$$\partial_t (S_m p_m + \alpha_m \operatorname{div} \boldsymbol{u}_m) + \operatorname{div} \boldsymbol{v}_m = \boldsymbol{s}_m \text{ in } I \times \Omega_m \tag{2}$$

where S_m is the storativity, $\boldsymbol{u}_m$ is the displacement, $\boldsymbol{v}_m$ is the Darcy flow velocity, and $\boldsymbol{s}_m$ is the volume source of the fluid. We consider Hooke's and Darcy's laws as the constitutive relations for the stress tensor and velocity, respectively:

$$\boldsymbol{\sigma}_m - \boldsymbol{\sigma}_{0m} = \mathbf{C}_m \, \varepsilon(\boldsymbol{u}_m), \qquad v_m = -\mathbf{K}_m (\nabla p_m + \boldsymbol{g}). \tag{3}$$

Here $\boldsymbol{\sigma}_{0m}$ is the initial stress, $\boldsymbol{g}$ is the gravity vector, $\mathbf{C}_m$ and $\mathbf{K}_m$ are the elasticity and hydraulic conductivity tensors, respectively.

2.2 Notes to dimensional reduction on fractures

As was mentioned above, we assume that fractures of the thickness δ are represented by weaker and more permeable materials than the rock mass. To emphasize this fact we use the notation $\mathbf{C}_f$, $\mathbf{K}_f$, α_f, $\boldsymbol{\sigma}_{0f}$, $\boldsymbol{f}_f$, $\boldsymbol{s}_f$ instead of the analogous notation introduced above with the subscript m. The dimensional reduction in the weaker zones is based on the integration of Biot's equations over the cross-section

parameter δ and on integral means of unknown fields denoted as p_f, $\boldsymbol{v}_f$, $\boldsymbol{u}_f$ and $\boldsymbol{\sigma}_f$ and defined in Ω_f. For example, separating the tangential and normal parts of the pressure gradient and integrating per partes, we obtain

$$\int_{-\frac{\delta}{2}}^{\frac{\delta}{2}} \nabla p \, d\boldsymbol{v} = \int_{-\frac{\delta}{2}}^{\frac{\delta}{2}} (\nabla_\tau p + \nabla_v p) d\boldsymbol{v} = \delta\big(\nabla_\tau p_f + [\![p]\!]\boldsymbol{v}\big) =: \delta \overline{\nabla} p,$$

where $[\![p]\!] = p_m^+ - p_m^-$ is the jump between values of p on the fracture sides. Similarly, we introduce differential operators $\overline{\operatorname{div}}\,\boldsymbol{u}$, $\overline{\operatorname{div}}\,\boldsymbol{v}$ and $\bar{\varepsilon}(\boldsymbol{u})$ for displacement and velocity fields, whose normal parts are given approximately by using finite difference schemes depending on $\boldsymbol{u}_f$, $\boldsymbol{u}^+$ and $\boldsymbol{u}^-$. Therefore, these operators are interpreted as *semi-discrete*. The resulting semi-discretized Biot equations defined in $I \times \Omega_f$ read:

$$-\overline{\operatorname{div}}\,\boldsymbol{\sigma} + \alpha_f \varrho g \overline{\nabla} p = \boldsymbol{f}_f,$$

$$\partial_t\big(S_f p_f + \alpha_f \overline{\operatorname{div}}\,\boldsymbol{u}\big) + \overline{\operatorname{div}}\,\boldsymbol{v} = s_f,$$

where the stress tensor and the flux vector are given by Hooke's and Darcy's law:

$$\boldsymbol{\sigma}_f = \boldsymbol{\sigma}_{0f} + \mathbf{C}_f \bar{\varepsilon}(\boldsymbol{u}), \qquad \boldsymbol{v}_f = -\mathbf{K}_f(\overline{\nabla} p + \boldsymbol{g}).$$

We refer to Březina and Stebel (2024) for more details.

2.3 Notes to dimensional reduction on fractures

To complete the DFM model, it is necessary to add suitable initial and boundary conditions, interface conditions guaranteeing the continuity of fluxes and tangential stresses between Ω_m and Ω_f and also assume the continuity of $\boldsymbol{u}_f$ and p_f on fracture intersections, see Březina and Stebel (2024).

In Stebel at al. (2023), the DFM model has been extended by two nonlinear effects on the fracture-matrix interface:

1. *Cubic law relating the permeability tensor to the hydraulic aperture, see Snow (1969):*

$$\mathbf{K}_f = k_f(\boldsymbol{u})\mathbf{I}, \qquad k_f(\boldsymbol{u}) = \frac{\eta \varrho g}{12\mu} \alpha_f(\boldsymbol{u})^2, \qquad \alpha_f = \alpha_f(\boldsymbol{u}) := \delta + (\boldsymbol{u}_m^+ - \boldsymbol{u}_m^-) \cdot \boldsymbol{v}\,;$$

2. *Non-penetration contact condition:*

$$\alpha_f(\boldsymbol{u}) \geq \delta_{min}\,,$$

where η represents the fracture roughness, μ is the fluid viscosity and δ_{min} is a given value defining a minimal fracture opening which must be positive for a well-defined model. This condition is completed by appropriate complementary relations as is usual.

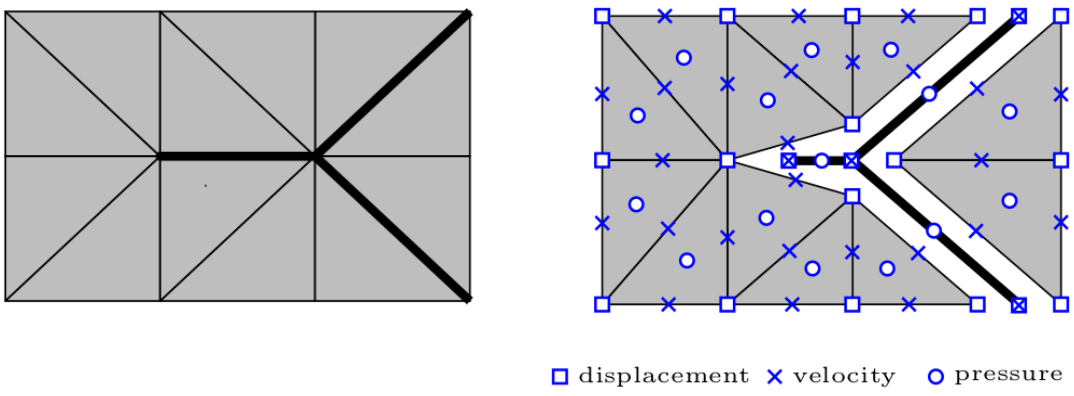

Figure 28 - Scheme of spacial discretization in 2D.

Let us note that the above model does not neglect the stiffness of fractures. In Blaheta et al. (2020), little bit different DFM model was considered where the unknown variables $\boldsymbol{u}_f$ and $\boldsymbol{\sigma}_f$ were not defined.

3. Numerical solution of the DFM model

In this section, we summarize our original solution concept for the DFM model consisting of the problem discretization, iterative methods and implementation details. The concept has been developed in Stebel et al. (2024).

3.1 Discretization

The DFM model described in the previous section is discretized by the implicit Euler timestepping and the finite element method. In particular, we use simplicial meshes for discretizing the rock matrix Ω_m and the fracture network Ω_f. We require compatibility of these meshes, which means that the fracture elements coincide with the faces of adjacent higher-dimensional elements (see Figure 28 on the left). We use piecewise linear elements (P_1) for the displacement, piecewise constant elements (P_0) for the pressure head and the lowest order Raviart-Thomas elements (RT_0) for the velocity. The corresponding distribution of degrees of freedom for these mixed finite elements is depicted in Figure 28 on the right.

Let K, Q and W denote discretized sets of admissible displacement, pressure head and velocity fields, respectively. For any time step $t_n = n\,\Delta t$, we are looking for the solution $(u^n, p^n, v^n) \in K \times Q \times W$ satisfying the following fully coupled system:

$$\begin{aligned} a(\boldsymbol{u}^n, \boldsymbol{z}-\boldsymbol{u}^n) - b(\boldsymbol{z}-\boldsymbol{u}^n, p^n) &\leq f_1(\boldsymbol{z}-\boldsymbol{u}^n), \\ c(p^n, q) + b(\boldsymbol{u}^n, q) + \Delta t d(\boldsymbol{v}^n, q) &= \Delta t f_2(q) + c(p^{n-1}, q) + b(\boldsymbol{u}^{n-1}, q), \\ e(\boldsymbol{u}^n; \boldsymbol{v}^n, \boldsymbol{w}) - d(\boldsymbol{w}, p^n) &= f_3(\boldsymbol{w}), \end{aligned}$$

for all test functions $(\boldsymbol{z}, q, \boldsymbol{w}) \in K \times Q \times W$. For the definitions of the forms $a, b, c, d, e, f_1, f_2, f_3$ we refer to Stebel et al. (2024). The inequality on the first line is a consequence of the non-penetration condition and represents the mechanical part of the model. The equation of the third line is nonlinear due to the dependence of the hydraulic conductivity on displacements. Let us note that the unknown stress field is eliminated from the system using the Hooke law.

3.2 Iterative solution of the coupled system

The solution of the discretized problem is obtained using the fixed-stress splitting method Stebel et al. (2024), which leads to the following iterative process for any time t_n:

$$(p_0, \boldsymbol{v}_0) \mapsto \boldsymbol{u}_0 \mapsto (p_1, \boldsymbol{v}_1) \mapsto \boldsymbol{u}_1 \ldots$$

It means that we alternately solve mechanical and flow subproblems.

The mechanical subproblems can be transformed to a *quadratic programming (QP) problem* having the following scheme:

$$\arg\min_{\boldsymbol{u}} \left\{ \frac{1}{2}\boldsymbol{u}^\top \mathbf{A}\boldsymbol{u} - \boldsymbol{u}^\top \boldsymbol{f}_1(\boldsymbol{p}) \right\} \text{ subject to } \mathbf{B}\boldsymbol{u} \leq \boldsymbol{c}_l; \tag{4}$$

The inequality constraints represent the non-penetration conditions. Enforcing these constraints by Lagrange multipliers $\boldsymbol{\lambda}$ we arrive at the following dual problem:

$$\arg\min_{\boldsymbol{\lambda}} \frac{1}{2}\{\boldsymbol{\lambda}^\top \mathbf{F}\boldsymbol{\lambda} - \boldsymbol{d}^\top \boldsymbol{\lambda}\} \text{ subject to } \boldsymbol{\lambda} \geq \mathbf{0}, \tag{5}$$

where $\mathbf{F} = \mathbf{B}\mathbf{A}^{-1}\mathbf{B}^\top$, $\boldsymbol{d} = \mathbf{B}\mathbf{A}^{-1}\boldsymbol{f}_1(\boldsymbol{p}) - \boldsymbol{c}_l$ and $\boldsymbol{x} = \mathbf{A}^{-1}[\boldsymbol{f}_1(\boldsymbol{p}) - \mathbf{B}^\top\boldsymbol{\lambda}]$. The problem (5) is solved by the MPGP (Modified Proportioning with Gradient Projections) algorithm proposed in Dostál (2009). The

action of the matrix inverse $\mathbf{A}^{-1}$ is realized by the Cholesky factorization of $\mathbf{A}$ and implemented using the SuperLU DIST library, see Li and Demmel (2003).

The flow subproblems lead to a *linear saddle-point system* having the following scheme:

$$\begin{bmatrix} \mathbf{C} & \boldsymbol{D}^{\top} \\ -\mathbf{D} & \mathbf{E}(\boldsymbol{u}) \end{bmatrix} \begin{bmatrix} \boldsymbol{p} \\ \boldsymbol{v} \end{bmatrix} = \begin{bmatrix} \boldsymbol{f}_2 \\ \boldsymbol{f}_3 \end{bmatrix}. \tag{6}$$

It is important to emphasize that the block matrix $\mathbf{C}$ contains a stabilization term ensuring the convergence of the splitting procedure. The system (6) is solved using the hybridization technique which introduces a Lagrange multiplier $\boldsymbol{\mu}$ enforcing the flux continuity on element faces. This leads to a dual problem of the form

$$\mathbf{G}\boldsymbol{\mu} = \boldsymbol{f},$$

where the symmetric positive definite matrix $\mathbf{G}$ is assembled with help of local Schur complements in the primal problem. The dual problem is then solved using the conjugate gradient method with algebraic multigrid preconditioner.

3.3 Implementation details

The coupled hydro-mechanical problem has been implemented in the in-house open-source code Flow123d. The software provides solution of finite element models of processes in porous media built on top of meshes which combine tetrahedral, triangular and line elements to represent the bulk material, fractures and their intersections. The implementation is natively parallel. The computational mesh is created using the tool GMSH, see Geuzaine and Remacle (2009), and partitioned into subdomains using the ParMETIS library, see Karypis and Kumar (1998). A new assembly algorithm with support for vectorization was implemented which also enables efficient evaluation of nonlinear stress/strain-permeability relations. Parallel matrices and vectors are assembled in the PETSc format. We use PETSc solvers to solve linear algebra problems. Specifically, for the hydraulic subproblems, we utilize the parallel version of conjugate gradients combined with the BoomerAMG algebraic multigrid preconditioner, see Henson and Yang (2002).

For the parallel solution of the mechanical subproblems with contacts on fractures, we have used in-house open-source software package PERMON (Parallel, Efficient, Robust, Modular, Object-oriented, Numerical toolbox). PERMON is built on top of PETSc, mainly its linear algebraic part. It extends PETSc by adding specific functionality and algorithms for large-scale sparse QP problems with various types of inequality and equality constraints as well as FETI-type domain decomposition methods. The same coding style is employed, allowing users familiar with PETSc to utilize these features with minimal effort. The parallelization is primarily done through the row-wise distribution of the matrices and vectors with communication realized by an MPI library.

PERMON has been included as an external library into Flow123d, providing the solution of mechanical problems. The primal problem (4) is assembled in Flow123d and passed to PERMON, where the transformation to the dual problem (5), its solution and backward substitution are performed.

4. 3D benchmark inspired by in-situ experiments

The aim of this section is to illustrate that the DFM model and the presented solution concept may be used for a 3D benchmark problem inspired by real in-situ experiments. The computational domain Ω_m has a fixed geometry given by the block $(-10{,}50) \times (-20{,}20) \times (-20{,}20)$ m from which we exclude the tunnel and the 40 m long cylindrical borehole. The dimensions of the domain, the tunnel and the borehole are given in Figure 29. A borehole excavation during 40 days and a consequent relaxation period (next 320 days) are considered. The excavation is simulated by using the fixed geometry and time-dependent boundary conditions prescribed on borehole walls.

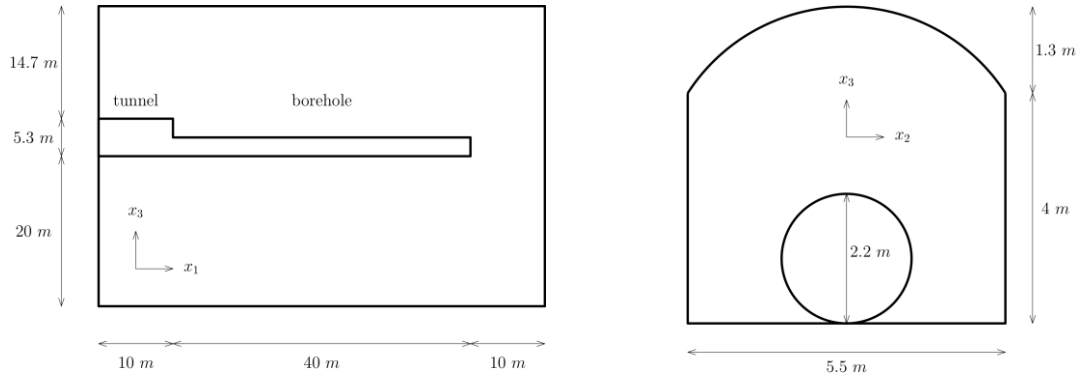

(a) Side view of the computational domain.

(b) Tunnel and borehole profile.

Figure 29 - The geometry of the borehole excavation test problem.

The initial conditions and material parameters for the intact rock matrix are taken from Rutqvist et al. (2009) where a part of the TSX experiment in URL Canada was simulated. In particular, the initial pressure in the domain (before excavation) is given by the steady-state solution with zero pressure on the tunnel surface and with a pressure head of 300 m on the block surface far away from the tunnel. The principal values of the initial stress $\boldsymbol{\sigma}_0$ are 60 MPa in the direction of excavation, 45 MPa in the orthogonal horizontal direction and 11 MPa in the vertical direction. Material parameters are summarized in Stebel et al. (2024). For example, the Young modulus and the hydraulic conductivity are set to $E_m =$ 60 GPa and $k_m = 3 \cdot 10^{-13}$ m/s. To incorporate the influence of EDZ to the model, the hydraulic conductivity is subsequently increased up to $k_m = 10^{-8}$ m/s in vicinity of the borehole with a smooth transition to its intact value.

The stochastic DFN model was taken from Öhman and Follin (2010), data for HDR – repository domain, locality Forsmark, Sweden. Two sets of square-shaped fractures were generated for the target set sizes 200 and 400, see Figure 30. The cross-sections δ vary between 0.1 − 0.6 mm depending on the fracture size. The initial hydraulic conductivity of the fractures is given by the cubic law $k_f = (\eta \varrho g/12\mu)\delta^2$ where η, ϱ and μ denote the roughness parameter, the fluid density and viscosity, respectively. We set $\eta =$ 0.01 to obtain realistic cross-sections for prescribed fracture transmissivities $T_f = k_f \delta$ fitted to the hydraulic tests in Öhman and Follin (2010). The Young modulus on fractures was reduced to $E_f =$ 60 MPa.

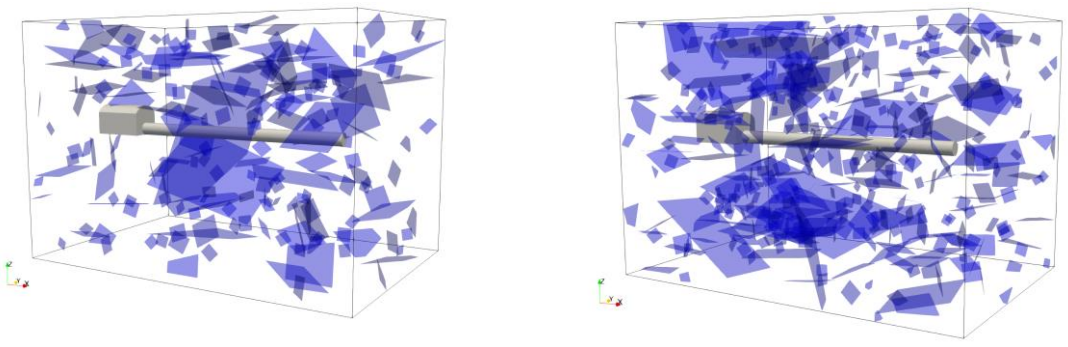

Figure 30 - Two DFN configurations in the borehole excavation test. Left: 200 fractures, right: 400 fractures.

We consider three different computational meshes (with 306, 502 and 1052 thousands elements) for the geometry with 200 fractures and one computational mesh (with 989 thousands elements) for the geometry with 400 fractures. A detail of this mesh is visualized in Figure 31.

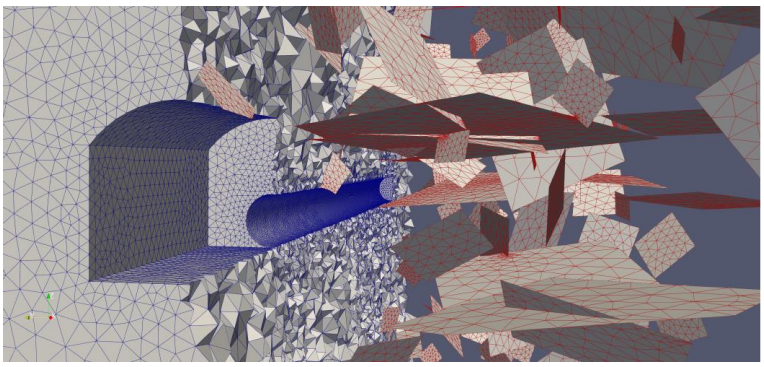

Figure 31 - A detailed view of the computational mesh of the domain with 400 fractures.

For numerical simulations, 1 node of the ARCHER2 supercomputer with 32 cores was used. The first time step needs 4 iterations of the splitting procedure, while the rest of the simulation needs 3 iterations except for the last few time steps going down to 2. Overall, the computations required 201-204 splitting iterations for 71 time steps, ranging from $\Delta t = 1$ on the interval (0, 40) to $\Delta t = 15$ on (120, 360). Total iteration numbers of the mechanical and hydraulic solvers and total computational times for the investigated meshes are compared in *Table 3*.

Problem	Hydr. iter.	Mech. iter.	Time [min]
200_306k	2,077	367	23
200_502k	2,751	587	33
200_1052k	2,053	672	78
400_989k	1,676	605	307

Table 3- Total iteration numbers and computational times for each of investigated meshes.

For illustration, pressure fields in the axial cut of the excavation and at selected time steps are visualized in Figure 32**Erreur ! Source du renvoi introuvable.**. The cases with 200 and 400 fractures are compared. While the overall behaviour of the pressure head is similar for both cases, one can observe differences in several parts of the domain which are due to the high permeability of adjacent fractures. We refer to Stebel et al. (2024) for other graphical outputs related to this benchmark.

5. Concluding remarks to the DFM modelling

In accordance with the project aims of the TUL and IGN teams, we have developed the DFM approach to modelling of coupled HM processes for fractured rocks. We have incorporated to the models non-linear effects like non-penetration conditions on fractures or aperture-dependent hydraulic conductivity. Further, an appropriate solution concept has been proposed and implemented within the in-house open-source libraries Flow123d and PERMON. The libraries support parallel computations. In addition, the ARCHER2 supercomputer has been used for demanding simulations in 3D.

Within our ongoing work, we would like to enrich our solution concept by FETI-type domain decomposition methods which enable parallel implementation of mechanical subproblems. Although the FETI methods have been implemented within the PERMON library, their usage for DFM models is not trivial. Further, we plan to use more advanced contact conditions, prediction of EDZ or multi-scale approaches.

For related uncertainty treatment and transport processes studied by the teams within WP DONUT, we refer to deliverable reports for Tasks 4 and 3, respectively.

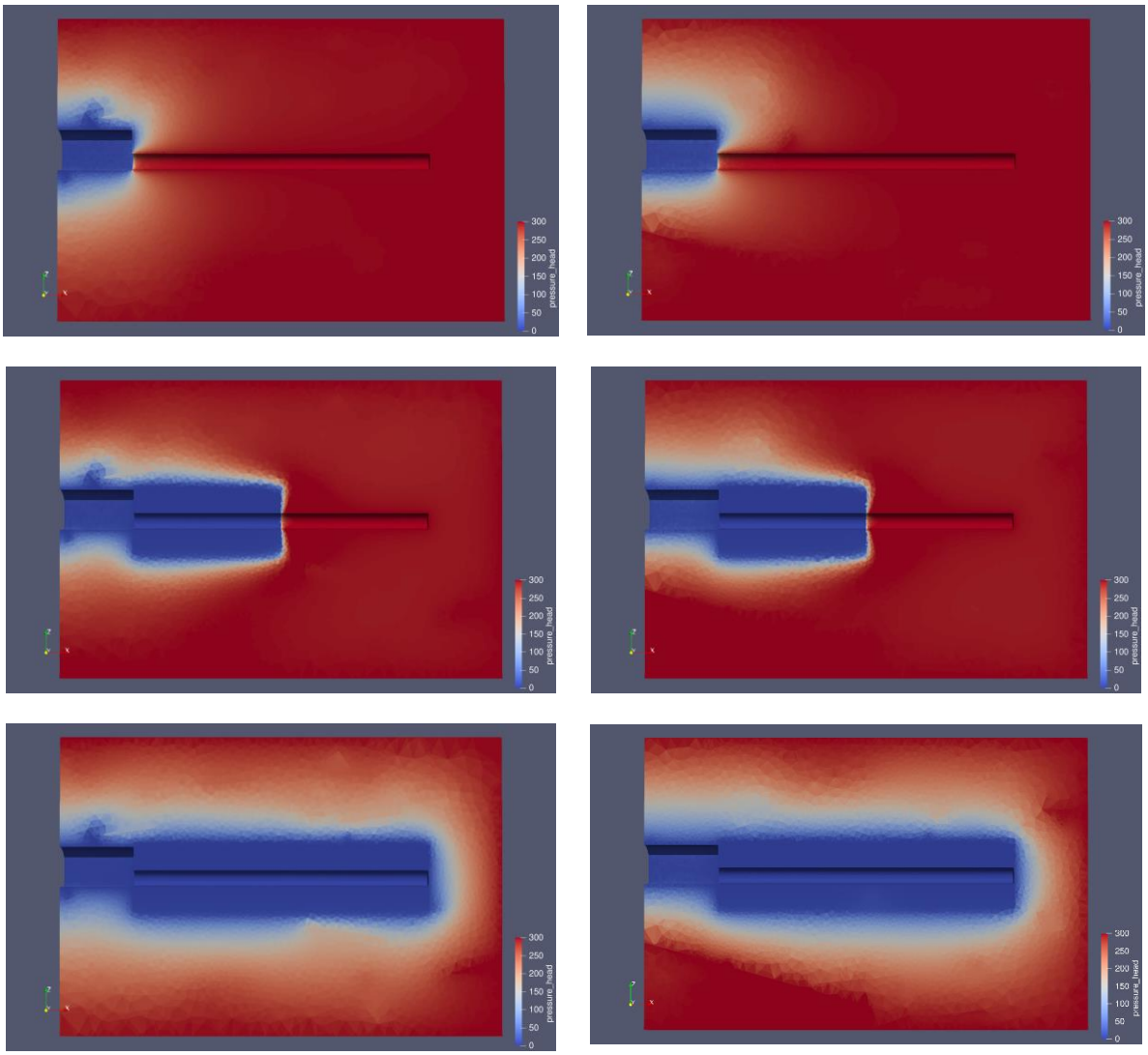

Figure 32 - Comparison of pressure head distribution. From top to bottom: initial time, after 20 days and after 360 days.

6. Other selected results of TUL and IGN teams

In this section, we briefly summarize other results of the TUL and IGN teams achieved in Task 2 of WP DONUT. These results are not directly related to the fractured porous media discussed above.

6.1 Advanced iterative solvers

In Section 3, the stress splitting procedure for solving fully coupled HM systems was presented. Alternative monolithic solvers have been developed in Luber (2022), Luber and Sysala (2024) and tested on a three-field formulation of Biot's poroelastic model. These solvers are based on block diagonal preconditioners and Schur complements. Convergence analysis has been done on a functional level, that is, independently of space discretization. We have shown on several numerical examples from geotechnical practice that these solvers are robust with respect to strong jumps in material parameters, especially in hydraulic conductivity. We have also used the developed monolithic solvers for the Biot-Barenblatt model or for higher-order time discretization, see Luber (2022). On the other hand, their extensions to nonlinear problems is a subject of ongoing work.

Other iterative solvers for HM processes developed by the TUL and IGN teams within Task 2 were published e.g. in Axelsson et al. (2021), Axelsson and Karátson (2021) or Karátson et al. (2024).

6.2 Modelling of THM processes in bentonite barriers

We have presented a coupled thermo-hydro-mechanical (THM) model suitable for bentonite barriers around canisters with spent nuclear fuel in a deep geological repository in Michalec et al. (2021). The model incorporates variably saturated water flow, vapour diffusion, nonlinear elasticity with swelling and heat conduction. A novelty of the model is representation of the water content by the gravimetric content, not by the saturation related to the volumetric content. In particular, the model uses a water retention curve relating the water gravimetric content to the suction, dry density and temperature by fitting measurement data. This allows to capture the oversaturation, that is, the phenomenon when bentonite is capable of storing more water than the amount corresponding to the pore space and the free water density. Implementation of this model with proper discretisation in space and time and solvers for coupled nonlinear systems has been done successfully by using tools provided by the COMSOL Multiphysics software. The model has been validated by simulating THM processes observed in the FEBEX in-situ test. Obtained results have been in a good agreement with experimental data or trends visible from them.

Besides, we have developed a general thermodynamical framework for HM poroelastoplastic models formulated in terms of the net and suction. This framework has been utilised particularly for derivation of a consistent HM coupling for the Barcelona Basic Model, which is used widely for unsaturated soils. The resulting coupling has been analysed thoroughly and it has been shown that it is not fully acceptable from the physical point of view. It has been demonstrated also on a numerical example that the complete HM model can lead to serious difficulties especially when simulating soils close to saturation. We have concluded that poromechanical models using the net stress and suction as stress variables generally (at least what poroelasticity concerns) should be developed and utilised carefully with respect to the thermodynamical consistency, see Ligurský and Michalec (2023).

Acknowledgements. The participation of the TUL and IGN teams within the EURAD project has been cofinanced by The Czech Radioactive Waste Repository Authority (SÚRAO) under grant agreement number SO2020-017.

Code source

https://flow123d.github.io - Homepage of the Flow123d project. The investigated DFM model is a part of Flow123d from version 3.9.0.

permon.vsb.cz - Homepage of PERMON library

https://petsc.org/release/ - Homepage of PETSc library

References

ARCHER2 web page. URL: https://www.archer2.ac.uk/.

Axelsson, O., Béreš, M., Blaheta, R., 2021. Computational methods for boundary optimal control and identification problems. Mathematics and Computers in Simulation,189, 276-290.

Axelsson, O., Karátson, J., 2021. Krylov improvements of the Uzawa method for Stokes type operator matrices. Numerische Mathematik, 148(3), 611-631.

Blaheta, R., Béreš, M., Domesová, S., Horák, D., 2020. Bayesian inversion for steady flow in fractured porous media with contact on fractures and hydromechanical coupling. Computational Geosciences 24, 1911-1932.

Březina, J., Stebel, J., 2024. Mixed-dimensional model of poroelasticity. Z Angew Math Mech. 104, e202200469.

Dostál, Z., 2009. Optimal Quadratic Programming Algorithms, with Applications to Variational Inequalities, Vol. 23, SOIA, Springer, New York, US.

Geuzaine, C., Remacle, J.-F., 2009. Gmsh: A 3-d finite element mesh generator with built-in pre-and post-processing facilities. International journal for numerical methods in engineering 79(11), 1309-1331.

Henson, V.E., Yang, U. M., 2002. BoomerAMG: A parallel algebraic multigrid. Applied Numerical Mathematics 41(1), 155-177.

Karátson, J., Sysala, S., Béreš, M., 2024. Quasi-Newton variable preconditioning for nonlinear elasticity systems in 3D. Numerical Linear Algebra with Applications 31, e2537.

Karypis, G., Kumar, V., 1998. A parallel algorithm for multilevel graph partitioning and sparse matrix ordering. Journal of Parallel and Distributed Computing 48(1), 71-95.

Li, X.S., Demmel, J.W., 2003. SuperLU_DIST: A scalable distributed-memory sparse direct solver for unsymmetric linear systems. ACM Transactions on Mathematical Software, 29(2), 110-140.

Ligurský, T., Michalec, Z., 2023. On thermodynamically consistent coupling of the Barcelona Basic Model with a hydraulic model for unsaturated soils. Computers and Structures, 285, 107082.

Luber, T., 2022. Efficient iterative methods and solvers for FEM analysis - Algebraic block preconditioners for poroelasticity. Ph.D. dissertation, VSB - Technical University of Ostrava, Ostrava, 2022.

Luber, T., Sysala, S., 2024. Robust block diagonal preconditioners for poroelastic problems with strongly heterogeneous material. Numerical Linear Algebra with Applications, 31, e2546.

Michalec, Z., Blaheta, R., Hasal, M., Ligurský, T., 2021. Fully coupled thermo-hydro-mechanical model with oversaturation and its validation to experimental data from FEBEX experiment. International Journal of Rock Mechanics and Mining Sciences 139, 104567.

Öhman, J., Follin, S., 2010. Site investigation SFR – Hydrogeological modelling of SFR – Model version 0.2. Technical Report R-10-03, Svensk Kärnbränslehantering AB.

Rutqvist, J., Börgesson, L., Chijimatsu, M., Hernelind, J., Jing, L., Kobayashi, A., Nguyen, S., 2009. Modeling of damage, permeability changes and pressure responses during excavation of the TSX tunnel in granitic rock at URL, Canada. Environmental Geology 57, 1263–1274.

Snow, D.T., 1969. Anisotropic permeability of fractured media. Water Resour Res. 5(6):1273–1289.

Stebel, J., Kružík, J., Horák, D., Březina, J., Béreš, M., 2024. On the parallel solution of hydro-mechanical problems with fracture networks and contact conditions. Computers and Structures 298, 107339.

Error control close to the boundary

[1]Kazymyrenko, C., [1,2]Fontana, I., [1]Escoffier, F., [3]Di Pietro, D.

[1] EDF R&D, 91120 Palaiseau, France

[2] ESAM, Northwestern University, USA

[3]IMAG, CNRS, Univ. Montpellier, France

The project leading to this application has received funding from the European Union's Horizon 2020 research and innovation programme under grant agreement No 847593.

Abstract

Nonlinear numerical simulations on large scale structures are highly challenging. In many cases, ensuring the convergence of studies is not a trivial task. In finite element codes, errors from spatial or temporal refinement are combined into a single stopping criterion, which can be inefficient or unsuitable, especially in complex applications like tunnel excavation. A posteriori error control aims to separate these errors for a more refined analysis. Without error estimators, we resort to analysis of variables of interest on more refined meshes.

During a tunnel excavation process, multiple contact interfaces can emerge, either due to construction geometry or through time evolution caused by crack propagation, progressive material softening, and plastification. It is essential to consider contact and potentially friction between two bodies to provide a more realistic description of the interface zones in civil engineering construction.

In this report, we concentrate on recent results obtained in our unit through the extension of a posteriori error estimation techniques to account for contact non-linearity. We focus on the fundamental concepts of a posteriori error estimation, its preliminary validation using three test cases, and discuss our additional discovery of spurious oscillations in the discretized solution within the cohesive zone region in the presence of stress singularity.

Significance Statement

The intricate geometry of nuclear waste disposal, specifically the intersections within the galleries, combined with the significant differences in length scales (such as the gallery longitudinal extension versus the thickness of concrete encasement), pose substantial challenges in numerical simulations. These simulations are imperative to ensure the safety of future installations. Furthermore, the highly non-linear nature of the coupled thermo-hydro-mechanical physics governs the evolution of underground structures and consequently adds to its complexity. Finite elements, which form the basis of these simulations, exhibit sometimes insufficient robustness with limited numerical efficiency.

In this work, our primary focus was on developing criteria to assess the accuracy of numerical simulations while simultaneously reducing their computational cost. Building upon our previous research in a posteriori error control estimation, we extended this technique to address the specific non-linearities introduced by contact interfaces. These interfaces can originate from construction geometries or emerge later with material degradation and crack formation.

Starting with initial finite elements simulation, we can generate an error map that highlights regions of concentrated errors, indicating where mesh refinement is needed to achieve rapid convergence toward continuous limit results. This error map also serves as a stopping criterion, optimizing computation time for desired result precision. The validity of our proposed technique was confirmed through testing on two challenging cases.

Moreover, in a third example, which closely resembles to industrially relevant tunnel excavation simulations, we identified and thoroughly examined spurious oscillations in the numerical solution. In the case of surface breaking cracks, the geometric singularity on its extremity reduces the regularity of the continuous solution, thereby affecting the quality of the discretized model. Although these results require further validation for more complex geometries, the oscillations likely contribute to the observed issues with the robustness of highly non-linear interface modelling under mixed compressive loading conditions.

In conclusion, our work within the EURAD project represents not only a significant enhancement of error estimation techniques but also a valuable contribution to addressing challenges in non-linear simulations. By doing so, we actively contribute to the advancement of numerical methods for large-scale structural simulations. Our research has been published and shared with the community, and all developments have been made within open-source software frameworks.

Table of content

List of figures

1. Introduction

Poor robustness and numerical efficiency make part of the cornerstones in nonlinear finite element simulation. Ensuring the convergence in presence of non-linearity for large scale structures are usually rather complex task. In practice in the case of difficulties one could opt for relaxing convergence criterion together with refinement of the loading steps or meshes. This basic engineering craftiness, acquired through their proper working experience, become trickier once it comes to coupled phenomena simulations (HM or THM). In the latter case the evolution is described by multi-origin variable and the relaxation in convergence criterion necessarily leads to physical results alteration. Moreover, in the standard finite element code the convergence errors sources, i.e., spatial, linearization or temporal refinement, are all agglomerated together to produce a single scalar stopping criterion. The idea is then to separate all this errors to be able to perform a more subtle convergence analysis depending on the physics. More than that, we could aim to provide the finite element code user with a heuristic algorithm which would automatically stop the code execution once the best possible convergence for the given mesh is attained.

There exist two main approaches that address the error estimation problem. The classical – “a priori” error approach - has a disadvantage of relying on the problem regularity, which is not known a priori for most of the industrial applications. On a contrary ”a posteriori” error analysis (see for example [Ainsworth2000]) seems to be more relevant as the solution regularity is “reconstructed” based on the current finite element solution. In most recent developments additional quantities of the associated fluxes (stress for displacement, hydraulic flux for pressure) are reconstructed from finite element solution, the latter dispose some important mathematical properties (smooth elements transition, symmetry) [RieDPiErn17]. The principal advantage of the following technique is that it simplifies comparison of all error’s sources and its classification. The last property leading to the possibility of implementation of different stopping algorithms.

A posteriori error estimation based of flux reconstruction on patches for mechanical and hydro-mechanical problems have been extensively studied during PhD of R. Riedlbeck [Riedlbeck2017], in particular with the aim to evaluate efficiency of current technic for industrial cases. The result obtained for the tunnel excavation-like test-case are encouraging as close to perfect efficiency is attained for error estimation compared to reference study on highly refined mesh [RieDPiErn17,Botti20].

In this report we extend error estimation technique to take into account boundary terms due to the presence of contact non-linearity. The approach developed hereafter paves the way for its future generalization to any cohesive interfaces, that are highly important for accurate tunnel excavation simulations.

2. Error control for contact problem

In this report we are principally interested in one of non-linearity generated by the presence of contact interface, no matter whether it takes its origin from construction geometries or appear later in the system’s temporal evolution through progressive material degradation and crack opening (see for ex. *Figure 33*).

Contact can be mathematically represented via a set of inequalities and nonlinear equations on the involved boundary part (Γ_C in *Figure 2*). While the inequality represents the non-penetration condition between two contact surfaces and seems to be compulsory, but at the same time it creates an important difficulty for discretized solution. In what follows, we briefly discuss a Nitsche trick [Nitsche1971] who was able back in 1971, to transform an inequality condition into implicit equality equation.

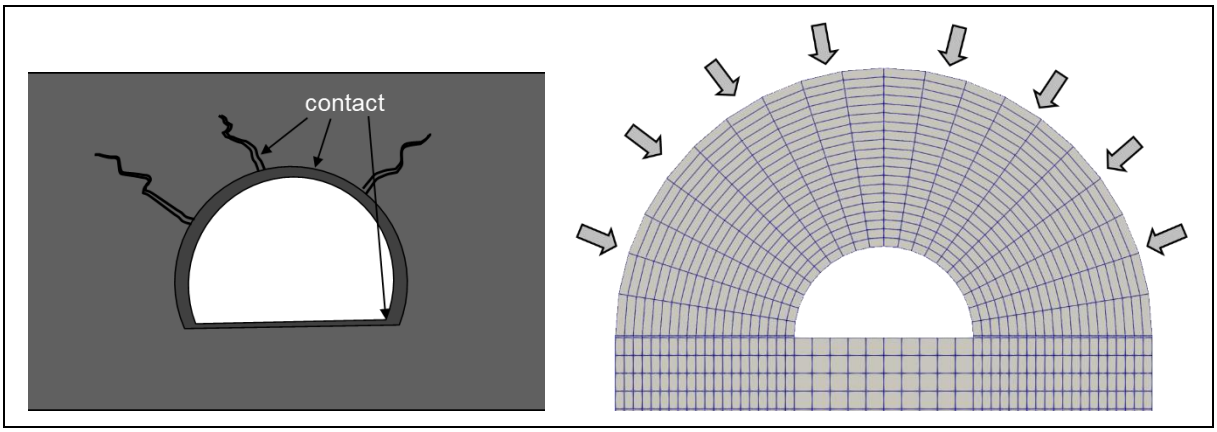

Figure 33 – One of the possible applications: contact interfaces in underground tunnel (on the left) and corresponding finite element mesh (on the right).

2.1 Nitsche-based contact description

In order to deal with contact and friction boundary conditions, many different numerical methods are proposed in literature, notably penalty methods, mixed methods and Nitsche-based methods. In this work we rely on the Nitsche method since it allows to treat contact boundary conditions in a weak sense with a consistent formulation and without the introduction of additional unknowns such as Lagrange multipliers. Moreover Nitsche-based contact description has an advantage of possible extension to regularized cohesive zone model.

We summarize here the most important equations describing mechanical contact in simplified case of single flat interface Γ_C without friction, as on schematic representation of contact problem figure. For further details on this and the other methods we refer to [Chouly-Mlika2017] and the references therein.

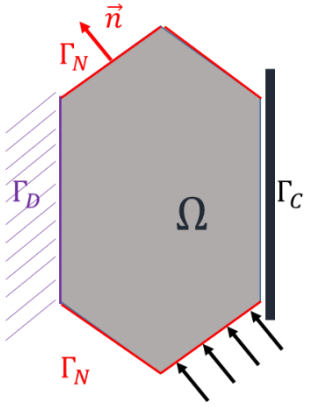

Figure 34 – schematic representation of contact.

First, a strong formulation of contact problem could be presented as a set of classic mechanical equilibrium equations together with two mutually exclusive inequalities (one for contact displacements and the other for stresses). Here we use standard notations of Dirichlet (Γ_D), Neumann (Γ_N) and contact boundary (Γ_C) (*Figure 2*), u, ε *and* σ being respectively displacement, strain, and stress fields. The

$$div\,\sigma(u) + f = 0 \quad \text{in } \Omega$$
$$\sigma(u) = A{:}\,\varepsilon(u) \quad \text{in } \Omega$$
$$u = 0 \quad \text{on } \Gamma_D$$
$$\sigma(u)n = g_N \quad \text{on } \Gamma_N$$
$$u^n \leq 0,\ \sigma^n(u) \leq 0,\ \sigma^n(u)u^n = 0 \quad \text{on } \Gamma_C$$
$$\sigma^t(u) = 0 \quad \text{on } \Gamma_C$$

elasticity tensor is noted by *A*, the pressure on Neumann boundary as g_N, and *f* represents the volumetric density force (e.g. weight).

As most system of partial differential equations, this set has its weak form, which is formulated once again as an inequality of the following form:

$$\int_\Omega \sigma(u){:}\,\varepsilon(v-u)\,d\Omega \geq \int_\Omega f(v-u)d\Omega + \int_\Omega g_N(v-u)d\Gamma\,; \qquad for\ \forall v \qquad \text{(Eq. 1)}$$

Where u and v must lay in the admissible displacement space. The weak or variational formulation are of great practical use in approximate solution estimation. For instance, restriction of variational testing field v on discretized space together with Galerkine inner approximation on solution u results in finite element method. In its current form the presence of inequality sign brings some supplementary complexity and is treated either with penalty or Lagrange multiplier methods. On the other hand, Nitsche's method which was originally introduced in [Nitsche1971] to handle weakly Dirichlet boundary conditions, transforms this inequality into implicit equality. Its application on problems involving linear conditions on the boundary or on the interface between different parts of the domain are cited for example in [Chouly-Mlika2017]. The Nitsche-based method for the unilateral contact problem in linear elasticity (with nonlinear conditions on the contact boundary) which we are considering in this work is presented in [Chouly2013]. One introduces first negative real axis $\mathbb{R}_-$ projection operator: $\forall x \in \mathbb{R}$; $[x]_{\mathbb{R}_-} := (x - |x|)/2$. Previous inequality condition is then equivalent to the equality:

$$u^n \leq 0, \sigma^n(u) \leq 0, \sigma^n(u) u^n = 0 \quad \Leftrightarrow \quad \sigma^n = [\sigma^n - \gamma u^n]_{\mathbb{R}_-}, \text{ where } \gamma \text{ is any positive constant} \quad \text{(Eq. 2)}$$

Finally, once regularized (*Figure 35*), obtained equality could be considered as implicit behavior law.

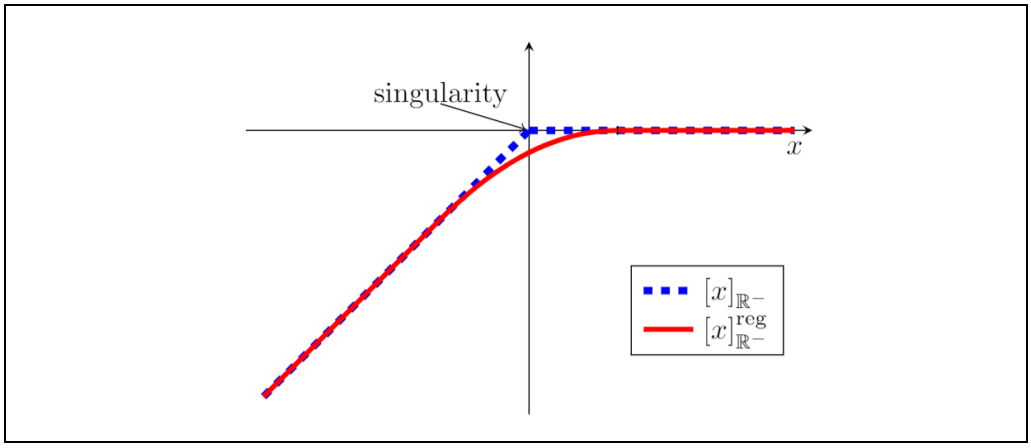

Figure 35 – Negative axes projection operator (blue) and its regularized form (red).

In its general form Nitsche-based variational formulation of unilateral contact problem reads [Chouly2013]:

$$\int_\Omega \sigma(u_h) : \varepsilon(v_h)\, d\Omega - \int_{\Gamma_C} \frac{\theta}{\gamma} \sigma^n(u_h)\sigma^n(v_h) d\Gamma + \int_{\Gamma_C} \frac{1}{\gamma} [P^n_{1,\gamma}(u_h)]_{\mathbb{R}^-} \cdot P^n_{\theta,\gamma}(v_h) d\Gamma = \int_\Omega f v_h d\Omega + \int_{\Gamma_N} g_N v_h d\Gamma$$
$$\forall v_h \in V_h \quad \text{(Eq. 3)}$$

We used standard notation of discretized fields and corresponding spaces with subscript $\{\ \}_h$. Moreover, a non-symmetric discrete linear projector on contact boundary is introduced: $P^n_{\theta,\gamma}(u^n) := \theta\sigma^n - \gamma u^n$. The choice of constant $\theta \geq 0$ creates a whole class of Nitsche-based formulations, where the underlying convergence properties may vary. Thanks to this new form, we can establish more easily the link between contact problem and eventual normal cohesive behavior law: the integral over contact boundary Γ_C would be transformed in the integral over flattened cohesive finite elements [R3.06.09] and cohesive behavior law could be obtained through the analysis of the regularization of negative axes projector. For instance, for $\theta = 0, \gamma = 1$, we have:

$$\int_{\Gamma_C} \frac{\theta}{\gamma} \sigma^n(u_h)\sigma^n(v_h) d\Gamma + \int_{\Gamma_C} \frac{1}{\gamma} [P^n_{1,\gamma}(u_h)]_{\mathbb{R}^-} \cdot P^n_{\theta,\gamma}(v_h) d\Gamma \Longrightarrow \int_{\Gamma_C} [P^n_{1,\gamma}(u_h)]_{\mathbb{R}^-} \cdot v_h d\Gamma \quad \text{(Eq. 4)}$$

Where the last expression is easily identified as standard cohesive zone variational term.

2.2 A posteriori error

In this report we focus on the results recently obtained by the extension of a posteriori error estimation technique to the contact non-linearity, its validation and the first case close to industrial case simulation. All the theoretical findings may be found in [DFK2022], while the study of possible industrial application

is available in internal report [Escoffier2023]. Here we restrict ourselves on the basic ideas of a posteriori error, with additional discovery of spurious oscillations in discretized solution. We believe the usage of such technique could be a game changer for many industrial applications.

Currently, most linear, and non-linear solvers in industrial finite element simulators rely on classical convergence criteria based, for example, on the reduction below a fixed threshold of the L^p norm of the nodal residuals. In complex applications, such those we are addressing in this report, these stopping criteria can lead to a significant additional cost in terms of computation time, or even be simply unsuitable for ensuring the convergence of computations.

An example comes from the behavioral analyzes of large structures, especially when it comes to materials exhibiting structuring non-linearities and/or a coupling of different physical phenomena. Indeed, the variation in time of the zones presenting the strongest non-linearities, as well as the various origins of the source of error, often do not allow in practice to continue the computations by finite element method until convergence in a sense defined just above. Even for converged studies, one does not have access to the indicators allowing to easily identify the error source, for instance those introduced by the spatial discretization of the problem. In the absence of a posteriori error estimators, the only valid strategy is the deeper study of the variables of interest on refined meshes. No need to point out the cumbersome nature of implementing such a strategy for large industrial calculations.

The mathematical background of the proposed technique relies on a posteriori error estimation. First, based on given finite element solution, one reconstructs the associated fluxes (stress for displacement, hydraulic flux for pressure, $u_h \Rightarrow \sigma_h$) which must dispose some important mathematical properties (smooth elements transition, symmetry). Then, the error estimation is decomposed element by element into two major contributions: the first one providing the shift between initial $\sigma(u_h)$ and reconstructed flux σ_h and the second one representing the ability of flux reconstruction to cancel external forces on the elementary level. The illustration of this technique is based on the analysis of a single triangle like inequality:

$$\left\|(u-u_h)\right\|^2 \leq \sum_{K\in T_h}\left(\left\|\sigma(u_h)-\sigma_h\right\|_{L^2(K)} + \frac{h_K}{\pi}\left\|f-\nabla\cdot\sigma_h\right\|_{L^2(K)}\right)^2$$

Where u is continuous solution of the problem; u_h its discretized finite element approximation and σ_h stress (called usually flux) reconstructed from discretized solution couple $(u_h;\sigma(u_h))$.

The principal advantage of the following technique is possible extraction and comparison of all error sources, like space discretization, linearization, regularization of the contact etc. The decomposition may be written schematically as (see [DFK2022] for more details):

$$||\,u-u_h)||^2 \quad \leq \sum_{K\in T_h}\left[\eta_{space}+\eta_{lin}+\eta_{contact}\right]^2 \text{ (Eq. 5)}$$

The last property opens the way to the development of different stopping algorithms like for example:

IF $\eta_{lin} < 0.1\eta_{space} \cup \eta_{contact} < 0.1\eta_{space}$ THEN STOP

In this work a priori error estimation adaptive algorithm was tested on the problem of elastic material (internal bulk) with flat normal contact without friction non-linearity (consult [DFK2022] for more details).

2.3 Flux reconstruction

As stated above, the efficiency of a posteriori error estimation is straightly related to the “quality” of flux reconstruction. Additionally, numerical issue arises while the reconstruction itself could be rather costly in CPU time. Prior to this work, the method of flux reconstruction on patches (see *Figure 36*) was tested in development version of finite element Code_Aster software (not available to end users up to now). The results obtained for the tunnel excavation-like test-case were encouraging as close to perfect efficiency is attained for error estimation compared to the reference study on highly refined mesh [RieDPiErn17,Botti20]. Nevertheless, error estimation on boundary/contact elements were not

performed. Moreover, it was pointed out the whole high computational cost of error estimation. These two constrains were blocking the extension of tested error estimation strategy to the large-scale industrial calculations. We have focused in this short report on the results of extension of flux reconstruction to the boundary elements that is a necessary step before its application to close to industrial applications.

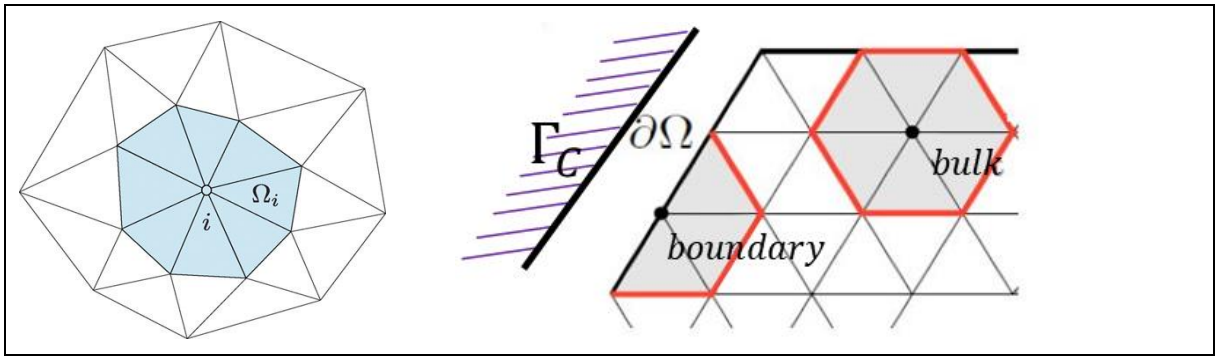

Figure 36 – Patch, as set of adjacent to node elements (on the left); distinction of internal (bulk) and external (boundary) patches (on the right).

3. Results

3.1 Academic test-case of contact cube

The first validation of our approach is made on the simple academic 2D-numerical test-case of cube with flat contact surface. The simulations are performed with the open source finite element software FreeFem++ (https://freefem.org/) [FreeFEM]. We consider the rectangular domain $\Omega = (0,1) \times (0,1)$ with mechanical parameters $E = 1$ and $\nu = 0.3$, corresponding to the Lamé coefficients $\mu \approx 0.385$ and $\lambda \approx 0.577$. Furthermore, the body is subjected to a weight force $f = (0, -0.01)$. Homogeneous Dirichlet boundary conditions are imposed on $\Gamma_D = \{0\} \times (0,1)$ and the the body is initially in contact with a rigid vertical interface on $\Gamma_C = \{1\} \times (0,1)$. The Nitsche parameter introduced previously is $\gamma = 100 \cdot E$. A pressure g_N acts on top of the body $\Gamma_N = (0,1) \times \{1\}$, and the rest of the boundary is free.

Since there is not a closed-form solution for this model, we take as reference solution u, as a function computed on very refined mesh. After deformation, the body will be in contact with the rigid foundation in a non-empty interval subset of Γ_C (see *Figure 37*).

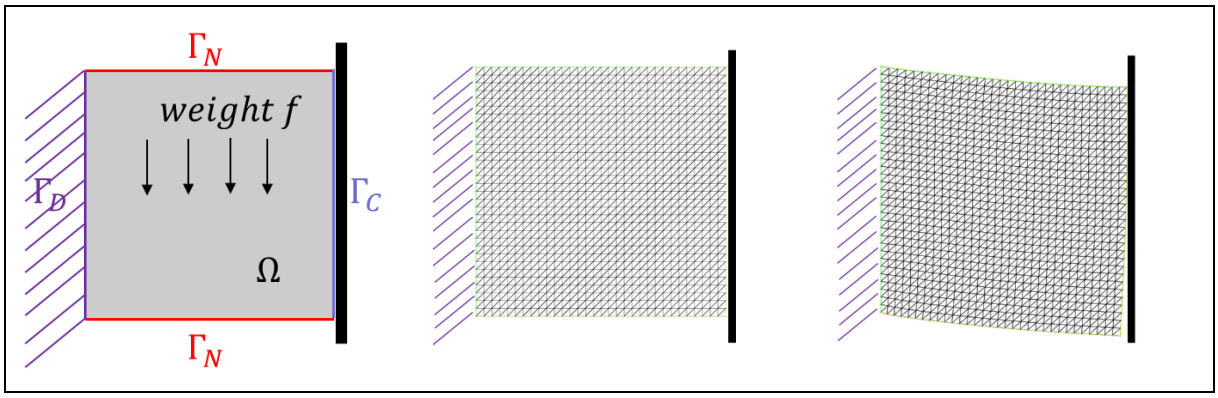

Figure 37 – Test case scheme (on the left); the corresponding refined mesh (in the center) and its deformed shape (on the right).

We refine adaptively the initial mesh following the distribution of the local total estimator, refining only the elements in which the value of this estimator is beyond the threshold. At each step at least 15 % of

elements are refined, i.e., are subdivided into 4 triangles dividing each edge by 2. The exact number of refined triangles is due also to the conformity and regularity conditions of the mesh.

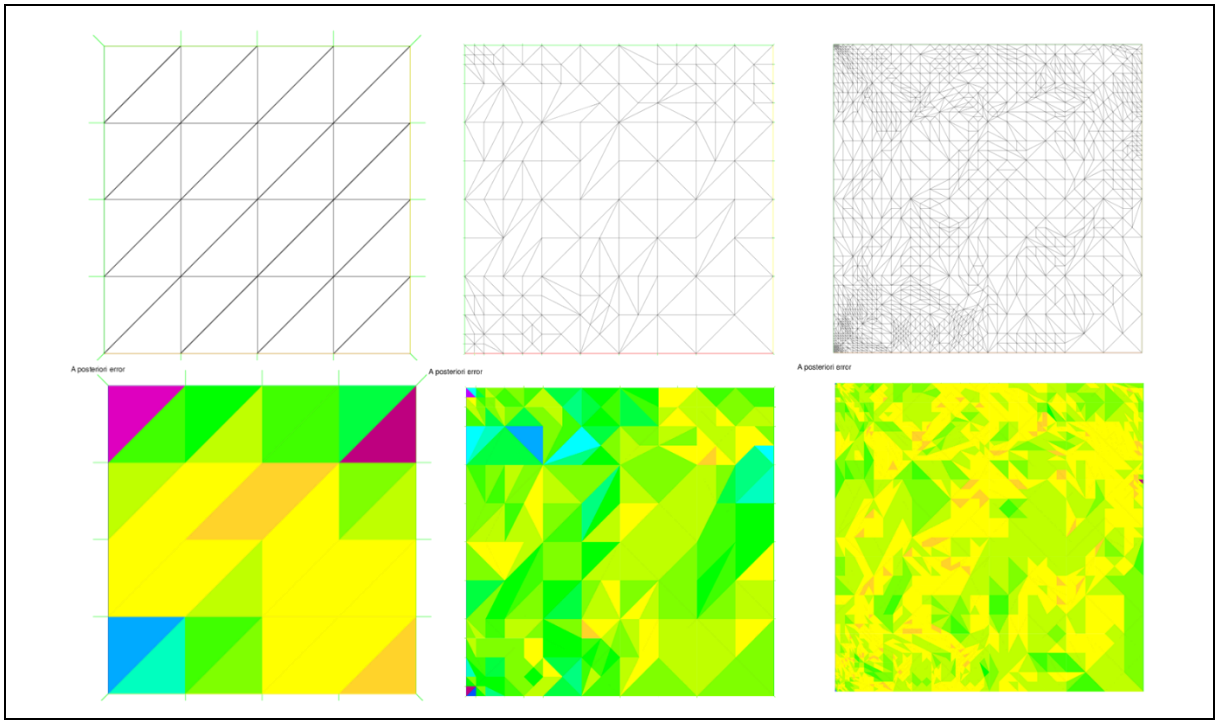

Figure 38 – Three intermediate steps of adaptive refinement, based on a posteriori error (on top) and corresponding colour map error distribution (on bottom).

Figure 38 shows the initial mesh and the result of adaptively refinement after 3 and 6 steps, respectively. We note that the refinement is concentrated on the two extrema of Γ_D (singularities due to the homogeneous Dirichlet conditions) and near the contact interval in Γ_C . It means that while the whole structure is linear elastic, the contact non-linearity influence error distribution into the bulk and not only to its boundaries.

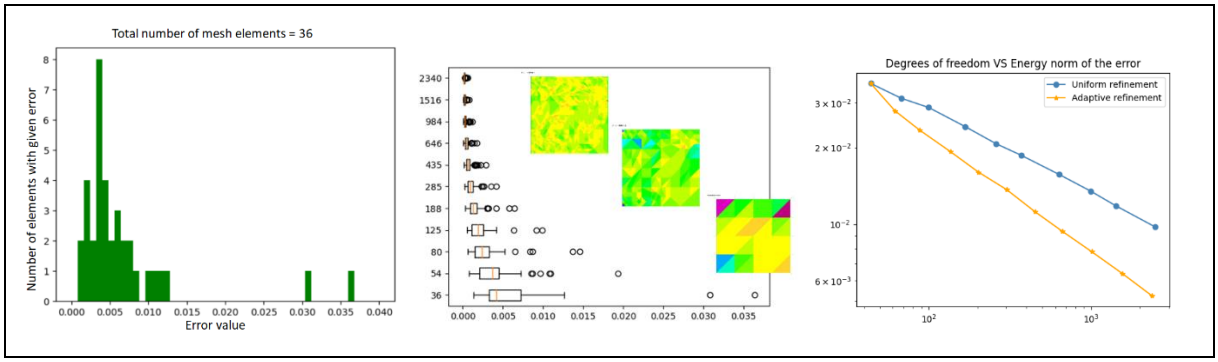

Figure 39 – Initial error distribution (left); its evolution in time (middle) and convergence rate (right).

Figure 39 emphasizes error homogenization acceleration within adaptive refinement scheme through its statistical distribution analysis. Moreover, we compare the convergence with uniform and adaptive refinement, plotting the corresponding curves as functions of the number of degrees of freedom. Note that the adaptive approach provides better convergence rates, i.e., adopting it, we achieve a fixed level of precision with a lower number of degrees of freedom. The convergence rate drops approximately by a factor of ≈ 2 in adaptive case compared in the uniform one.

These results validate our procedure and open the way to its usage for other more complex situation, that we developpe in what follows.

3.2 Contact with singularity test

We notice that in the first test-case the refinement domain is concentrated not only in the contact surface, but also on the clamped cube's edges where the stress field became singular within the elastic solution. Our scheme is then less relevant as the solution for both optimized and unoptimized methodologies are quite close, for example human guided optimization would result in the same choice of refinement domain. As it was stated before we gain only in numerical performance. The discriminate contact test that we have specially developed in this work gives not only numerical improvement, but also shows its sensitivity to the refinement domain choice that is impossible to guess a priori without initial simulation.

The proposed test has two regions that need to be refined: stress singularity region and contact region. Its particularity is that it is constructed in the way that refinement of the singularity region impacts contact region position. At each refinement iteration not only the mesh become finer, but also the contact domain is updated.

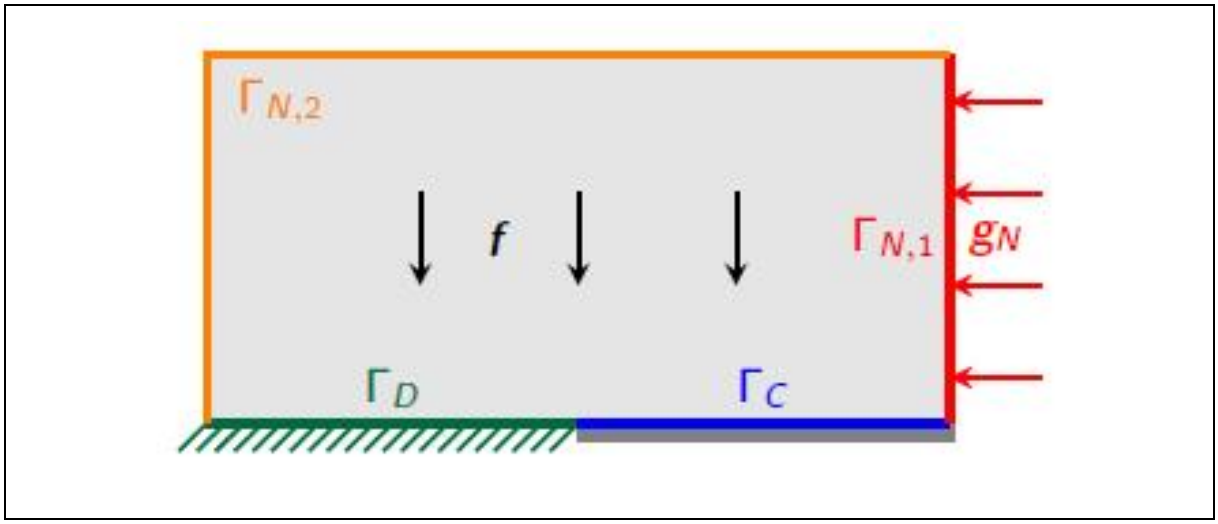

Figure 40 – Discriminate contact with singularity test.

The rectangular domain is clumped on the left half side of its support, then a combination of gravitation loadings and lateral pressure is applied. In the final solution the activated contact region is situated somewhere in the middle of the contact surface Γ_C (*Figure 40*). Its precise position is dependent on the ratio of external forces $g_N \; and \; f$.

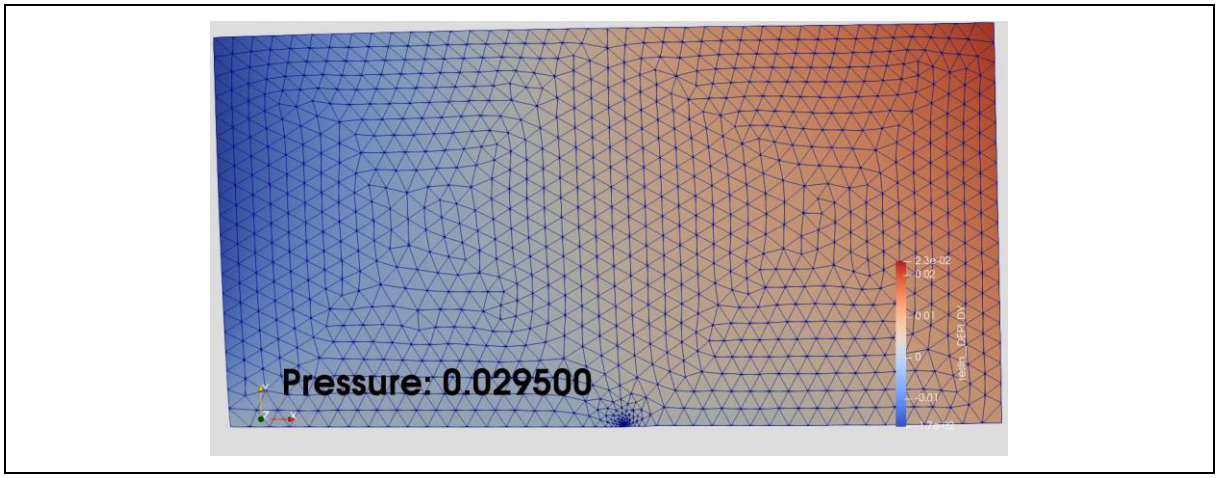

Figure 41 – The deformed shape on the sample (Fig. 8) reveals the result of the combination of shear and weight loading.

For the finite element solution, the quality of refinement at the stress singularity has significant impact on the calculated actual contact position. For some very coarse mesh, there is no contact points at all (see illustration on *Figure 42* with vertical displacement along Γ_c).

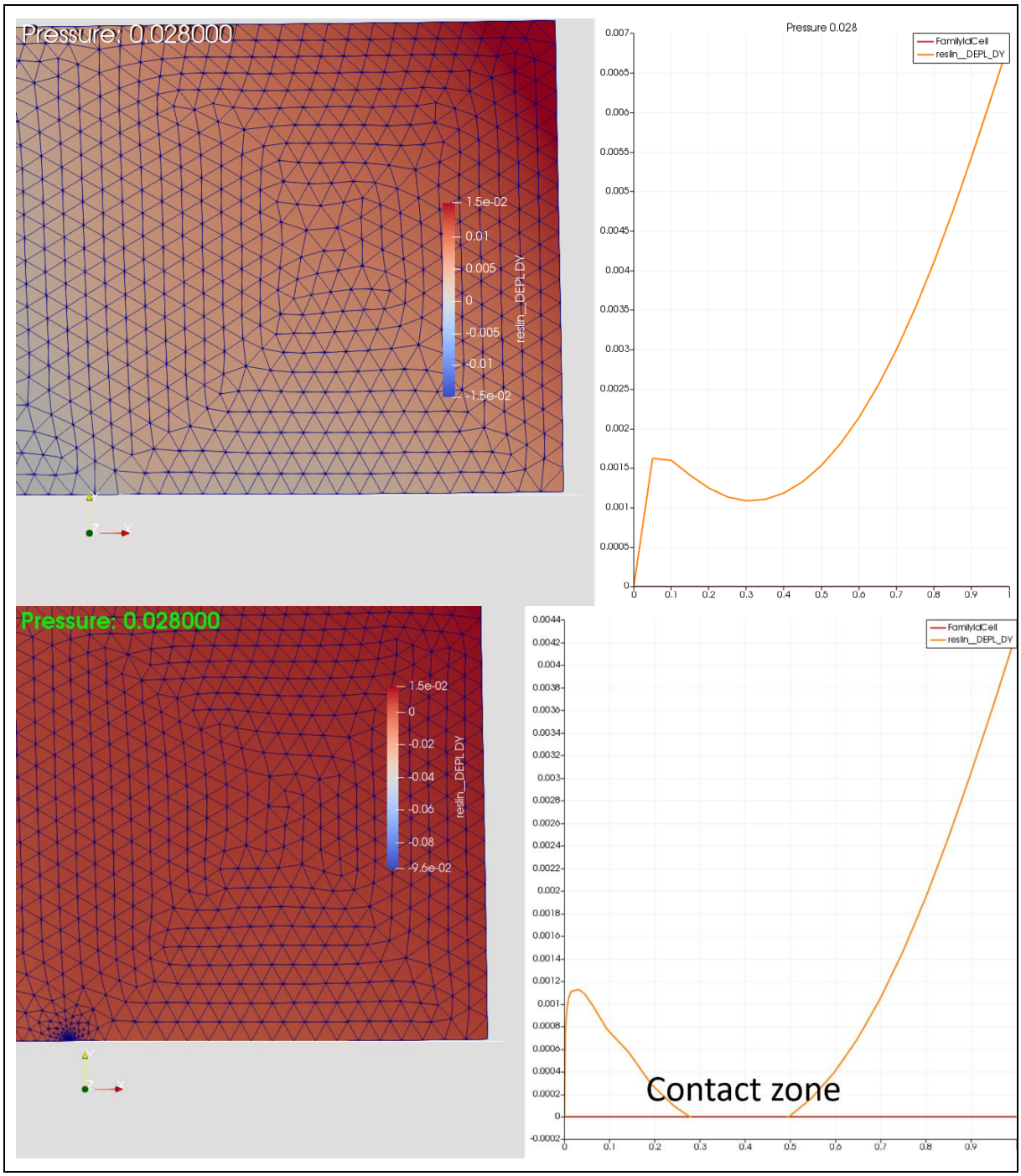

Figure 42 – Illustration of the contact zone dependance on refinement quality close to the stress singularity region: for the homogeneously refined mesh (top) there is no contact, while it is present for the mesh with refined stress singularity region (bottom).

The first simulations of this test were performed with the open-source finite element software FreeFem++ (see [Fontana2022]). Starting with very coarse mesh of 68 elements, 11 refinement steps were done with nearly 30% increase in elements number at each step.

If we analyse the *Figure 43* in details, while contact is not realised, we observe first the refinement in the singularity region, then the contact is realized at step 7 and finally the refinement is initiated in the contact region.

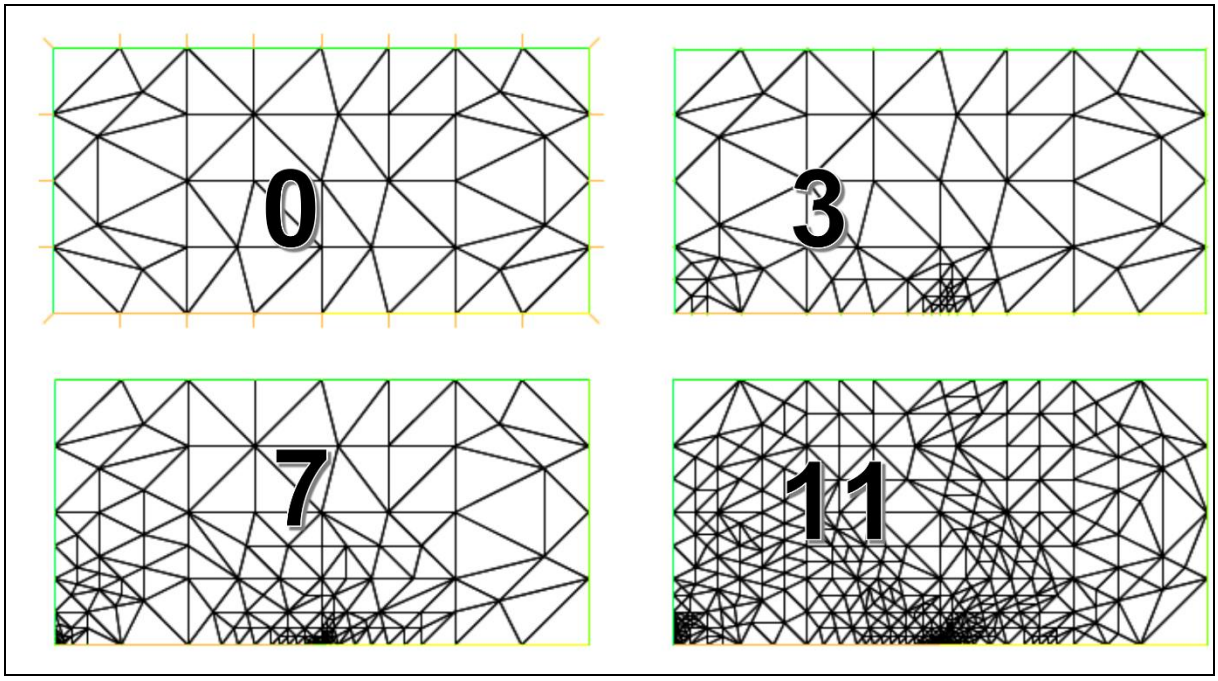

Figure 43 – Initial mesh (0) and adaptively refined mesh after 3, 7 and 11 steps.

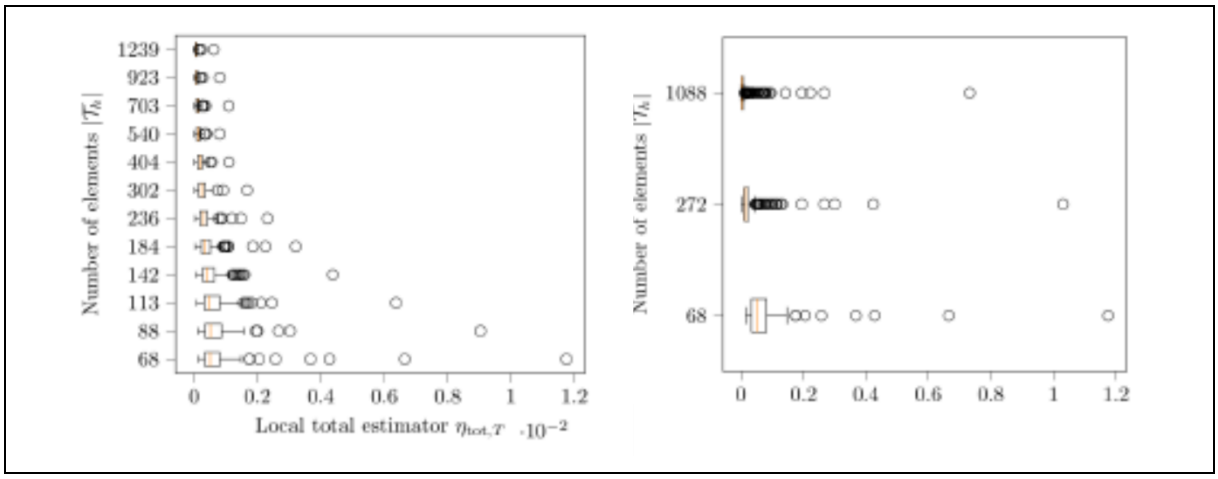

Figure 44 – Statistical error distribution for each refinement step for adaptive (left) and homogeneous (right) meshes.

As in previous test-case the *Figure 44* illustrates the error homogenization acceleration within adaptive refinement scheme through its statistical distribution analysis by comparison of the uniform and adaptive refinement.

3.3 Tunnel under compression test

In the final part of our work we realized more complex case close to industrial test. The schematized underground tunnel is studied under homogeneous hydrostatic loading (*Figure 33*), which simulates with given surrounding geometry real boundary conditions. On the tunnel edges horizontal cohesive zone is inserted with the aim to simulate possible fracture path and corresponding sliding zone. In order to

eliminate possible rigid body motion, the bottom of the mesh is clamped in vertical movement and the central part - in the horizontal movement.

Unfortunately, during numerical simulations of the current test with the presence of cohesive contact non-linearity we encountered convergence problem which did not allow us to investigate the efficiency of developed error control scheme. However, the issue of convergence problem was studied in detail (see [Escoffier2023]), we summarize here some of the most relevant characteristics.

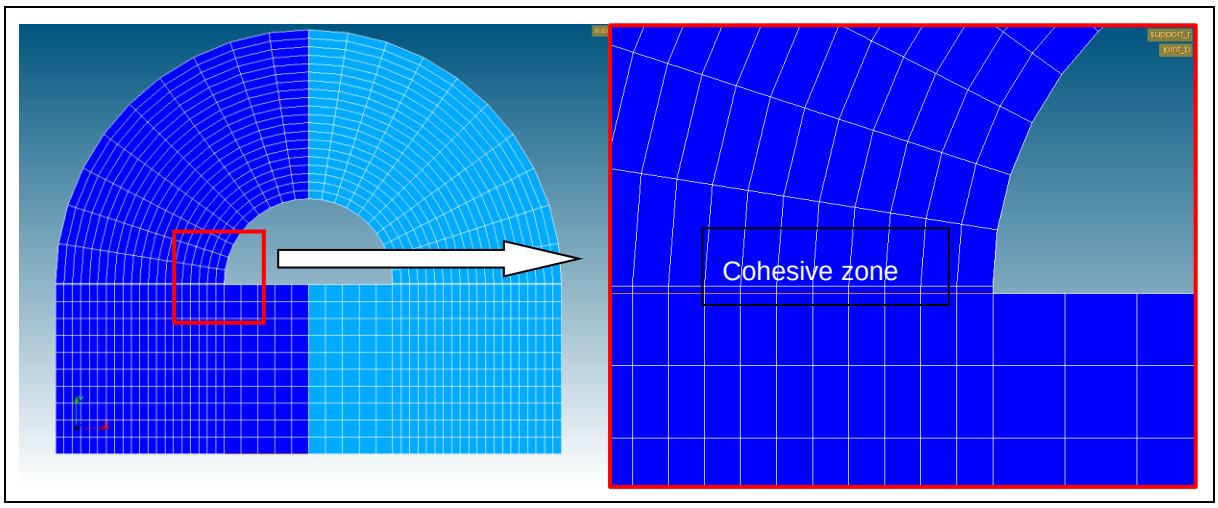

Figure 45 – Schematical mesh of the tunnel with zoom on cohesive zone.

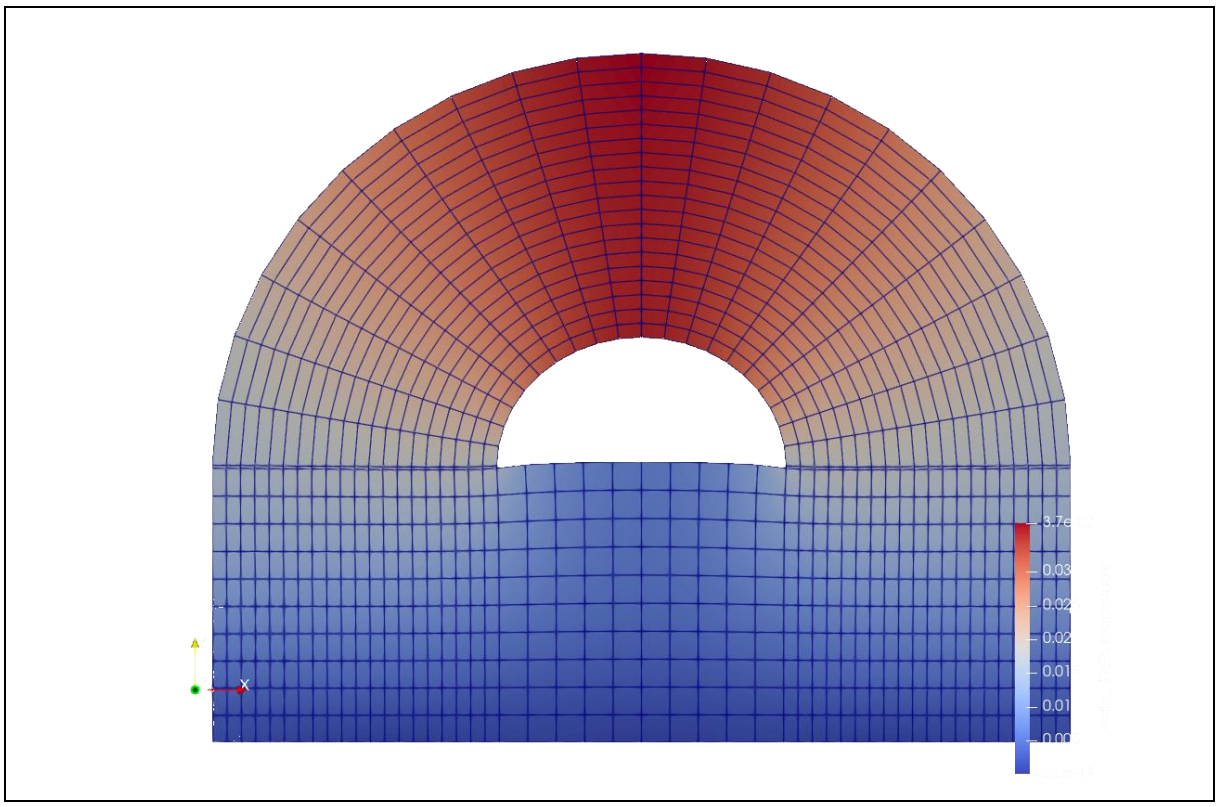

Figure 46 – Deformed shape of elastic solution.

3.3.1 Spurious oscillations

In this section we briefly describe the spurious oscillations that are observed inside cohesive zone elements close to the stress singularity point. It's by looking for the origin of this convergence problem,

that it appeared that oscillations, present at the integration points of cohesive finite elements, generate stresses and false local displacements. The convergence problems had already been raised in the past studies but has until now been attributed to strong nonlinearity of constitutive relation. But once the most simplistic situation was considered it became obvious that the oscillation is a specific model feature.

A study was therefore carried out first on a simplified case, with the aim to identify more precisely the origin of these oscillations. Two rectangles with contact geometry (*Figure 47*) was considered where the contact condition was ensured by penalisation condition. While the loading of the sample should have resulted in full contact condition, in practice some elements close to the singularity were shifted to the traction domain.

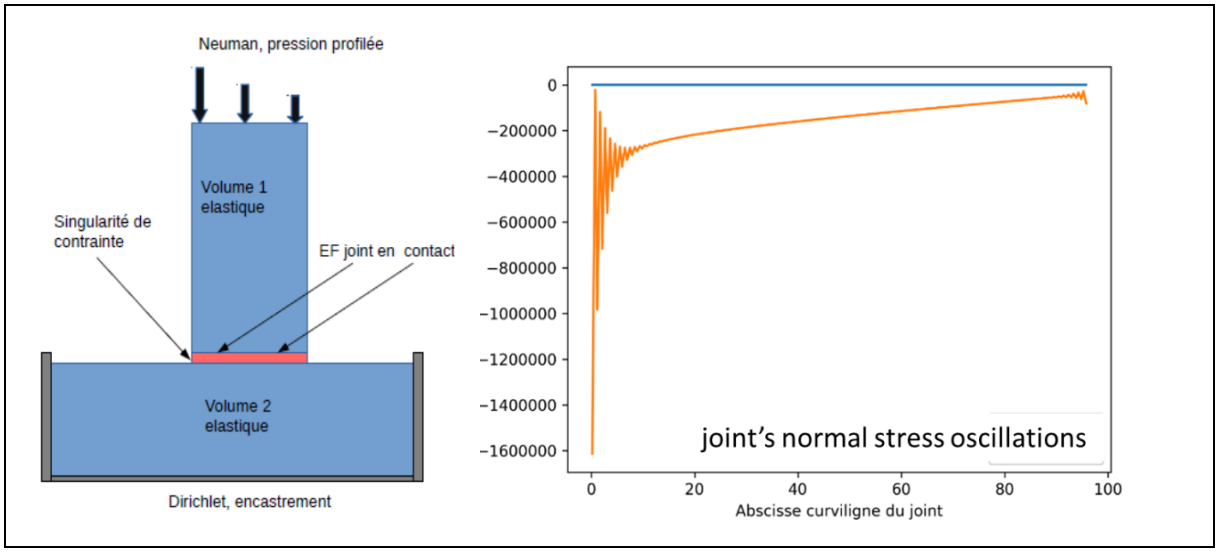

Figure 47 – Schematical representation of the simplified model (left) and illustration of the corresponding stress oscillation on the contact interface (right).

The same study in the elastic case for tunnel geometry (*Figure 45*) was performed. While the whole displacement field seems to be continuous as it should to be (*Figure 48* center), the plotting of the relative displacement in both directions (*Figure 48* right) on the cohesive zone boundary reveals the origin of the problem: close to the stress singularity the first element is significantly compressed on the singularity boundary, while being deformed in the opposite to loading direction on the opposite boundary. If this change of the displacement sign is not a real issue for ideal elastic case, where the first element distortion is compensated by neighboring elements, for the contact problem it generates partial detachment and another singularity for the next element. The phenomenon propagates through the sample as it's illustrated in *Figure 47* (right).

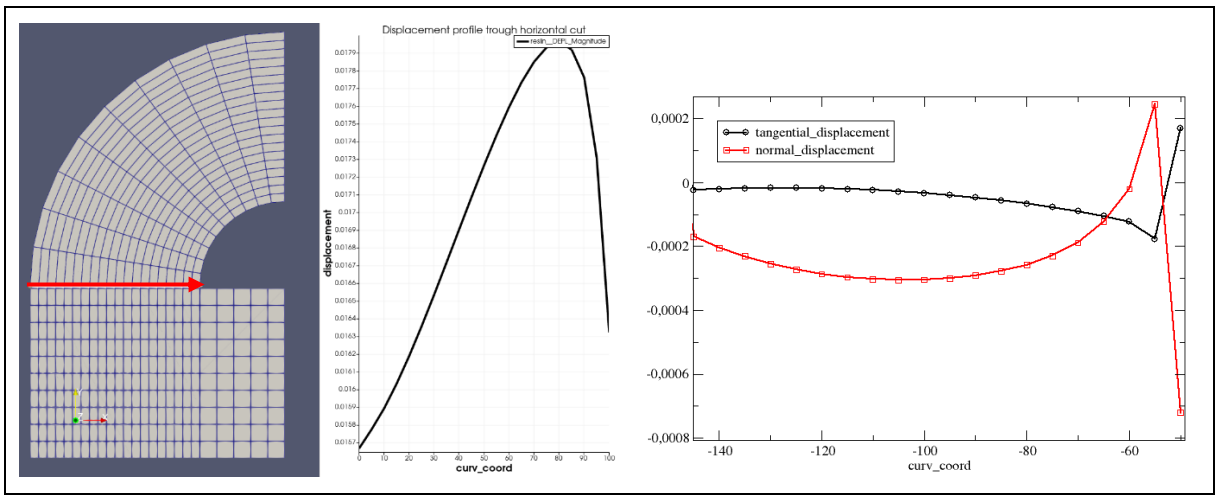

Figure 48 – Displacement field (center) plotted over cohesive zone line (in red on the left) is perfectly smooth, while relative displacement field (right) shows unphysical oscillation going to the traction domain.

The oscillations strongly impact the robustness of cohesive zone finite element calculations. Bibliographic research shows that this phenomenon has been known for a long time (works of K. Bathe, F. Brezzi, M. Fortin [BB2001]). However, up to our knowledge there is currently no formal solution to eliminate these oscillations for arbitrary cohesive constitutive relation. One of the possible solutions for simplified unilateral contact problem may be relied on the introduction of Nitsche formulation, that is under development in the finite element code_aster software.

4. Summary

Efficiency of a posteriori error calculated on flux reconstructed on patches is proven theoretically for simplified Nitsche contact problem. Adaptive refinement procedure is implemented numerically in FreeFem++ software. It seems to be highly efficient, as we obtain close to theoretical convergence rate in the test-cases. Extension of flux reconstruction for boundary elements is proposed, the relevance of these elements for correct error estimation in shown numerically. Finally, some specific finite element solution close to the stress singularity region was identified and studied in detail.

References

[Nitsche1971] Nitsche J. (1971). *Über ein variationsprinzip zur lösung von dirichlet-problemen bei verwendung von teilr äumen, die keinen randbedingungen unterworfen sind.* Abhandlungen aus dem Mathematischen Seminar der Universität Hamburg, 36, pp. 9–15.

[Ainsworth2000] Ainsworth, M., & Oden, J. T. (2000). *A Posteriori Error Estimation in Finite Element Analysis* (Vol. 37). John Wiley & Sons.

[BB2001] Bathe, K., & Brezzi, F. (2001). *Stability of finite element mixed interpolations for contact problems*. Matematica e Applicazioni 12.3 : pp. 167-183.

[FreeFEM] Hecht, F. (2012). *New development in FreeFem++*. Journal of numerical mathematics, 20(3-4), pp. 251-266.

[Chouly2013] Chouly, F., & Hild, P. (2013). *A Nitsche-based method for unilateral contact problems: numerical analysis.* SIAM Journal on Numerical Analysis, 51(2), pp. 1295-1307.

[Riedlbeck2017] Riedlbeck, R. (2017). *Adaptive algorithms for poromechanics and poroplasticity* (Doctoral dissertation, Université Montpellier).

[Chouly-Mlika2017] Chouly, F., Fabre, M., Hild, P., Mlika, R., Pousin, J., & Renard, Y. (2017). *An overview of recent results on Nitsche's method for contact problems.* In Geometrically Unfitted Finite Element Methods and Applications: Proceedings of the UCL Workshop 2016 (pp. 93-141). Springer International Publishing

[RieDPiErn17] Riedlbeck, R., Di Pietro, D. A., Ern, A., Granet, S., & Kazymyrenko, K. (2017). *Stress and flux reconstruction in Biot's poro-elasticity problem with application to a posteriori error analysis.* Computers & Mathematics with Applications, 73(7), 1593-1610.

[Botti20] Botti, M., & Riedlbeck, R. (2020). *Equilibrated stress tensor reconstruction and a posteriori error estimation for nonlinear elasticity.* Computational Methods in Applied Mathematics, 20(1), 39-59.

[DFK2022] Di Pietro, D. A., Fontana, I., & Kazymyrenko, K. (2022). *A posteriori error estimation via equilibrated stress reconstruction for unilateral contact problems without friction approximated by Nitsche's method.* Computers & Mathematics with Applications, 111, pp. 61-80.

[Fontana2022] Fontana, I. (2022). *Interface problems for dam modeling.* (Doctoral dissertation, Université Montpellier).

[Escoffier2023] Escoffier F., Kazymyrenko K. (2023). *Robustesse des calculs avec éléments finis de joint,* EDF technical report N 6125-1723-2023-02169.

[R7.01.25] *Lois de comportement des joints des barrages: JOINT_MECA_RUPT et JOINT_MECA_FROT*, Code_Aster technical notes.

[R3.06.09] *Éléments finis de joint mécaniques et éléments finis de joint couplés hydromécaniqu*e, Code_Aster technical notes.

A cost effective and reliable numerical method using GPU-CPU unit for complex multiphysic problems

[1]Bator, G., [1]Bednar, A., [1]Kovacs, T.

[1]Social Organization for Radioecological Cleanliness, Jozsef Attila str. 7/A, II/10., 8200 Veszprem, Hungary

The project leading to this application has received funding from the European Union's Horizon 2020 research and innovation programme under grant agreement No 847593.

Abstract

SORC was comparing different programming modules (CUDA, OpenCL, OpenMP, OpenACC) and optimizing a module for a cost effective, reliable numerical method. Our work was an effective solution for increasing the computational time and the parallelization of the source codes. The technological improvement of graphics hardware created a possibility to use desktop video cards to solve numerically intensive tasks. We have created a hardware system capable of performing a huge amount of parallelized calculations. We compared the four most well-known parallelized frameworks. The results indicate that, of all the 4 examined cases the OpenMP and OpenACC performed the worst. From the remaining two candidates the performance gap is not that expressed, but it can be concluded that in all cases the CUDA framework performed about 3,5% better than OpenCL. As the next step our aim was to implement some of the currently available, more sophisticated models in the field of continuum models. We have worked on a continuum model using the CUDA platform. We used the NVIDIA CUDA toolkit to compile and run the CUDA code on the GPU, which was optimized for parallel execution, which allowed us to achieve significant speedup compared. This continuum model has required to build a mathematical model that is based on a new, more accurate numerical solution of diffusion mass transfer Partial Differential Equations. This model is based on the central finite differences solved by Cranck-Nicholson method and use to verify diffusion models as well as analysing concentration distribution of leaching material within a specimen body and to calculate Incremental Fraction Leached (IFL) and Cumulative Fraction Leached (CFL) summing IFL values till a given leach. The model is based on the standard continuum model equations that describe diffusion and convection, and the calculations for the model were made with CUDA. We used the finite difference method to solve the equations numerically and simulated the movement of liquid. The continuum model is capable of accurately predicting the movement of liquid through different types of granite formations and can be used to optimize the design of engineering structures that involve the movement of liquid through rock formations.

Significance Statement

Our plan was to compare different programming modules and optimize a module for a cost effective and reliable numerical method. Nowadays, most computers got multiple processors that can handle multitasking with great performance using the available resources. A possible, effective solution for reducing the computational time can be the parallelization of the source codes. A possible solution could be the use of a GPU as they got a heavy parallel architecture, making them ideal for arithmetic operations and calculations. Our aim was to implement some of the currently available, more sophisticated models in the field of continuum models.

The continuum model is capable of accurately predicting the movement of liquid through different types of granite formations and can be used to optimize the design of engineering structures that involve the movement of liquid through rock formations. Our simulations showed that the movement of liquid through the granite formations is strongly influenced by the porosity and permeability of the rock.

In conclusion, our continuum model provides a valuable tool for predicting the movement of liquid through granite formations and has the potential to contribute to the development of more efficient and sustainable engineering solutions.

Table of content

List of figures

1. Development and Improvement Of NUmerical methods and Tools for modelling coupled processes

1.1 The main contribution of SORC

1.1.1 First task

To compare different programming modules (CUDA, OpenCL, OpenMP, OpenACC) and optimize a module for a cost effective and reliable numerical method.

- Nowadays, most computers got multiple processors that can handle multitasking with great performance using the available resources.
    - A possible, effective solution for reducing the computational time can be the parallelization of the source codes.
    - A possible solution could be the use of a GPU as they got a heavy parallel architecture, making them ideal for arithmetic operations and calculations.
- A large problem can usually be divided into smaller tasks that operate together in order to create a solution.
- Our main plan to compare different programming modules (CUDA, OpenCL, OpenMP, OpenACC) and optimize a module for a cost effective and reliable numerical method.
- As for the benchmarking calculations, we conducted several tests from more simplistic problems towards the more sophisticated, computationally intensive problems.
- The benchmarking tests we used easily parallelized, but besides this, easily calculated algorithms. To diversify the results, we used the algorithms found in the SHOC benchmark suite. Others use the full set of benchmarks provided with the suite, As we were mainly interested in the performance of the systems in real world applications, we chose the following benchmarks:
    - 1D FFT (1 dimension Fast-Fourier Transform)
    - MD5 hashing (data encryption)
    - SGEMM (matrix-matrix multiplication)
    - S3D (turbulent combustion simulation)
- Also, we tested a self-developed CT data array generator which should generate data for the verification of a currently developed CT imaging software.
- The calculation of the results is pretty straightforward: given a great amount of calculations to the examined system, the time to return the results were used as an indicator of performance.
- The results are then normalised to be easily interpreted afterwards. The base for normalization is always the fastest performing algorithm in any given benchmark type, as calculated by the following equation:
- $RP = \frac{t_n}{t_{fastest}}$
- RP (relative performance) values being closer to 1 are better than the others, which are always RP>1.
- The results indicate that, of all the 4 examined cases the OpenMP and OpenACC performed the worst.
- From the remaining two candidates the performance gap is not that expressed, but it can be concluded that in all cases the CUDA framework performed about 3,5% better than OpenCL.

- As it is easily seen, OpenCL has another layer between the software driver and the hardware itself, as opposed to CUDA driver, which, thanks to being native in the GPU does not need this additional layer. As a conclusion we decided that for the ongoing research the CUDA framework will be used.
- As per the currently investigated performance tests, the most suitable computational platform is the native CUDA framework.

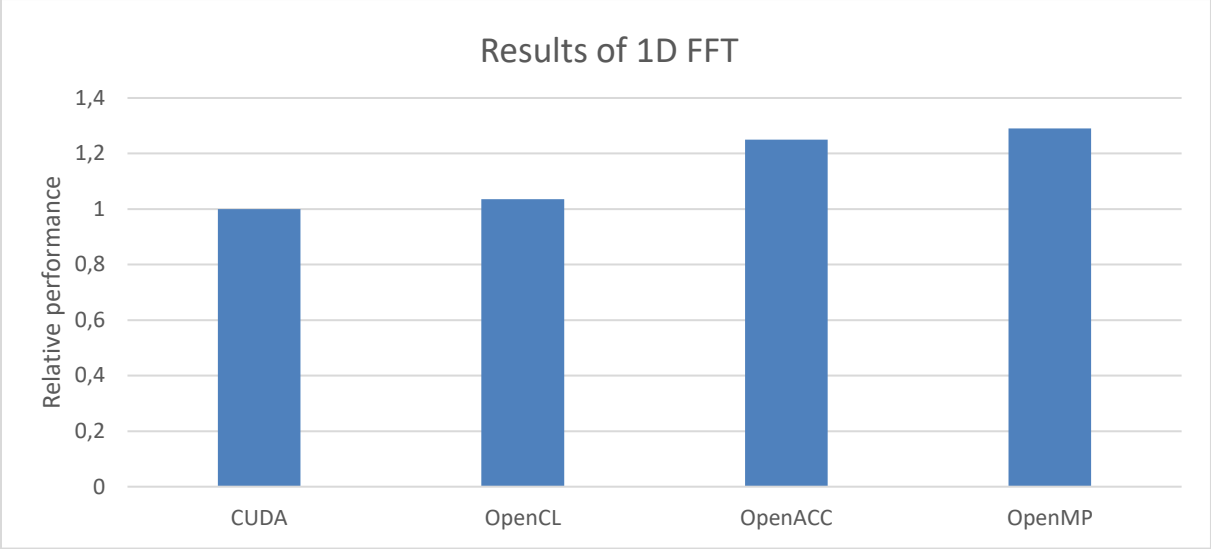

Figure 49 – The results of a 1D Fast Fourier Transform

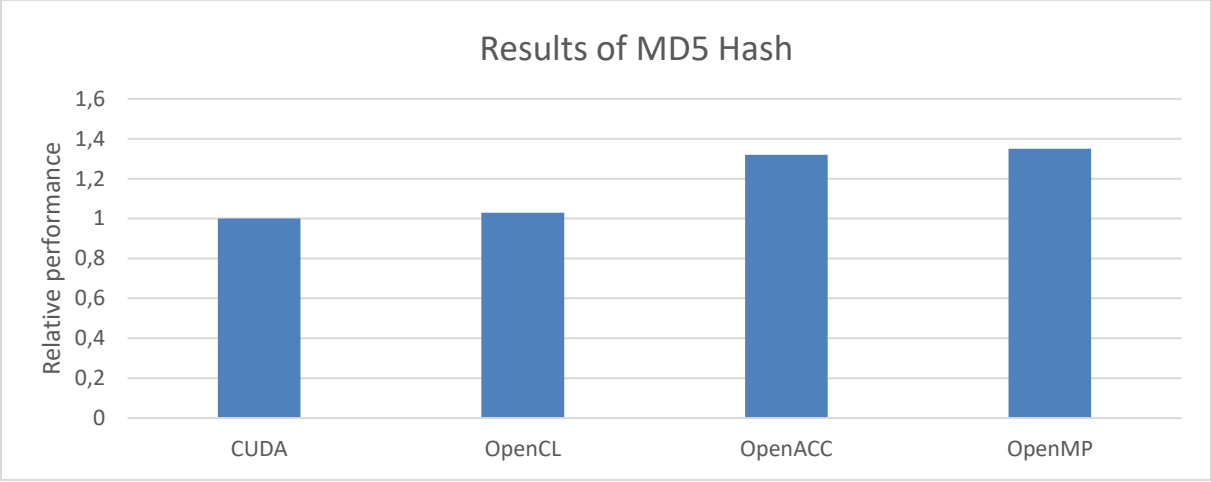

Figure 50 – The results of the MD5 hashing benchmark test

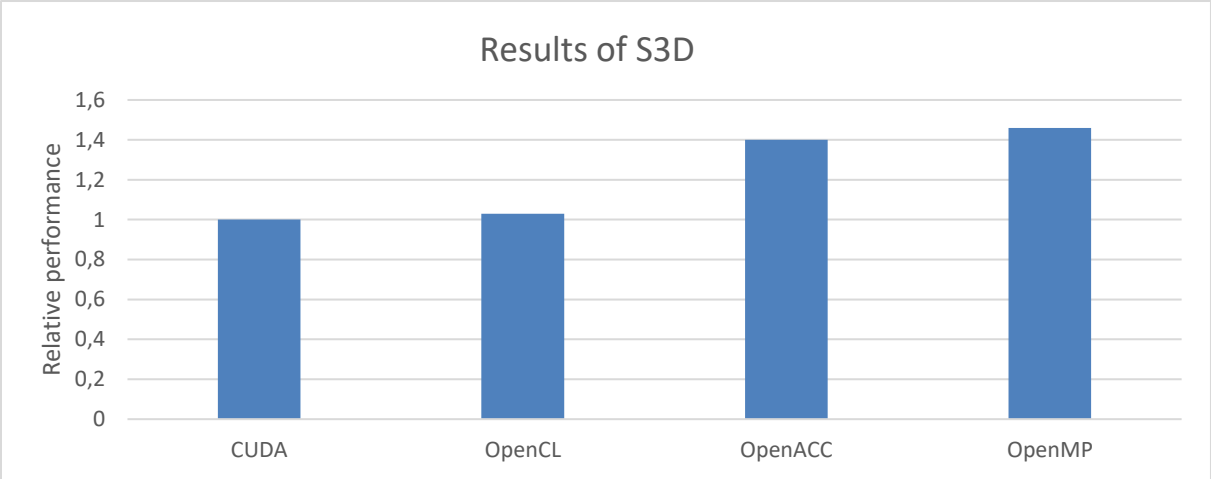

Figure 51 – The results of the S3D benchmark test

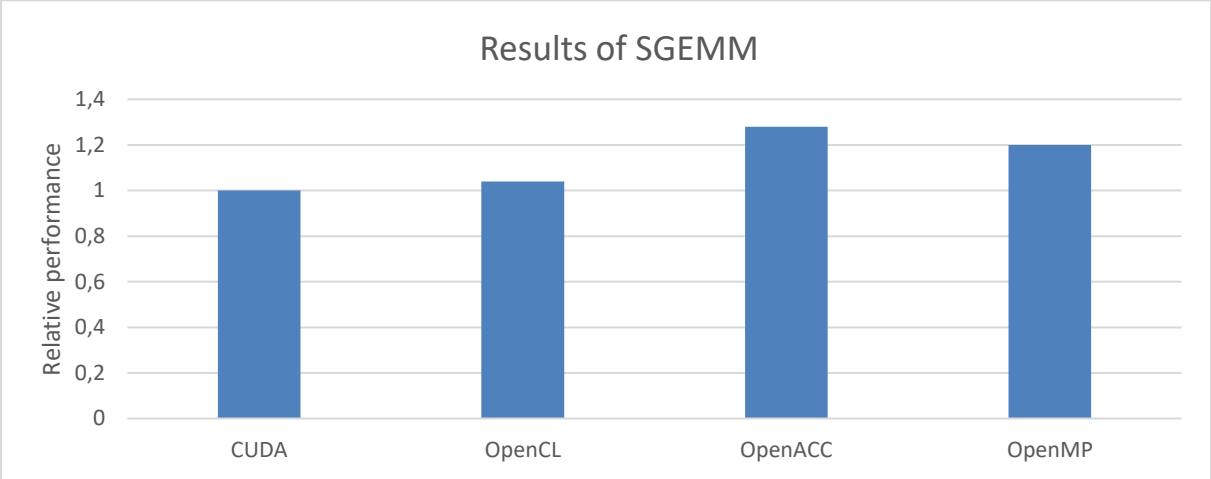

Figure 52 – The results of the SGEMM benchmark test

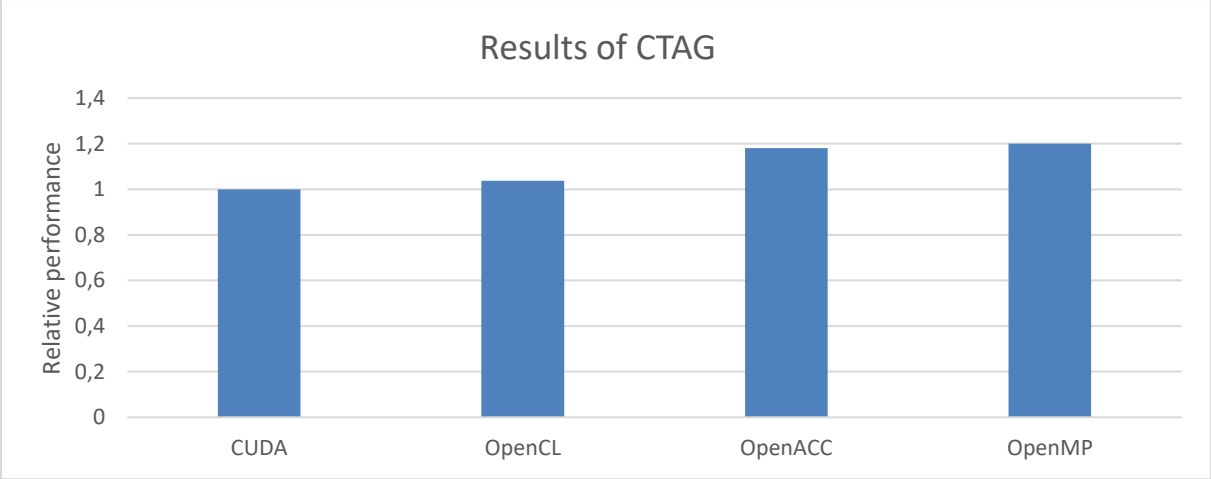

Figure 53 – The results of the CT model array generator test

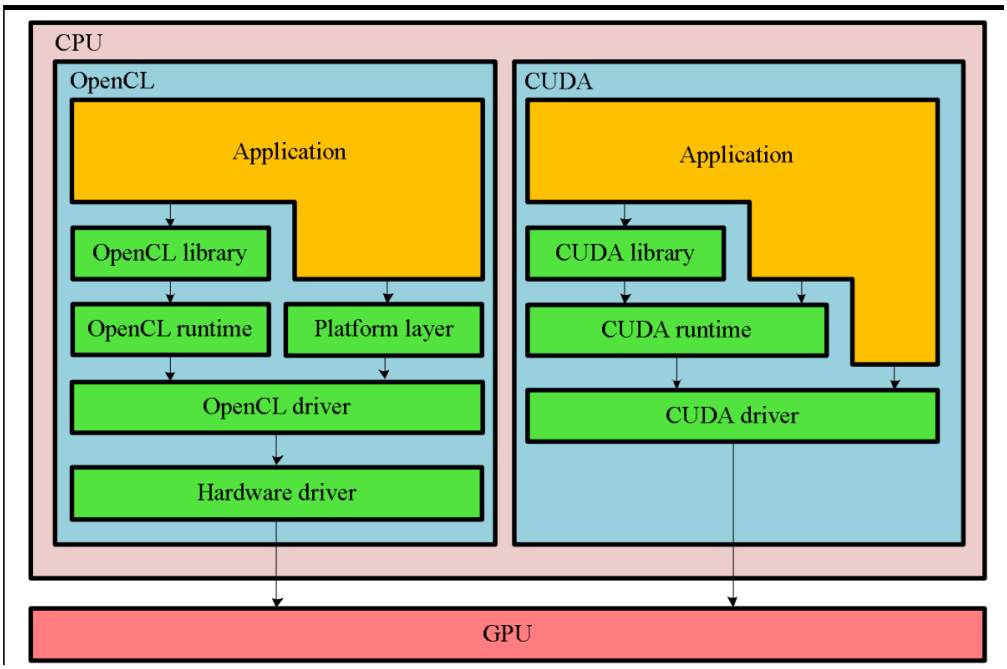

Figure 54 – Result of the tests

1.1.2 Second task

Development of continuum models (for the full scale performance assessment calculation).

As the next step in this kind of research, our aim is to implement some of the currently available, more sophisticated models in the field of continuum models like (Keller & Suckale, 2019; Zhang et al., 2017). Models like this are likely to be developed in the current project, and a verified system capable of performing these kinds of computations is a must. At this period, we have worked on a continuum model (for the full-scale performance assessment calculation) using the CUDA platform. We used the NVIDIA CUDA toolkit to compile and run the CUDA code on the GPU. The CUDA code was optimized for parallel execution, which allowed us to achieve significant speedup compared. This continuum model has required to build a mathematical model that is based on a new, more accurate numerical solution of diffusion mass transfer Partial Differential Equations. This model is based on the central finite differences solved by Cranck-Nicholson method and use to verify diffusion models as well as analysing concentration distribution of leaching material within a specimen body and to calculate Incremental Fraction Leached (IFL) and Cumulative Fraction Leached (CFL) summing IFL values till a given leach. The model is based on the standard continuum model equations that describe diffusion and convection, and the calculations for the model were made with CUDA. We used the finite difference method to solve the equations numerically and simulated the movement of liquid through different types of granite formations.

Our simulations showed that the movement of liquid through the granite formations is strongly influenced by the porosity and permeability of the rock. The continuum model is capable of accurately predicting the movement of liquid through different types of granite formations and can be used to optimize the design of engineering structures that involve the movement of liquid through rock formations.

In conclusion, our continuum model provides a valuable tool for predicting the movement of liquid through granite formations and has the potential to contribute to the development of more efficient and sustainable engineering solutions.

Code source

the code is not yet available on public platforms, it cannot be publicized in its current form. Python routine have been developed and can be discussed on demand.

Development of a C++ version of the ORCHESTRA geochemical solver

Johannnes C.L. Meeussen,

Nuclear Research and consultancy Group (NRG) , Petten The Netherlands

The project leading to this application has received funding from the European Union's Horizon 2020 research and innovation programme under grant agreement No 847593.

Abstract

The main goal of this contribution was to develop a C^{++} version the ORCHESTRA geochemical solver module that was originally developed in Java.

Modern Java is an efficient language that runs via a virtual machine on many different operating systems, however it is difficult to combine it with native compiled languages such as C(++) or FORTRAN.

Translation of the Java chemical solver module to C++ makes this much easier, as it possible to directly link the solver module with existing transport codes that are usually also written in C(++) or FORTRAN.

The developed code was tested on a range of different systems and was shown to produce exactly the same results as the Java version. The computational efficiency of the C++ module appeared to be very similar to that of the the Java version.

The code is open source and available on GITHUB: https://github.com/hansmeeussen/orchestra_cpp

Significance Statement

In large reactive transport simulations, the chemical sub-module generally takes up the main fraction of the calculation time. This work makes the ORCHESTRA chemical solver module available for use in combination with transport frameworks by providing a C++ version of the original Java version. The ORCHESTRA solver module is very efficient, has predefined native C++ parallel processing wrapper, and has a large user definable text library with state of the art adsorption models.

The new C++ version of the ORCHESTRA solver may significantly reduce the calculation times of reactive transport codes.

List of figures

1. Introduction

Combined reactive transport simulations usually contain a specific separate chemical module that calculates the chemical composition of cells or nodes, including distribution of substances over phases with a different mobility at each timestep. This information is subsequently used by the transport module to calculate mass transport in spatial systems.

Typically the chemical sub-module takes up the main fraction of the total model calculation time. Improving the efficiency of such a chemical module or solver therefore directly improves the performance of combined reactive transport models.

The existing ORCHESTRA chemical solver is relatively fast and flexible, but because it is written in Java it is more difficult to couple to reactive transport models that are usually written in C++ (or FORTRAN).

In this contribution to the DONUT project we have overcome this disadvantage by developing a translation of the ORCHESTRA chemical solver module in C++ . This makes the solver available for use in combination with transport frameworks. The resulting ORCHESTRA C++ module is very efficient, can make use of parallel processing, and has a large user definable text library with state of the art adsorption models.

Furthermore, because in ORCHESTRA all chemical model definitions are stored in external text file(s) and the C++ solver can read the same external text files as the Java version, both versions are automatically up to date with new (chemical) model developments.

The new C++ module is also easy to use from the PYTHON scripting language.

2. Original and revised plan

The original plan to make the Java version ORCHESTRA solver easier available to external transport frameworks was to create a wrapper or shell around the existing Java module that would take care of the communication between the solver and external C++ code (Figure 55). The advantage of this approach would be that the original Java module could be used.

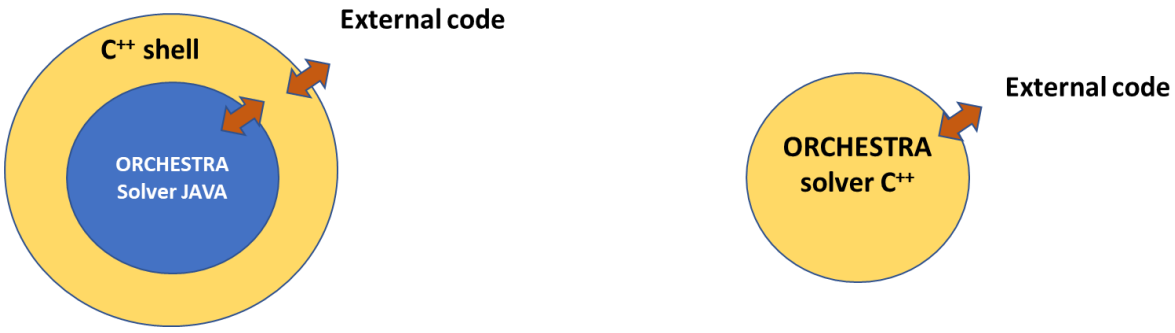

Figure 55 - Two options for implementing ORCHESTRA solver. Left C++ wrapper around Java module, right translation of complete module to C++ .

The disadvantage of this approach is that this shell or wrapper code was completely new and non-trivial. Furthermore it was most likely more difficult to use and potentially less efficient. For that reason, and because the ORCHESTRA solver code is relatively small (explained in next chapter) we decided to translate the complete solver module from Java in C++ .

3. The ORCHESTRA structure and its benefits for translating solver into another language

The choice to translate the complete ORCHESTRA solver from Java into C++ , instead of creating a wrapper around the existing Java module was, also motivated by the fact that in the ORCHESTRA solver is very small in comparison with other chemical equilibrium solvers. So only a small amount of code needed to be translated. Furthermore, because of the similarity in syntax and structure between Java and C++ , literal translation is relatively straightforward.

In case of ORCHESTRA the amount of executable code that represents the solver is extremely small because in contrast with all other existing models/solvers, the chemical model definitions are separated from the generic calculation kernel. This means that the generic solver code does not contain any chemical model definitions, which are instead all defined in external text file that is read as input during run-time. The original rationale behind this structure (Figure 56) was to allow chemical models to be added or updated without the need to change or access the solver source code. However, in this case the structure also makes it possible to change the solver code from Java to C++ without the need to change the chemical models.

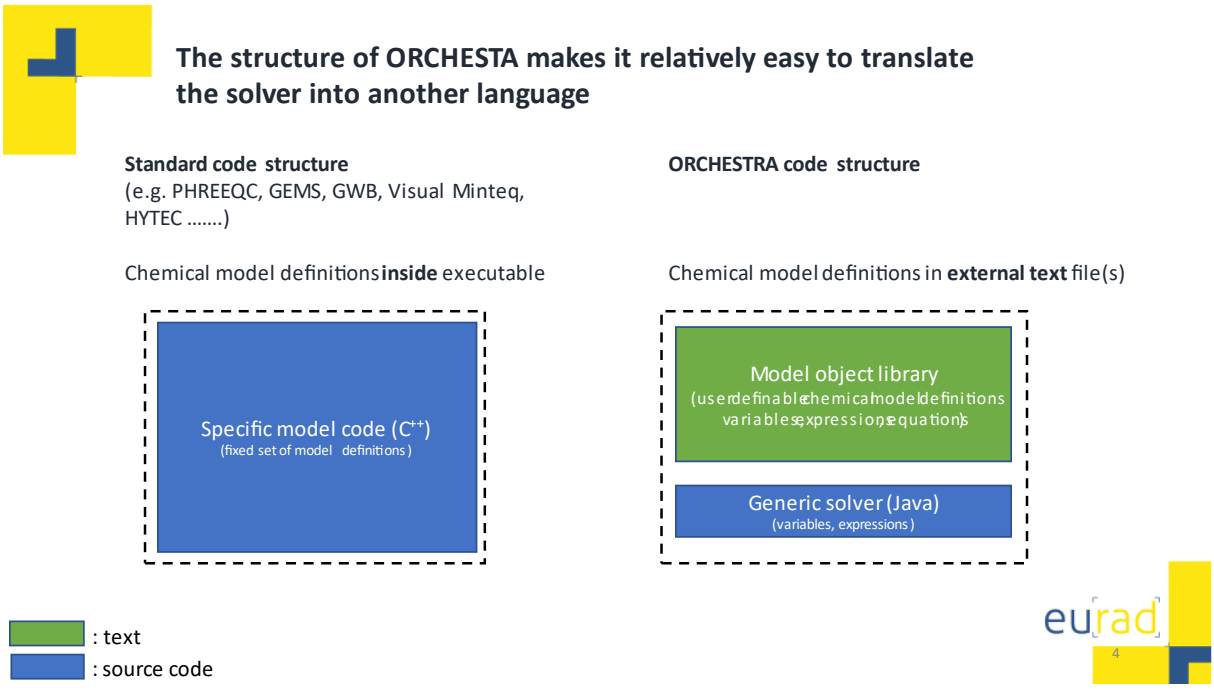

Figure 56 – Comparison between traditional solver structure and ORCHESTRA solver structure

So because of this structure automatically the C++ solver has and will keep the same functionality, in terms of chemical models, as the Java version (Figure 57). As no separate maintenance is needed for the C++ version and both versions can be used interchangeably. (The Java version is not discontinued).

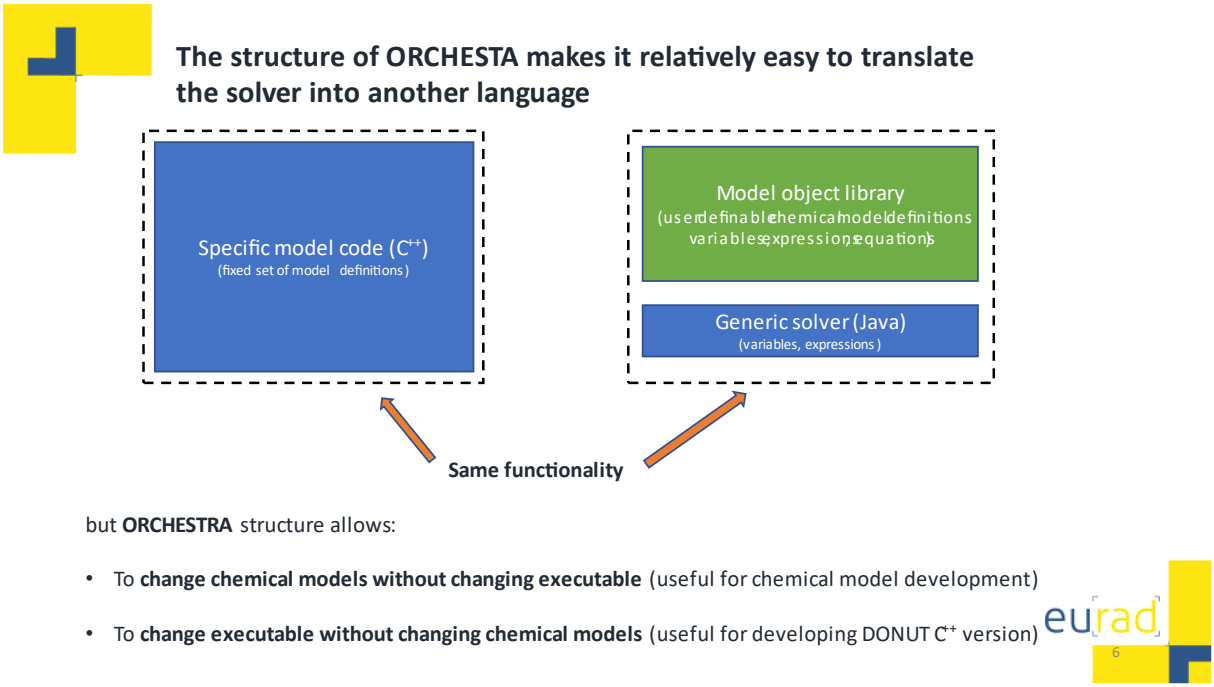

Figure 57 – In case of ORCHESTRA, chemical models can be added/changed without changing the executable. Vice versa, the executable can be changed (into C++) without changing the external mode definition file. The Java and C++ versions use the same external model object library.

4. Test results

The new C++ module fits in the existing model structure in which a separate Graphical User Interface (GUI) can be used to compose a chemical system using standard PHREEQC type database files. This GUI creates a text file with a complete description of the chemical system that can be read by either the Java or the new C++ version of the solver (Figure 58) .

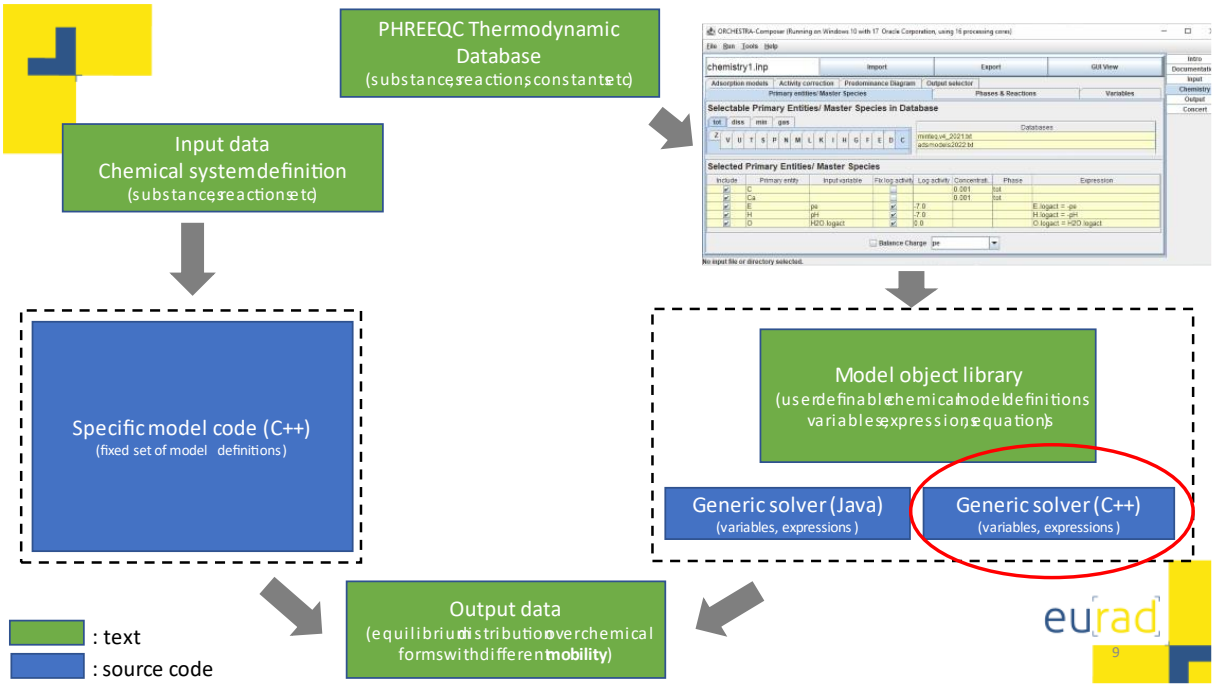

Figure 58 The new C++ module (inside red oval) fits in existing structure an can be used as alternative for Java version. Chemical models are automatically up to data as C++ version can read same external model object library and input files.

The calculated results were successfully tested against the results of the Java module and appeared the same within machine accuracy (Figure 59). Calculation times of the C++ module were very similar to those of the Java version, although C++ is generally considered to be a more efficient language.

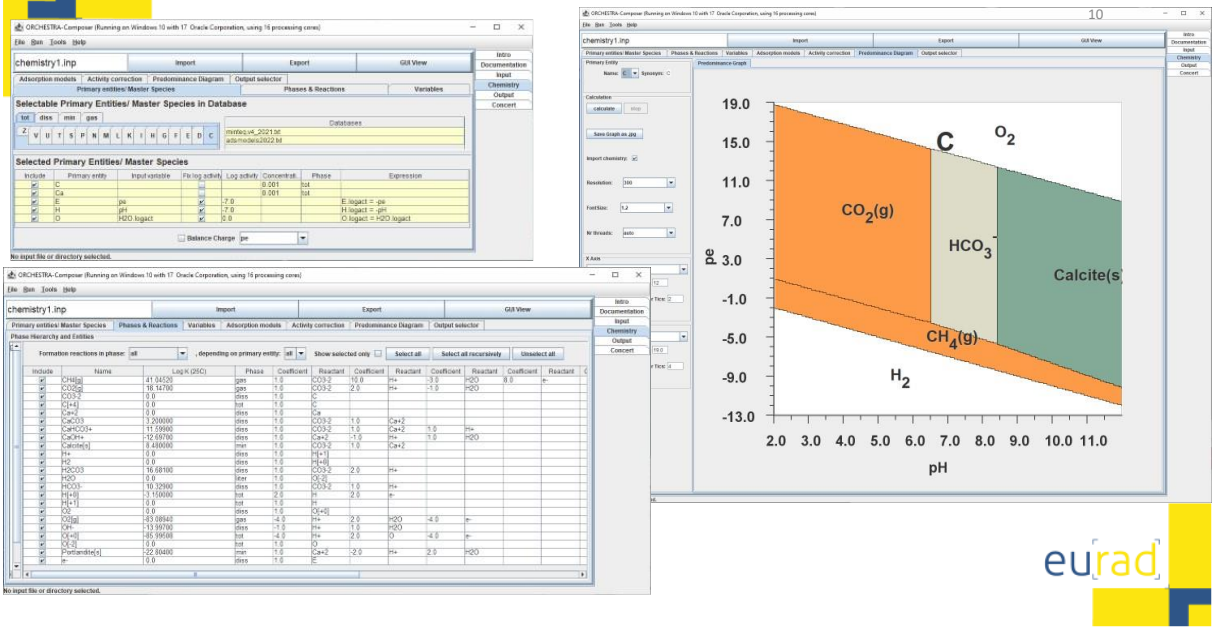

Figure 59 – Example calculated output

In collaboration with SCK, the C++ solver was also tested as alternative chemical module for PHREEQC in combination with the HYDRUS code within the HPx Software. As shown in (Figure 60) calculated results were exactly the same.

Results Comparison HPx-PHREEQC -- HPx-ORCHESTRA
Cement leaching– 1D simulations (SCK, Diederik Jacques)
Identical concentrationprofiles

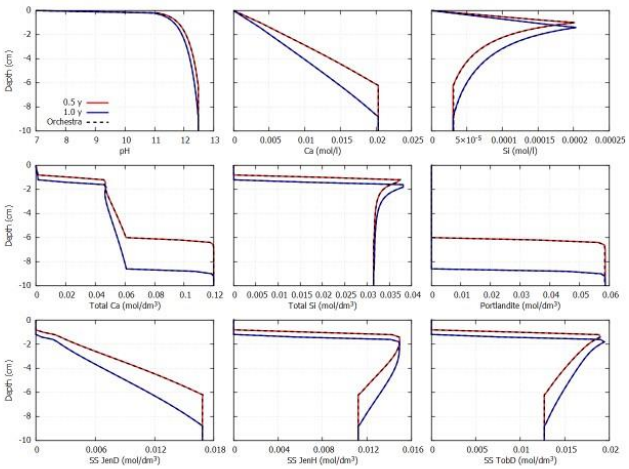

Figure 60 – Test results of solver module in combination with HYDRUS. ORCHESTRA – HYDRUS results are the same as PHREEQC HYDRUS results.

5. Conclusions

The main conclusions of this contribution are:

- We have developed a C++ version of the fast ORCHESTRA C++ chemical solver
- The source code is open and available on GITHUB
- The new solver has been tested in the DONUT Machine Learning Benchmark exercise and produces the same results as the Java version
- The solver has also been tested as replacement for PHREEQC in combination with Hydrus transport code, in collaboration with SCK.
- Apart from calculation efficiency and parallel processing a main advantage of the ORCHESTRA module is the availability of a large set of state-of-the-art adsorption models for oxides and organic matter that can be extended and changed by users.
- The execution speed of the C++ module is very similar to the original Java module (in contrast with general expectations).
- The new C++ solver can easily be used from Python code (Interface developed in collaboration with TU Delft)
- The new solver code, including Python interface, is available from https://github.com/hansmeeussen/orchestra_cpp

Code source

The source code of the ORCHESTRA C++ solver is available on GITHUB hansmeeussen/orchestra_cpp (github.com) but can also be made available as additional information with this document.

Study of the impact of capillary gas entry pressure and hysteresis on compositional two-phase flow models of hydrogen migration in a DGR for the disposal of HLW

[1]Saâdi, Z., [1,2]Amri A.

[1]IRSN, Institut de Radioprotection et de Sûreté Nucléaire, France

[2]IMFT, Institut de Mécanique des Fluides de Toulouse, France

The project leading to this application has received funding from the European Union's Horizon 2020 research and innovation programme under grant agreement No 847593.

Abstract

This work aims to improve the knowledge of the physics of 2-phase 2-component (water-hydrogen) flow and transport in porous media by introducing capillary gas entry pressure ($P_{c,ge}$ or $P_{c,e}$) and hysteresis that are usually neglected in the modelling of gas migration at various scales of the disposal facility. Here, theoretical development of models representing the both phenomena, their implementation in iTOUGH2 and TOUGH2-MP, their verification, and their experimental validation are presented and discussed.

The first part of the paper presents two new numerical approaches for solving the two-phase flow problem incorporating the modified Van Genuchten-Mualem model including $P_{c,e}$ (VGM-PE). Both methods showed to give similar results through their verification on a numerical experiment of 1D capillary rise of water in vertical clay column. These results showed also that the uncertainty on waterfront advance in the column is highly underestimated when $P_{c,e}$ is neglected (relative error more than 65 %). Moreover, the experimental validation of VGM-PE at the scale of a borehole, excavated in the Callovo-Oxfordian (COx) clay rock (PGZ1 gas injection experiment - Meuse/Haute Marne Underground Research laboratory), showed that both numerical methods simulate fairly well the gas pressure measured within the chamber, and that the accumulation of gas within the chamber is higher when $P_{c,e} \neq 0$. This leads to the increase of gas pressure and high desaturation of the EDZ and COx near the borehole at later times. After verification and validation of VGM-PE, an example simulation of hydrogen transport in a 3D HLW cell is presented to demonstrate the impact of $P_{c,e}$ on the simulation of maximum gas pressure within the backfilled drift.

The second part consists of a study of two-phase flow with hysteresis and $P_{c,e} = 0$: a comparative study of 5 different conceptual hysteresis models on 5 different materials (3 sands, bentonite, cement), with an application to an intermediate laboratory scale experiment of injection of a non-wetting fluid in a saturated reservoir with a wetting fluid. As a result, the conceptual hysteretic model with gas entrapment Beriozkin and Mualem 2018 showed to be accurate for simulating scanning curves with less CPU times.

Significance Statement

- **Capillary gas entry pressure ($P_{c,e}$)**: The introduction of this parameter in hydraulic properties of the materials composing a deep geological repository (DGR) for radioactive waste highly impacts the results of the maximum gas pressure within the backfilled drifts of this DGR. This is essentially due to the higher value of $P_{c,e}$ of the host rock (COx) by comparison to the other materials. The gas migrates preferentially towards the materials with the lowest $P_{c,e}$-values (EDZ and backfill), which increases the maximum gas pressure in the drifts that can reach values more than the lithostatic pressure of the host rock, thus leading to its hydraulic fracturing. This study suggests that solutions must be considered to reduce this maximum gas pressure, whether by reducing the mass of metallic components or by changing hydraulic properties of the bentonite seal (so that the gas can be released easily to the outlet of the DGR) or by increasing the volume of the drifts.
- **Hysteresis**: It is challenging to apply hysteretic models to simulate gas migration at the scale of a DGR. The main difficulty lies on the application of the current models which need a very high number of iterations (high CPU-time) to derive scanning curves during the numerical solution of the non-linear equations of the two-phase flow mathematical problem, usually leading to non-convergence problems of this solution. In this study, it has been shown that Beriozkin and Mualem 2018 is a good alternative to other hysteretic models. In addition to its accurate prediction of scanning curves, it uses explicit equations to derive scanning curves that need less CPU time during numerical simulations. The application of this model is promising for first testing at the scales of waste cell and a module of a DGR. From the results of the simulation of a two-phase intermediate laboratory scale experiment, it can be concluded that gas entrapment phenomenon can play a significant role after the period of hydrogen generation. In fact, the hydrogen could be entrapped within the backfilled repository for many years before hydrostatic equilibrium is reached. A priori, this gas entrapment period is still difficult to estimate by modelling.

Table of content

List of figures

1. Capillary gas entry pressure

1.1 The new model VGM-PE

The capillary gas entry pressure ($P_{c,e}$) is defined as the threshold capillary pressure at which gas penetrates a saturated porous medium (Brooks and Corey, 1964). Once a saturated porous medium becomes unsaturated, a visco-capillary flow of gas and water is developed which can lead to the development of dilatant preferential pathways, micro-fissuring, and eventually hydraulic fracturing during the gas transfer in clay-based materials of the facility (Marschall et al., 2005). This can have a direct impact on the performance of the DGR sealing system in reducing radionuclides transport to the outlet.

This phenomenon which defines the transition between single-phase liquid to two-phase flow conditions is introduced through modification of the van Genuchten-Mualem (VGM) model (van Genuchten, 1980; Mualem 1976a; Parker et al., 1987) for rocks hydrodynamic properties (i.e., water retention curve and curves of relative permeability to liquid and gas) as shown in Figure 61. This model, called **VGM-PE**, is a generalization of single-phase liquid flow models of Vogel et al. (2001) and Ippisch et al. (2006) to two-phase liquid-gas flow models (Amri, 2021):

(7) $$S_l(P_c) = \begin{cases} S_{lr} + \frac{S_{ls}^* - S_{lr}}{[1+(\alpha P_c)^n]^m} & if \quad P_c \geq P_{c,e} \\ S_{ls} & if \quad P_c \leq P_{c,e} \end{cases}$$

(8) $$k_{r,l}(P_c) = \frac{k_l(S_l)}{k_{0,l}} = \begin{cases} \left[\frac{S_{le}}{S_{le}^*}\right]^{\tau} \left[\frac{1-(1-(S_{le}(P_c))^{\frac{1}{m}})^m}{1-(1-(S_{le}^*)^{\frac{1}{m}})^m}\right]^2 & if \quad P_c \geq P_{c,e} \\ 1 & if \quad P_c \leq P_{c,e} \end{cases}$$

(9) $$k_{r,g}(P_c) = \frac{k_g(S_l)}{k_{0,g}} = \begin{cases} \left[1 - \frac{S_{le}}{S_{le}^*}\right]^{\tau'} \left[1 - \frac{1-(1-(S_{le}(P_c))^{\frac{1}{m}})^m}{1-(1-(S_{le}^*)^{\frac{1}{m}})^m}\right]^2 & if \quad P_c \geq P_{c,e} \\ 0 & if \quad P_c \leq P_{c,e} \end{cases}$$

With

$$S_{le} = \frac{S_l(P_c) - S_{lr}}{S_{ls}^* - S_{lr}}$$

$$S_{ls}^* = S_{lr} + (S_{ls} - S_{lr}) \times \left[1 + \left(\alpha P_{c,e}\right)^n\right]^m$$

where S_{lr} (-) and S_{ls} (-) are the residual and full liquid saturations; n (-) and m (-) are shape parameters, with $m = 1 - \frac{1}{n}$; $\alpha = 1/P_{c0}$ (Pa^{-1}) is a pressure scale parameter; τ and τ' are dimensionless parameters representing tortuosity for permeability to liquid and gas respectively; the two parameters $k_{0,l}$ (m^2) and $k_{0,g}$ (m^2) are intrinsic permeabilities for single-phase liquid and single-phase gas, respectively.

The VGM-PE model can be reduced to the classical VGM model by putting $P_{c,e} = 0$, $\tau = \tau' = \frac{1}{2}$ and $k_{0,l} = k_{0,g} = k_0$ in equations (7), (8) and (9).

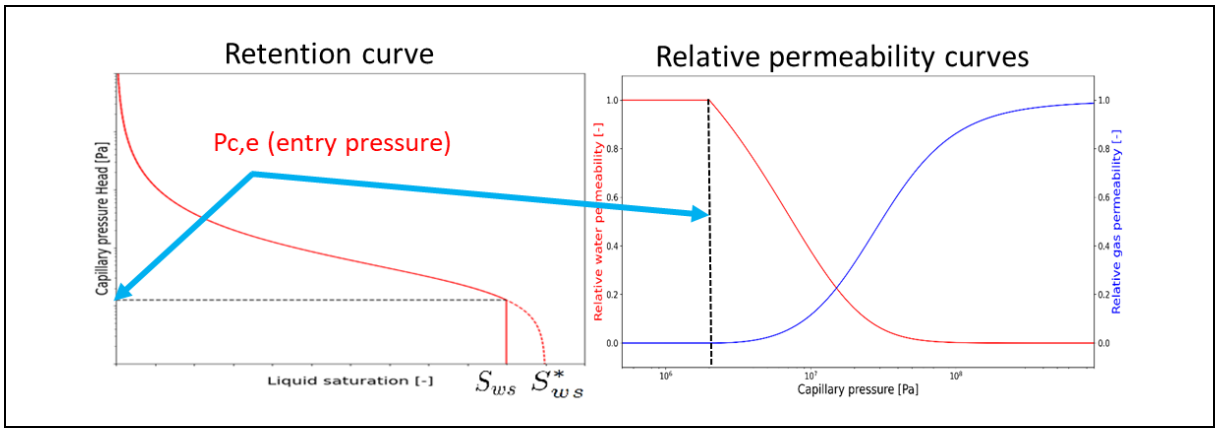

Figure 61 – The modified van Genuchten-Mualem model (VGM-PE) including capillary gas entry pressure in the water retention curve and relative permeability curves to gas and water.

1.2 Optimisation of the parameters of hydraulic properties

The simultaneous optimization of $P_{c,e}$ and the other shape and scale parameters of VGM-PE hydraulic properties from experimental data is not an obvious task. It is carried out in our work by using two different approaches. The first one is based on a single optimization function by modification of the RETC code (van Genuchten et al., 1991), by adding the function relative permeability to gas in the optimization (Eq. (10)):

(10) $$O_{bj}(\boldsymbol{P}) = O_{bj}(\boldsymbol{P})_{S_l} + W_{k_l} O_{bj}(\boldsymbol{P})_{k_l} + W_{k_g} O_{bj}(\boldsymbol{P})_{k_g}$$

(11) $$O_{bj}(\boldsymbol{P})_Y = \frac{MSE\left([\hat{Y}_i(\boldsymbol{P}) - Y_i]_{i=1\ldots N_{dataY}}\right)}{\overline{Y_{data}}^2}$$

where Y can be S_l, $\log(k_l)$ or $\log(k_g)$; $\boldsymbol{P} = (m, \alpha, S_{ls}, S_{lr}, k_{0,l}, \tau, k_{0,g}, \tau', P_{c,e})$ is the parameter vector to be optimised, unique for the three curves $S_l(P_c)$, $k_l(P_c)$, et $k_g(P_c)$ described by Eqs. (7), (8) and (9), from experimental data $(S_{l,i})_{i=1\ldots N_{dataS}}$, $(k_{l,i})_{i=1\ldots N_{datak_l}}$, et $(k_{g,i})_{i=1\ldots N_{datak_g}}$ with N_{dataS}, N_{datak_l}, et N_{datak_g} are respectively numbers of measured data for the curves water retention, permeability to liquid, and la permeability to gas. The function $\hat{Y}_l(\boldsymbol{P})$ represents the adjusted model formulated by Eqs. (7), (8) and (9); W_{k_l} and W_{k_g} are weighting factors which allow to give more or less weight to a specific hydraulic property compared to the other two properties.

The second approach is based on a multi-objective optimization method (Eq. (12)) using Pareto optimal solutions, as in Twarakavi et al. (2008) and Hadka (2015):

(12) $$\min_{\boldsymbol{P}\in\mathbb{R}^q} y = f(\boldsymbol{P}) = \left(f_1(\boldsymbol{P}), f_2(\boldsymbol{P}), f_3(\boldsymbol{P})\right)$$

under constraints $g(\boldsymbol{P}) = \left(g_1(\boldsymbol{P}), g_2(\boldsymbol{P}) \ldots g_n(\boldsymbol{P})\right) \leq 0$

with $\boldsymbol{P} = (m, \alpha, S_{ls}, S_{lr}, k_{0,l}, \tau, k_{0,g}, \tau', P_{c,e}) \in X \subseteq \mathbb{R}^q$

f_1, f_2, and f_3 respectively denote the cost functions of the curves water retention, permeability to liquid and permeability to gas. The function g translates the constraints on the q parameters of the vector $\boldsymbol{P}$, and X denotes the decision space of the solution $\boldsymbol{P}$.

1.3 Implementation of VGM-PE model in TOUGH suite of codes

To solve the problem of the discontinuity of the derivatives of functions $S_l(P_c)$, $k_{r,l}(P_c)$, and $k_{r,g}(P_c)$ near $P_{c,e}$ in the compositional two-phase flow equations in iTOUGH2 (Finsterle, 2007; 2016) and TOUGH2-MP (Zhang et al., 2008) codes, two numerical approaches have been developed (Amri et al., 2021):

i) ***SG-method (SGM)***: this approach is similar to that proposed by Battistelli et al. (2017) in that the primary variables of the solution are kept the same to the classical ones, i.e., liquid or gas pressure (P_l or P_g) and gas mass fraction in liquid phase (X_l^g) for single-phase liquid or gas flow conditions; gas pressure and gas saturation (S_g) for two-phase liquid-gas flow conditions. However, the switch between single-phase liquid to two-phase liquid-gas conditions is handled by assuming physical continuity of the mobile liquid phase pressure during this transition, and that the gas phase evolves when the "bubbling pressure" of the "hypothetical" gas phase pressure exceeds liquid pressure plus capillary entry pressure (i.e., P_l + $P_{c,e}$).

ii) ***PC-method (PCM)***: in this approach, the second primary variable capillary pressure (P_c) is used instead of S_g in two-phase liquid-gas flow conditions (i.e., changing from (P_g, S_g) to (P_g, P_c)). This change allows implicit continuity of liquid pressure during the switch from single-phase liquid to 2-phase liquid-gas conditions.

1.4 Numerical verification: Vogel et al. (2001) experiment

The numerical verification of both methods is carried out on the numerical experiment of Vogel et al. (2001) for capillary-rise of water in a 1D clay column of 1 m height. Hydric profiles for $P_{c,e} = 0$ and for $P_{c,e} = -196\ Pa$ (equivalent to a capillary pressure head of – 1 cm) calculated by SGM at different times (Figure 62a) are like those calculated by Vogel et al. (2001) who solved Richards' equation instead of two-phase flow equations. One can see that the advance of waterfront to the soil surface in the case of $P_{c,e} = -196\ Pa$ is faster than in the case of $P_{c,e} = 0$. For $P_{c,e} = -196\ Pa$, the waterfront arrived at the soil surface after two days, whereas it is still at -0.6 m depth in the case of $P_{c,e} = 0$. The uncertainty in terms of the relative error is more than 65 %.

The PCM solution is in good agreement with that of SGM in the case of $P_{c,e} = -196\ Pa$ (Figure 62b). This indicates the good implementation of both numerical methods.

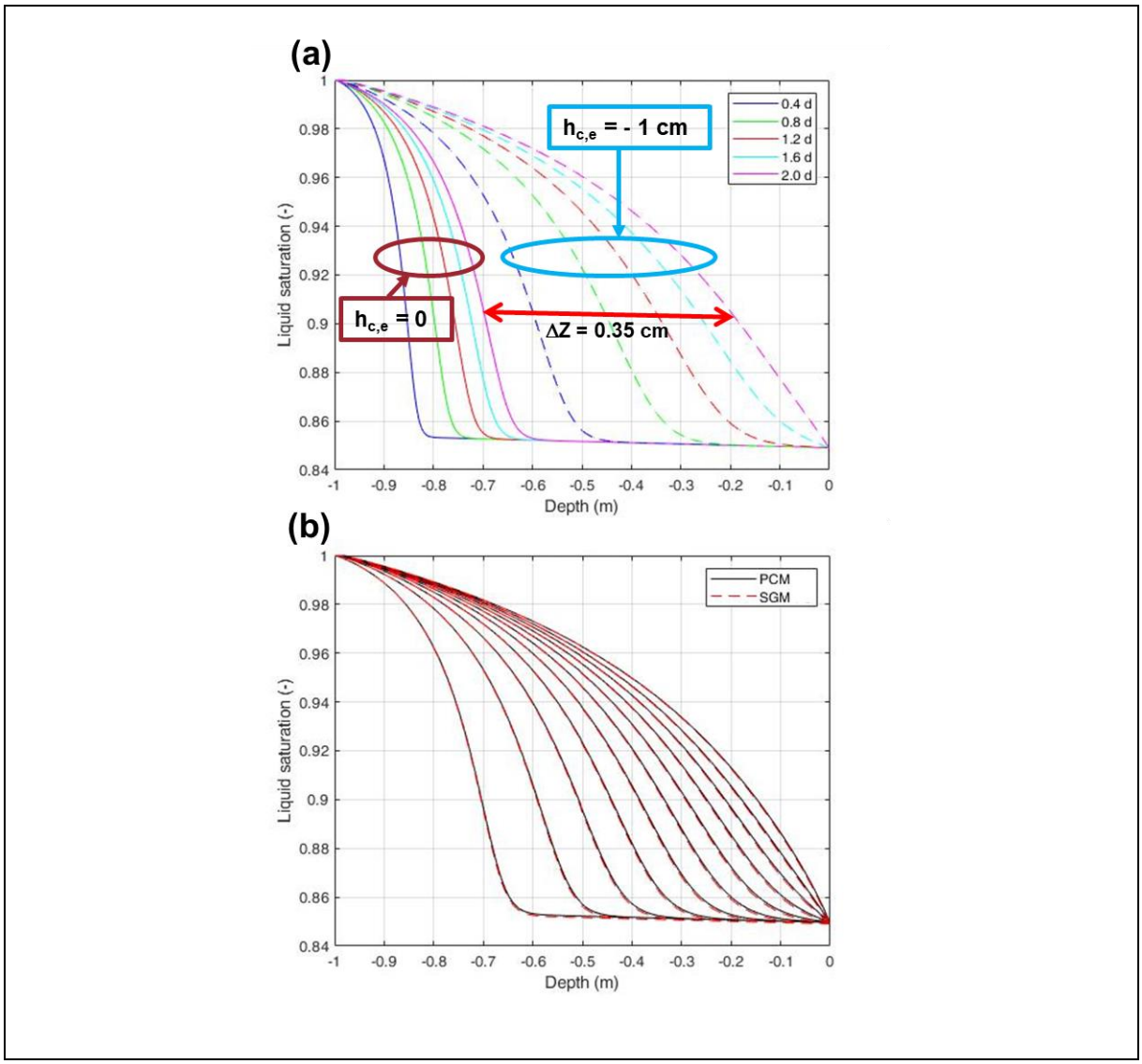

Figure 62 – Water saturation profiles simulated for the capillary-rise of water in a 1 m height clay column at different times: (a) $P_{c,e}$ = 0 vs $P_{c,e}$ = -196 Pa with SGM; (b) SGM vs PCM for $P_{c,e}$ = -196 Pa.

1.5 Experimental validation at the borehole scale: PGZ1-GAS experiment

The experimental validation of the two numerical approaches is dealt with by using the PGZ1-experiment carried out by Andra (De La Vaissière, 2011) at the Meuse/Haute Marne Underground Research laboratory (North-East France). This experiment consists of nitrogen gas injection at different time intervals in the chamber of a borehole inside the Callovo-Oxfordian (COx) clay formation (Figure 63a), candidate host rock for the HLW and ILLW disposal facility for CIGEO project (Andra, 2005). The purpose is to characterize the hydraulic properties of the COx through gas transport within it.

A new analysis of the measured data of COx hydraulic properties has been carried out in this work and the optimized parameters of the modified VGM-PE model are obtained using both methods of the optimization discussed in section 1.2 (Amri, 2021). The optimized $P_{c,e}$ value is about -1,9977 MPa. The model of PGZ1 domain is discretized by finite volumes (rectilinear meshes).

Without calibration of any of the parameters of the model hydraulic properties, both SGM and PCM with $P_{c,e}$ = -1,9977 MPa simulate remarkably the measured gas pressure in the chamber (Figure 63b). Notice, however, that simulations with $P_{c,e}$ = 0 underestimate the measured gas pressure in the chamber. This result can be explained by differences in the dynamics of gas flow inside the COx when the capillary pressure exceeds $P_{c,e}$. In fact, simulations with $P_{c,e}$ = 0 show a faster penetration of nitrogen gas in the COx, with a higher spatial extend of an unsaturated zone around the chamber with higher gas mass fractions, increasing by increasing time (Figure 64a), compared to simulations with $P_{c,e}$ = -1,9977 MPa (Figure 64b).

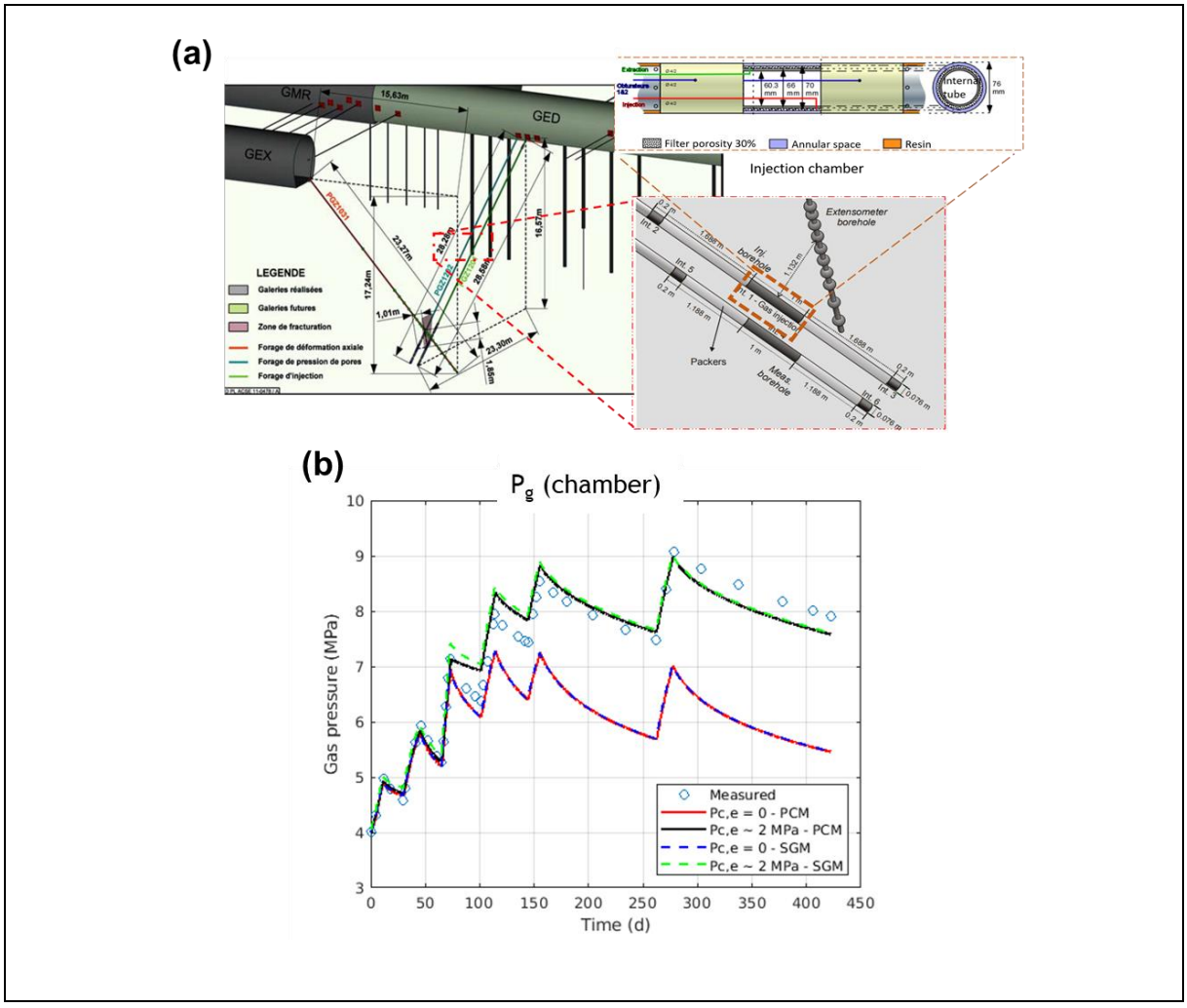

Figure 63 – (a) PGZ1-GAS experiment – Bure URL (Galleries, boreholes, gas injection chamber) (b) Measured vs simulated gas pressure in the chamber inside the borehole using both SGM and PCM solutions with $P_{c,e}$ = 0 and $P_{c,e}$ = -1.9977 MPa.

The capillary entry pressure of the COx can be considered as a capillary barrier to gas penetration that has to be reached before the gas dissolution and diffusion become dominant in the COx (see contours of liquid saturation at time 101 days in Figure 64c and Figure 64d for $P_{c,e}$ = 0 and $P_{c,e}$ = -1,9977 MPa, respectively).

Notice the good agreement between SGM and PCM in simulating the gas pressure in the chamber of the PGZ1 experiment in both cases (i.e., $P_{c,e}$ = 0 and $P_{c,e}$ = -1,9977 MPa).

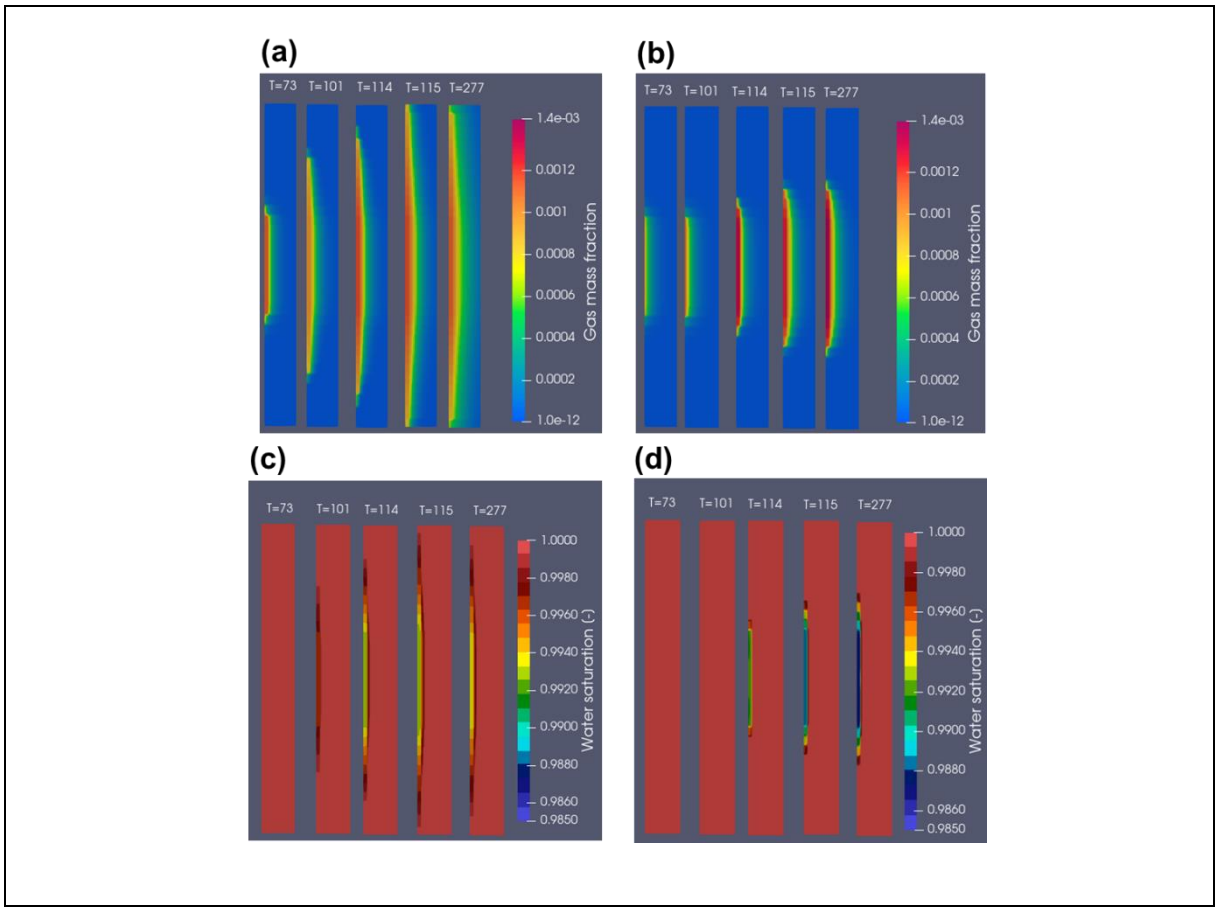

Figure 64 – (a),(b) Nitrogen mass fraction in liquid phase, (c),(d) Liquid saturation, simulated by PCM with $P_{c,e}$ = 0 and $P_{c,e}$ = -1.9977 MPa, respectively, in the flow domain at different times T.

1.6 Application to the study of H_2 migration in a 3D HLW cell (benchmark of EURAD WP GAS Task4.2)

In this subsection, we present results from the IRSN contribution to this benchmark, which consists in studying the impact of capillary gas entry pressure on hydrogen transfer at the cell scale, especially the HLW cell in storage zone C designed according to French concept by Andra (Figure 65a). The new VGM-PE developed in this work, which also has been proposed in the framework of WP DONUT (Deliverable 4.1, SotA DONUT, Ahusborde et al., 2021), will be tested by considering the parametrization proposed in Milestone 61 (Levasseur et al., 2021) for the host rock and engineered barriers materials. The numerical model developed is based on the two-phase (liquid-gas) and two-component (water-hydrogen) equation of state EOS5 (Pruess et al., 1999, 2011) of TOUGH suite of codes (iTOUGH2, Finsterle, 2007; TOUGH2-MP, Zhang et al., 2008).

1.6.1 Model description

The repository (Figure 65a) is located at 600 m depth from the surface (z = 0) in the center of the host rock layer of 150 m thickness (between z = 525 m and z = 675 m from the surface).

The purpose is to evaluate the contribution of one isolated HLW cell of storage zone C to the flow and transport of hydrogen generated by metallic components in the cell and the drift by considering appropriate initial and boundary conditions. The studied domain is that bounded by the small broken black rectangular line shown in Figure 65a. It includes a HLW disposal cell and a part of the access drift,

all embedded within the host rock layer. The domain volume is 125 x 353,5 x 150 m^3, it is delimited along the x-axis by the surface X = 0 m (central axis between the studied cell and its neighbor cell, 50 m apart) and by the surface X = 125 m corresponding to the end of the drift (100 m away from the studied cell, Figure 65a); Along the y-axis the domain is delimited by the surface Y = 0 corresponding to the central axis of the drift, and the surface boundary Y = 353.5 m (mid-length of the square cross section of the drift of 3.5 m, plus cell length of 150 m, plus 200 m of the host rock to the boundary; Figure 65a).

Geometries of drifts and cells (length and section) as well as those of the EDZs (inner and outer) and constitutive materials of the engineered barriers (concrete, bentonite, and backfill) are all shown in Figure 65 and Figure 66. Preprocessing under PetraSim (Thunderhead Engineering, Inc.) of the domain geometry as well as attribution of the material type to the different components of the cell and the drift, as well as their surrounding EDZs is shown in Figure 67. Properties of steel-liners of 2 cm thickness adjacent to the waste packages are considered as those of voids, while steel-liners of 2 cm thickness adjacent to the buffer (backfill or bentonite) are considered as part of the cell buffer (Figure 66b). The circular shape of the main drift is assumed rectangular (Figure 67a,b).

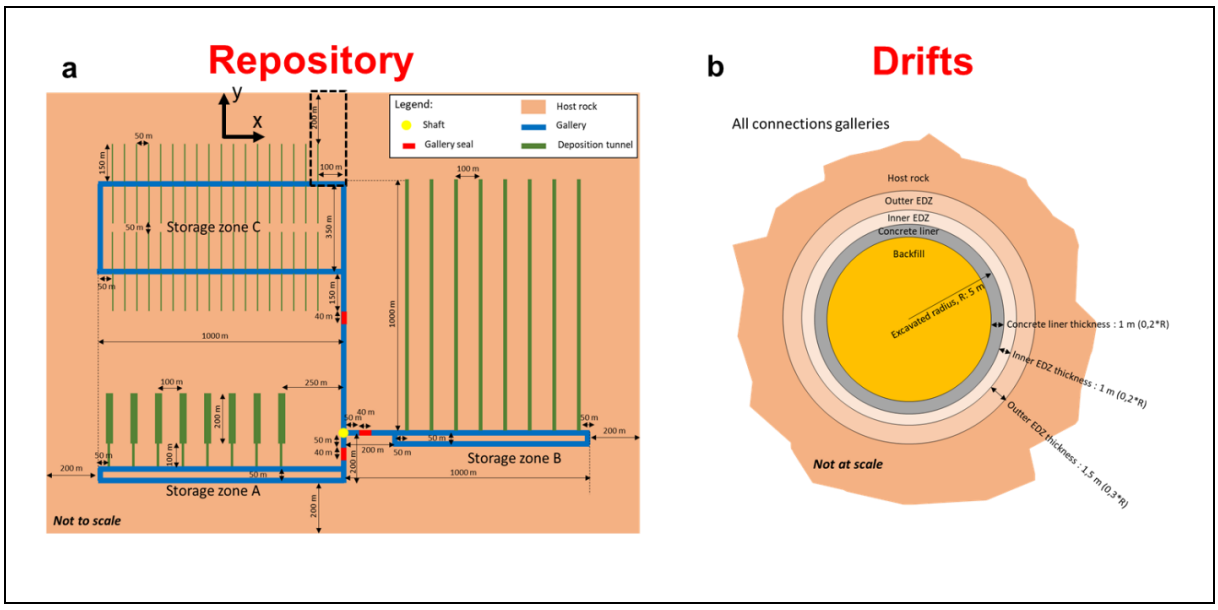

Figure 65 – (a) Schematic horizontal slice at the generic repository depth; (b) Schematic vertical slice of a gallery.

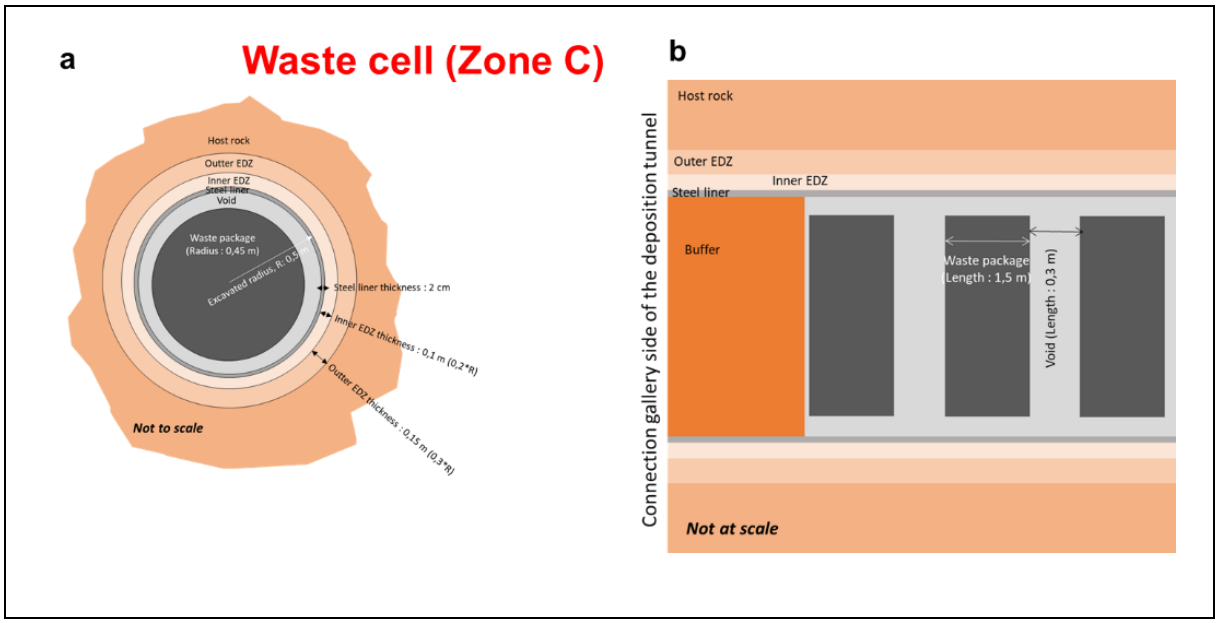

Figure 66 – Schematic representation of a deposition tunnel in storage zone C (inspired by Andra HA deposition micro-tunnel): (a) Cross section inside the waste cell; (b) Longitudinal side of the waste cell.

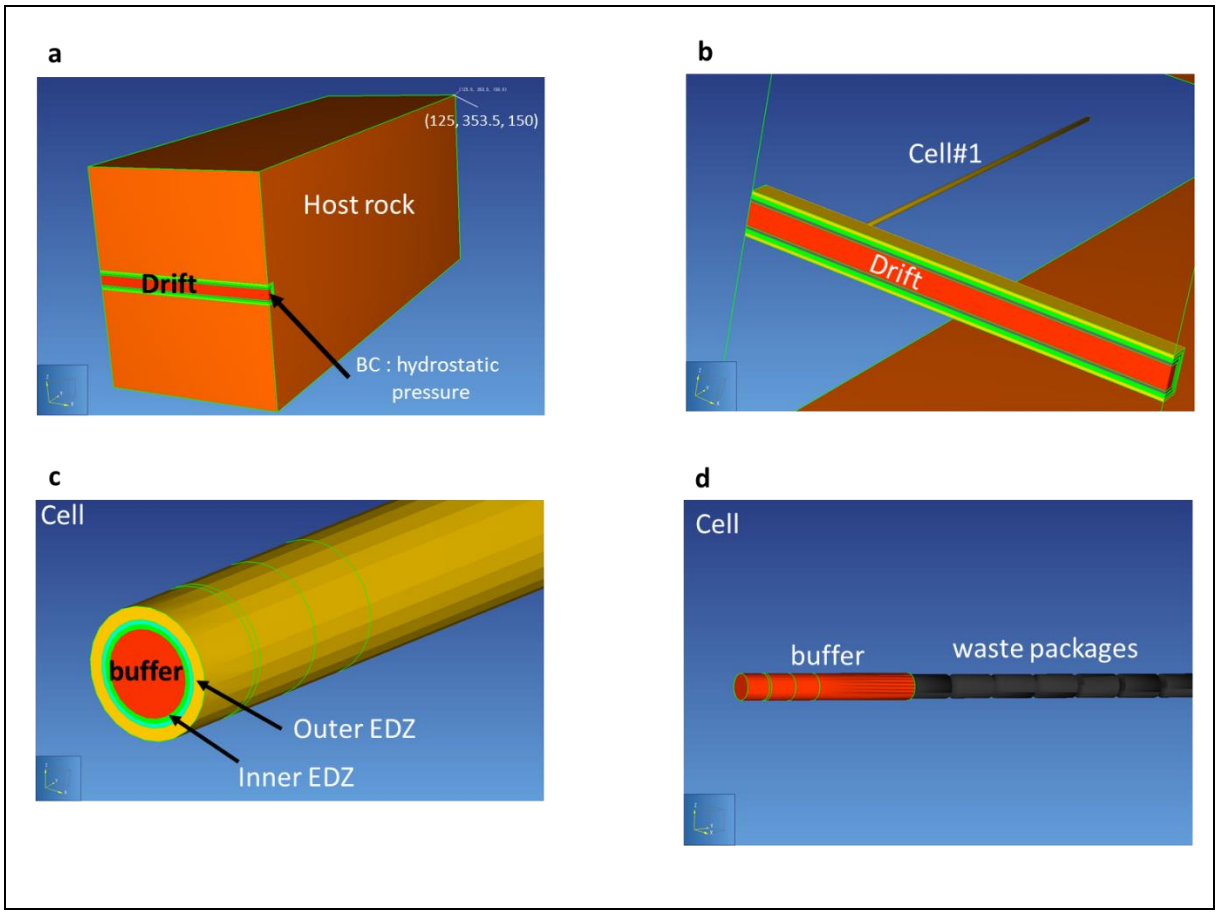

Figure 67 – (a) Studied domain; (b) Cell and drift embedded in the domain; (c) Cell geometry; (d) Buffer and HLW packages of the cell.

The performed model is based on the new fluid property module EOS5 of TOUGH (iTOUGH2 and TOUGH2-MP) including the VGM-PE model of hydraulic properties to solve the problem of non-isothermal two-phase (liquid-gas) flow and two components (water-hydrogen) transport in both liquid and gas phases in the different porous materials.

In the mass balance equation of hydrogen, production of hydrogen due to anoxic corrosion of metals is modelled as a source term. For all galleries, the hydrogen generation rate, due concrete rebars of 0.5 cm thickness, is about 21.5 mol y^{-1} m^{-1} of gallery and can last about 50 000 y (time needed to corrode thickness of 0.5 cm). For HLW waste cell in storage zone C, this rate, essentially due to the metallic liner and waste container, is about 1.9 mol y^{-1} m^{-1} of HLW cell and can last about 40 000 y. The waste form is assumed to be made of high level nuclear glass. A schematic representation of the emplacement of the different gas source terms can be found in Figure 65b and Figure 66. The H_2 source terms in the micro-tunnel are in the liner and waste containers of the cell, while those in the drift are in the concrete liners. These source terms are modelled by injection of H_2 fluxes in the inner-EDZ of the micro-tunnel (Figure 67c), and in the concrete liners of the drift (Figure 67b).

The thermal power generated by waste wells is also modelled as a source term in the heat transfer equation according to the tabulated data given in Levasseur et al. (2021) (see their table in Figure 10 for thermal power varying between 300 to 29,5 Watt/'m canister' for years between 0 and 930 years, respectively).

The model needs to specify physical, thermal, hydraulic, and hydrogen transfer properties for each porous medium as well as initial and boundary conditions. Therefore, values of the shape (*m*, *n*) and scale (α, $P_{c,e}$, $k_{0,l}$, $k_{0,g}$) parameters of the VGM-PE hydraulic properties (i.e., Eqs. (7)-(9)) as well as values of the physical, thermal, and mechanical parameters of each constitutive material of the domain (undisturbed host rock, outer and inner EDZ, bentonite, concrete, backfill), such as porosity, liquid and gas intrinsic permeability, pore compressibility and expansivity, heat conductivity, dry material specific heat, Young modulus, Poisson ratio and Biot coefficient, are those tabulated in Levasseur et al. (2021). Recall, here, that $P_{c,e}$ values are taken equal to 6.0, 4.0 and 2.0 MPa for the host rock, bentonite and outer-EDZ, respectively. For the other materials (inner-EDZ, backfill, concrete), $P_{c,e} = 0$.

The effective diffusion coefficients of water vapor and hydrogen in unsaturated porous materials $D_{\beta=l,g}^{\kappa=H_2O,H_2}$ (m²/s) are deduced from their diffusion coefficients in free liquid and gas phase $D_{0,\beta=l,g}^{\kappa=H_2O,H_2}$ (m²/s) through a proportionality constant (tortuosity factor) calculated by a modified version of Millington and Quirk (1961) formula (MQ):

(13) $$D_\beta^\kappa = D_{0,\beta}^\kappa \omega^{1+a_\beta}(S_e)^{b_\beta} \qquad \kappa = H_2O, H_2 \qquad \beta = l, g$$

with ω is the porosity; a_β and b_β are liquid (or gas) phase- and porous material- dependent parameters. As an example, host rock material: a_g = b_g = 2.5 for gaseous H_2, a_l = 1.5 and b_l = 10 for dissolved H_2; bentonite material: a_g = b_g = 3.0 for gaseous H_2, a_l = 2.5 and b_l = 15 for dissolved H_2.

Diffusion coefficients of hydrogen in free liquid and gas phases are equal to 5.0×10^{-9} and 9.0×10^{-5} m²/s, respectively, whereas those of water vapor in free liquid and gas phases are equal to 1.0×10^{-9} and 9×10^{-5} m²/s, respectively. The inverse Henry's constant of hydrogen is equal to 1.4×10^{-10} Pa^{-1}. These values are like those specified in the benchmark (Levasseur et al., 2021).

Initial conditions are such that temperature is constant equal to 20 °C and the pressure is hydrostatic between depths z = 525 m and z = 675 m before the micro-tunnel and drift excavation. Thereafter, all engineered barriers materials implemented in the micro-tunnel and the drift are initialized with a water saturation of 80 %. At top (z = 525 m) and bottom (z = 675 m) of the domain, liquid phase pressures are fixed to their hydrostatic ones, and temperatures are fixed to 23 °C and 27 °C, respectively. At all lateral boundaries, zero fluxes are considered, except at the exit of the access drift (slice plane X = 125 m) where the pressure is hydrostatic (Figure 67a).

The structured mesh used by the model is rectilinear as shown in Figure 68. The number of mesh elements is 49 x 18 x 68 = 59976, but it is reduced to 58712 once the void and packages elements of the cell are deactivated (not considered in the model). Although of this high number of elements, this mesh guarantees the orthogonality of the distance between the center of mass of any element and any surface connection of its neighbor (VORONOI approximation).

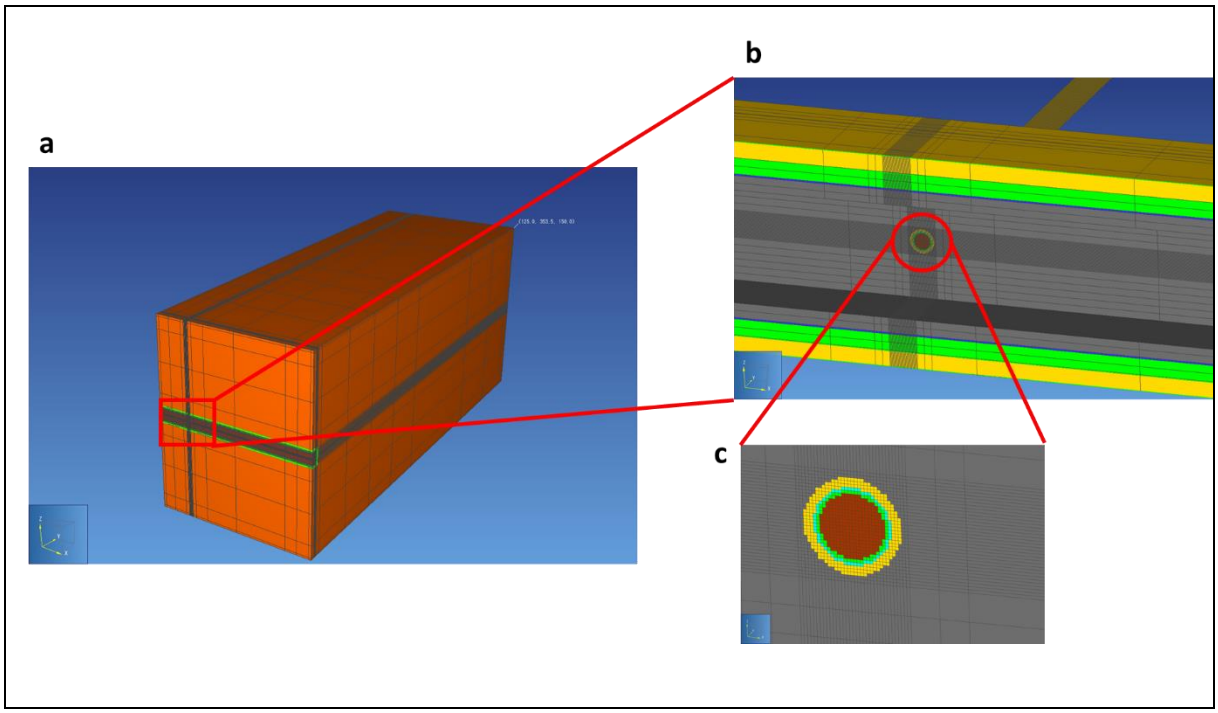

Figure 68 – (a) Structured and rectilinear mesh of the studied domain; (b) Zoom on the drift mesh; (c) Zoom on the meshed section of the micro-tunnel where the HLW cell is placed.

1.6.2 Simulated scenarios

Three scenarios#1,2,3 have been proposed depending on the deviations from the benchmark specifications:

- ✓ Scenario#1

  i) *Isothermal two-phase flow*,
  ii) *Diffusion coefficient*: the original model of Millington and Quirk (1961) for the tortuosity factor is used instead of that used in Eq. (13). The porosity and phase saturation power parameters a_β and b_β are assumed identical for any porous material type and for both liquid and gas phases, i.e., are taken equal to 1/3 and 10/3, respectively,
  iii) *Intrinsic permeability to water and gas*: assumed identical for the host rock and outer-EDZ ($k_{0,l} = k_{0,g} = k_0$),
  iv) *VGM-PE* $P_c(S_l)$: implicit $P_{c,e}$, SGM method without any linearization near full liquid saturation ($S_l = 1$).

- ✓ Scenario#2

  Idem hypotheses in S#1 but simulations are performed with a parameterization $P_{c,e} = 0$, with a linearization near full liquid saturation ($S_l = 1$).

- ✓ Scenario#3

  i) *Non-isothermal two-phase flow*,
  ii) *Diffusion coefficient*: idem S#1 (original model of Millington and Quirk (1961),
  iii) *Intrinsic permeability to water and gas*: $k_{0,l} \neq k_{0,g}$ for the host rock and outer-EDZ.
  iv) *VGM*-PE $P_c(S_l)$: explicit $P_{c,e}$ with linearization near full liquid saturation ($S_l = 1$), i.e. between $P_c(S_l = 1 - \varepsilon)$ and $P_c(S_l = 1)$, with ε is an infinitesimal value equal to 0.01 or 0.001.

N.B. Parametrization of Scenario#3 differs from that specified in the benchmark specification only by the new formulation for the diffusion coefficient that has not yet been implemented in TOUGH2.

1.6.3 Results and discussions

Simulations results obtained by Scenarios#1,2, performed by considering the buffer material of the waste cell made from backfill or bentonite were very similar. Therefore, in what follows, all scenarios will be performed with bentonite as the buffer material of the waste cell. The simulated maximum time is 100 000 years.

The purpose is to follow the time evolution of gas pressure and gas saturation in the elements' centroids (points) located in the backfilled access drift (P-C1-d in front of the cell (Cell#1) with coordinates (24.925, 0.5, 75.075) m, and P-Pd adjacent to the exit boundary with coordinates (118.375; 0.5; 75.075) m. These two elements' points are ~ 100 m apart along the x-axis of the drift, Figure 69), and around the waste cell (P-C1-EDZOUT_5, P-C1-COx_6, P-C1-COx_7, P-C1-COx_8, all located at Y = 64.125 m and Z = 74.975m, and are 0.175, 0.325, 1.025 and 9 m away from the waste canister edge (at X = 25.5 m) along the X-axis; not shown here).

Figure 70a and Figure 70b show, respectively, time-evolution of gas pressure and gas saturation in the drift at element points P-C1-d et P-Pd, simulated by scenarios#2 with parametrization $P_{c,e} = 0$. These evolutions are approximately similar for both elements points. We simulate a gas pressure build-up in the drift during the periods of hydrogen generation in both cell and drift (discontinuous lines), which later stabilizes at a maximum value of around 9.6 MPa from ~1,000 years. In parallel to this pressure build-up, the drift backfill highly desaturates (S_g increases from 0.2 to 0.47).

Simulations by scenarios#2 with $P_{c,e} \neq 0$ did not reach 100 000 years because of premature numeric divergence of the solution at time t ~ 817 y, as shown in Figure 70c and Figure 70d. This divergence occurs earlier when gas pressure becomes very high in the backfilled drift (reaches a value of ~ 20 MPa) and the latter becomes highly desaturated (S_g ~ 0.5).

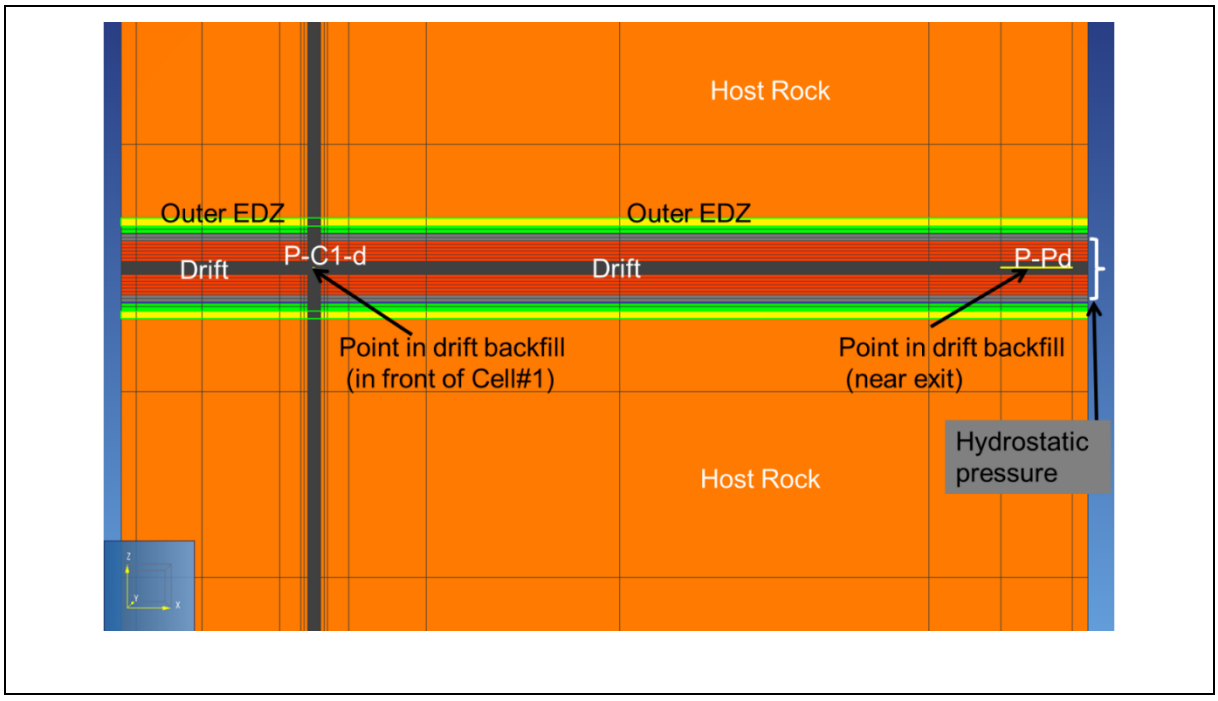

Figure 69 – Elements points in the backfilled drift P-C1-d and P-Pd where results of gas pressure and gas saturation evolutions in time are plotted.

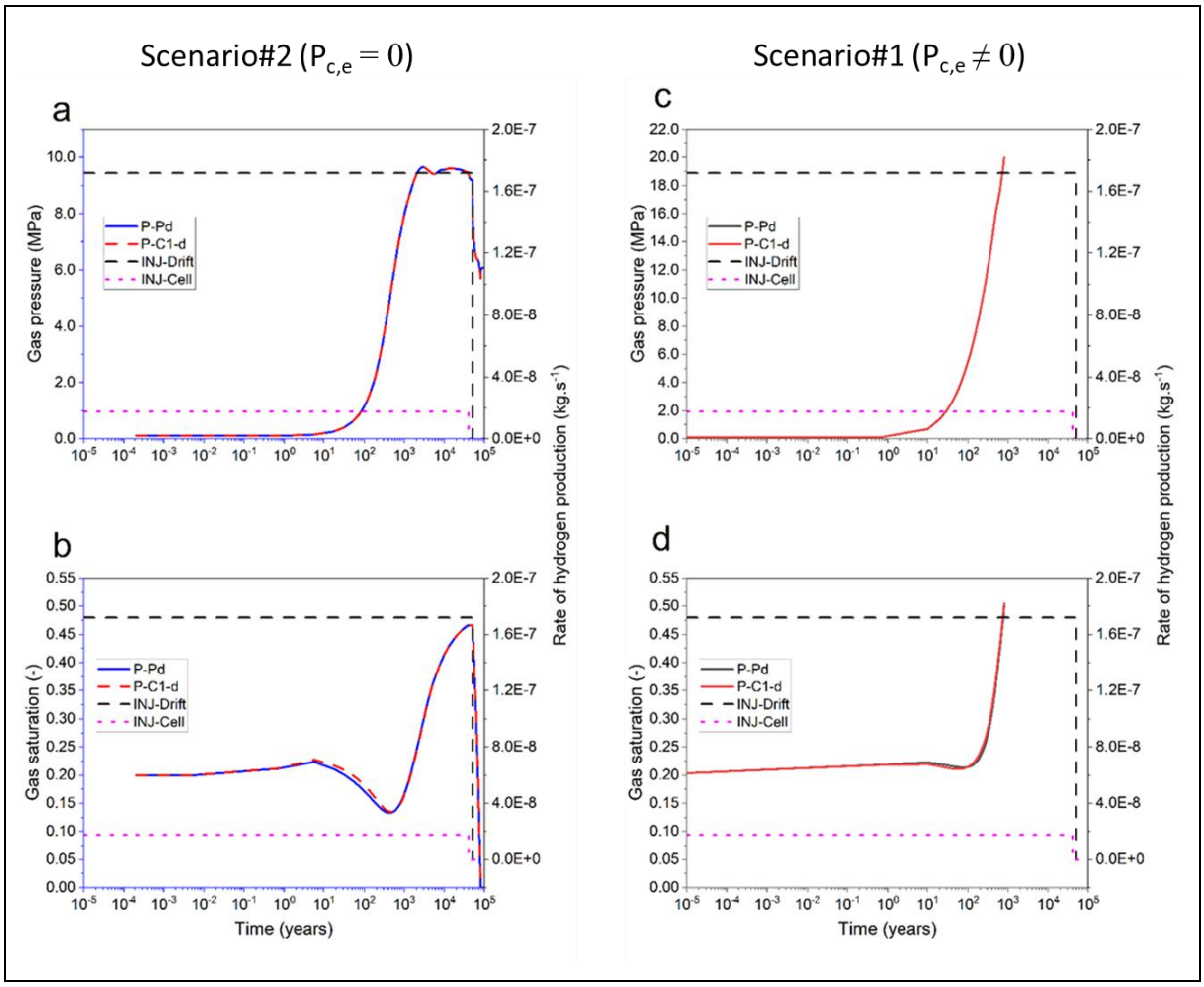

Figure 70 – (a,c) Gas pressure vs time; (b,d) Gas saturation vs time. (a,b) S#2 with $P_{c,e}$ = 0. (c,d) S#1 with $P_{c,e} \neq 0$.

Gas saturation profiles at mid-height (i.e., slice plane at depth z = 75 m) and in the whole flow domain at 817 y, shown in Figure 71a and Figure 71d, respectively, confirm well the maximum gas saturation at elements points P-C1-d and P-Pd in the drift simulated after 817 y (orange color with a gas saturation of ~ 0.5). Moreover, one can see development of an important unsaturated zone around the drift, which is much higher than that is developed around the waste cell. This zone is also characterized by high gas pressures that are more than 11 MPa around a radial surface of about 25 m from the drift center (Figure 71c). These high gas pressures are the result of the accumulation of gas due, on the one hand, to the highest $P_{c,e}$ value of the host rock compared to those of the EDZ and the engineered barriers materials, and on the other hand, to the corrosion of concrete metallic rebars in the drift in addition to that of the metallic components of the HLW cell (liner and containers).

The main reason of this divergence problem can mainly be explained by these significant pressures that can be much bigger than breakthrough and lithostatic pressures of the host rock, and which can trigger development of micro-fissures (micro-fissuring) due to pore dilation, and indeed hydraulic fracturing, that are not considered in our model. It is likely to enhance the evacuation of hydrogen masses from the drift to the host rock if such phenomena are modelled during substantial gas pressure build-up periods. Another reason could be the high pore gas velocity (not shown here), which can reach more than 10^{-5} m/s in the drift, and which may violate the validity limit of Darcy's law developed solely for low Reynolds numbers (laminar flow). Perhaps the mesh developed is not appropriate for simulating

these high gas velocities, and therefore it has to be reconstructed to avoid high gas pressure gradients in some zones of the mesh when $P_{c,e} \neq 0$.

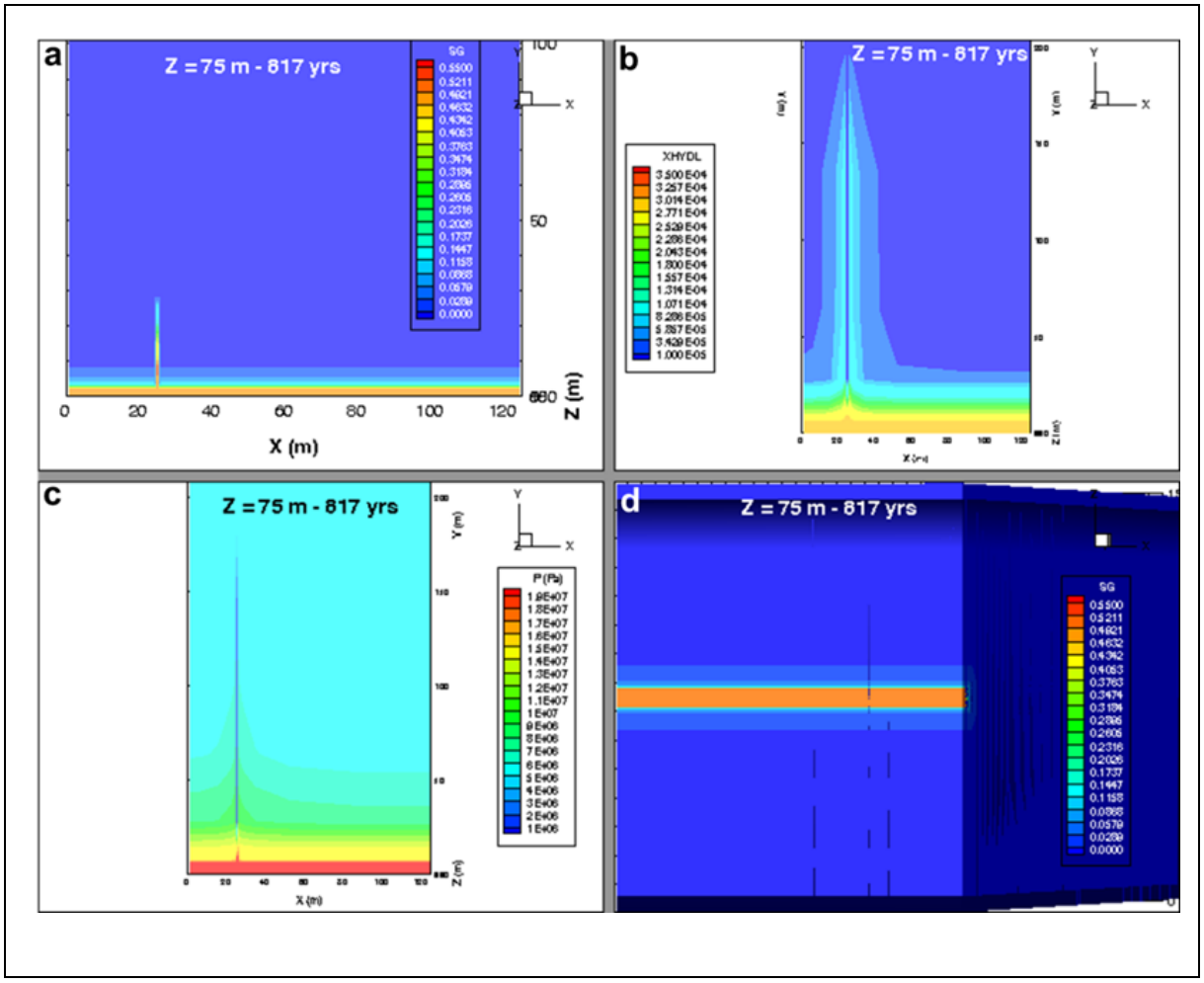

Figure 71 – Simulated profiles at down-time of ~ 817 y (Scenario#1): (a) Gas saturation at slice plane z = 75 m; (b) Dissolved H_2 mass fraction in water at slice plane z = 75 m; (c) Pressure at slice plane z = 75 m; (d) Gas saturation in the 3D domain.

The alternative proposed by scenario#3 for linearization of $P_c(S_l)$ near full saturation, as specified in the benchmark, avoids the problem of this divergence problem but at the expense of the under-estimation of maximum gas pressure within the backfilled drift. Even with this linearization, we still show the impact of $P_{c,e}$ on this maximum gas pressure as shown in Figure 72a. The maximum gas pressure increases by about 3.5 MPa, i.e., from 9.6 MPa for $P_{c,e} = 0$ parametrization to 13.1 MPa for $P_{c,e} \neq 0$ parametrization. This high increase of gas pressure is accompanied by a substantial drainage of water in the backfilled drift leading to a high gas saturation of about 0.623 (Figure 72b). Notice, however, the important decrease of gas saturation during the first 930 years (time period of the heat generated by the waste cell) in the case of $P_{c,e} \neq 0$ parametrization due to the temperature effect (Figure 72c). Notice, also, the decrease of temperature by increasing distance (along the X-axis) from the waste canister edge in the outer EDZ and host rock (Figure 72d).

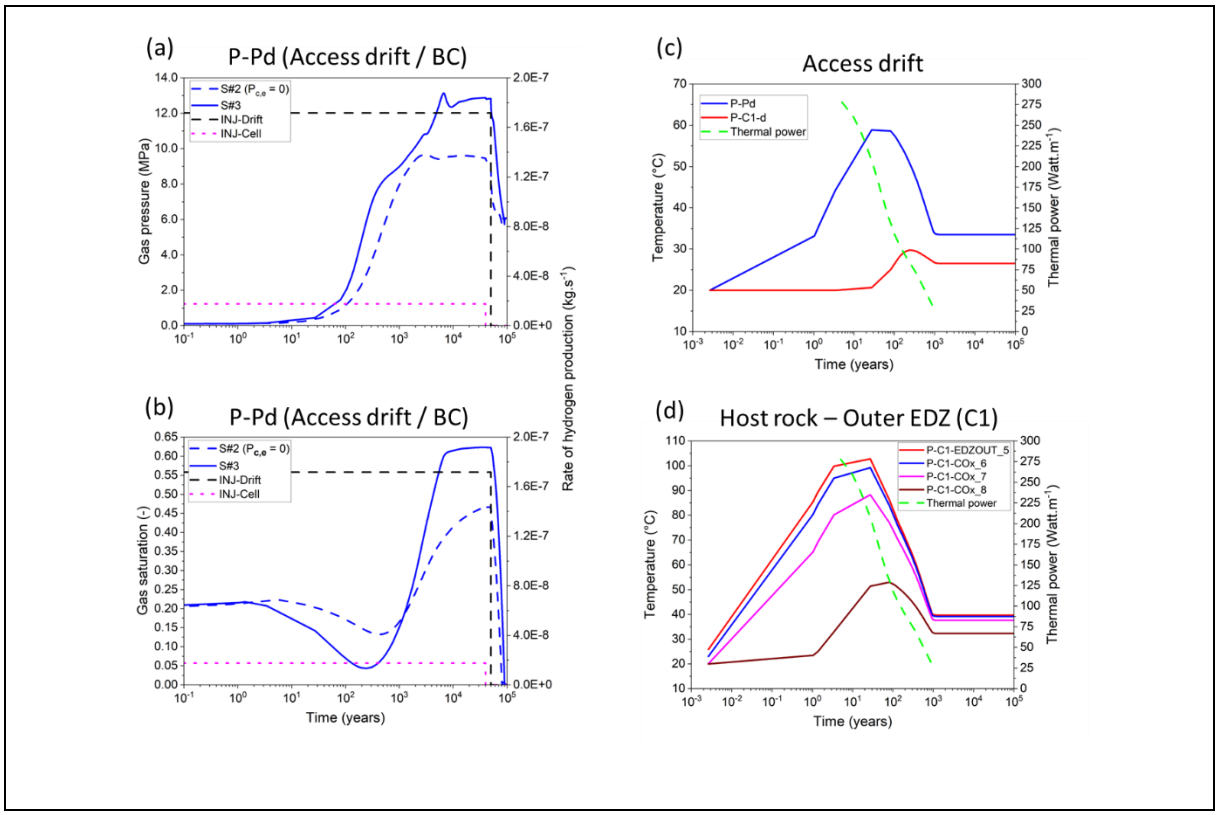

Figure 72 – Evolutions in time at element point P-Pd (Figure 69) simulated by scenarios#2,3 for: (a) Gas pressure; (b) Gas saturation. Evolutions in time of temperature simulated by scenario#3: (c) Access drift (elements points P-Pd and P-C1-d, Figure 69); (d) Host rock and Outer EDZ around the cell.

2. Hysteresis

Many studies highlighted the importance of hysteresis in unsaturated single-phase water flow (Richard's approximation). However, few studies have been performed under 2-phase liquid-gas flow conditions. The main difficulty lies on the high nonlinear nature that is added by solving the problem of gas transport within the heterogeneous structure of the porous medium and to the divergence problems that are produced during water drainage (or drying) and imbibition (or wetting) cycle.

Simulating gas migration within the repository by considering the combining effect of hysteresis and entry pressure is still a challenging task. In this study, we focus only on the study of the impact of hysteresis on two-phase flow within porous materials with a parametrization $P_{c,e} = 0$. The study of the simultaneous impact of entry pressure and hysteresis on two phase flow is beyond the scope of this work (Saâdi, 2023). The main purpose of this study is to look for the appropriate hysteretic model which is accurate for determining scanning curves of different material types, easy to implement, and which calculates less CPU times. The advantage of having such model can ease studying the hysteresis impact on the simulations at large spatial (DGR) and time (100 000 y) scales.

2.1 Comparative study between conceptual hysteretic models

2.1.1 The studied hysteretic models

Figure 73a summarises the conceptual hysteretic models for $P_c(S_l)$ commonly used in the literature and that will be tested in this study. On can distinguish 2 categories of models. The first one considers models without non-wetting (*nw*) phase entrapment: Mualem (1974) and Mualem

(1984), that are based on independent- and dependent-domain theories (IDT and DDT), and Haverkamp et al. (2002) model, which is based on a geometrical scaling approach (Parlange, 1976). The second one considers models with nw-phase entrapment: Doughty (2007), and Beriozkin & Mualem (2018) (B&M18) models which use DDT and IDT, respectively, and Parker and Lenhard (1987) model which is a modification of Scott et al. (1983) hysteresis model. Scanning curves derived from this category of models assume that relationships between the initial nw-phase saturation ($S_{nw,i}$) and the entrapped (residual) nw-phase ($S_{nw,r}^{\Delta}$) can be modelled by using a linear law or Land (1968) or Aissaoui (1983) formula.

The relative permeability to gas and water are derived from any hysteretic $P_c(S_l)$ model by using a modified version of Mualem (1976b) model (Figure 73b), by introducing effective and apparent saturations as described in Lenhard and Parker (1987).

More details on the mathematical equations describing these models can be found in Amri et al. (2023).

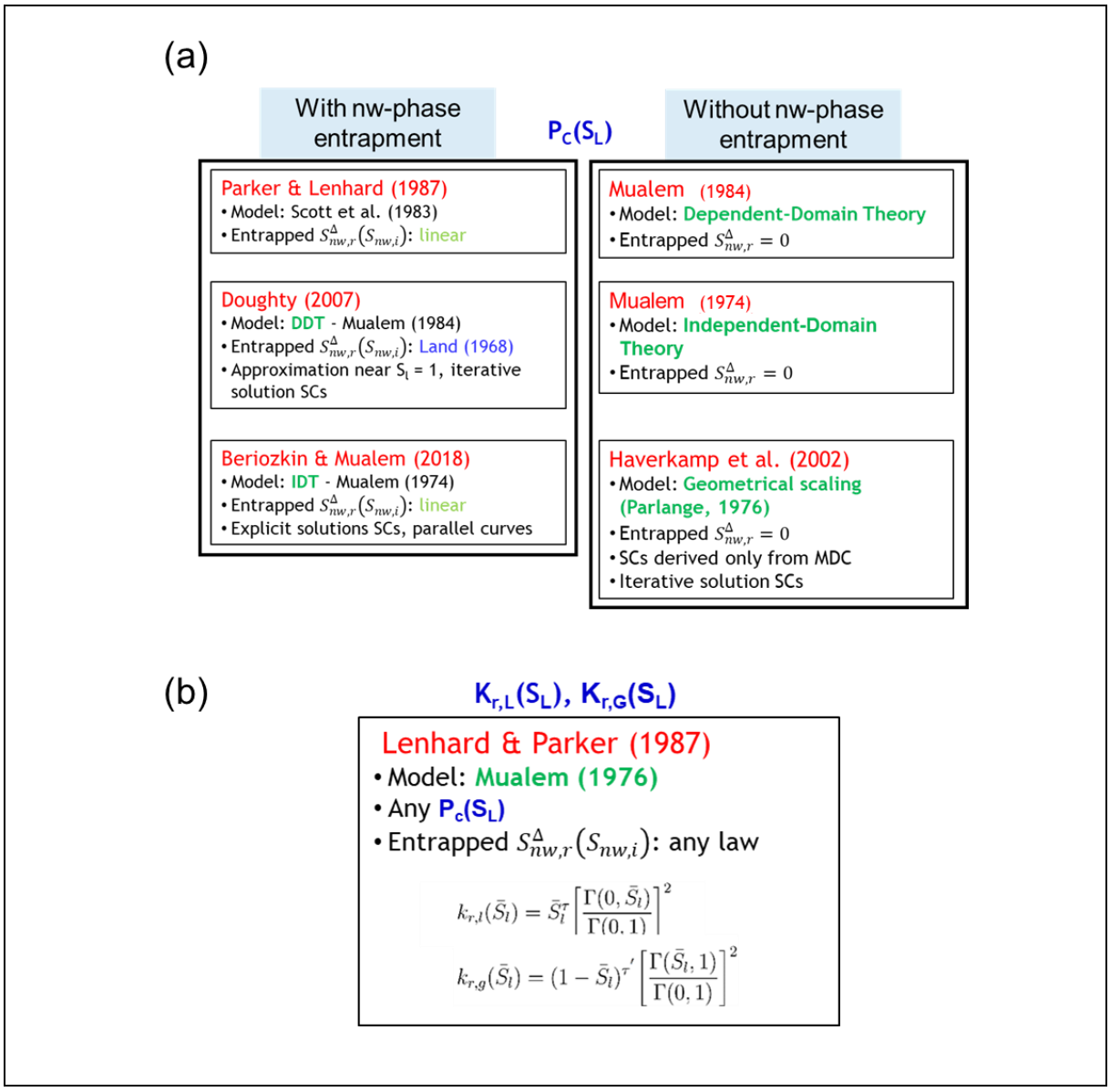

Figure 73 – (a) The five conceptual hysteretic models of capillary pressure – liquid (water) saturation ($P_c(S_l)$) studied in this work. (b) The model's relative permeability to gas and water derived from any hysteretic $P_c(S_l)$ model (Γ is the incomplete beta function).

2.1.2 Comparison between hysteretic models on different materials

The 5 models described above have been compared to experimental data of main wetting, main drying, and scanning curves of 5 materials with different textures and structures: 3 sands, a cement paste CEM I, and bentonite MX80.

Analysis of the global mean absolute error (GMAE) between measured and modelled VGM curves showed that B&M18 performed well for all the five materials and with less GMAE. Figure 74a and Figure 74b show examples of scanning curves calculated by models of Doughty (2007) and B&M18, respectively, for a compacted sand (N° 3). As one can see, B&M18 model predicts better the scanning curves from the main drying curve than Doughty (2007) model does. Moreover, B&M18 model calculates the smallest CPU time among the other models, because it does not need iterations for calculating scanning curves. Therefore, it can be suitable for simulations at large spatial and temporal scales.

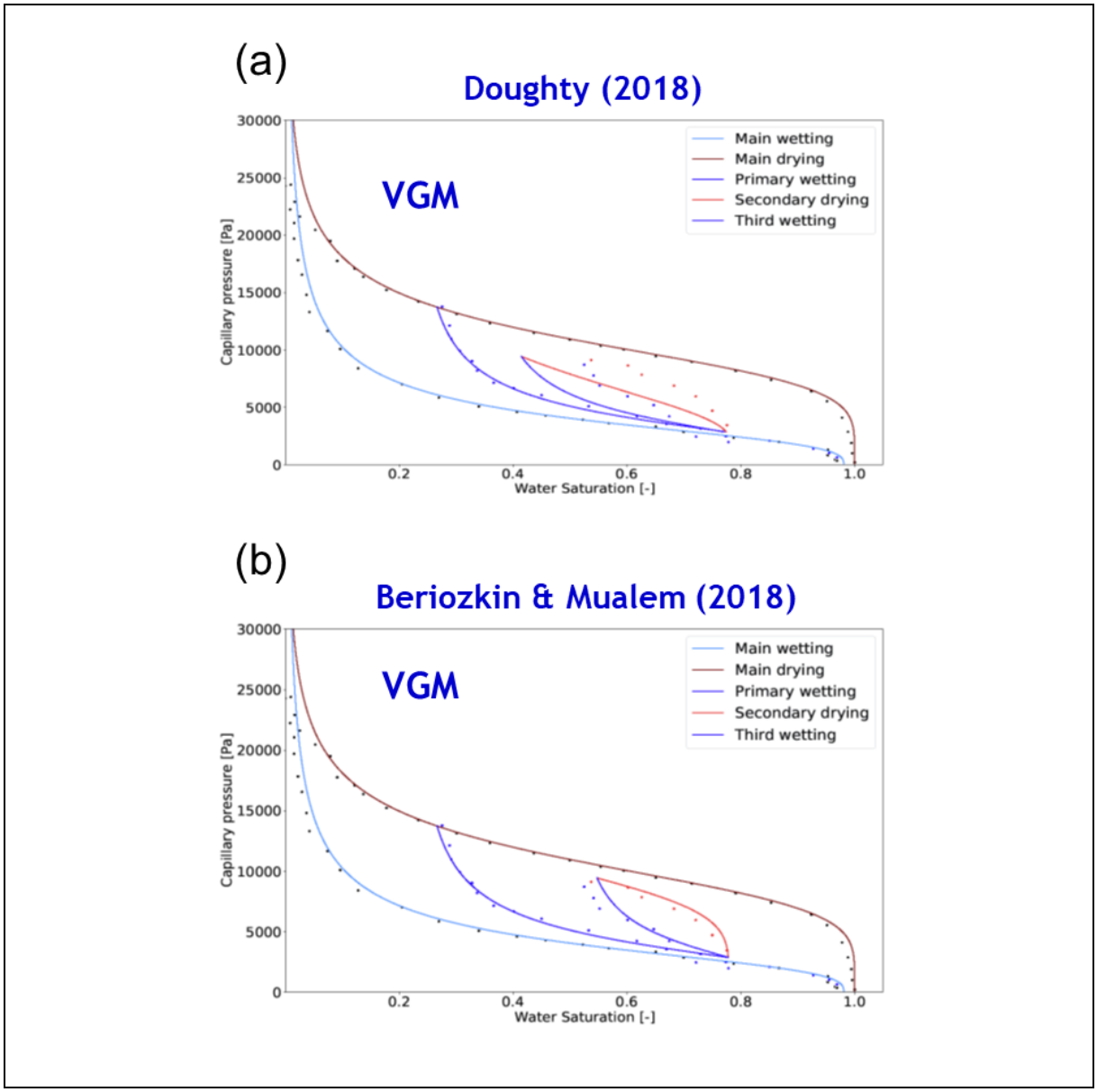

Figure 74 – Adjustment of the measured main wetting and main drying water retention curves of a compacted sand (sand N°3; Amri et al., 2023) by Van Genuchten-Mualem (VGM) $P_c(S_l)$ theoretical curves, and predictions of the measured scanning curves by two hysteretic models with gas entrapment from the main drying curve: (a) Doughty (2007); (b) Beriozkin & Mualem (2018).

2.2 Numerical modelling of a 2-phase laboratory scale experiment emulating scCO2 trapping

2.2.1 The studied experiment

The intermediate laboratory scale experiment carried out by Trevisan et al. (2014) has been chosen for the validation of the hysteresis models with gas entrapment (i.e., Doughty (2007), and Beriozkin and Mualem (2018) models). To mimic supercritical CO_2 ($scCO_2$) trapping in an aquifer, the experimental setup is shown in Figure 75a. It consists of a pulse injection of a non-wetting fluid (Soltrol-220) at a rate of 0,7 ml/s for the time interval 0 < t < 5,5 h in a sand 40/50 aquifer reservoir saturated by a wetting fluid (Glycerol-water).

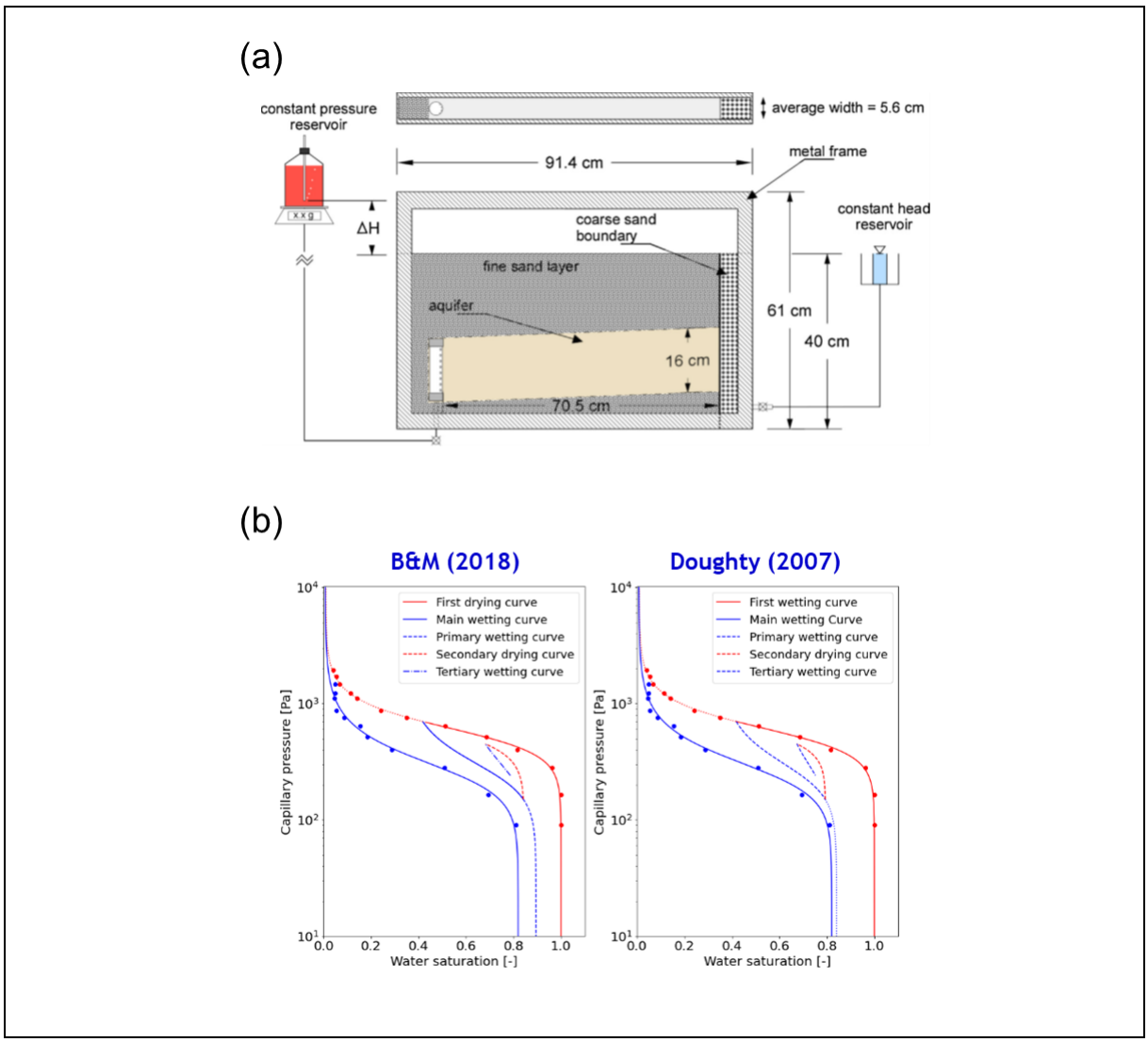

Figure 75 – (a) Experimental setup of Soltrol-220 injection in a glycerol-water saturated aquifer reservoir (from Trevisan et al., 2014). (b) Adjustment of the measured data of main wetting and main drying water retention curves of the studied aquifer sand 40/50 by Van Genuchten-Mualem (VGM) $P_c(S_l)$ theoretical curve, and estimation of scanning curves from the main drying curve by the two hysteretic models Beriozkin & Mualem (2018) (left) and Doughty (2007) (right).

2.2.2 The mathematical model

To apply the two hysteretic models of Beriozkin & Mualem (2018) and Doughty (2007) to the sand 40/50, the measured data of main wetting and main drying water retention curves of this material are fitted by Van Genuchten-Mualem (VGM) $P_c(S_l)$ theoretical curve (Figure 75b). The scanning curve calculated by each model from the same turning point on the main drying curve is different, essentially for low capillary pressures. This is essentially due to the use of different approaches for modelling the relationship $S_{nw,r}^{\Delta} = f(S_{nw,i})$ to estimate the entrapped non-wetting fluid Soltrol-220 ($S_{nw,r}^{\Delta}$) from the turning point (initial) of the non-wetting phase saturation in the main drying curve, $S_{nw,i}$. The Beriozkin & Mualem (2018) model uses a linear model, whereas Doughty (2007) model uses the formula of Land (1968).

To simulate the evolution in time of Soltrol-220 distribution within the sand reservoir during post-injection times (5,5 h < t < 15 d), both hysteresis models have been implemented in iTOUGH2/EOS10 (T2VOC).

2.2.3 Model vs experiment

Because experimental data are not entirely available from the experimental study of Trevisan et al. (2014) and the simulation study of Cihan et al. (2017), due also to missing physical parameters of the experiment, the comparison between simulated and measured spatial moments was not possible in this study. However, comparison was possible between the measured Soltrol-220 plume distribution (picture shown in Figure 76a, taken from Trevisan et al., 2014) and that is simulated using Beriozkin and Mualem (2018) (Figure 76b) during the end of the post-injection period (-15 d). The hysteresis model presents the observed migration plume better than the non-hysteretic model. Uncertainties in the input parameters may affect the simulation results, but the trends are clear enough to confirm the accuracy of the hysteretic model to represent the migration of non-wetting phase during the post-injection period.

Other simulations using the hysteresis model of Mualem (1974) showed that neglecting the non-wetting phase entrapment may affect the simulation results at larger times (Amri et al., 2023).

From the 2D simulations results, we can conclude that the hysteresis models are more accurate to predict the nonwetting plume migration during the post-injection period.

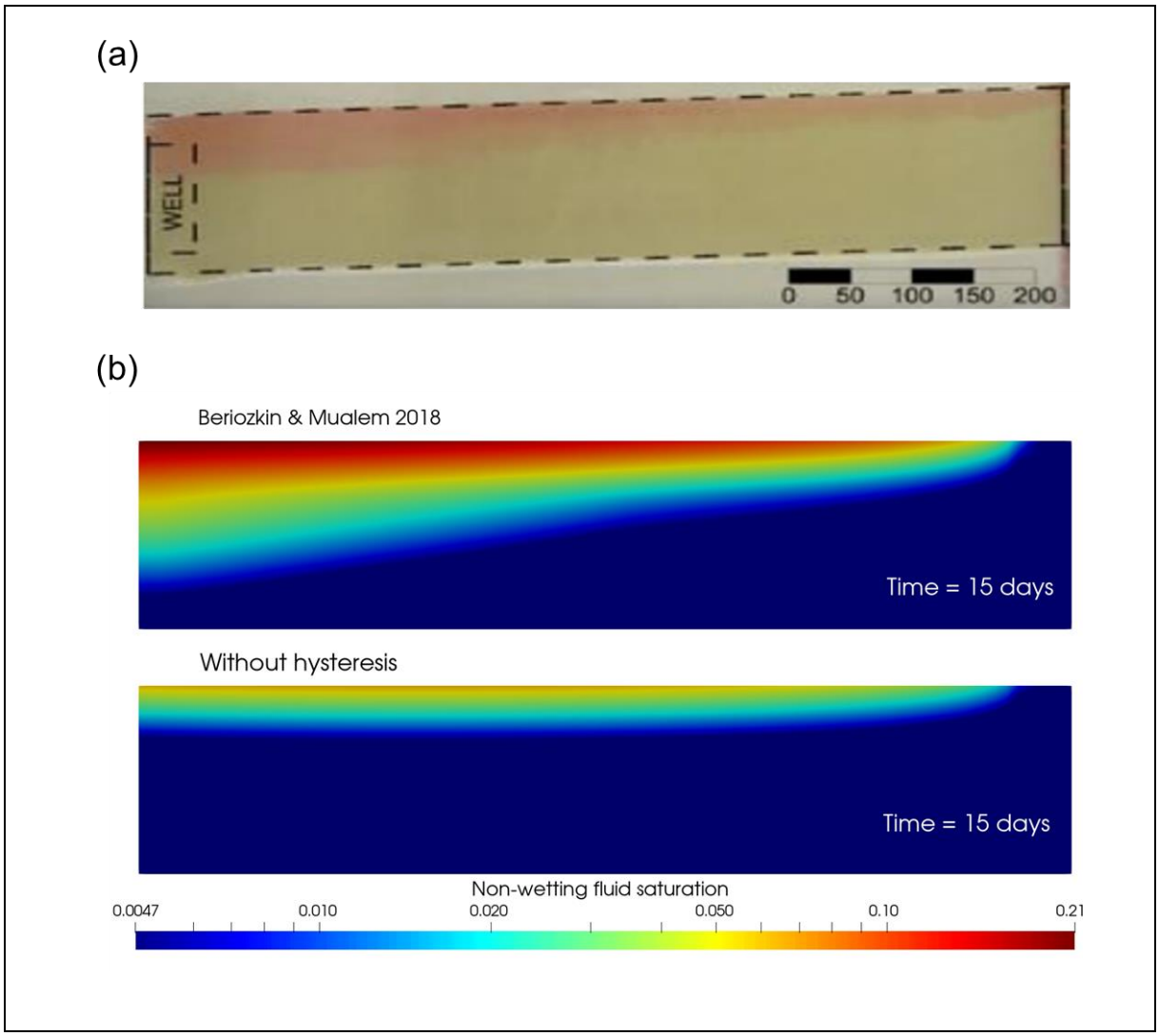

Figure 76 – Soltrol-220 distribution in the sand reservoir after 15 days from its post injection: (a) measured (from Trevisan et al., 2014); (b) simulated by the hysteresis model of Beriozkin & Mualem (2018) (above) and without hysteresis model (below).

Code source

Methods and theoretical approaches that have been developed in this study are implemented in TOUGH code which is the property of Lawrence Berkeley National Laboratory (LBNL, University of California at Berkeley, USA). These methods are published in two papers in the framework of EURAD project:

- **Gas entry pressure**: Amri A., Z. Saâdi, R. Ababou, Parametric sensitivity to gas-entry pressure in two-phase flow models for a deep geologic repository of radioactive waste. Transp Porous Med 145: 13–43, 2022 https://doi.org/10.1007/s11242-022-01780-w

- **Hysteresis**: Amri A., Z. Saâdi, R. Ababou, Modeling two-phase flow with hysteresis: comparative study of hysteresis models and application. Rock Mechanics and Rock Engineering (2023) https://doi.org/10.1007/s00603-023-03501-1

References

Ahusborde, E., Amaziane, B., Baksay, A., Bátor, G., Becker, D., Bednár, A., Béreš, M., Blaheta, R., Böhti, Z., Bracke, G. , Brazda, L., Brendler, V., Brenner, K. Březina, J., Cancès, C., Chainais-Hillairet, C. , Chave, F. , Claret, F., Domesová, S., Havlova, V., Hokr, M., Horák, D., Jacques, D., Jankovsky, F. Kazymyrenko, C., Kolditz, O., Koudelka, T., Kovács, T., Krejci, T., Kruis, J., Laloy, E., Landa, J., Lipping, T., Lukin, D., Mašin, D., Masson, R., Meeussen, J.C.L, Mollaali, M., Mon, A., Montenegro, L., Montoya, V., Pepin, G., Poonoosamy, J., Prasianakis, N., Saâdi, Z., Samper, J., Scaringi,G., Sochala, P., Tournassat, C., Yoshioka, K., Yuankai, Y. (2021): State Of the Art Report in the fields of numerical analysis and scientific computing. Final version as of 16/02/2020 of deliverable D4.1 of the HORIZON 2020 project EURAD. EC Grant agreement no: 847593. https://hal.archives-ouvertes.fr/hal-03165686

Aissaoui A. (1983) : Etude théorique et expérimentale de l'hystérésis des pressions capillaires et des perméabilités relatives en vue du stockage souterrain de gaz. Thèse de doctorat, École des Mines de Paris, Paris, France, 1983.

Amri A., Z. Saâdi, R. Ababou, 2023. Modeling two-phase flow with hysteresis: comparative study of hysteresis models and application. Rock Mechanics and Rock Engineering https://doi.org/10.1007/s00603-023-03501-1

Amri A., Z. Saâdi, R. Ababou, 2022. Parametric sensitivity to gas-entry pressure in two-phase flow models for a deep geologic repository of radioactive waste. Transp. Porous Med. 145: 13–43. https://doi.org/10.1007/s11242-022-01780-w

Amri A. (2021): A revisited hydrogen transfer model for the study of hydraulics-gas transient in a deep geological disposal facility. PhD Thesis, Toulouse University, Institut National Polytechnique de Toulouse (INP Toulouse), 213p.

Andra (2005) : Evaluation de la faisabilité du stockage géologique en formation argileuse. Dossier 2005 Argile, https://www.andra.fr/sites/default/files/2017-12/266.pdf

Battistelli, A., D. Swenson, A. Alcott, 2017. Improved petrasim-tough2 capabilities for the simulation of geothermal reservoirs. In: Proc of 42nd workshop on geothermal reservoir engineering, Stanford, California (USA).

Beriozkin, A., Y. Mualem, 2018.Comparative analysis of the apparent saturation hysteresis approach and the domain theory of hysteresis in respect of prediction of scanning curves and air entrapment, Adv. Water Resour. 115: 253-263. https://doi.org/10.1016/j.advwatres.2018.01.016

Brooks, R.H., A.T., Corey (1964): hydraulic properties of porous media, Hydrology Paper, Fort Collins, Colorado State University.

De La Vaissière, R., 2011. Interpretation of in-situ gas experiment PGZ1. FORGE Report D5.9, 70 pp.

Doughty, C., 2013. User's Guide for Hysteretic Capillary Pressure and Relative Permeability Functions in TOUGH2, Report LBNL-6533E, Lawrence Berkeley National Laboratory, Berkeley, Calif., March 2013.

Doughty, C., 2007, Modeling geologic storage of carbon dioxide: Comparison of non-hysteretic and hysteretic characteristic curves. Energy Convers. Manage. 48: 1768–1781.

Finsterle, S., 2016. Enhancements to the TOUGH2 Simulator Integrated in iTOUGH2, Report LBNL-7016E, Lawrence Berkeley National Laboratory, Berkeley, Calif., 2016.

Finsterle, S., 2007. iTOUGH2 User's Guide. LBNL-40040, Earth Sciences Division, Lawrence Berkeley National Laboratory, University of California, Berkeley, CA 94720, February 2007.

Hadka, D., Moea framework: a free and open source java framework for multiobjective optimization (2012).

Haverkamp, R., Reggiani, P., Ross P.J., Parlange, J.Y., 2002. Soil water hysteresis prediction model based on theory and geometric scaling. In: Raats PAC, Smiles D, Warrick A (eds) Environmental mechanics: Water, mass and energy transfer in the biosphere. Geophysical Monograph 129. American Geophysical Union, Washington, DC, pp 213–246.

Ippisch, O., H.-J. Vogel, P. Bastian, 2006. Validity limits for the van Genuchten–Mualem model and implications for parameter estimation and numerical simulation. Adv. Water Resour. 29(12): 1780-1789.

Land, C.S., 1968. Calculation of imbibition relative permeability for two-and three-phase flow from rock properties. Society of Petroleum Engineers Journal, 8(2): 149-156.

Lenhard R., J. Parker, 1987. A model for hysteretic constitutive relations governing multiphase flow: 2. Permeability-saturation relations. Water Resour. Res., 23(12): 2197- 2206.

Levasseur S., Collin F., Daniels K., Dymitrowska M., Harrington J., Jacops E., Kolditz O., Marschall P., Norris S., Sillen X., Talandier J., Truche L., Wendling J. (2021): Initial State of the Art on Gas Transport in Clayey Materials. Deliverable D6.1 of the HORIZON 2020 project EURAD, Work Package Gas. EC Grant agreement no: 847593.

Marschall P, Horseman ST, Gimmi T., 2005. Characterisation of gas transport properties of the Opalinus Clay, a potential host rock formation for radioactive waste disposal in Oil & Gas Science and Technology. Revue de l'Institut Français du Pétrole. 60: 121–139. https://doi.org/10.2516/ogst:2005008

Mualem, Y., 1984. A modified dependent-domain theory of hysteresis. J. Soil Sci. 137(5): 283-291. https://doi.org/10.1097/00010694-198405000-00001

Mualem, Y., 1976a. A new model for predicting the hydraulic conductivity of unsaturated porous media. Water Resour. Res., 12(3): 513-522. https://doi.org/10.1029/WR012i003p00513

Mualem, Y., 1976b. Hysteretical models for prediction of the hydraulic conductivity of unsaturated porous media. Water Resour. Res. 12(6): 1248-1254. https://doi.org/10.1029/WR012i006p01248

Mualem, Y., 1974. A Conceptual Model of Hysteresis. Water Resour. Res. 10(3): 514-520. https://doi.org/10.1029/WR010i003p00514

Parker, J., R. Lenhard, T. Kuppusamy, 1987. A parametric model for constitutive properties governing multiphase flow in porous media. Water Resour. Res. 23(4): 618–624.

Parker J.C., R.J. Lenhard, 1987. A model for hysteretic constitutive relations governing multiphase flow, 1. Saturation-pressure relations. Water Resour. Res. 23(12): 2187-96.

Parlange, J.-Y., 1976. Capillary hysteresis and the relationship between drying and wetting curves. Water Resour. Res. 12(2): 224-228.

Pruess, K., Oldenburg, C., Moridis, G.J. (2011): TOUGH2 User's Guide, Version 2.1. Report LBNL-43134 (revised), Lawrence Berkeley National Laboratory, Berkeley, California, USA, 197 p.

Pruess K., C. Oldenburg, G. Moridis (1999): TOUGH2 User's Guide, Version 2.0. LBNL-43134, Lawrence Berkeley National Laboratory, Berkeley, California, USA, 197 p.

Saâdi, Z., M. Dymitrowska, F. Deleruyelle, F. Marsal, 2020. An evaluation model of the impact of hydrogen 'piston effect' on water displacement in a deep geological disposal of radioactive waste. Environ. Earth Sci. 79:434 https://doi.org/10.1007/s12665-020-09166-1

Saâdi, Z., 2023. A numerical study of the simultaneous impact of entry pressure and hysteresis on two-phase flow in porous media for the evaluation of gas migration in a high-level waste cell of a deep geological repository. TOUGH symposium 2023, Oral presentation, 18-20 September 2023, Lawrence Berkeley National Laboratory, Berkeley, California.

Scott, P.S., Farquhar G.J., Kouwen N. (1983) Hysteretic effects on net infiltration. Advances in Infiltration. In: Proc. Natl. Conf. on Advances in Infiltration, Chicago, IL, Dec. 12-13, 1983, pp. 163–170

Trevisan, L., Cihan, A., Fagerlund, F., Agartan, E., Mori, H., Birkholzer, J.T., Zhou, Q., Illangasekare, T.H., 2014. Investigation of mechanisms of supercritical CO_2 trapping in deep saline reservoirs using surrogate fluids at ambient laboratory conditions. International Journal of Greenhouse Gas Control 29: 35–49. https://doi.org/10.1016/j.ijggc.2014.07.012

Twarakavi, N. K., H. Saito, J. Šimunek, M. T. van Genuchten, 2008. A new approach to estimate soil hydraulic parameters using only soil water retention data. Soil Sci. Soc. Am. J. 72(2): 471–479.760.

Van Genuchten, M. Th., F. J. Leij, S. R. Yates, 1991. The RETC Code for Quantifying the Hydraulic Functions of Unsaturated Soils. Report EPA/600/2-91/065, R. S. Kerr Environ. Res. Laboratory, US Environmental Protection Energy, Ada, Oklahoma; p. 85, December 1991.

Van Genuchten, M. Th., 1980. A closed form equation for predicting the hydraulic conductivity of unsaturated soils. Soil Sci. Soc. Am. J., 44:892–898, 1980.

Vogel, T., M. Th., van Genuchten, M., Cislerova, 2001. Effect of the shape of the soil hydraulic functions near saturation on variably-saturated flow predictions. Adv. Water Resour. 24: 133–44.

Wei, C., M.M. Dewoolkar, 2006. Formulation of capillary hysteresis with internal state variables. Water Resour. Res. 42, w07405, 2006. https://doi.org/10.1029/2005wr004594

Zhang K., Y.-S. Wu, K. Pruess (2008): User's Guide for TOUGH2-MP — A Massively Parallel Version of the TOUGH2 Code. LBNL-315E, Lawrence Berkeley National Laboratory, University of California, Berkeley, CA 94720.

Acceleration of numerical calculations for multiphysics couplings and high performance computing

[1]Prasianakis N.I., [1]Mokos A., [1,3]Mahrous M., [1]Pfingsten W., [2]Poonoosamy J., [1,3]Churakov S.V.

[1]Laboratory for Waste Management (LES), Villigen PSI, Paul Scherrer Institute, Switzerland

[2]Institute of Energy and Climate Research, Nuclear Waste Management (IEK-6), Forschungszentrum Juelich, Germany

[3]University of Bern, Institute of Geological Sciences, Bern, Switzerland

The project leading to this application has received funding from the European Union's Horizon 2020 research and innovation programme under grant agreement No 847593.

Abstract

The processes which will take place in the nuclear waste repositories are of multiscale nature and span a timeframe of several thousands of years. Reactive transport modelling supports the understanding of the involved phenomena, and allows to make assessments relevant to the evolution, the design and optimization of the repository. In this project, the performance of the codes which couple complex chemistry with porous media flow has been drastically improved. In such simulations, the geochemical solver consumes most of the computational effort. To accelerate the simulations, surrogate models for chemical systems have been created using machine learning and neural networks. The surrogate models resulted in an acceleration of the geochemical calculations by two to three orders of magnitude. The surrogate models have been coupled to a pore-level lattice Boltzmann solver. The methodology was tested in several setups including the evolution of porosity and its effect on diffusivity / permeability of clay at cement-clay interface. For that, the precipitation of minerals within clays in realistic geometries, at different geochemical contrasts is modelled. In the next step, a variable time-step method has been developed and tested in microfluidic experiments where oscillatory zoning of mineral precipitation is observed. The method was based on the clear separation time scales for the diffusion, reaction and mineral growth. A final step in accelerating the calculations was conducted by implementing the surrogate neural network models in a C/Cuda lattice Boltzmann code capable of performing parallel GPU computations at hybrid CPU/GPU supercomputing units like the Swiss Supercomputing Center (CSCS). With the code porting to supercomputing architecture it has been possible to achieve an unprecedented calculations efficiency of more than one billion computational grid point update per second. Finally, a web-based collaborative platform (geoml.eu) has been created to facilitate code development and information exchange across EURAD.

Significance Statement

The multiphysics processes which will take place in the nuclear waste repositories are of multiscale nature and span a timeframe of several thousands of years. Reactive transport modelling supports the understanding of the involved phenomena, and allows to make assessments relevant to the evolution, the design and optimization of the repository. Performing such multiphysics (flow, heat, chemistry, mechanics) simulations at high resolution and for a long period of time is computationally prohibitive. Furthermore, for process understanding and design optimization of the waste repositories a large number of such simulations are needed. This work provides a framework for accelerating reactive transport calculations by several orders of magnitude. For that, machine learning (neural networks) techniques proved to be the key to accelerate the calculations without loss of accuracy. Additionally, modified algorithms and the parallelization of the code to be able to run in supercomputing clusters provides an overall acceleration of several orders of magnitude paving the way to efficient high resolution multiphysics simulations. This speed up, allows to explore at a faster pace the dynamics of the systems of interest, relevant to nuclear waste management, and even perform simulations which were previously considered impossible due to the high computational cost. Finally, a prototype web-based collaborative platform (geoml.eu) has been created to facilitate code development, information exchange across EURAD and dissemination of results to the general public.

Table of content

List of figures

List of Tables

1. Machine learning and hardware acceleration of coupled reactive transport calculations.

1.1 Computational needs of coupled reactive transport pore-level simulations

The processes which take place in the nuclear waste repository are of multiscale nature (Churakov and Prasianakis, 2018) and span a timeframe of several thousands of years. Model based simulations of repository evolution provides insight into understanding of the repository evolution mechanisms, the long term performance of repository systems and the means for assessing design optimization. In a typical reactive transport simulation, a flow solver is coupled with a geochemical solver. The flow solver is responsible for the solution of the differential equations, which describe the advection and diffusion of the chemical species. At the same time, the geochemical solver provides the solution of the geochemical reactions taking into account the number of chemical species and their thermodynamic properties. Two established geochemical codes for coupled transport problems relevant to nuclear waste management are the PHREEQC (Parkhurst and Appelo, 2013) and GEMS (Kulik et al., 2013). The geochemical computations are executed at each grid point of the discretized computational domain and at every time step of the solution. For a typical simulation the number of grid points exceeds 1 million (10^6), while for more detailed simulations the number of grid points might be of the order of 1 billion (10^9). The number of time-steps of a simulation highly depends on the problem at hand, and typically lies in the range of 10^4-10^6 time steps. High resolution computations correspond for example to pore-scale simulations using as input a direct X-ray tomogram, and due to the high computational effort, they can be calculated at high performance computing clusters in parallel CPU architecture, or in parallel hybrid CPU/GPU architectures (GPU: Graphics Processing units).

A rough estimate of the number of geochemical calculations per simulation may be provided, to be in the range of 10^{10}-10^{15} depending on the system complexity. For the pore-level lattice Boltzmann simulators investigated here, the geochemical calculations accounts for 99.9% of the total computational effort, with the flow being only 0.1% as seen in *Figure 77* (left). It is then evident that a significant acceleration of the overall code is expected once the geochemical solver is accelerated. Moreover, with a typical performance of a geochemical code being at 10^3 calculations per second, the heaviest of the aforementioned cases would require 10^{12} seconds to complete or ~10^4 years, if run on a single CPU core, which is absolutely prohibitive.

1.2 Geochemical solver acceleration in reactive transport coupled processes using machine learning

A methodology which has been explored already in the past in the field of reactive transport relevant to combustion, is to replace the chemical solver during the simulation with a surrogate model based on artificial neural networks (Christo et al., 1996). While this was tried in the past it has not been established as a methodology mainly due to the difficulty in training efficient neural networks and of the resulting accuracy. In the next decades, computer technology and algorithms have advanced at a stage where now it is possible to use open source software for the training of several machine learning models of very high accuracy. Such data-driven approaches have started emerging also in the field of geochemical reactive transport (De Lucia et al., 2017; Jatnieks et al., 2016; Laloy and Jacques, 2019, 2022; Leal et al., 2020; Nikolaos I Prasianakis et al., 2020) and have been also investigated by several teams within EURAD-DONUT in the realms of the geochemistry and machine learning benchmark exercise. Conceptually, the machine learning based acceleration is depicted in *Figure 77* (right), for the example of neural networks.

The typical workflow requires that a sufficient training dataset is produced using the geochemical solver, This dataset should covers the range of expected variation of the variables relevant for the system evolution (e.g. concentrations of species). After sufficient training, the resulting mathematical model

(neural network) is tested for its accuracy using a different test dataset. The accuracy of the model is a crucial aspect, since even small errors might accumulate or propagate during the simulation, and result in large deviations. Such models have been trained in (Nikolaos I Prasianakis et al., 2020) where it has also been demonstrated that with sufficient training the predictions of the full solver and the machine learning assisted solver are practically indistinguishable. However, the latter being two to three orders of magnitude faster. It has been concluded that at least for low complexity chemical systems the computational efficiency is drastically improved by two to three orders of magnitude. The production of efficient chemistry surrogate models is always a trade-off between the resulting accuracy and the effort spent in training the models.

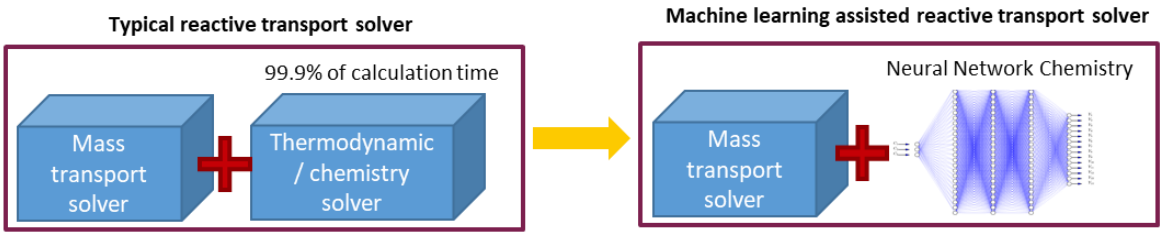

Figure 77 – In a typical lattice Boltzmann pore-level reactive transport simulation, the chemical solver accounts for 99.9% of the overall computational cost. If the chemical solver is replaced by a neural network computational overhead related to chemistry is removed and result in an acceleration of calculations between 2-3 orders of magnitude.

An example of such a surrogate model in shown in *Figure 78* (left) with two-dimensional input and nine-dimensional output. In *Figure 78* (right), the predictions of the model versus the geochemical solver results are plotted for the aqueous concentration of SiO_2 for the range of the input variables. The specific network shown here was trained, validated and tested using a sample of 90'000 pre-calculated geochemical calculations. The samples were lying on a cartesian equidistant grid. Using more advanced sampling techniques can potentially provide equivalent results with a smaller number of samples. Overfitting was avoided as was seen from the validation and test curves as well as from the smoothness of the resulting manifolds. The hyperparameters of the network were selected after a few implementations by selecting the best performing combination that balanced accuracy versus cost of training (e.g. number of hidden layers, number of neurons, activation function) Metrics of accuracy include the mean square error and the mean absolute percentage error. We note by passing that the overall time needed to create the sampling dataset, the training, and the validation of the neural network model can be automated. For the case presented here this cycle can be completed in a small fraction of time compared to the time which would be needed for the same simulation using a typical reactive transport and geochemical solver coupling. For more complex simulations which can include also a sensitivity analysis on parameters other than the chemical system parameters, the gains in time and feasibility are much larger. The same trained model can be used only for simulations which can be described by the specific chemical system. In case of change of the chemical system or model, a retraining is needed. If the change in the chemical system is small, transfer learning techniques can be applied which reduce significantly the training time.

This model has been used for reactive transport simulations to resolve the mineralogical reactions occurring at cement-clay interfaces relevant to geological disposal. Of interest is to understand how the transport properties of cement and clay are altered due to mineral dissolution and precipitation, which alters the pore-space topology in a non-linear way. The precipitation of CSH phases (Kulik, 2011) when cementitious pore water solution reacts within the clay environment has been studied. Due to precipitation the clay microstructure is altered affecting the mass transport pathways. The evolved microstructures have been further subjected to a diffusion test to measure the evolved transport properties.

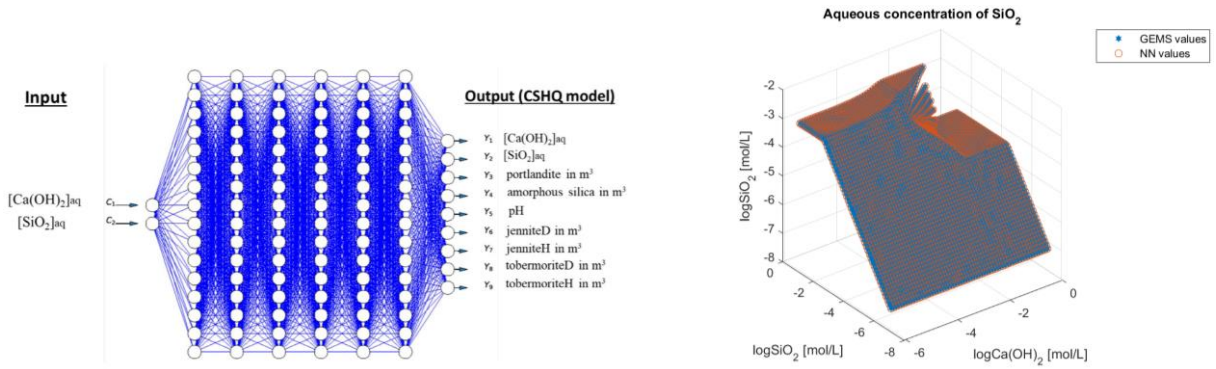

Figure 78 – (left) A neural network model used for reactive transport simulations relevant to cement-clay interaction in a nuclear waste repository. Input is the species concentrations in solution and the output is the thermodynamic equilibrium of the CSH phases and the resulting aqueous species. (right) Graphical representation of the comparison of the neural network values (NN values, red circles) Vs the geochemical solver values (GEMS, blue stars). The two manifolds practically overlap.

A 2D conceptual clay geometry has been used for the preliminary simulations as shown in *Figure 79* (left). From the left boundary of the clay geometry a cementitious pore-water rich in $Ca(OH)_2$ is entering the domain. The clay pore water is rich in SiO_2 and the occurring chemical reactions result in the precipitation of CSH solid solution phases. In *Figure 79* (right) the percentage of the volume occupancy be freshly formed CSH precipitates is plotted. Depending on the local geochemical conditions a different phase assemblage can be observed. In *Figure 80* the frequency of the CSH phases across the computational domain is plotted. It is noted that the different CSH phases are also described by nano-porosity through which diffusive mass transport continues to take place. During the diffusion test this sub-grid nano-porosity is also taken into account in order to evaluate the change in effective diffusivity.

A relevant publication describing the methodology and the major results is currently finalized.

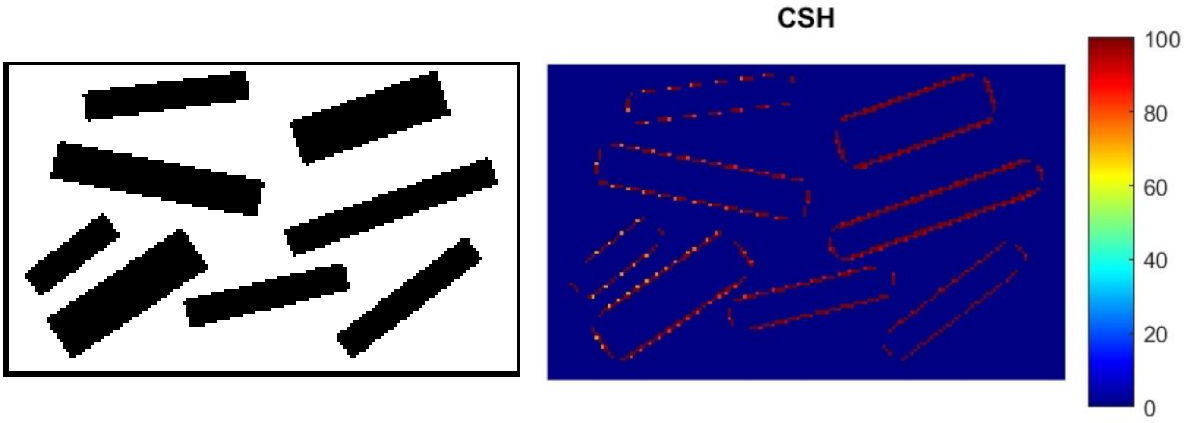

Figure 79 – (left) a 2D conceptual clay structure, with black being the clay particles and white the pore space. (right) precipitate growth on the clay surfaces due to reaction between clay pore water containing SiO_2 and cementitious pore water containing $Ca(OH)_2$. Colour represents the percentage of volume occupancy of the CSH phases at each voxel with 100% meaning that the computational voxel is not any more part of the free pore space.

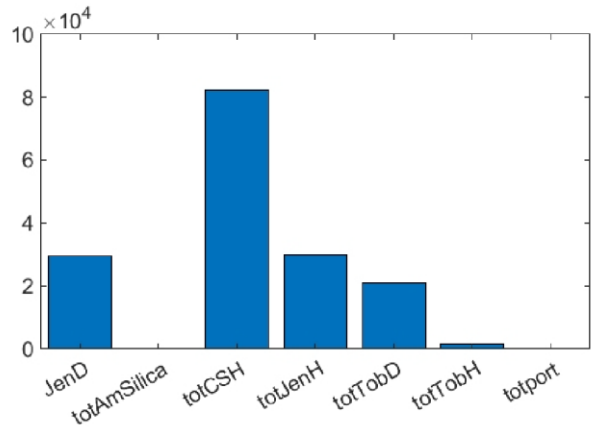

Figure 80 – Phase assemblage of the total CSH precipitates (totCSH) across the computational domain, with the following end members: two jennite-like end members JenD and JenH, and two tobermorite-like end members TobD and TobH according to (Kulik, 2011)*. The frequency of each phase along the domain is plotted.*

1.3 Multivariable time-stepping for modelling diagnostics

Another technique which was investigated to accelerate the calculations was the multivariate time-stepping. The technique is based on the separation of scales between advection, diffusion, reaction kinetics. In various systems, the system evolution is limited by reaction kinetics, so that the concentration field is typically reaching a steady state at the computational domain of interest quickly. By taking advantage of this physical time-scale separation it is possible to accelerate the numerical simulations by dynamically adjusting the simulation time-step. This allowed to simulate and model the experiments of (Poonoosamy et al., 2021) conducted within the WP-Future. A lab-on-a-chip experiment was designed to unravel the solid solution formation in tightly confined media and more specific to understand the (Ba,Sr)SO_4 oscillatory zoning. In a specific setup $SrCl_2$ and $BaCl_2$ was injected from one side of the microfluidic chip while Na_2SO_4 was injected from the opposite direction as shown in *Figure 81* (left). This resulted in the formation of crystals with alternating layers as show in *Figure 81* (right). For the modelling diagnostics a model has been created which included the following descriptions: a) classical nucleation theory adapted for solid solutions, b) subgrid resolution of nucleation, c) cross-scale simulations using the Lattice Boltzmann framework for the diffusive transport and the pore-space evolution and d) transient simulations with full chemistry via machine learning surrogate models, e) multivariate time-stepping.

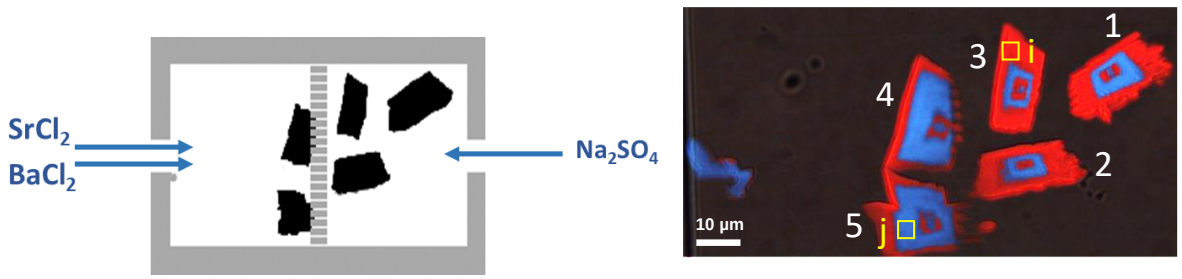

Figure 81 – (left) Schematic of the setup showing the boundary conditions and including the appearance of the first precipitates after ~250 minutes. (right) Raman imaging highlighting the composition of the alternating zonation of the precipitation phases, with alternating layers being ***$(Ba_{0.5}Sr_{0.5})SO_4$*** *(blue) and* ***$(Ba_{0.05}Sr_{0.95})SO_4$*** *(red) adapted from* (Poonoosamy et al., 2021)

The simulation results (M. Mahrous et al.) are shown in *Figure 82*. On the top row the concentration fields at the stationary state after t=250 minutes of the experiment are calculated. On the bottom of *Figure 82* the precipitation rate for the snapshot at t=250 minutes, of the solid solution ***$(Ba_{0.05}Sr_{0.95})SO_4$*** is shown. The reaction rates calculated by the modelling were found to be of similar order of magnitude as the experimental observations. Further investigations are on-going.

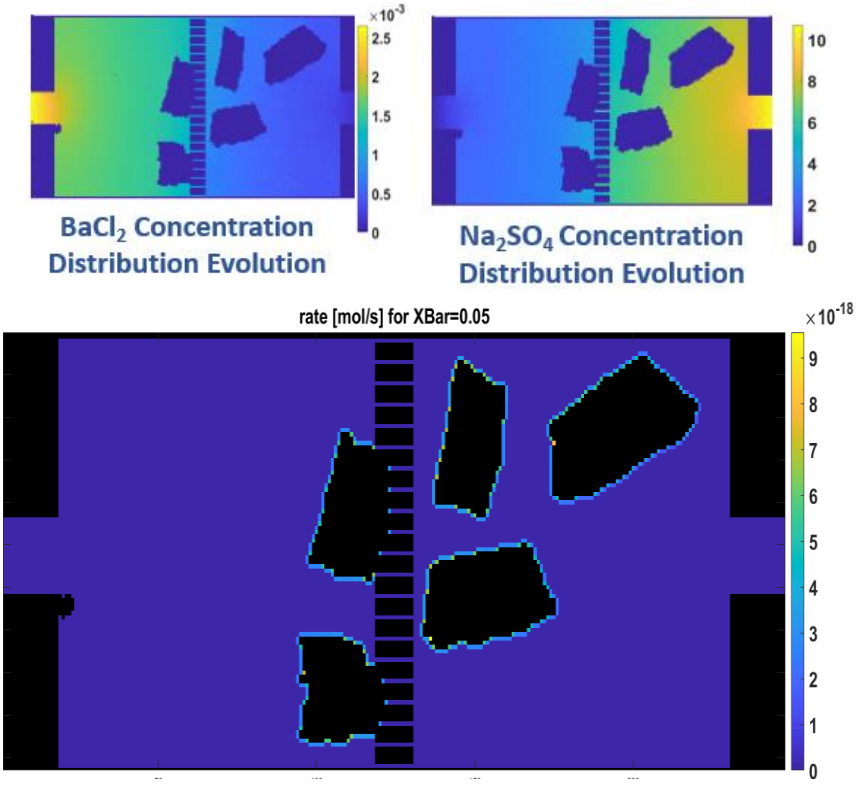

Figure 82 – Cross-scale modelling of the precipitation experiment of (Poonoosamy et al., 2021). *(top) concentration profiles at time ~250 minutes. (bottom) modelling prediction of the precipitation rate of the $(Ba_{0.05}Sr_{0.95})SO_4$ phase. Colours depict the local precipitation rate which is dictated by the local concentrations.*

1.4 Hardware acceleration

The lattice Boltzmann method is a very promising approach to study reactive transport processes at the pore-scale (Kang et al., 2002; Molins et al., 2021; Succi, 2001). The method is based on the solution of the kinetic Boltzmann equation, which recovers at the macroscopic limit the Navier-Stokes equations of fluid motion. Such solvers are suitable for advection-diffusion transport problems where the pore-space is explicitly resolved. By design, the lattice Botlzmann method which is an evolution of the cellular automata and the lattice-gas method (Frisch et al., 1986), is suitable for parallel computations. The main feature of the method is the communication and propagation of information, during one time step, with the immediate next neighbouring computational grid point. This essentially allows to efficiently split the computational domain in sub-domains and assign each subdomain to one CPU core. During the calculations, each subdomain requires to transmit/receive information only from its boundary nodes to the boundary nodes of the neighbouring subdomains. This communication step adds only a small overhead to the computations (Heuveline and Krause, 2010; Latt et al., 2020; Mazzeo and Coveney, 2008). Parallel computing is key to performing high resolution multiphysics simulations as required in the area of nuclear waste management. In the last years the general purpose graphics processing hardware units (GP-GPU) have emerged as an extension to the CPU computational nodes of supercomputing units. The GPU hardware architecture is different than the CPU and for a program to run efficiently, it needs to be re-written in a hardware specific language e.g. Cuda for NVIDIA GPUs.

Through this project, the PSI in-house parallel CPU/GPU code has been further developed to be able to simulate reactive transport problems in 2D/3D complex geometries (Khatoonabadi et al., 2021; Safi et al., 2017). Simulations may run in a single GPU e.g. on a workstation, but is also possible to exploit the parallel GPU cluster architectures. The Swiss Supercomputing Center in Switzerland (www.cscs.ch) possesses such a system with more than 5000 GPU nodes (Potter et al., 2017). For this specific system, where the Nvidia P100 GPU cards with 16GB memory are the basic computational units, it is possible to store and conduct simulations sub-domains of the order of 10 million lattice grid points per GPU.

The code has been highly optimized to run in hybrid CPU/GPU architectures, since at the moment direct communication of GPU's in computing clusters is not available and the communication has to pass through the available CPU's at each computational hardware node. For that a CUDA/C++ code using the Message Passing Interface (MPI) has been developed.

Among several validation benchmarks, a simple diffusion benchmark of a Gaussian hill is shown in *Figure 83 Figure 7* using the multi-component guided equilibrium lattice Boltzmann model (Prasianakis et al., 2017) for two different diffusion coefficients and the comparison with the analytical solution (Ginzburg, 2005).

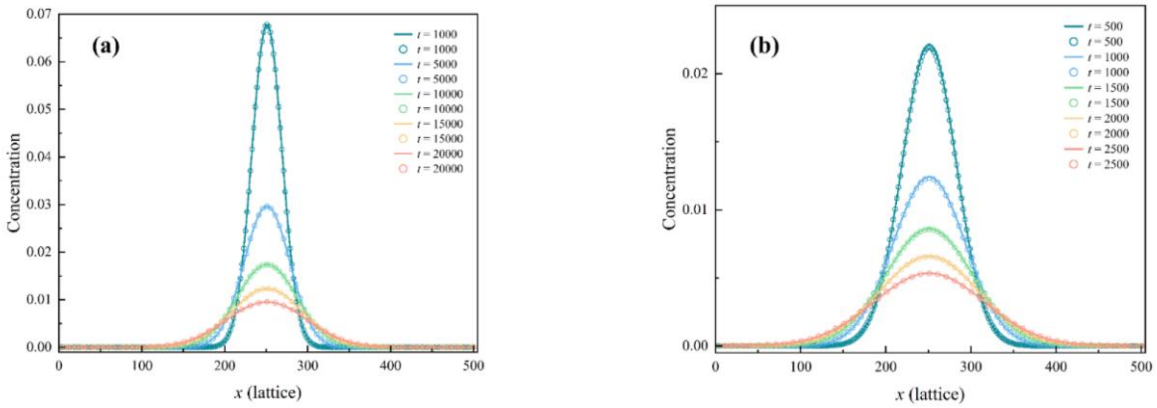

Figure 83 – Validation of the multi-component lattice Boltzmann model and the GPU/CPU code via the simulation of the diffusion of a Gaussian hill at initial concentration C=1.0. Solid lines are the results of the simulatons at different times and the circles represent the analytical solution. The diffusion coefficient for (a) D=4x10^{-10} m^2/s, and (b) D=6x10^{-9} m^2/s

For the lattice Boltzmann codes, the GPU performance is 1-2 orders of magnitude faster than the same simulation on a single CPU making the transition to GPU very attractive. While the flow solver has been ported to GPU, it is currently impossible to run the geochemical solvers which are programmed in Fortran and C, directly on the GPU. For that it would be needed to re-write the full PHREEQC or GEMS code in CUDA programming language, which is not foreseen by their developers to occur in the near future. The solution to run the geochemistry on the GPU comes again via the surrogate models. The neural networks, being simpler mathematical representations than the geochemical codes can be readily ported on the GPU, while several open source neural network algorithms already perform the training and predictions (inferring) directly on the GPU hardware. The lattice Boltzmann code has been also extended to this aspect and first simulations using detailed geochemistry via surrogate models has been conducted.

The performance of the newly developed code for has been benchmarked at the Swiss Supercomputing Center (CSCS) at the Cray XC50 architecture (Piz Daint) (https://www.cscs.ch/computers/piz-daint). The weak scaling benchmark is shown in *Figure 84*. For that a problem which is occupying the full memory of the GPU and solves for five chemical species is run. With 32 GPU's the code can update 1.2 Billion lattice nodes per second.

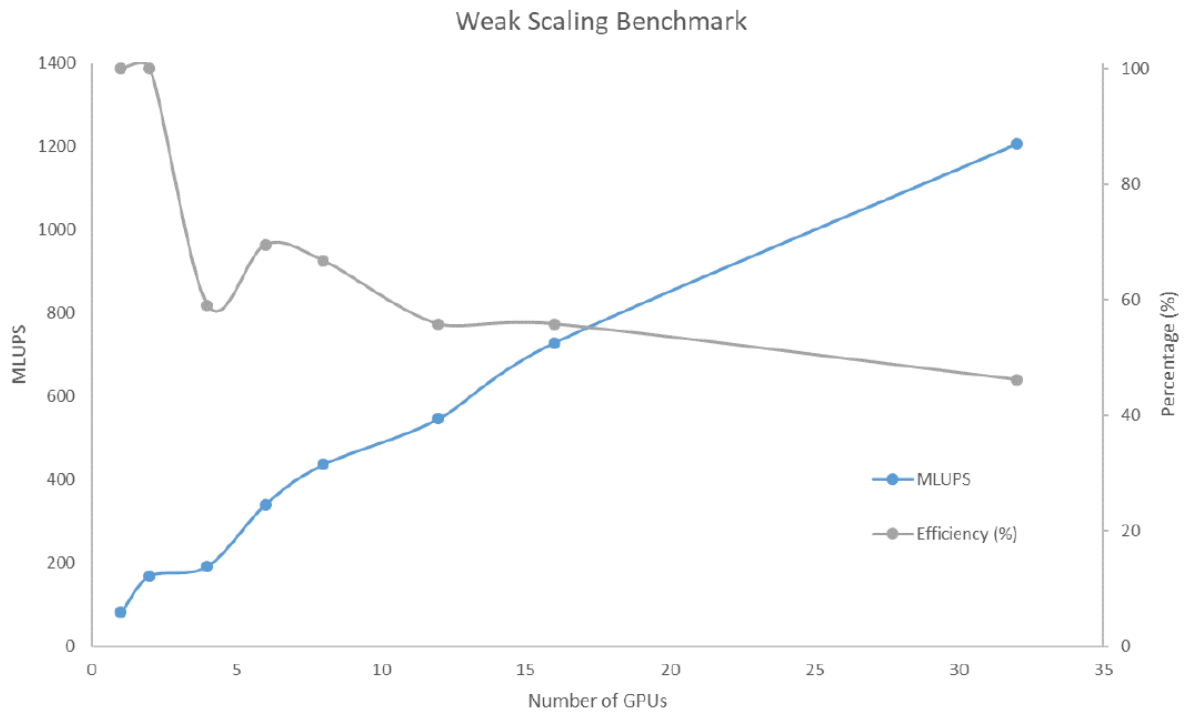

Figure 84 – Weak scaling benchmarking of the reactive transport lattice Boltzmann code at CSCS supercomputing cluster. In the y-axis the metric of million lattice (grid points) updates per second (MLUPS) is depicted (with the corresponding blue curve), and the x-axis represents the number of GPU's used. An efficiency more than 50%, achieved here (shown by the grey curve) with up to 16 GPU's is considered efficient enough.

The *Table 4* highlights the advancements of using hardware and software acceleration. As discussed in the previous sections in a typical reactive transport pore-scale simulator like the lattice Boltzmann solver, chemistry is the main computational bottleneck being almost three orders of magnitude slower (with 10^3 updates/s), compared to the transport solver which on a single CPU core achieves 10^6 updates/s. Surrogate models of the chemistry as for example the neural networks remove the bottleneck posed by the chemical solver since they can perform at a pace of > 10^6 updates per second (N I Prasianakis et al., 2020). At the same time by using GPU architecture and parallel computing it has been possible to increase by two orders of magnitude the flow solver on a single GPU (~10^8 updates/s) and break the barrier of 10^9 updates/sec using multiple GPU's. Last but not least, the lack of possibility of running the geochemical solvers directly on the GPU has been compensated by the surrogate geochemical models (neural networks) which have been also integrated into the GPU code.

Chemistry GEMS / PHREEQC	Transport (flow) Lattice Boltzmann	Chemistry Neural Network
1 CPU-core ~ 1'000/s	1 CPU-core, 4 species ~ 1'000'000/s	1 CPU-core (depending on system) ->more than 1'000'000/s
1 GPU -> Impossible Code not available	1 GPU, 4 species -> 100'000'000/s	1 GPU -> Expected speedup 10-100 times the CPU

Table 4 – Typical example of reactive transport simulation within the Lattice Boltzmann framework. Performance indicator used is the number of computational grid point update per second. Flow equations (middle column) are solved at a pace of three orders of magnitude faster compared to the geochemical reactions (left column). Neural network based surrogate model (using the network presented in the previous section) speeds up the geochemical calculations to match the flow solver pace (right column) this providing a significant overall acceleration.

1.5 Educational, collaborative and modelling platform: https://geoml.eu and https://geoml.ai

In the course of the project and to cover the needs of collaboration and education in the area of machine learning (ML), artificial intelligence (AI) relevant to multiphysics and geochemical modelling, an online open platform has been created corresponding to the following web links: https://geoml.eu and https://geoml.ai (see screenshots in *Figure 85*) . The platform provides a common workspace where jupyter notebooks and other software (Java/C) may be developed, edited and run online. The most important software libraries are pre-installed including machine learning packages saving a lot of time for newcomers since the computational environment and dependencies are already resolved, allowing scientists to focus at research. The platform was deployed by PSI in collaboration with Congineer GmbH (https://congineer.com) and users can login and work via a web browser from any device, without the need for special computer hardware or software.

Figure 85 – Online collaborative and modelling platform: (left) https://geoml.eu *, (right)* https://geoml.ai

Online demonstrators maybe be also conveniently produced. In the following link https://neuralnetrt.geoml.ai/ a demonstrator of a reactive transport solver where the geochemical calculations are accelerated with machine learning is presented. The interface allows the user to parametrise the machine learning model, train the neural network model, produce the surrogate model and finally to test its accuracy in a reactive transport environment by comparing the results of the fully coupled solver with the results of the machine learning accelerated code (see *Figure 86*).

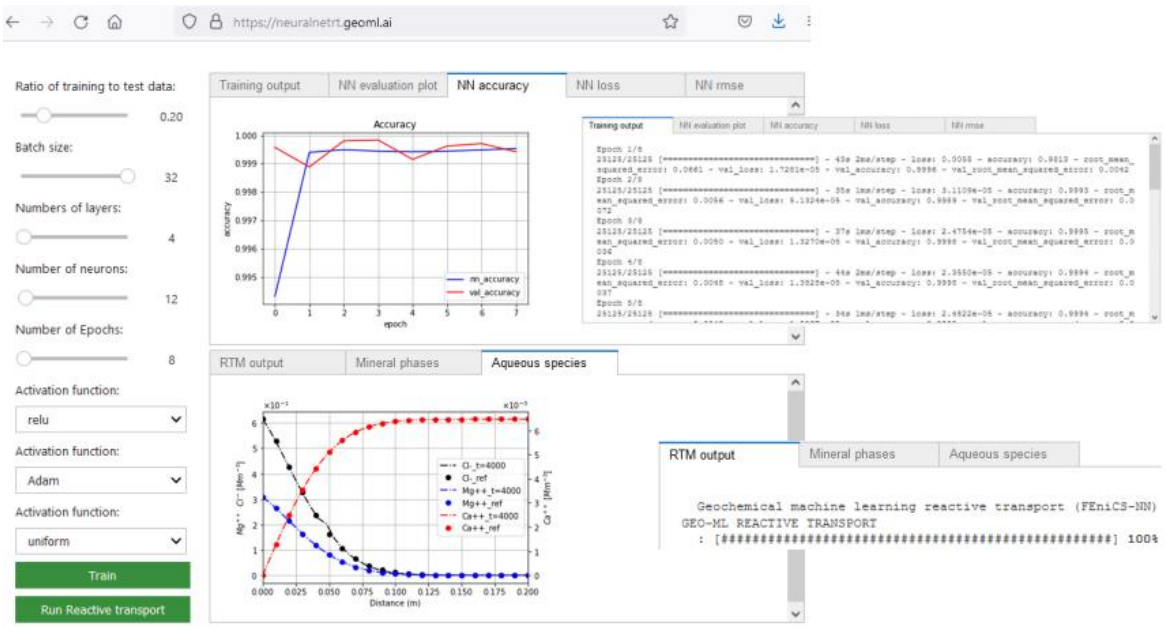

Figure 86 – The online demonstrator https://neuralnetrt.geoml.ai/ *where the neural network accelerated reactive transport calculation is running on the GeoML platform.*

1.6 Acknowledgements

We acknowledge partial financial support by Nagra, Swiss National Science Foundation (SNSF) and Paul Scherrer Institut (PSI)

Code source

The online collaborative platform may be accessed at the following links :

https://geoml.eu , https://lab.geoml.eu/ , https://geoml.ai

Information about the surrogate models, reactive transport and the methodology may be found in (N I Prasianakis et al., 2020).

References

Christo, F.C., Masri, A.R., Nebot, E.M., 1996. Artificial neural network implementation of chemistry with pdf simulation of H_2/CO_2 flames. Combust. Flame 106, 406–427.

Churakov, S.V., Prasianakis, N.I., 2018. Review of the current status and challenges for a holistic process-based description of mass transport and mineral reactivity in porous media. Am. J. Sci. 318. https://doi.org/10.2475/09.2018.03

De Lucia, M., Kempka, T., Jatnieks, J., Kuhn, M., 2017. Integrating surrogate models into subsurface simulation framework allows computation of complex reactive transport scenarios. Eur. Geosci. Union Gen. Assem. 2017, Egu Div. Energy, Resour. Environ. 125, 580–587. https://doi.org/10.1016/j.egypro.2017.08.200

Frisch, U., Hasslacher, B., Pomeau, Y., 1986. Lattice-gas automata for the Navier-Stokes equation. Phys. Rev. Lett. 56. https://doi.org/10.1103/PhysRevLett.56.1505

Ginzburg, I., 2005. Equilibrium-type and link-type lattice Boltzmann models for generic advection and anisotropic-dispersion equation. Adv. Water Resour. 28. https://doi.org/10.1016/j.advwatres.2005.03.004

Heuveline, V., Krause, M.J., 2010. OpenLB: towards an efficient parallel open source library for lattice Boltzmann fluid flow simulations, in: International Workshop on State-of-the-Art in Scientific and Parallel Computing. PARA.

Jatnieks, J., De Lucia, M., Dransch, D., Sips, M., 2016. Data-driven surrogate model approach for improving the performance of reactive transport simulations. Eur. Geosci. Union Gen. Assem. 2016 97, 447–453. https://doi.org/10.1016/j.egypro.2016.10.047

Kang, Q., Zhang, D., Chen, S., He, X., 2002. Lattice Boltzmann simulation of chemical dissolution in porous media. Phys. Rev. E 65, 36318.

Khatoonabadi, M., Safi, M.A., Prasianakis, N.I., Roth, J., Mantzaras, J., Kirov, N., Büchi, F.N., 2021. Insights on the interaction of serpentine channels and gas diffusion layer in an operating polymer electrolyte fuel cell: Numerical modeling across scales. Int. J. Heat Mass Transf. 181. https://doi.org/10.1016/j.ijheatmasstransfer.2021.121859

Kulik, D.A., 2011. Improving the structural consistency of C-S-H solid solution thermodynamic models. Cem. Concr. Res. 41. https://doi.org/10.1016/j.cemconres.2011.01.012

Kulik, D.A., Wagner, T., Dmytrieva, S. V., Kosakowski, G., Hingerl, F.F., Chudnenko, K. V., Berner, U.R., 2013. GEM-Selektor geochemical modeling package: Revised algorithm and GEMS3K numerical kernel for coupled simulation codes. Comput. Geosci. 17, 1–24. https://doi.org/10.1007/s10596-012-9310-6

Laloy, E., Jacques, D., 2022. Speeding Up Reactive Transport Simulations in Cement Systems by Surrogate Geochemical Modeling: Deep Neural Networks and k-Nearest Neighbors. Transp. Porous Media 143, 433–462. https://doi.org/10.1007/s11242-022-01779-3

Laloy, E., Jacques, D., 2019. Emulation of CPU-demanding reactive transport models: a comparison of Gaussian processes, polynomial chaos expansion, and deep neural networks. Comput. Geosci. 23, 1193–1215. https://doi.org/10.1007/s10596-019-09875-y

Latt, J., Malaspinas, O., Kontaxakis, D., Parmigiani, A., Lagrava, D., Brogi, F., Belgacem, M. Ben, Thorimbert, Y., Leclaire, S., Li, S. %J C., Applications, M. with, 2020. Palabos: Parallel Lattice Boltzmann solver.

Leal, A.M.M., Kyas, S., Kulik, D.A., Saar, M.O., 2020. Accelerating Reactive Transport Modeling: On-Demand Machine Learning Algorithm for Chemical Equilibrium Calculations. Transp. Porous Media 133. https://doi.org/10.1007/s11242-020-01412-1

Mazzeo, M.D., Coveney, P. V., 2008. HemeLB: A high performance parallel lattice-Boltzmann code for large scale fluid flow in complex geometries. Comput. Phys. Commun. 178. https://doi.org/10.1016/j.cpc.2008.02.013

Molins, S., Soulaine, C., Prasianakis, N.I.N.I., Abbasi, A., Poncet, P., Ladd, A.J.C.A.J.C., Starchenko, V., Roman, S., Trebotich, D., Tchelepi, H.A.H.A., Steefel, C.I.C.I., 2021. Simulation of mineral

dissolution at the pore scale with evolving fluid-solid interfaces: review of approaches and benchmark problem set. Comput. Geosci. 25, 1285–1318. https://doi.org/10.1007/s10596-019-09903-x

Parkhurst, D.L., Appelo, C.A.J., 2013. Description of input and examples for PHREEQC version 3—a computer program for speciation, batch-reaction, one-dimensional transport, and inverse geochemical calculations. US Geol. Surv. Tech. methods 6, 497.

Poonoosamy, J., Mahrous, M., Curti, E., Bosbach, D., Deissmann, G., Churakov, S. V., Geisler, T., Prasianakis, N., 2021. A lab-on-a-chip approach integrating in-situ characterization and reactive transport modelling diagnostics to unravel (Ba,Sr)SO4 oscillatory zoning. Sci. Rep. 11. https://doi.org/10.1038/s41598-021-02840-9

Potter, D., Stadel, J., Teyssier, R., 2017. PKDGRAV3: beyond trillion particle cosmological simulations for the next era of galaxy surveys. Comput. Astrophys. Cosmol. 4. https://doi.org/10.1186/s40668-017-0021-1

Prasianakis, N.I., Curti, E., Kosakowski, G., Poonoosamy, J., Churakov, S.V., 2017. Deciphering pore-level precipitation mechanisms. Sci. Rep. 7. https://doi.org/10.1038/s41598-017-14142-0

Prasianakis, Nikolaos I, Haller, R., Mahrous, M., Poonoosamy, J., Pfingsten, W., Churakov, S. V, 2020. Neural network based process coupling and parameter upscaling in reactive transport simulations. Geochim. Cosmochim. Acta.

Prasianakis, N I, Haller, R., Mahrous, M., Poonoosamy, J., Pfingsten, W., Churakov, S. V, 2020. Neural network based process coupling and parameter upscaling in reactive transport simulations. Geochim. Cosmochim. Acta 291, 126–143.

Safi, M.A., Prasianakis, N., Turek, S., 2017. Benchmark computations for 3D two-phase flows: A coupled lattice Boltzmann-level set study. Comput. Math. with Appl. 73. https://doi.org/10.1016/j.camwa.2016.12.014

Succi, S., 2001. The lattice Boltzmann equation: for fluid dynamics and beyond. Oxford university press.

VAG discretization of a 3D-2D-1D mixed-dimensional model with resolved interface, application to the drying process between an operating tunnel and a radioactive storage rock

[1]Brenner Konstantin, [1]Chave Florent, [1]Masson Roland

[1]University Côte d'Azur, CNRS, Inria, LJAD

The project leading to this application has received funding from the European Union's Horizon 2020 research and innovation programme under grant agreement No 847593.

Abstract

We consider a 3D-2D-1D mixed-dimensional model in a fractured porous medium coupling the 1D model along the centerline skeleton of a tubular network, the 2D model on a network of planar fractures and the 3D model in the surrounding matrix domain. The transmission conditions are based on a potential continuity assumption at matrix fracture interfaces, and on Robin type conditions at the resolved interfaces between the tubular network and the matrix and fracture network domains. The discretization of this mixed-dimensional model is formulated in the gradient discretization framework, which covers a large class of conforming and nonconforming schemes and provides stability and error estimates based on general coercivity, consistency and limit-conformity properties. As an example of discretization fitting this framework, the mixed-dimensional version of the vertex approximate gradient (VAG) scheme is developed. It is designed to allow nonconforming meshes at the interface between the 1D and 3D-2D domains, to provide a conservative formulation with local flux expressions and to be asymptotic preserving in the limit of high transfer coefficients. Numerical experiments are provided on analytical solutions for simplified geometries, which confirm the theoretical results.

Using its equivalent finite volume formulation, the VAG discretization is extended to a drying mixed-dimensional model coupling the Richards equation in a fractured porous medium and the convection diffusion of the vapor molar fraction along the 1D domain. It is applied to simulate the drying process between an operating tunnel and a radioactive waste storage rock with explicit representation of the fractures in the excavated damaged zone.

Significance Statement

In this work, we introduce a mixed-dimensional 3D-2D-1D model accounting for the coupling between an embedding matrix domain and embedded fracture and tubular networks. The reduction of dimension for the tubular network is based on a resolved interface formulation. The transmission conditions assume the continuity of the potential across fractures, and Robin type conditions across the interface Γ between the 3D-2D fractured porous medium and the 1D centerline of the tubular network.

The discretization of the mixed-dimensional model is formulated in the abstract Gradient Discretization (GD) framework accounting for both conforming and nonconforming approximations. It allows to derive stability and error estimates, assuming that the GD verifies generic coercivity, consistency and limit conformity properties. The VAG scheme, accounting for unstructured polyhedral meshes, was previously developed for Discrete Fracture Matrix models. It is here extended to the coupling with the 1D model using a 1D Finite Element discretization possibly nonconforming with the VAG discretization at the interface Γ. It is based on a simple interpolation operator and a lumping of the VAG basis functions at the tubular interface. Although the presentation assumes for readability a single cylindrical tube intersected by the fracture network, the framework and the discretization can be readily extended to more general tubular networks, based on the definition of a surjective mapping from the tubular network interface to its centerline. The VAG scheme is proven to meet the GD properties and provide first order error estimates on piecewise smooth solutions. It is also asymptotic preserving in the limit of large transfer coefficients. These results are confirmed numerically on analytical solutions using a simplified geometry based on a plane interface.

Exploiting the VAG equivalent finite volume formulation and the local flux expression, the discretization is extended to a nonlinear drying model coupling the Richards equation in the fractured porous medium to the convection diffusion of the vapor molar fraction along the 1D domain. It is successfully applied to simulate the drying process between an operating tunnel and a radioactive waste storage rock with explicit representation of the fractures in the excavated damaged zone.

Table of content

List of figures

1. Mixed-dimensional 3D-2D-1D drying model

The computational domain represents an excavated tunnel embedded in a fractured porous medium. To simplify the notations and focus on the difficulties raised by the fracture network, the porous geometrical domain is assumed to be an hollow cylinder (see Figure 87 – *mixed-dimensional geometry*). From a mathematical viewpoint, let ω and $\omega_g \subset \omega$ be two open, bounded, simply connected polygonal sets of R^2 with Lipschitz boundaries and $L > 0$ be the excavation length. The porous medium can be seen as a cylindrical domain $\Omega_p := (0,L)\times(\omega\backslash\omega_g)$ with an axial hole $(0,L)\times\omega_g$ corresponding to the excavated tunnel, along the x-axis for simplicity. The 1-dimensional axis of the tunnel is denoted by $\Omega_g = (0, L) \times \{\boldsymbol{x}_g\}$, with $\boldsymbol{x}_g$ the center of gravity of ω_g to fix ideas. The porous medium Ω_p contains a 2-dimensional fracture network Ω_f. The 3-dimensional matrix domain is denoted by $\Omega_m := \Omega_p \setminus \Omega_f$. The interface between the tunnel and the porous medium is denoted by $\Gamma := (0, L) \times \partial\omega_g$ and we denote by Σ_Γ the intersection between the fractures and the interface Γ.

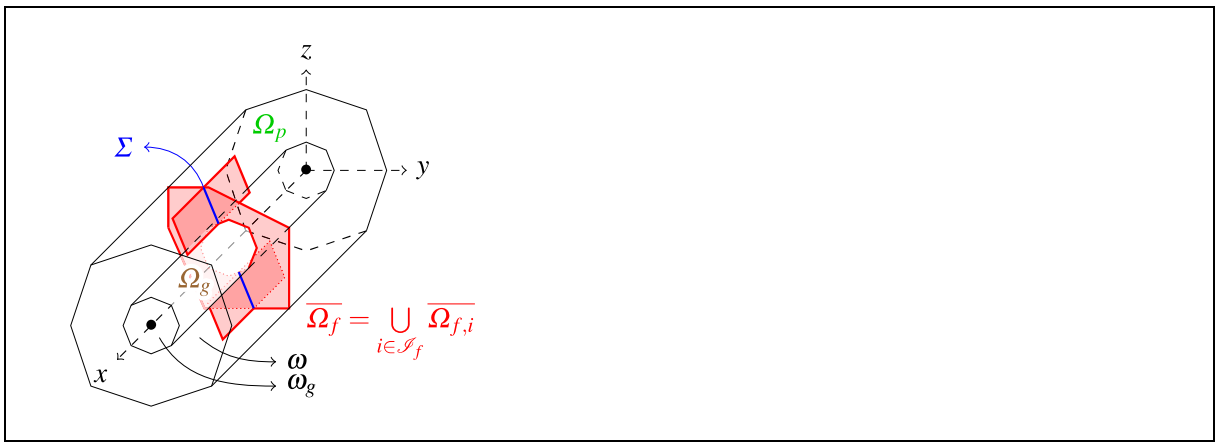

Figure 87 – *mixed-dimensional geometry*

We denote by p^l the liquid pressure in the porous medium and by c^g the vapor molar fraction in the tunnel and by $t_F = 100$ years the simulation time. Let $\mathrm{rt} \in \{m,f\}$ denote the matrix or fracture rocktypes. The liquid saturation as a function of the liquid pressure is denoted by $S_{\mathrm{r}\,\mathrm{t}}^{l}$ and the liquid relative permeability as a function of the liquid saturation by $k_{r}^{l}{}_{,\mathrm{rt}}$. The liquid molar density is denoted by ζ^{l} and the liquid dynamic viscosity by μ^l. Using the fixed gas pressure $p^g = 10^5$ Pa and temperature $T = 303$ K, the gas molar density is set to $\zeta^g = p^g/RT$ mol.m^{-3} with $R = 8.314$ J.mol^{-1}.K^{-1}. In the matrix, the permeability is denoted by $\Lambda_m = 5 \cdot 10^{-20}$ m^2 and the porosity is $\phi_m = 0.15$. The fractures are assumed to be filled only by the gas and liquid phases, the porosity is hence set to $\phi_f = 1$, the fracture aperture to $d_f = 1$ mm and the tangential permeability Λ_f is given by the Poiseuille law. In the tunnel, we denote by $v = 0.1$ m.s^{-1} the constant gas velocity, by $\Lambda_g = 2 \cdot 10^{-3}$ m^2.s^{-1} the turbulent diffusion coefficient, and by $H_m = H_f = 1.46 \cdot 10^{-2}$ mol.m^{-2}.s^{-1} the molar convective transfer coefficients computed from the Dittus–Boelter correlation accounting for the turbulent boundary layer of the vapor molar fraction at the interface Γ. Note that this choice of the transfer coefficients with $H_m = H_f$ implicitly assumes that we can neglect the influence of the porous media flow on the gas velocity in the tunnel, which is consistent with the constant gas velocity assumption along the tunnel. The function $\bar{c}$ defined below computes the vapor molar fraction at the interface Γ and Σ_Γ as a function of the liquid pressure. It is based on the liquid-gas thermodynamical equilibrium for water assuming the vaporization of the liquid phase at the interface between the porous medium and the tunnel.

$$\bar{c}(p^l) := \frac{p_{sat}(T)}{p^g}\, e^{-(p^g - p^l)/(\zeta^l RT)},$$

We consider the following mixed-dimensional model coupling the Richards equation in the matrix and in the fracture network together with the convection dominated transport of the vapor molar fraction along the tunnel (Figure 88 – *mixed-dimensional drying model*). This model is a good approximation of an isothermal drying process at the interface between the fractured porous medium and the ventilated tunnel.

$$
\begin{cases}
\phi_m \zeta^l \partial_t(S_m^l(p^l)) + \mathrm{div}(\boldsymbol{q}_m) = 0 & \text{in } (0,t_F)\times\Omega_m,\\
d_f\phi_f\zeta^l\partial_t(S_f^l(\gamma_f p^l)) + \mathrm{div}_f(\boldsymbol{q}_p) = 0 & \text{in } (0,t_F)\times\Omega_f,\\
\zeta^g|\omega_g|\partial_t c^g + \mathrm{div}_g(\boldsymbol{q}) = 0 & \text{in } (0,t_F)\times\Omega_g,\\
\boldsymbol{q}_m = -\dfrac{\zeta^l}{\mu^l}k^l_{\mathrm{r},m}(S_m^l(p^l))\boldsymbol{\Lambda}_m\nabla p^l & \text{in } (0,t_F)\times\Omega_m,\\
\boldsymbol{q}_f = -d_f\dfrac{\zeta^l}{\mu^l}k^l_{\mathrm{r},f}(S_f^l(\gamma_f p^l))\boldsymbol{\Lambda}_f\nabla_\tau\gamma_f p^l & \text{in } (0,t_F)\times\Omega_f,\\
q_g = \zeta^g|\omega_g|(vc^g - \Lambda_g\partial_x c^g) & \text{in } (0,t_F)\times\Omega_g,\\
\boldsymbol{q}_m\cdot\boldsymbol{n}_\Gamma = H_m(\overline{c}(\gamma_\Gamma p^l) - c^g) & \text{on } (0,t_F)\times\Gamma,\\
\boldsymbol{q}_f\cdot\boldsymbol{n}_{\Sigma_\Gamma} = d_f H_f(\overline{c}(\gamma_{\Sigma_\Gamma}\gamma_f p^l) - c^g) & \text{on } (0,t_F)\times\Sigma_\Gamma,
\end{cases}
$$

Figure 88 – *mixed-dimensional drying model*

2. Vertex Approximate Gradient (VAG) Finite Volume discretization

The VAG 3D-2D-1D mixed-dimensional discretization is a Finite Volume scheme based on cell, matrix node, fracture face and tunnel node DOFs as illustrated in Figure 89 – *VAG DOFs*. Its main features are to apply to polyhedral cells, to rely on compact fluxes (see Figure 90 – *VAG flux connectivity*), to account for non-matching meshes between the tunnel and the porous medium, and to be asymptotic preserving in the limit of large transfer coefficients at the interface between the porous medium and the tunnel. Let us refer to (K. Brenner, 2022) for details.

The numerical analysis of the scheme is based on the Gradient Discretization framework which has been extended to the 3D-2D-1D mixed-dimensional framework. The first order convergence in energy norm for a linear diffusion model has been proven theoretically and checked numerically on a manufactured analytical solution as exhibited in Figure 91 – *Numerical convergence of the mixed-dimensional VAG scheme for a manufactured analytical solution* (see (K. Brenner, 2022)] for details).

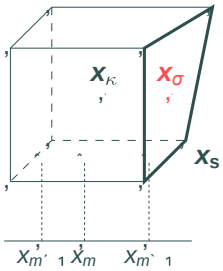

Figure 89 – *VAG DOFs*

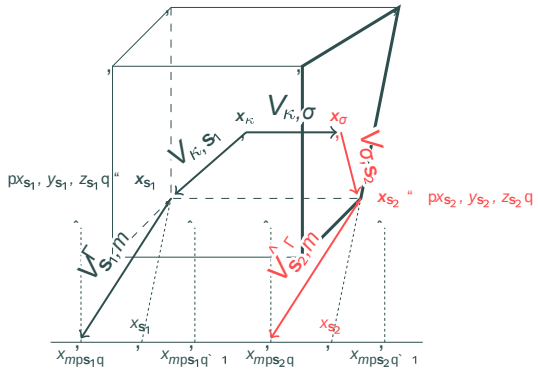

Figure 90 – *VAG flux connectivity*

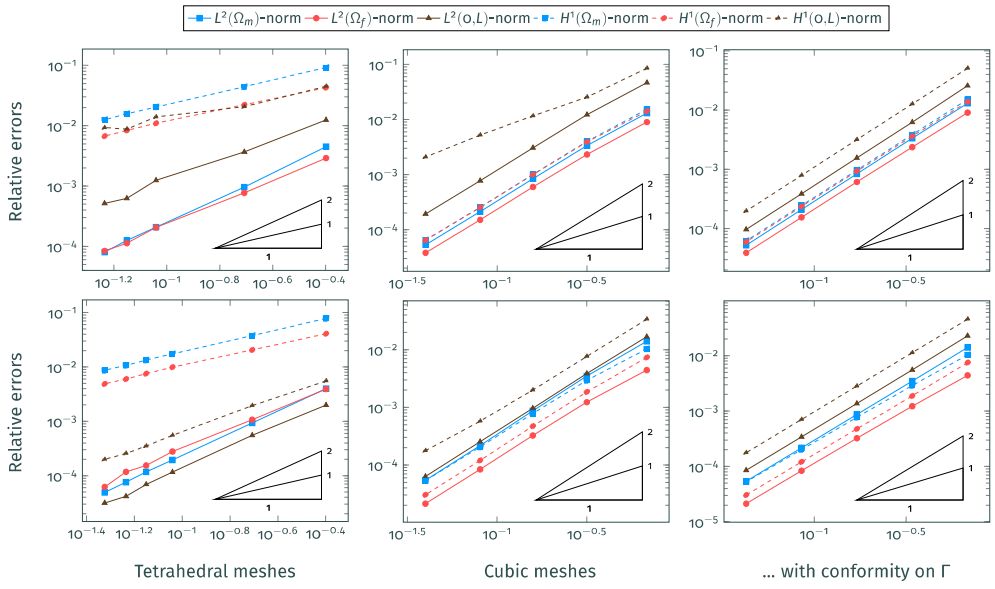

Figure 91 – *Numerical convergence of the mixed-dimensional VAG scheme for a manufactured analytical solution*

The VAG finite volume discretization is extended to the drying model coupling the Richards equation in the fractured porous medium with the convection diffusion of the vapor molar fraction along the tunnel. The spatial discretization is based on the VAG fluxes combined with an upwind approximation of the mobilities in the matrix and fracture equations and of the convective term in the tunnel (see (K. Brenner, 2022)). A standard implicit Euler method with an adaptive time step is used to discretize in time. The nonlinear systems are solved at each time step of the simulation using a Newton algorithm with exact computation of the Jacobian and a relaxation of the Newton step based on a specified maximum variation of the Newton increment.

3. Numerical Results for the 3D-2D-1D drying model

The physical domain represents a quarter of a cylinder with an axial hole along the x-axis corresponding to the excavated tunnel. The fracture network is composed of 10 slightly inclined fractures, evenly distributed along the x-axis and at equal distance from each other.

The time step is set to 1 second initially and increases up to 1 year. The simulation requires 190 time steps, and the Newton's algorithm never failed to converge with an average of 4.2 iterations by time step. We display in Figure 92 – *hexahedral mesh of the quarter of cylinder* the mesh used to discretize the geometry, composed of 354354 parallelepipedic cells and where each fracture is composed of 585 mesh faces.

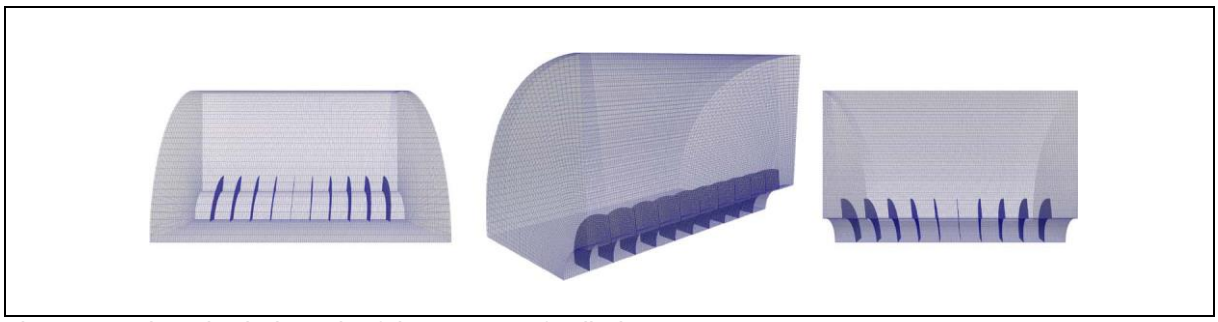

Figure 92 – *hexahedral mesh of the quarter of cylinder*

We depict in Figure 93 – *Interface(a) and tunnel (b) relative humidity as a function of time* the relative humidity average as a function of time on Γ and in Ω_g, respectively, in Figure 94 – *Relative humidity along the interface at different times* the relative humidity on Γ at different times, in Figure 95 – *evolution of the vapor molar fraction (dimensionless) along the tunnel (time scale in years)* the vapor molar fraction on Ω_g at different times, and in Figure 96 – *evolution of the matrix (up) and fracture (bottom) gas saturation* the gas saturation in the matrix and the fracture network at different times.

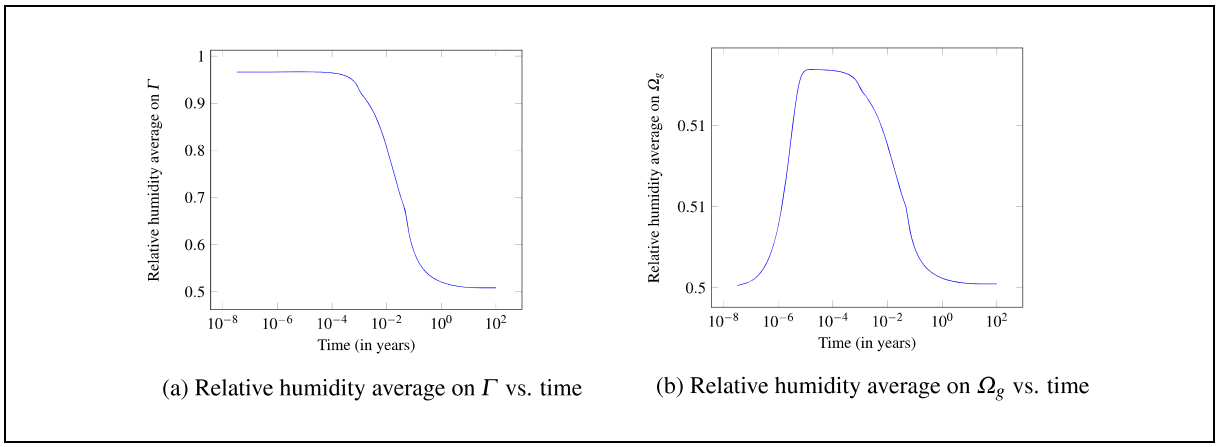

(a) Relative humidity average on Γ vs. time

(b) Relative humidity average on Ω_g vs. time

Figure 93 – *Interface(a) and tunnel (b) relative humidity as a function of time*

We can identify four stages of drying: (i) the first stage appears at the early stage of the simulation, where the relative humidity at the interface is roughly constant and close to 1; (ii) in the second stage, the gas is entering the matrix and the molar flow rate on the interface decrease, but the fracture stay saturated; (iii) the third stage is very short and corresponds to the desaturation of fractures that causes a quick drop of humidity; (iv) the last stage corresponds to the gas spreading into the matrix leading to convergence towards the steady state, with a small but nonzero molar flow rate at the interface and a relative humidity close to its initial value.

The main interest of this test case is to show the different drying dynamics induced by the highly contrasted properties of the matrix and fracture rocktypes (capillary pressures, relative permeabilities and absolute permeabilities). Although these dynamics remain here short compared with the global time scale of the exploitation phase of the storage, note that it will no longer be the case when taking into account the heating induced by the radioactive wastes in the storage rock, which is the next objective of this work.

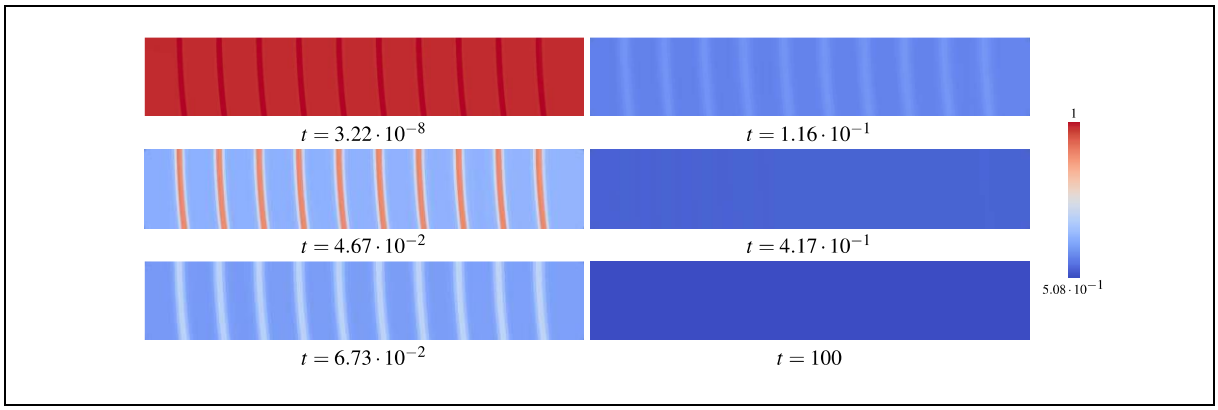

Figure 94 – *Relative humidity along the interface at different times*

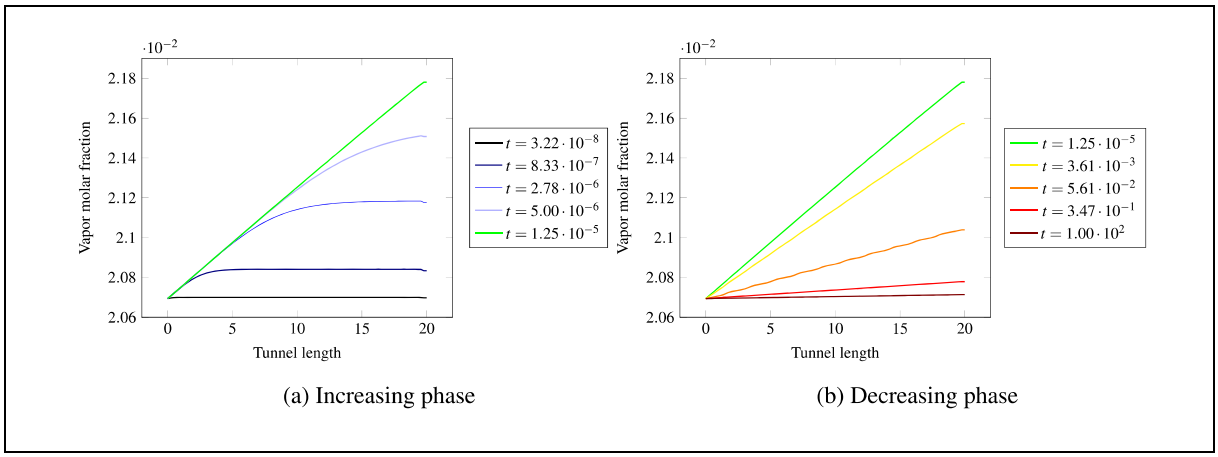

(a) Increasing phase (b) Decreasing phase

Figure 95 – *evolution of the vapor molar fraction (dimensionless) along the tunnel (time scale in years)*

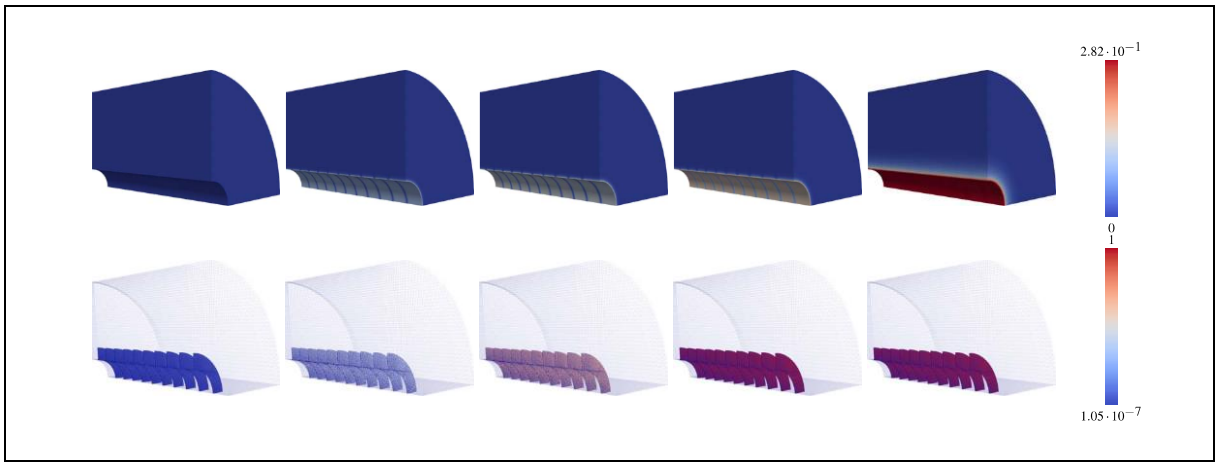

Figure 96 – *evolution of the matrix (up) and fracture (bottom) gas saturation (air)*

Code source

The drying model has been implemented in a prototype code that can be provided on demand.

References

(K. Brenner, 2022)K. Brenner, F. Chave, R. Masson, Gradient discretization of a 3D-2D-1D mixed-dimensional model with resolved interface, application to the drying of a fractured porous medium, IMA Journal of Numerical Analysis, 23 dec. 2022, https://hal.archives-ouvertes.fr/hal-03426471